UNIVERSITÀ
DI TRENTO

Doctoral School in Mathematics

Numerical methods for efficient blood flow simulations: application to coronary artery disease

Alessia Lucca

UNIVERSITY OF TRENTO
DEPARTMENT OF MATHEMATICS

November 1, 2023

UNIVERSITÀ DI TRENTO | Department of Mathematics

Doctoral thesis in **Mathematics**, XXXVI Cycle

Department of Mathematics, **University of Trento**

Accademic year: 2022/2023

Supervisors: **Prof. Lucas Omar Müller**, *University of Trento*
Prof. Saray Busto Ulloa, *Universidade de Vigo*
Prof. Eleuterio Francisco Toro, *University of Trento*

University of Trento
Trento, Italy
November, 2023

Acknowledgments

Over the years there have been many people who have helped me on this long-term project. Their support and teachings were fundamental for each of my achievements.

First and foremost, I am extremely grateful to my supervisors, Prof. Lucas O. Müller, Prof. Saray Busto Ulloa and Prof. Eleuterio F. Toro, for their invaluable advice, guidance and continuous support during my PhD program. Their knowledge, experience and dedication to science have inspired and encouraged me in all the time of my academic research.

I would like to offer my special thanks to Prof. Michael Dumbser. I have been extremely fortunate to have had the opportunity to work with him during my studies. I am grateful for his guidance, continuous support, ideas and help, which have been instrumental in the development of the numerical part of my PhD research, as well as for the many opportunities that he has offered me. I hope to have fully absorbed his dedication to research and will always be grateful for this opportunity.

An essential aspect of my PhD research project was the opportunity offered to me by Prof. Leif R. Hellevik (NTNU, Trondheim, Norway) to visit his research facility and join his biomedical group during a research period of four months. During my stay in Trondheim I learned a lot about blood flow modelling and became familiar with medical data processing and imaging segmentation technique. I sincerely thank Prof. Hellevik and Dr. Fredrik E. Fossan for providing the clinical data used in this thesis, sharing their invaluable know-how in FFR predictions and their fundamental collaboration in the development of the research project presented in Chapter 3.

I am pleased to acknowledge Prof. Luigi Fraccarollo for all the time we met working on the inclusion of the pressure guidewire in the modeling pipeline and for his support during this troubled project. I would like to thank also to Prof. Christian Vergara for his instructive advice on our medical applied work.

A special thought and thank goes to Prof. Saray Busto Ulloa, from Universidade de Vigo, Spain. Her unmissable support and helpful advice have been crucial at every stage of my studies and in my daily life. I would like to warmly thank her to all the help she gave me in developing the numerical methodologies and codes as well as to offer me the opportunity to visit her in Spain. Working together has allowed me to enrich my personal baggage of knowledge and professionalism and to achieve goals and rewards.

I also thank the University of Trento, and in particular the Department of Mathematics, for providing the financial and academic support to carry out this PhD research project in terms of scholarship and allowances for participating in relevant conferences and advanced courses and workshops.

I conclude this section expressing my profound gratitude to my parents, my sister, Pier Luca and the rest of my family. Without their tremendous understanding, encouragement and patience, it would be impossible for me to complete this long journey.

Contents

Preface

The heart plays a role of primary importance for human life and, as all other organs and muscles, needs a continuous supply of oxygen and other metabolic substrates to work. The oxygen needed by the cardiac muscle is provided by specific arteries, the coronary arteries, that depart from the aorta and encircle the heart branching throughout the tissue. Since the myocardium lacks the ability to contract anaerobically, the constant supply of oxygen by the coronary vessels is crucial for the regular function of the heart. Hence, this mechanism can not work properly if an abnormal narrowing is present in the main coronary arteries reducing the blood flow. It is, therefore, of major importance to study this type of issues.

Stable Coronary Artery Disease (CAD) is a common disease characterized by the buildup of atherosclerotic plaques in the coronary vessel wall leading to a lumen constriction. As the coronary blood vessels become occluded, blood flow to the myocardium is limited, leading to a condition of ischemia. Accordingly, the heart does not receive optimal quantities of oxygen. This situation can lead to chest pain, potential scarring of the heart muscle without regrowth of cells and, ultimately, death.

According to the World Health Organization (WHO) [165], ischemic heart disease was the leading cause of death worldwide in 2019, accounting for 16% of total deaths, and in 2020 it confirmed itself at the top of the list of the main causes of death in the USA, registering an increase of 5% compared to the previous year [2]. Cardiovascular diseases thus represent a massive public health problem, also in terms of monetary cost.

In the case of stable CAD, the most recent guidelines [123] recommend deciding whether and which treatment should be adopted after evaluating, not only the anatomical location and size of a stenosis caused by an atherosclerotic plaque, but also its functional significance, i.e. the actual extent of coronary blood flow restriction caused by the lesion. In fact, Fractional Flow Reserve (FFR), which measures the trans-stenotic pressure drop, is the gold standard for the functional assessment of coronary stenosis in stable CAD. Currently, FFR is assessed invasively, during transfemoral or transradical catherization, under drug-induced hyperemia, i.e. maximal blood flow is induced by the administration of vasodilatory drugs, such as adenosine or papaverine. The obtained measurements are then compared against FFR thresholds defined in order to guide the therapy for stable CAD and to decide whether surgical procedure is needed or if patients can just be treated with optimal medical therapy.

Despite European Society of Cardiologists recommendation [123], FFR remains under-used due to its associated costs, the high price of a single FFR-wire as well as the additional substantial cost of using adenosine [15]; due to its invasive nature, with the associated risk for the patient [206]; and due to the need of trained interventionalists. Therefore, it emerges the need of developing non-invasive diagnostic tests that can hypothetically act

as an effective gatekeeper for the cardiac revascularization in patients with stable CAD suspicion.

This clinical problem has inspired the research developed in this thesis. The prediction of pressure and flow in the arterial system for the diagnosis of coronary artery disease evaluating non-invasively FFR involves two main fields. One mostly regards cardiovascular modeling aspects. The model has to capitalise on non-invasive subject-specific clinical data in order to reliably represent the patient-specific pathological condition as well as the clinical setting. On the other hand, numerical methods, which can solve blood flow equations in tortuous multi-generation systems of branching and merging junctions of deformable vessels with widely different diameters and lengths, are crucial to deliver efficiently accurate predictions. Our research is therefore focused on this two main aspects which correspond to the two parts in which this thesis is organized.

Regarding the first point, we extend the CCTA-based FFR model proposed in [89, 149] to incorporate the presence of a catheter in the FFR modeling pipeline analyzing its impact on local fluid dynamics and FFR prediction. In order to investigate these modeling features, we exploit the open source library CBCFLOW [76] which allows us to efficiently solve the incompressible Navier-Stokes equations in complex and rigid three-dimensional coronary trees. Even if this work is presented in the second part of the thesis, it corresponds to the earlier period of the research and has motivated the development of novel numerical methods that could be easily extended to deal with more complex haemodynamics problems.

Therefore, aiming at proposing a geometrical multiscale model and having in mind also a possible development of more complex mathematical models such as extension to an arbitrary Lagrangian-Eulerian formulation for solving moving boundary problems or even considering a fluid-structure interaction problem, we direct our research to the design of new efficient numerical methods able to solve haemodynamics at a reasonable computational effort. To this end, we extend the projection hybrid finite volume/finite element method first put forward in [24, 46, 185] to a fully implicit methodology providing an efficient incompressible Navier-Stokes equations solver for 3D blood flow simulations.

It is nonetheless true that the numerical simulation of the entire cardiovascular system or even of large number of vessels has an unaffordable computational cost in the three-dimensional case, typically requiring high-performance computers and a huge amount of processing resources. Seeking for reasonable trade-off between accuracy and computational cost, also a novel semi-implicit finite volume scheme is developed for blood blow in one dimensional viscoelastic vessels and networks.

In what follows, we include a detailed description of the contents of each part of the thesis.

Part I. Mathematical modeling and numerical methods. We devote this part of the thesis to the development of numerical methods for the simulation of incompressible flows with particular emphasis on the simulation of human cardiovascular haemodynamics.

First, we present a novel fully implicit hybrid finite volume/finite element (FV/FE) method for the solution of incompressible flows in unstructured staggered grids. Following some ideas from previous works on semi-implicit hybrid FV/FE schemes, [24, 46, 185], and on splitting strategies, [219], the algorithm decouples the computation of the pressure field and the conservative variables. The resulting transport-diffusion

equations for the momentum are then solved at the aid of an implicit finite volume approach making use of an inexact Newton-Krylov method with an SGS preconditioner. On the other hand, a finite element method supplies the solution of the Laplace problem related to a pressure correction step. In this way, the implicit discretization yields an efficient scheme avoiding the severe CFL condition that may arise when using explicit or semi-implicit methods for blood flow dynamics. Several classical fluid dynamics problems are presented in order to study empirical convergence rates and to validate the proposed numerical approach comparing the obtained results obtained against either analytical solutions, numerical reference solutions or available experimental data.

The second chapter of this thesis describes a novel staggered semi-implicit finite volume method for the simulation of one-dimensional blood flow in networks of elastic and viscoelastic vessels. The one-dimensional blood flow model is derived from the incompressible Navier-Stokes equations, specifying the adopted tube law. Then, following the ideas behind the fully implicit hybrid finite volume/finite element method presented in Chapter 1, the governing equations are split into a convective subsystem, which is discretized explicitly in time, a diffusive subsystem and a pressure subsystem, both implicitly treated. This leads to a semi-implicit scheme characterized by a CFL-type time step restriction which depends only on the bulk velocity of the flow and not on the speed of the pressure waves nor on viscoelasticity. To extend the proposed methodology to the case of networks, a novel and very simple 3D approach for the treatment of junctions is proposed. This methodology is able to capture the main features of the junction geometry so that the flow computation accounts for the angles between the incident vessels. Finally, a set of tests are run both for single elastic and viscoelastic vessels and to assess the new 3D approach proposed for the simulation of junctions.

The fully implicit hybrid FV/FE methodology to solve the 2D and 3D incompressible Navier-Stokes equations has been presented in [135]. Besides, the semi-implicit approach for the simulation of networks of vessels has been introduced in [136].

Part II. Model-based FFR Prediction. This second part of the thesis focuses on the modeling of coronary trees in the pathological condition which occurs when a lumen narrowing is presented. In particular, the goal is to present a CCTA-based FFR model which incorporates clinical imaging and patient-specific characteristics to predict the haemodynamics behavior and properties of particular individuals, reducing invasive measurements.

Computation of CCTA-FFR requires several steps going from an accurate construction of a patient-specific 3D anatomic model of the epicardial coronaries, based on clinical images outlining the computational domain, to the definition and solution of a blood flow model, specifying micro-circulatory models for coronary bed during hyperemia. Although the presence of the guidewire is often neglected, studies conducted both in vitro [10] and computationally with idealized geometries and in a patient-specific domain [21] have shown that the haemodynamic alteration caused by the presence of the guidewire can lead to an underestimation of the predicted FFR. So we aim to quantify the impact of considering the presence of the pressure guidewire in FFR prediction for a wide range of FFR values and considering several

patients. We extend the CCTA-derived FFR model first put forward in [89] and [149] to incorporate the presence of the pressure guidewire in the modeling pipeline and we perform three dimensional simulations in the configuration with and without the presence of the pressure guidewire on a sample of 18 patients with suspected stable CAD. Flow rates, pressure distributions and predicted FFR in both configurations are then analyzed and compared.

The main results concerning this part have been presented in [137].

Appendices.

Appendix A is devoted to the explicit FORCE-MUSCL-Hancock scheme developed for comparison and validation of the semi-implicit finite volume scheme proposed in Chapter 2 for 1D blood flow simulations.

Appendix B recalls the scientific articles where the main results of this thesis are presented.

Appendix C contains a brief summary of this dissertation.

Part I

Mathematical models and Numerical Methods

Introduction

The development of numerical methods for the simulation of incompressible flows is a wide research field that allows the solution of many industrial, environmental and biological problems [129, 105, 215, 183]. One of those applications, in which this thesis is particularly focused, is the simulation of blood flow in the human cardiovascular system. Nowadays, the development of efficient mathematical models and numerical methods for the study of haemodynamics is becoming increasingly prominent, especially in the analysis of pathological states of the cardiovascular system [211, 175, 220, 214, 176]. More and more, numerical models represent an invaluable tool for a consistent support in the medical diagnosis and treatment of diverse pathologies supplying meaningful data that otherwise would require the need of classical invasive medical techniques, which might be a risk for the patients and generate high healthcare costs. As we will see in the second part of the thesis, a common example of this situation is the presence of stenosis in a vessel. An abnormal narrowing in an artery may lead to many syndromes, lowering the life quality of the patient and even causing his death. To analyze in detail its impact on normal physiological functioning of the cardivascular system, an alternative to invasive techniques may be the use of simulation tools, see e.g. [211, 78, 89, 137]. The physical geometry can be obtained via medical images and segmentation algorithms which allow the definition of a computational domain [204]. Then, appropriate numerical methods can be applied to simulate the clinical problem under study. Therefore, having a methodology able to efficiently solve this kind of flows would constitute an important step forward in personalized medicine that might help the medics in the decisions they need to take for the optimal treatment of each patient. For a non-exhaustive overview of some computational methods that have already been successfully applied to the simulation of the human cardiovascular system, the reader is referred to [80, 82, 66, 176, 84, 92, 175, 174, 197, 198, 154, 153, 148] and references therein.

From the numerical point of view, some of the most widespread methodologies to simulate incompressible flows fall in the framework of pressure based semi-implicit solvers, see e.g. [108, 60, 168, 169, 16, 52, 105]. After performing an adequate flux-vector splitting of the governing PDE system, they compute the pressure field by deriving a Poisson-type equation from the mass and momentum conservation equations. Meanwhile, the velocity field is approximated solving a proper transport-diffusion subsystem complemented with a pressure correction stage where the velocity is updated using the new pressure in order to obtain a divergence-free velocity. This results in the decoupling of the bulk flow velocity from the fast sound waves, [219]. As a consequence, the CFL condition depends only on the mean flow velocity and not on pressure waves yielding to efficient numerical schemes.

Within this framework, many families of methods have been developed depending on the approach selected to solve each subsystem. One of them is the hybrid finite volume/finite

element (hybrid FV/FE) methodology initially put forward in [24, 46] for incompressible flows and which is one of the basis for the development of the novel fully implicit hybrid FV/FE methodology proposed in this thesis. The aforementioned semi-implicit hybrid family deals with a wide variety of mathematical models in the context of computational fluid dynamics, including Newtonian and non Newtonian incompressible flows [24, 46, 45], weakly compressible flows [22, 44], all Mach number flows [47, 185] and the shallow water equations [43]. They rely on the use of a primal triangular/tetrahedral mesh for the implicit discretization of the pressure subsystem according to a classical finite element method, while the convective-viscous subsystem is solved on a edge-based/face-based staggered dual mesh exploiting an explicit finite volume scheme for the convective terms combined with a Galerkin approach to handle diffusion terms. Moreover, diffusion can also be treated implicitly leading to a semi-implicit scheme characterized by a CFL condition which does not depend neither on the sound waves nor on the diffusion terms, but only on the bulk flow velocity, [45]. Nevertheless, even if the time step restriction, imposed by the CFL condition, is less restrictive than for fully explicit schemes, the main concern of this methodology is that the step time still results too computational demanding when addressing haemodynamics in complex 3D geometries, leading to very high time-consuming simulations.

With the scope of obtaining an efficient method suitable for haemodynamic applications, in the first chapter of this thesis, we propose the extension of the hybrid FV/FE family to a fully implicit methodology. In particular, the most significant innovations concern the convective-viscous subsystem. More precisely, the novel approach is based on the combination of Crouzeix-Raviart basis functions and of an implicit finite volume scheme to solve the convective-viscous system. Its implicit discretization will lead to a nonlinear and nonsymmetric system which will be solved with the aid of a Newton-Krylov approach. Specifically, we will employ a Newton algorithm combined with one of the following Krylov subspace methods: either a generalized minimal residual approach (GMRES) [188] or a stabilized biconjugate gradient algorithm (BiCGStab) [223]. Moreover, the use of the LU factorization symmetric Gauss-Seidel preconditioner together with a proper reordering of the nodes are also proposed in order to improve the convergence behavior of these iterative algorithms, [73, 63].

Although many contributions have already been made in the context of fully implicit schemes for the incompressible Navier-Stokes equations, see e.g. [221, 138, 13, 14, 162, 184, 131, 194] and references therein, most of them discretize the complete system of Navier-Stokes equations without considering a splitting of the momentum and pressure computation and/or employing a unique family of numerical methods for the spatial discretization, in contrast with the new hybrid method proposed in this thesis. In addition, the presented methodology is compatible with MPI parallelization. The use of a splitting technique, jointly with the discretization of the two resulting subsystems using different numerical methods in staggered grids, as well as the use of a matrix-free approach for the computation of the pressure and momentum subsystems provides a compact stencil that is well suited for an efficient parallelization.

3D solvers comprise an accurate tool to solve Navier-Stokes equations, however their use is not always possible in the study of blood flow. Due to the large number of vessels involved and the multitude of different length scales required to accurately reproduce haemodynamics in the various regions of the cardiovascular system, blood flow simulations

based on full physics-based models could be very challenging in terms of computational effort. As it will clearly emerge later, even if the use of an efficient fully implicit numerical method allows us to greatly reduce the computational cost of addressing haemodynamics problems, the numerical modeling of the entire cardiovascular system or even of medium networks of vessels by means of 3D models turns out to be computationally unaffordable. A natural step towards the development of a numerical strategy able to simulate a complete cardiovascular network is the use of reduced order models, either as stand-alone models or coupled with 3D ones. These models are designed to retain the essential features of blood flow while reducing the dimension and therefore the final cost of the network simulation. In addition, they allow to model the interaction of the fluid flow with the mechanical response of the vessel wall in a cheaper way respect to 3D models, resulting a reasonable trade-off between accuracy and computational cost. Indeed, the suitability of 1D blood flow models to numerous applications has been validated *in-silico* by comparing their results against those obtained with more complex models [103, 234, 35], *in-vitro* by assessing 1D blood flow model output with respect to highly controlled experiments [141, 29] and *in-vivo* by assessing the capacity of these models to reproduce pressure and flow waveforms observed in the clinical context [164, 182, 205]. On the other hand, 1D models can be also coupled to 3D models, providing the needed realistic boundary conditions for the definition of localized 3D problems. Consequently, the detailed 3D analysis focuses on the study of confined pathological conditions and allows a high accuracy study of patient-specific phenomena, [85, 176, 32, 30].

From the mathematical point of view, 1D blood flow models fall within the category of hyperbolic systems of balance laws or in that of systems of partial differential equations with a hyperbolic-dominant behavior. Since the first 1D blood flow models were proposed a long time ago, [125, 11, 114], with the earliest references in works by Leonhard Euler (in 1775) and Thomas Young (in 1808) [75, 237], it is not a surprise that the literature on numerical schemes for blood flow is rather rich. Indeed, the employed methods range from classical finite difference methods such as Lax-Wendroff and MacCormack methods, [130, 110], to first- and high-order finite volume methods, [41, 151], as well as discontinuous Galerkin and Taylor-Galerkin methods, [197]. The nature of the model to be solved will depend strongly on the adopted relation between the vessel deformation and the internal blood pressure, i.e., on the so-called tube law. This relation can include terms related to elastic, viscous and other vessel wall material properties, [81, 27]. If one considers only the elastic component, then the resulting mathematical problem can be shown to be hyperbolic, provided that the pressure-area relation satisfies certain properties [218, 201]. On the other hand, when vessel wall viscoelasticity is taken into account, a second order spatial derivative of the flow arises in the momentum balance equation, potentially leading to a final hyperbolic-parabolic model. While the use of the elastic component of the tube law is mandatory and thus widely used in one-dimensional blood flow models, the viscous component is less common, both because its effect on cardiovascular haemodynamics is secondary, respect to that of the elastic deformation, and since its inclusion may increase the computational cost and the complexity of the final numerical approach due to the presence of parabolic or stiff source terms. However, since the viscoelasticity behavior of arterial and venous walls is a well-established feature, the inclusion of this term is becoming more common in scientific works. Recent bibliographical reviews on the importance of viscous terms and the different approaches available, including the introduction of alternative

natively hyperbolic models accounting for the viscous effects, can be found, e.g., in [217, 146, 145, 27, 28].

Due to the hyperbolic nature of the 1D blood flow models, most of the aforementioned numerical schemes designed for their solution are of the fully explicit type. Therefore, the eigenvalues of the complete PDE system must be taken into account to determine the CFL stability condition of the scheme. As described in Appendix A, they are affected by both pressure waves and mean flow velocity. As a consequence, in a low Mach regime, the velocity of pressure waves limits the time step of the simulation even if the bulk velocity would allow larger time steps. This phenomena has been widely studied for several models, such as the Euler equations, and may become a problem in terms of computational efficiency, [22]. A common approach to avoid this issue is the use of unconditionally stable fully implicit methods, [138, 182, 162, 50, 131, 194, 135], which however may require the solution of a potentially highly non-linear system which may also be computationally expensive. An alternative, combining both approaches, consists on the use of a splitting strategy which divides the original system into two subsystems allowing the decoupling of the mean flow velocity and pressure waves computation, [167, 219]. Then the first system, dominated by convection effects, can be still efficiently solved using an explicit algorithm while the second subsystem, related to the pressure, could be approximated using an implicit scheme. As such, the CFL condition of the overall algorithm is independent of the pressure waves and thus the time step could be larger than in a fully explicit approach. Meanwhile, the algebraic system to be solved is much simpler, and thus faster to be solved, with respect to the one arising in a fully implicit algorithm. Although this kind of semi-implicit schemes has already shown a promising behavior for several PDE systems, e.g. in the framework of all Mach number flow solvers, [167, 163, 207, 213, 47], they have been rarely employed so far in the context of 1D blood flow dynamics, [53, 139, 210, 77].

Therefore, the aim of Chapter 2 is to develop a novel semi-implicit method for 1D blood flow simulation following previous works in the context of fluid dynamics in networks of ducts, [53, 72, 117]. Besides, a viscoelastic model embodied by the Kelvin-Voigt unit is considered to define the employed tube law. As already mentioned, one of the most significant numerical difficulties that we encounter when addressing viscoelastic wall models is the time step restriction that may result from an explicit discretization of the parabolic terms. To circumvent this issue, we again apply an operator splitting in this case to decouple the pure convective terms and the diffusive terms. Consequently, we end up with a simple and computationally efficient algorithm, where the hyperbolic convective terms of the governing equations are discretized explicitly, while the viscous parabolic terms and the elliptic pressure terms are treated implicitly.

As 1D models focus on the description of wave propagation phenomena, they are rarely applied to study blood flow in single vessels. In fact, they are prominently applied to analyze wave propagation phenomena at a systemic level, i.e. 1D blood flow simulations normally regard networks of vessels of a certain extent which can be seen as one dimensional domains connected by junctions. In this case, one has to deal with coupling conditions between the 1D domains, [36, 150, 17, 64], as well as with the coupling of 1D domains to zero-dimensional models usually employed to describe peripheral circulation [4]. Hence, 1D models in compliant tubes can be extended to handle networks by incorporating a proper description of flow motion at the bifurcation or branching points of the network. Let us note that, due to the multidimensional nature of this phenomenon, passing from a

pipeline to a network may not be straightforward and the scientific community is making an effort to develop efficient and accurate strategies, not only in the framework of blood flow dynamics, but also in gas dynamics or shallow water equations, where the use of networks of 1D models to approximate 3D problems is also relevant, [25, 17, 132, 39].

One widespread choice for the treatment of junctions is the domain decomposition approach. Whereby the bifurcation is assumed to be represented by a single point and the effect of the bifurcation angles are neglected. In such models the communication between the one-dimensional segments is handled at branch junctions imposing proper interface conditions coming from conservation assumptions, [156, 170, 61]. A common choice is simply the enforcement of mass conservation, while discrepancies arise in the interface condition for the momentum equation. Indeed, in many works the pressure losses occurred inside the junction due to the three dimensional flow pattern are simply neglected. In this energy-conserving approach, the continuity of the total or static pressure is enforced, [197, 83, 141, 158, 89, 100]. On the other hand, in order to account for the energy dissipation and consequently for a decrease in the total pressure in the direction of the flow field across the bifurcation, some works have introduced estimated loss coefficients related to the fluid velocity and to the bifurcation angles for a general branching with any flow condition, see [86, 160, 62] and references therein.

As an alternative to the domain decomposition technique, some works assign to the junction a spatial 2D/3D domain, extending the one-dimensional flow description to branching points, [53, 210], or coupling the fluid-dynamical equations describing flow inside the one-dimensional tubes to a confluence model which can be embodied by a elastic tank characterized by a volume, a pressure and its entry flow rates [91], by a container in which the fluid is modeled by the two-dimensional Euler equations, [25], or by fully three-dimensional domains containing the junctions and able to capture the three-dimensional features of the flow, [17, 229]. Following the ideas on these latter methodologies, we propose a novel but highly simplified three-dimensional approach for the treatment of junctions. Within the proposed methodology, the junction is represented as a single three-dimensional cell to be modeled using the Euler equations and the numerical approach for its discretization is fully coupled to the proposed semi-implicit method used for the 1D vessels.

The main improvements made in this thesis compared to existing semi-implicit schemes for flows in compliant vessels, [53, 139, 210, 77], are: the extension of the type of tube law from arteries to veins, the addition of viscoelastic effects and the development of a new simplified 3D approach to describe junctions.

The outline of this part of the thesis is as follows. In Chapter 1, we develop the novel fully implicit hybrid FV/FE methodology in order to solve incompressible flows in two and three space dimensions. We start by introducing the overall algorithm and the staggered mesh used. Then, the transport diffusion stage is described focusing on the key aspects to get an efficient implicit method. Next, we recall the projection stage and we detail the boundary conditions treatment. The performance of the proposed methodology is assessed through several benchmarks. Moreover, the flow on a real 3D coronary tree is analyzed as last test case. On the other hand, Chapter 2 is devoted to the development of a novel staggered semi-implicit finite volume method for the simulation of one-dimensional blood flow in networks of elastic and viscoelastic vessels. We start describing the derivation of the one dimensional blood flow system from the three dimensional incompressible

Navier-Stokes equations and introducing the employed vessel wall model. Then, the splitting strategy and the staggered mesh used are presented, followed by a detailed description of the different methodologies exploited to solve each of the three subsystems in which the associated semi-discrete system in time has been divided. Next, the treatment of boundary conditions is detailed and the extension of the proposed methodology to networks, including the description the novel 3D junction model, is presented. Finally, the proposed semi-implicit method is validated by comparing the numerical results obtained with analytical, experimental and numerical data.

Chapter 1

The implicit staggered hybrid finite volume/finite element solver for the incompressible Navier-Stokes equations

In this chapter, we present a novel fully implicit hybrid finite volume/finite element method for incompressible flows, [135]. The proposed methodology extends, to the implicit framework, previous works on semi-implicit hybrid FV/FE schemes, [24, 46, 185]. This family of schemes combines finite volume and finite element methods for solving different mathematical models in the framework of pressure based semi-implicit solvers. The idea behind this methodology is to split the Navier-Stokes equations into a pressure subsystem, treated implicitly, and a transport-diffusion subsystem, solved explicitly, allowing the decoupling of the bulk flow velocity from the fast sound waves. However, in some cases the time step restriction imposed by the CFL condition, even if depending only on the mean velocity and not on the eigenvalues of the full system, as for a fully explicit scheme, it still results too demanding. As it will be shown later in this chapter, the need of a fully implicit approach clearly emerges when we address haemodynamic problems in 3D patient-specific geometries. To meet this need, a fully implicit scheme on staggered unstructured meshes has been developed. The pressure system is discretized implicitly according to a classical finite element method. On the other hand, the transport-diffusion subsystem is solved with the aid of an implicit finite volumes approach using an inexact Newton-Krylov method, based either on the BiCStab or the GMRES algorithm, in combination with Crouzeix-Raviart finite elements for the discretization of the viscous stress tensor. In contrast to the semi-implicit approach employed in the former algorithms proposed within the family of hybrid FV/FE methods, in which the convective terms are treat explicitly, the presented methodology is fully implicit and leads to an unconditional stable scheme allowing larger time steps. Consequently, the method results computationally efficient with respect to the semi-implicit methodology, especially in haemodynamic applications.

The chapter proceeds as follows. In Section 1.1, we recall the incompressible Navier-Stokes equations. Then, in Section 1.2, we outline the overall algorithm, focusing on the semi-discretization in time and the splitting of the equations into a convective-diffusive subsystem and a pressure subsystem and introducing the staggered unstructured grids

used. Next, each stage is deeply described. Within the convective-diffusive stage presented in Section 1.3, we use an implicit finite volume methodology for the convective terms, while the viscous terms are discretized with the aid of implicit Crouzeix-Raviart elements. In particular, we describe the inexact Newton-Krylov methods that are used to solve the resulting large and sparse nonlinear systems, based on matrix-free SGS-preconditioned BiCGStab or GMRES algorithms. To gain in computational efficiency also a simple but effective strategy for the reordering of the dual elements is proposed. Then, in Section 1.4, the projection stage is discretized using classical continuous Lagrange finite elements and the final correction step is performed in the post-projection stage described in Section 1.5. Section 1.7 presents several classical benchmarks from computational fluid mechanics and the results obtained with the proposed algorithm are validated against either analytical solutions, numerical reference solutions or available experimental data. Moreover, to show the capability of the proposed methodology to deal with real haemodynamic simulations, a last test on the study of the flow on a real 3D coronary tree is studied.

1.1 Governing equations

A well-established model for the simulation of blood flow dynamics consists on the incompressible Navier-Stokes equations coupled with the equation of state for ideal gases. This system can be derived from general continuum mechanics principles, [21, 107, 84], by supposing that

- the fluid is incompressible;
- the stress is Galilean invariant, i.e. the stress does not depend directly on the flow velocity but on its gradient;
- the viscous stress is linearly correlated to the strain rate tensor.

These assumptions are approximations of the real mechanical properties of blood, which is, rigorously speaking, not a fluid but a suspension of particles in the plasma. However, the above hypothesis are well accepted in medium to large vessels, in which shear thinning and viscoelastic effects, distinctive features of a non-Newtonian behavior, are negligible, [175]. Further details regarding the rheological properties of blood can be found in [175, 231] and references therein.

The incompressible Navier-Stokes system for Newtonian fluids is composed by the momentum equation and the divergence-free equation of the velocity field. Denoting $\mathbf{w} = \rho\mathbf{u}$ the momentum, ρ the density, $\mathbf{u}$ the velocity vector, and p the pressure, the governing equations are given by

$$\nabla\cdot\mathbf{u} = 0, \tag{1.1.1a}$$

$$\frac{\partial\rho\mathbf{u}}{\partial t} + \nabla\cdot\mathcal{F}(\rho,\mathbf{u}) + \nabla p - \nabla\cdot\boldsymbol{\tau} = \rho\mathbf{g} \tag{1.1.1b}$$

where $\mathcal{F}(\rho,\mathbf{u})$ is the convective flux tensor, defined as $\mathcal{F}(\rho,\mathbf{u}) = \rho\mathbf{u}\otimes\mathbf{u}$, $\boldsymbol{\tau} = \mu(\nabla\mathbf{u} + \nabla\mathbf{u}^t)$ corresponds to the viscous part of the Cauchy stress tensor, with μ the dynamic viscosity coefficient, and $\mathbf{g}$ denotes the gravity vector.

1.2 Numerical discretization

The numerical discretization of the complete system extends the algorithm already employed in [24, 46, 185] and it has been presented in [135]. The methodology makes use of a projection method which decouples the computation of the momentum and pressure unknowns leading to a split of the Navier-Stokes system into two subsystems: the convective-diffusive subsystem and the pressure subsystem.

1.2.1 Overall algorithm

We start by considering a semi-discretization in time of (1.1.1) still keeping continuous all the spatial operators. Denoting by $\mathbf{w}^n$, p^n the discrete approximations of the momentum and pressure at time t^n, namely $\mathbf{w}(\mathbf{x}, t^n)$ and $p(\mathbf{x}, t^n)$, and assuming a constant density ρ, we have

$$\frac{1}{\Delta t}(\mathbf{w}^* - \mathbf{w}^n) + \nabla\cdot\mathcal{F}(\rho\mathbf{u}^*) + \nabla p^n - \nabla\cdot\boldsymbol{\tau}^* = \rho\mathbf{g}, \tag{1.2.1a}$$

$$\frac{1}{\Delta t}(\mathbf{w}^{n+1} - \mathbf{w}^*) + \nabla(p^{n+1} - p^n) = 0, \tag{1.2.1b}$$

$$\nabla\cdot\mathbf{w}^{n+1} = 0. \tag{1.2.1c}$$

We note that to evaluate the pressure gradient in the momentum equation, we have exploited the previously obtained approximation p^n of the pressure. Hence, the variable $\mathbf{w}^*$ introduced in the former system has to be considered as an intermediate approximation of the momentum field, which accounts for the update of convective and diffusive terms but it does not necessarily verify the divergence free condition yet. Therefore, to get the final value of the momentum, $\mathbf{w}^*$ must be corrected using the pressure at the new time step as

$$\mathbf{w}^{n+1} = \mathbf{w}^* - \Delta t\,\nabla(p^{n+1} - p^n). \tag{1.2.2}$$

We observe that the former discretization is actually implicit for both momentum and pressure. If an explicit approach is preferred for the computation of the velocity field, it would suffice to choose the momentum on the convective and viscous terms of (1.2.1a) to be the one given at time t^n. On the other hand, focusing on the fully implicit approach, the momentum and velocity can be computed within three stages where different numerical methods are employed according to the nature of the equations:

1. **Transport-diffusion stage.** The transport-diffusion stage is devoted to the computation of the intermediate approximation of the momentum, $\mathbf{w}^*$, by implicitly solving the system given by (1.2.1a), namely,

$$\frac{1}{\Delta t}(\mathbf{w}^* - \mathbf{w}^n) + \nabla\cdot\mathcal{F}(\mathbf{w}^*) + \nabla p^n - \nabla\cdot\boldsymbol{\tau}(\mathbf{w}^*) = \rho\mathbf{g}, \tag{1.2.3}$$

making use of a Newton-Krylov approach. The spatial discretization of the equations is done by combining an implicit finite volume scheme, for the computation of the convective terms, and the Crouzeix-Raviart basis functions, for the calculus of the viscous terms.

2. **Projection stage.** The remaining equations in (1.2.1) form the pressure subsystem which reads:

$$\frac{1}{\Delta t}(\mathbf{w}^{n+1} - \mathbf{w}^*) + \nabla(p^{n+1} - p^n) = 0, \tag{1.2.4}$$

$$\nabla\cdot \mathbf{w}^{n+1} = 0. \tag{1.2.5}$$

   We observe that combining (1.2.4) with (1.2.5) yields the well-known pressure-Poisson equation for the pressure correction

$$\nabla^2 \left(p^{n+1} - p^n\right) = \frac{1}{\Delta t}\nabla \cdot \mathbf{w}^*. \tag{1.2.6}$$

   It can be efficiently solved using classical $\mathbb{P}^1$ continuous finite elements to first obtain the pressure correction $\delta p = p^{n+1} - p^n$ and then recover the approximation of the pressure at the new time step.

3. **Post-projection stage.** In this last stage, the information computed in the previous two stages is combined providing the final approximation of the momentum field, $\mathbf{w}^{n+1}$. More precisely, the intermediate momentum, $\mathbf{w}^*$, obtained at the first stage, is updated using the pressure computed in the projection stage according to (1.2.2).

In what follows, we describe in detail each of the stages previously outlined. However, we first need to introduce the staggered unstructured mesh used for the spatial discretization.

1.2.2 Staggered unstructured mesh

The spatial discretization of the presented methodology is performed using staggered grids of the face-type, i.e., the dual grids are generated from the faces/edges of a primal mesh made of triangles/tetrahedra, depending if the problem to solve is defined in a two-dimensional or a three-dimensional space, respectively. Further details on the construction and fruitful application of this kind of staggered grids can be seen, for instance, in [23, 225, 71, 46, 48].

The computational domain is initially covered by a set of primal elements, $\{T_k,\, k = 1, \ldots, n_{\text{primal}}\}$. Then, to construct the dual grid, we first compute the barycentres of the primal cells, B_k, and connect them to the vertices of the primal edges/faces, V_m. Hence, each primal element is divided into 3/4 subelements which will correspond to the so-called half dual elements. Then, for the edges/faces located at the interior of the domain, the two subelements related to each face are merged so that the resulting quadrilateral/polyhedron will constitute the related dual cell C_i. Otherwise if the edge/face belongs to the boundary, the related dual element coincides with the corresponding primal subelement. A sketch on the staggered mesh construction in 2D is shown in Figure 1.1.

We can observe that the nodes N_i, $i = 1, \ldots, n_{\text{dual}}$, of the dual mesh are defined as the barycentres of the edges/faces of the elements of the primal mesh, which correspond to the location of the nodes of the Crouzeix-Raviart basis functions used later in this work. Each node N_i has as neighboring nodes the set $\{N_j,\, j \in \mathcal{K}_i\}$ consisting of the nodes of the remaining dual cells built on the edges/faces of the two primal elements to which it belongs. Besides, we define the boundary of C_i as $\partial C_i = \Gamma_i = \bigcup_{j\in\mathcal{K}_i} \Gamma_{ij}$ where Γ_{ij} is

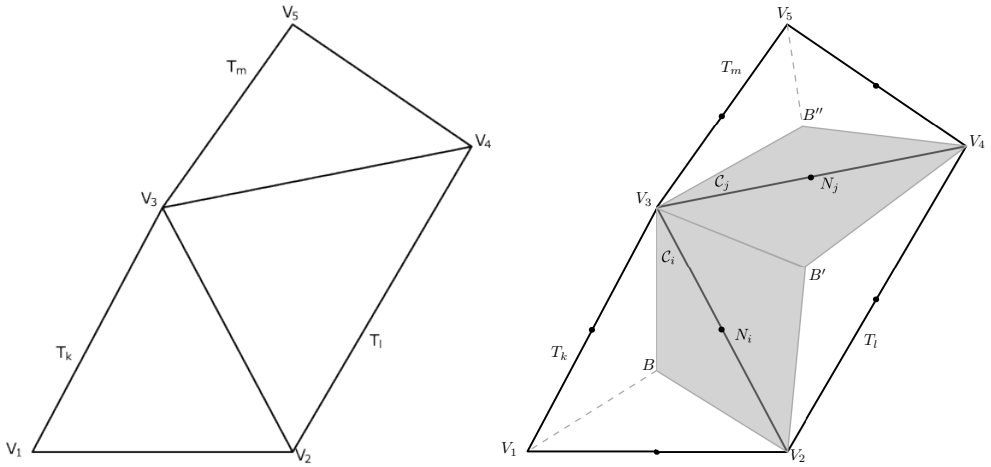

Figure 1.1: Construction of the staggered grids in 2D. Left: primal triangular grid with elements T_k, T_l, T_m of vertex $\{V_1, V_2, V_3\}$, $\{V_2, V_3, V_4\}$ and $\{V_3, V_4, V_5\}$ respectively. Right: dual elements C_i and C_j (shadowed in gray) with corresponding nodes N_i, N_j and vertex the barycentres of the primal elements B, B', B'' and the primal vertex V_2, V_3 and V_4.

the interface between cells C_i and C_j while $|C_i|$ represents the area/volume of C_i. We denote the outward unit normal vector of Γ_{ij} as $\boldsymbol{n}_{ij}$ and we define $\boldsymbol{\eta}_{ij} = \boldsymbol{n}_{ij}||\boldsymbol{\eta}_{ij}||$, where $||\boldsymbol{\eta}_{ij}|| = |\Gamma_{ij}|$ is the length/area of Γ_{ij}. In addition, the barycentre of the edge/face between two dual cells C_i and C_j is denoted by N_{ij}.

The choice of this type of mesh brings several advantages which will be clear in the following sections of this chapter. Firstly, complex geometries can be easily discretized thanks to the use of primal meshes composed of simplex elements, such as triangles/tetrahedra, capturing all features of very tortuous domains. Secondly, a very compact stencil can be obtained for a second order accurate scheme in space, easing its parallel implementation. Moreover, an exact interpolation from the primal vertex to the dual cells and back to the primal mesh can be developed to accurately commute between the staggered grids, [45]. Last, the dual mesh structure together with an appropriate choice for the location of the degrees of freedom results on an easy coupling between the finite volume and the Crouzeix-Raviart approaches as well as on a simple transfer of data with the continuous finite element scheme.

1.3 Transport-diffusion stage

As we advanced in Section 1.2, the transport-diffusion stage aims to provide an intermediate approximation of the momentum at time t^{n+1} using an implicit finite volume methodology, for the treatment of convective terms, combined with an implicit approach based on Crouzeix-Raviart finite elements, to discretize viscous terms.

The convective-diffusive system to be solved is

$$\mathbf{w}^* + \Delta t\, \nabla\cdot \mathcal{F}(\mathbf{w}^*) - \Delta t\, \nabla\cdot \boldsymbol{\tau}^* = \mathbf{w}^n - \Delta t\, \nabla\, p^n + \Delta t \rho \mathbf{g}. \tag{1.3.1}$$

Note that the pressure gradient term is computed explicitly from the pressure obtained at the previous time step. Therefore, the momentum will be updated in the post-projection

stage to account for the new pressure. Since an implicit method is employed, the choice of a solver is commonly headed towards Newton's methods. However, due to the nonlinearity of the convective term, which couples all momentum equations, the use of a direct solver at each time step may result too demanding from a computational point of view. Therefore, we consider the class of inexact Newton methods which provides the solution of (1.3.1) at a reasonable cost by linearizing the discretization of the nonlinear convective term. Then, we solve the resulting equations numerically employing a Krylov subspace method, see [67, 20, 18, 19] and references therein.

Therefore, to get $\mathbf{w}^* := \mathbf{w}^n + \Delta\mathbf{w}^*$ we have to find the root of the vector function

$$\mathbf{f}\left(\mathbf{w}^*\right) = \mathbf{w}^* - \mathbf{w}^n + \Delta t\, \nabla\cdot \mathcal{F}(\mathbf{w}^*) - \Delta t\, \nabla\cdot \boldsymbol{\tau}^* + \Delta t\, \nabla\, p^n - \Delta t \rho \mathbf{g} = 0 \tag{1.3.2}$$

which is achieved via a iterative process. Given $\mathbf{w}_0^* = \mathbf{w}^n$ as initial guess, we compute a sequence of steps $\Delta\mathbf{w}_k^*$ and iterates $\mathbf{w}_k^*$ as follows

$$\mathbf{J}\left(\mathbf{w}_k^*\right)\, \Delta\mathbf{w}_k^* = -\mathbf{f}(\mathbf{w}_k^*), \tag{1.3.3}$$

$$\mathbf{w}_{k+1}^* = \mathbf{w}_k^* + \tilde{\delta}_k\, \Delta\mathbf{w}_k^*, \tag{1.3.4}$$

where $\Delta\mathbf{w}_k^*$ is the Newton step, $\mathbf{J}\left(\mathbf{w}^*\right) = \partial\mathbf{f}\left(\mathbf{w}^*\right)/\partial\mathbf{w}^*$ is the Jacobian of the nonlinear function $\mathbf{f}\left(\mathbf{w}^*\right)$ in (1.3.2) and $0 \leq \tilde{\delta}_k \leq 1$ in (1.3.4) is a suitably chosen scalar for a simple linear search globalization technique that in each Newton iteration guarantees

$$\left\|\mathbf{f}\left(\mathbf{w}_{k+1}^*\right)\right\| < \left\|\mathbf{f}\left(\mathbf{w}_k^*\right)\right\|. \tag{1.3.5}$$

In practice, we initially set $\tilde{\delta}_k = 1$ and then divide it by two until (1.3.5) holds.

Once the residual $\|\mathbf{f}\left(\mathbf{w}_k^*\right)\|$ is below a prescribed tolerance ϵ, the Newton iterations stop and the last $\mathbf{w}_k^*$ computed is taken as the input value for the projection stage. In the proposed Newton algorithm the value of the tolerance of the linear solver for (1.3.3) depends on the numerical flux function employed to compute the convective term. As we will see later, two numerical flux functions are considered: an implicit Rusanov flux function and a semi-implicit Ducros flux function. In particular, the tolerance is dynamically set to $\epsilon_k = 10^{-2}\left\|\mathbf{f}\left(\mathbf{w}_k^*\right)\right\|$ in the cases where the implicit Rusanov flux is used for the discretization of the nonlinear convective terms. Otherwise, if the semi-implicit Ducros flux is selected, the resulting system (1.3.2) is already linear and hence only one Newton iteration is needed. In this latter case, we set $\epsilon = 10^{-10}$.

At this point two main issues arise. The first one is the computation of the residual needed to define the stop criterium for the Newton method. The second one is the solution of the resulting linear system (1.3.3), hence, the computation of the approximated solution at the new time. In what follows the two subjects are addressed.

1.3.1 Residual computation

To calculate the residual $\mathbf{f}\left(\mathbf{w}^*\right)$ needed in Newton's system (1.3.3), we proceed in two steps. First, the contribution of the nonlinear convective terms, of the pressure at time t^n and of the gravity source, namely,

$$\delta\mathbf{w}^{**} = \Delta t\, \nabla\cdot \mathcal{F}(\mathbf{w}^*) + \Delta t\, \nabla\, p^n - \Delta t \rho \mathbf{g}, \tag{1.3.6}$$

is computed via an implicit finite volume method on the dual mesh. Then, the obtained result is included in the final equation that contains also the viscous contribution, i.e.,

$$\mathbf{f}\left(\mathbf{w}^*\right) = \mathbf{w}^* - \mathbf{w}^n + \delta\mathbf{w}^{**} - \Delta t\, \nabla\cdot \boldsymbol{\tau}^* = 0, \tag{1.3.7}$$

where $\nabla\cdot \boldsymbol{\tau}^*$ will be approximated using Crouzeix-Raviart finite elements on the primal grid.

Convective-pressure contribution to the residual. As we have already mentioned, in order to compute (1.3.6), we employ a finite volume method on the dual mesh. Hence, the discrete approximation of $\delta\mathbf{w}^{**}$ represents an integral averaged on each control volume. Given a control volume C_i, we integrate (1.3.6) on C_i and apply Gauss theorem to the convective term getting

$$\delta\mathbf{w}_i^{**} = \frac{\Delta t}{|C_i|}\int\limits_{\Gamma_i} \mathcal{F}(\mathbf{w}^*)\cdot\boldsymbol{n}_i \,\mathrm{dS} + \frac{\Delta t}{|C_i|}\int\limits_{C_i} \left(\nabla\, p^n\right)_i \mathrm{dV} - \frac{\Delta t}{|C_i|}\int\limits_{C_i} \rho_i \mathbf{g}\,\mathrm{dV} \tag{1.3.8}$$

where $\boldsymbol{n}_i$ denotes the outward unit normal of Γ_i at each point. The convective contribution can be then rewritten as the sum of integrals applying on each cell interface Γ_{ij} which form Γ_i, namely,

$$\frac{\Delta t}{|C_i|}\int\limits_{\Gamma_i} \mathcal{F}(\mathbf{w}^*)\cdot\boldsymbol{n}_i \,\mathrm{dS} = \frac{\Delta t}{|C_i|}\sum_{j\in\mathcal{K}_i}\int\limits_{\Gamma_{ij}} \mathcal{F}(\mathbf{w}^*)\cdot\boldsymbol{n}_{ij}. \tag{1.3.9}$$

Next, the integral on Γ_{ij} is approximated by an upwind scheme using a numerical flux function ϕ as

$$\int\limits_{\Gamma_{ij}} \mathcal{F}(\mathbf{w}^*)\cdot\boldsymbol{n}_{ij} \approx \phi(\mathbf{w}_i^*,\mathbf{w}_j^*,\mathbf{w}_i^n,\mathbf{w}_j^n,\boldsymbol{n}_{ij}). \tag{1.3.10}$$

In this thesis we consider two types of flux functions ϕ. One choice is the implicit Rusanov flux function, ϕ^{R}, of the form

$$\begin{aligned}\phi^{\mathrm{R}}(\mathbf{w}_i^*,\mathbf{w}_j^*,\mathbf{w}_i^n,\mathbf{w}_j^n,\boldsymbol{n}_{ij}) &= \frac{1}{2}\left(\mathcal{F}(\mathbf{w}_i^*)+\mathcal{F}(\mathbf{w}_j^*)\right)\cdot\boldsymbol{n}_{ij} - \frac{1}{2}\alpha_{ij}^r\left(\mathbf{w}_j^*-\mathbf{w}_i^*\right),\\ \alpha_{ij}^r &= 2\left|u_{ij}^n\right| + c_\alpha,\end{aligned} \tag{1.3.11}$$

with c_α an extra artificial numerical viscosity coefficient which may increase the robustness of the final scheme (a detailed analysis on the role and use of this coefficient can be seen in [47, 44]). As an alternative, to discretize the nonlinear convective term a semi-discrete Ducros flux can also be employed, [68, 70, 69]. In this case the numerical flux function ϕ^{D} reads

$$\begin{aligned}\phi^{\mathrm{D}}(\mathbf{w}_i^*,\mathbf{w}_j^*,\mathbf{w}_i^n,\mathbf{w}_j^n,\boldsymbol{n}_{ij}) &= \frac{1}{2}\left(\mathbf{w}_i^* + \mathbf{w}_j^*\right)u_{ij}^n - \frac{1}{2}\alpha_{ij}^d\left(\mathbf{w}_j^*-\mathbf{w}_i^*\right),\\ \alpha_{ij}^d &= \left|u_{ij}^n\right| + c_\alpha, \qquad u_{ij}^n = \frac{1}{2}\left(\mathbf{u}_i^n+\mathbf{u}_j^n\right)\cdot\boldsymbol{n}_{ij}.\end{aligned} \tag{1.3.12}$$

We highlight that ϕ^{D} is linear in $\mathbf{w}^*$, hence the Newton iterations outside the Krylov subspace algorithm are no longer needed. Consequently, the computational cost of the

overall algorithm reduces. Moreover, another advantage of using the Ducros flux function as numerical flux is that it leads to a kinetic energy stable scheme, as it will be demonstrated in Section 1.3.3.

Let us note that both numerical flux functions provide a first order scheme in space. Hence, in order to obtain second-order schemes, a CVC Kolgan-type methodology is introduced, [124, 226]. Accordingly, in the numerical viscosity, the conservative values $\mathbf{w}_i$, $\mathbf{w}_j$ are replaced by the boundary extrapolated values, $\mathbf{w}_{ij}^-$, $\mathbf{w}_{ij}^+$, at both sides of each dual face Γ_{ij}, namely,

$$\mathbf{w}_{ij}^- = \mathbf{w}_i + \nabla \mathbf{w}_i \cdot \Delta \mathbf{x}_{ij}^-, \qquad \mathbf{w}_{ij}^+ = \mathbf{w}_j + \nabla \mathbf{w}_j \cdot \Delta \mathbf{x}_{ij}^+, \tag{1.3.13}$$

with $\Delta \mathbf{x}_{ij}^-$, $\Delta \mathbf{x}_{ij}^+$ the vectors between the nodes of cells C_i, C_j and the barycenter of the common face Γ_{ij}. To compute the discrete gradients of the momentum needed in (1.3.13), we employ the Crouzeix-Raviart basis functions applied to the primal elements. Then, the gradients obtained at the primal elements are interpolated to the dual cells as a weighted average following the approach presented in [47, 44]. In particular, assuming that the value on the dual node corresponds to the averaged quantity on dual cells, we define an exact interpolation technique to pass data between the staggered grids. Specifically, given an arbitrary variable q in the primal vertex, its value at each dual node can be obtained as

$$q_i = \sum_{j \in \mathcal{V}_i} \omega_j P_1 \left(V_j \right) \tag{1.3.14}$$

where $q_i = q\left(N_i\right)$, $\mathcal{V}_i$ is the set of indexes of the vertex of the face/edge containing the dual node N_i, $\{\omega_j\}_{j \in \mathcal{V}_i}$ is a set of weights such that $\sum\limits_{j \in \mathcal{V}_i} \omega_j = 1$ and $P_1(\mathbf{x})$ is the interpolation polynomial of degree one built making use of the classical finite element basis functions having as nodes the vertex of the primal mesh.

Regarding the second integral in (1.3.8), to evaluate the pressure gradient we make use of the pressure at the previous time step, p^n, which is defined at the vertices of the primal grid. Thus its gradient can be easily approximated inside each primal element using a classical Galerkin approach based on $\mathbb{P}^1$ finite element basis functions. Then, a weighted average of the obtained values at the two parts of each finite volume gives a constant value in each dual element, $\left(\nabla p^n\right)_i$ that is integrated in the cell.

Finally, assuming the gravity and the density to be constant in the dual elements, the source term can be directly integrated in each cell. In case more complex algebraic source terms are given, they are integrated on each cell using a sufficiently accurate numerical quadrature rule.

Viscous contribution to the residual. Once $\delta \mathbf{w}_i^{**}$ is computed, we can calculate the final residual by adding the viscous contribution. To this end, we make use of Crouzeix-Raviart finite elements applied on the primal grid. The degrees of freedom of these elements are located at the barycentres of the faces of the primal mesh, which can been also seen as the centers of the staggered face-based dual mesh, used in this methodology to discretize the nonlinear convective terms. Therefore, the degrees of freedom of Crouzeix-Raviart finite elements and the data used in the finite volume method can be assimilated, explaining the choice to use this type of finite elements to discretize the viscous terms.

We first multiply (1.3.7) by a test function φ_ℓ of the Crouzeix-Raviart type. Then, we integrate the equation over the domain Ω and, finally, by applying integration by parts to the viscous terms and neglecting boundary contributions, we get

$$\mathbf{f}\left(\mathbf{w}^*\right) = \int_\Omega \left(\mathbf{w}^* - \mathbf{w}^n\right) \varphi_\ell \, \mathrm{dV} + \int_\Omega \delta\mathbf{w}^{**} \varphi_\ell \, \mathrm{dV} + \Delta t \int_\Omega \mu \, \nabla \mathbf{w}^* \cdot \nabla \varphi_\ell \, \mathrm{dV} \,. \tag{1.3.15}$$

We now write $\mathbf{w}^*$, $\mathbf{w}^n$ and $\delta\mathbf{w}^{**}$ as a linear combination of the basis functions and the degrees of freedom $\hat{\mathbf{w}}^*$, $\hat{\mathbf{w}}^n$ and $\delta\hat{\mathbf{w}}^{**}$,

$$\mathbf{w}^* = \sum_{i=1}^{N} \varphi_i \hat{\mathbf{w}}_i^*, \qquad \mathbf{w}^n = \sum_{i=1}^{N} \varphi_i \hat{\mathbf{w}}_i^n, \qquad \delta\hat{\mathbf{w}}^{**} = \sum_{i=1}^{N} \varphi_i \delta\hat{\mathbf{w}}_i^{**} \tag{1.3.16}$$

with N the number of basis functions, that is, three in 2D and four in 3D. Substituting (1.3.16) in (1.3.15), and denoting by $\mathbf{M}$ and $\mathbf{K}$ the global mass and stiffness matrices,

$$M_{ij} = \int_\Omega \varphi_i \cdot \varphi_j \, \mathrm{dV} \qquad \text{and} \qquad K_{ij} = \int_\Omega \nabla \varphi_i \cdot \nabla \varphi_j \, \mathrm{dV}, \tag{1.3.17}$$

yield the following discrete nonlinear system

$$\mathbf{f}\left(\hat{\mathbf{w}}^*\right) = \mathbf{M}\left(\hat{\mathbf{w}}^* - \hat{\mathbf{w}}^n\right) + \mathbf{M}\,\delta\hat{\mathbf{w}}^{**} + \Delta t \mu \mathbf{K}\,\hat{\mathbf{w}}^*. \tag{1.3.18}$$

The above equation provides the value of the residual on each Crouzeix-Raviart vertex, which coincide with the node of the dual elements, thus it can be directly taken as the approximation on the corresponding dual cell. Note that it is not necessary to construct the global mass and stiffness matrices, since we proceed via a loop on the primal elements. This computation in a matrix-free manner is profitable when MPI parallelization is considered, since communication between CPUs is minimized. The element-local mass matrices of Cruzeix-Raviart elements are diagonal in two space dimensions, but they are not in 3D. We therefore employ *mass lumping* in order to obtain a diagonal mass matrix in three-dimensional calculations.

1.3.2 Computation of $\mathbf{w}^*$

The final step to compute the intermediate velocity $\mathbf{w}^*$ is to solve at each Newton iteration the problem (1.3.3)-(1.3.4). To do so, we employ a relevant class of inexact Newton methods, the so-called Newton-Krylov methods. Consequently, a Krylov subspace projection method is used to compute each Newton step $\Delta\mathbf{w}_k^*$. A significant feature of Krylov methods is that they require only the action of the Jacobian $\mathbf{J}\left(\mathbf{w}_k^*\right)$ on a vector $\Delta\mathbf{w}_k^*$. Moreover, for an appropriate chosen scalar $\tilde{\delta}_k$, this action can be approximated by finite differences

$$\mathbf{J}\left(\mathbf{w}_k^*\right)\Delta\mathbf{w}_k^* \approx \frac{\mathbf{f}\left(\mathbf{w}_k^* + \tilde{\delta}_k \Delta\mathbf{w}_k^*\right) - \mathbf{f}\left(\mathbf{w}_k^*\right)}{\tilde{\delta}_k} \tag{1.3.19}$$

allowing us to make use of a matrix-free implementation of the solver, without the need to assemble or compute the Jacobian directly. Then, assuming a linearized flux function, the system to be solved at each time step is reduced to

$$\begin{aligned} &\Delta\mathbf{w}_k^* + \Delta t \, \nabla\cdot \mathcal{F}(\Delta\mathbf{w}_k^*) - \Delta t \, \nabla\cdot \boldsymbol{\tau}(\Delta\mathbf{w}_k^*) \\ &= -\mathbf{w}_k^* - \Delta t \, \nabla\cdot \mathcal{F}(\mathbf{w}_k^*) + \Delta t \, \nabla\cdot \boldsymbol{\tau}(\mathbf{w}_k^*) + \mathbf{w}^n - \Delta t \, \nabla \, p^n + \Delta t \rho \mathbf{g}, \end{aligned} \tag{1.3.20}$$

where the right hand side in the above equation is the opposite of the residual, i.e. $-\mathbf{f}\left(\mathbf{w}_k^*\right)$, and it can be calculated as shown in Section 1.3.1. Hence, the former linearized system, that we need to solve at each Newton iteration, can be written in delta formulation and recast into

$$\mathcal{A}\,\Delta\mathbf{w}_k^* = -\mathbf{f}\left(\mathbf{w}_k^*\right). \tag{1.3.21}$$

As we have already mentioned the above system is solved by exploiting a Krylov subspace method embedded within the inexact Newton algorithm. We consider two options: the generalized minimal residual method (GMRES), [188], and a biconjugate gradient stabilized method (BiCStab), [223]. Both methods can be used to solve general nonsymmetric linear systems like the one in (1.3.20), thus a linearisation of the numerical flux needs to be introduced in the computation of the matrix-vector product of the Jacobian with the sought Newton step. Consequently, once a numerical flux function is selected we need to define its corresponding linearized version to be used inside the Krylov subspace algorithm. For instance, the Rusanov flux function, which is quadratic in $\mathbf{w}^*$, is linearized in normal direction and the associated matrix-vector product reads

$$\frac{\partial\mathcal{F}^R(\mathbf{w}_i^*,\mathbf{w}_j^*)\cdot\boldsymbol{n}_{ij}}{\partial(\mathbf{w}_i^*,\mathbf{w}_j^*)}\cdot(\Delta\mathbf{w}_i^*,\Delta\mathbf{w}_j^*) = \left(u_i^*\Delta\mathbf{w}_i^* + u_j^*\Delta\mathbf{w}_j^*\right) - \frac{1}{2}\alpha_{ij}^r\left(\Delta\mathbf{w}_j^* - \Delta\mathbf{w}_i^*\right). \tag{1.3.22}$$

with the normal velocities given by

$$u_i^* = \frac{1}{\rho_i}\mathbf{w}_i^*\cdot\boldsymbol{n}_{ij}, \qquad u_j^* = \frac{1}{\rho_j}\mathbf{w}_j^*\cdot\boldsymbol{n}_{ij}, \tag{1.3.23}$$

and where $\mathbf{w}_i^*$, $\mathbf{w}_j^*$ denote the intermediate momentum in cell C_i and C_j of the current Newton iteration, $\Delta\mathbf{w}_i^*$, $\Delta\mathbf{w}_j^*$ identify the associated Newton steps, while, in order to ease the linearization of the Rusanov flux, the numerical dissipation coefficient α_{ij}^r has deliberately been computed at the previous time, t^n. Alternatively, if we want to avoid this duplicity of numerical flux functions, we can choose the semi-implicit Ducros flux function (1.3.12) which is already linear in the velocity field. Thus, the associated matrix-vector product needed by the linear solver simply reads

$$\frac{\partial\mathcal{F}^D(\mathbf{w}_i^*,\mathbf{w}_j^*)\cdot\boldsymbol{n}_{ij}}{\partial(\mathbf{w}_i^*,\mathbf{w}_j^*)}\cdot(\Delta\mathbf{w}_i^*,\Delta\mathbf{w}_j^*) = \frac{1}{2}u_{ij}^n\left(\Delta\mathbf{w}_i^* + \Delta\mathbf{w}_j^*\right) - \frac{1}{2}\alpha_{ij}^d\left(\Delta\mathbf{w}_j^* - \Delta\mathbf{w}_i^*\right). \tag{1.3.24}$$

which coincides with the corresponding expression used to compute the residual $\mathbf{f}$, (1.3.12). Finally, to account for the viscous fluxes, we use the Crouzeix-Raviart approach presented in Section 1.3.1, which is already linear in the unknowns and thus the application of the matrix-vector product in the linear solver is immediate.

In what follows we briefly recall the Krylov subspace methods used to solve the already derived system. We moreover present the numerical techniques we have exploited in order to improve the efficiency of the resulting scheme. A more complete description of the two Krylov methods can be found, e.g., in [188, 223].

GMRES. The generalized minimal residual method is an iterative Krylov method for the numerical solution of a nonsymmetric system of linear equations, $\mathbf{Ax} = \mathbf{b}$. It is based

on the idea of approximating the solution $\mathbf{x}$ by a vector with minimal residual in a Krylov subspace. The algorithm makes use of the Arnoldi's method to compute an L^2-orthogonal basis $\mathbf{v}_1, \mathbf{v}_2, \cdots, \mathbf{v}_k$ of the Krylov subspace $K_k \equiv \text{span}\{\mathbf{v}_1, A\mathbf{v}_1, \cdots, A^{k-1}\mathbf{v}_1\}$. The result is the upper $k \times k$ Hessenberg matrix $\mathbf{H}_k$ which satisfies the important relation $\mathbf{V}_k\mathbf{H}_k = \mathbf{A}\mathbf{V}_k$, where $\mathbf{V}_k$ is the $N \times k$ matrix whose columns are the L^2-orthogonal basis. Then, in order to solve $\mathbf{A}\mathbf{x} = \mathbf{b}$, we seek an approximate solution $\mathbf{x}_k$ of the form $\mathbf{x}_k = \mathbf{x}_0 + \mathbf{z}_k$, where $\mathbf{x}_0$ is an initial guess to the solution $\mathbf{x}$ and $\mathbf{z}_k$ is a member of the subspace K_k with $\mathbf{r}_0 = \mathbf{b} - \mathbf{A}\mathbf{x}_0$ which minimizes the norm. Hence, we would like to solve the following least squares problem:

$$\min_{\mathbf{z}\in K_k} \|\mathbf{b} - \mathbf{A}(\mathbf{x}_0 + \mathbf{z})\| = \min_{\mathbf{z}\in K_k} \|\mathbf{r}_0 - \mathbf{A}\mathbf{z}\| . \tag{1.3.25}$$

Now, setting $\mathbf{z} = \mathbf{V}_k\mathbf{y}$ and assuming that the Arnoldi's algorithm has been carried out starting with $\mathbf{v}_1 = \mathbf{r}_0/||\mathbf{r}_0||$, the norm to be minimized can be recast as

$$\| \, \|\mathbf{r}_0\| \, \mathbf{v}_1 - \mathbf{A}\mathbf{V}_k\mathbf{y} \, \| = \|\mathbf{V}_k(\|\mathbf{r}_0\| \, \mathbf{e}_1 - \mathbf{H}_k\mathbf{y}) \, \| = \| \|\mathbf{r}_0\| \, \mathbf{e}_1 - \mathbf{H}_k\mathbf{y} \, \| \tag{1.3.26}$$

where we have introduced the vector $\mathbf{e}_1$ representing the first column of the $k \times k$ identity matrix and in the last step we have exploited the L^2-orthogonality of $\mathbf{V}_k$. Thus, the solution of the least squares problem is given by

$$\mathbf{x}_k = \mathbf{x}_0 + \mathbf{V}_k\mathbf{y}_k \tag{1.3.27}$$

where $\mathbf{y}_k = \mathbf{H}_k^{-1} \, \|\mathbf{r}_0\| \, \mathbf{e}_1$ minimizes the norm defined in (1.3.26). The overall pseudocode of the algorithm can be seen in Algorithm 1.

Choose $\mathbf{x}_0$ as initial guess
Compute $\mathbf{r_0} = \mathbf{b} - \mathbf{A}\mathbf{x}_0$
Set $\mathbf{v}_1 = \frac{\mathbf{r}_0}{\|\mathbf{r}_0\|}$
Set $m = 0$
while $\|\mathbf{r}_m\| >$ tolerance **do**
    for $i = 1, 2, \cdots, m$ **do**
        $h_{im} = (\mathbf{A}\mathbf{v}_m, \mathbf{v}_i)$
        $\hat{\mathbf{v}}_{m+1} = \mathbf{A}\mathbf{v}_m - \sum_{i=1}^{m} h_{im}\mathbf{v}_m$
    end for
    $h_{m+1\,m} = \|\hat{\mathbf{v}}_{m+1}\|$
    $\mathbf{v}_{m+1} = \frac{\hat{\mathbf{v}}_{m+1}}{h_{m+1\,m}}$
    Find $\mathbf{y}$ that minimizes $\|\|\mathbf{r}_0\| \, \mathbf{e}_1 - \mathbf{H}_{m+1}\mathbf{y}\|$
    $\mathbf{x}_{m+1} = \mathbf{x}_0 + \mathbf{V}_{m+1}\mathbf{y}$
    $\|\mathbf{r}_{m+1}\| = \| \|\mathbf{r}_0\| \, \mathbf{e}_1 - \mathbf{H}_{m+1}\mathbf{y} \, \|$
    $m = m + 1$
end while

Algorithm 1: Pseudocode of the GMRES algorithm.

BiCGStab. The biconjugate gradient stabilized method is an iterative Krylov subspace method for the numerical solution of nonsymmetric linear systems, $\mathbf{A}\mathbf{x} = \mathbf{b}$, which

combines ideas of both the conjugate gradient squared method (CGS) and the successive over relaxation algorithm (SOR). In particular, we want the residuals and the search directions to be given by

$$r_i = Q_i(\mathbf{A})P_i(\mathbf{A})\mathbf{r_0}, \quad p_i = Q_i(\mathbf{A})T_i(\mathbf{A})\mathbf{r_0}, \tag{1.3.28}$$

where $P_i(\mathbf{A})$ and $T_i(\mathbf{A})$ are the polynomials which deliver the residual and the search direction of the original biconjugate gradient algorithm, while $Q_i(\mathbf{A})$ is additional polynomial describing a steepest descent update. The i-th degree polynomials satisfy the following recursive relation:

$$P_{j+1}(t) = P_j(t) - \alpha_j t T_j(t), \quad T_{j+1}(t) = P_j(t) + \beta_j t T_j(t), \quad Q_{j+1}(t) = (1-\omega_j t)Q_j(t), \tag{1.3.29}$$

where the constant α_j and β_j are chosen to be

$$\alpha_j = \frac{\sigma_j}{(\hat{\mathbf{r}}_\mathbf{0}, \mathbf{A}p_j)}, \quad \beta_j = \frac{\alpha_j \sigma_{j+1}}{\omega_j \sigma_j}, \tag{1.3.30}$$

with $\sigma_j = (\hat{\mathbf{r}}_\mathbf{0}, r_j)$ and $\hat{\mathbf{r}}_\mathbf{0}$ an arbitrary vector such that $(\hat{\mathbf{r}}_\mathbf{0}, \mathbf{r_0}) \neq 0$. On the other hand, ω_j is the stabilizing parameter and is calculated so that the next residual $r_{j+1} = Q_{j+1}(\mathbf{A})P_{j+1}(\mathbf{A})\mathbf{r_0}$ is minimized in L^2 norm as a function of ω_j. Thus, introducing the quantity

$$s_j = r_j - \alpha_j \mathbf{A}p_j \tag{1.3.31}$$

then, the next residual can be expressed as

$$r_{j+1} = (I - \omega_j \mathbf{A})s_j. \tag{1.3.32}$$

Consequently, the optimal value of ω_j to minimize the r_{j+1} results to be

$$\omega_j = \frac{(\mathbf{A}s_j, s_j)}{(\mathbf{A}s_j, \mathbf{A}s_j)}. \tag{1.3.33}$$

Finally, the next approximation of the sought solution is given by

$$x_{j+1} = x_j + \alpha_j p_j + \omega_j s_j. \tag{1.3.34}$$

The overall algorithm is summarized in Algorithm 2.

Preconditioner To improve the convergence of the iterative solver, a preconditioner is used together with the GMRES or BiCGStab algorithms. In particular, we consider a Symmetric Gauss-Seidel (SGS) method, [236, 138, 57, 143]. Accordingly, instead of directly addressing (1.3.3) we solve an equivalent, explicitly preconditioned system of the form

$$\widetilde{\mathbf{J}}\left(\mathbf{w}_k^*\right) \Delta \mathbf{w}_k^* = -\widetilde{\mathbf{f}}\left(\mathbf{w}_k^*\right), \tag{1.3.35}$$

where the preconditioned Jacobian matrix $\widetilde{\mathbf{J}}\left(\mathbf{w}_k^*\right)$ and the preconditioned right hand side $\widetilde{\mathbf{f}}\left(\mathbf{w}_k^*\right)$ are obtained by multiplying the original system by a preconditioning matrix $\mathcal{P}^{-1}$ from the left as

$$\mathcal{P}^{-1}\mathbf{J}\left(\mathbf{w}_k^*\right) \Delta \mathbf{w}_k^* = -\mathcal{P}^{-1}\mathbf{f}\left(\mathbf{w}_k^*\right). \tag{1.3.36}$$

Choose $\mathbf{x_0}$ as initial guess
Compute $\mathbf{r_0} = \mathbf{b} - \mathbf{A}\mathbf{x_0}$
Choose $\hat{\mathbf{r}}_0$ such that $(\hat{\mathbf{r}}_0, \mathbf{r}_0) \neq 0$
Set $\mathbf{p_0} = \mathbf{r}_0$
for $j = 1, 2, \ldots$ **do**
    $\alpha_j = \frac{(\hat{\mathbf{r}}_0, \mathbf{r}_j)}{(\hat{\mathbf{r}}_0, \mathbf{A}\mathbf{p}_j)}$
    $\mathbf{s}_j = \mathbf{r}_j - \alpha_j \mathbf{A}\mathbf{p}_j$
    $\omega_j = \frac{(\mathbf{A}\mathbf{s}_j, \mathbf{s}_j)}{(\mathbf{A}\mathbf{s}_j, \mathbf{A}\mathbf{s}_j)}$
    $\mathbf{x}_{j+1} = \mathbf{x}_j + \alpha_j \mathbf{p}_j + \omega_j \mathbf{s}_j$
    $\mathbf{r}_{j+1} = (\mathbf{I} - \omega_j \mathbf{A})\mathbf{s}_j$
    if $\|\mathbf{r}_{j+1}\| <$ tolerance **then**
        exit
    end if
    $\beta_j = \frac{\alpha_j (\hat{\mathbf{r}}_0, \mathbf{r}_{j+1})}{\omega_j (\hat{\mathbf{r}}_0, \mathbf{r}_j)}$
    $\mathbf{p}_{j+1} = \mathbf{r}_{j+1} + \beta_j (\mathbf{p}_j - \omega_j \mathbf{A}\mathbf{p}_j)$
end for
$\mathbf{x} = \mathbf{x}_{j+1}$

Algorithm 2: Pseudocode of the BiCGStab algorithm.

The LU-SGS preconditioner developed for hyperbolic equations, and employed in [236, 138, 57, 143], is based on the idea of using the Jacobian matrix already computed inside the Krylov algorithm, to construct $\mathcal{P}$. Formally, the Jacobian matrix $\mathbf{J}(\mathbf{w}_k^*)$ is decomposed into a diagonal matrix $\mathcal{D}$, a lower triangular matrix $\mathcal{L}$ and an upper triangular matrix $\mathcal{U}$ as follows:

$$\mathbf{J}(\mathbf{w}_k^*) = \mathcal{L} + \mathcal{D} + \mathcal{U}. \tag{1.3.37}$$

Then, the SGS preconditioner reads

$$\mathcal{P}^{-1} = (\mathcal{D} + \mathcal{U})^{-1} \mathcal{D} \, (\mathcal{D} + \mathcal{L})^{-1}. \tag{1.3.38}$$

The application of the preconditioner to a generic vector $\mathbf{q}$, i.e. the calculation of $\mathcal{P}^{-1}\mathbf{q}$, can be performed in two steps, each of them involving only simple block matrix inversion. The first one consists in a forward sweep

$$\widetilde{\mathbf{q}} = (\mathcal{D} + \mathcal{L})^{-1} \mathbf{q}, \tag{1.3.39}$$

which is followed by a backward sweep

$$\mathcal{P}^{-1}\mathbf{q} = (\mathcal{D} + \mathcal{U})^{-1} \mathcal{D} \, \widetilde{\mathbf{q}}. \tag{1.3.40}$$

Thanks to the linearization of the numerical flux functions (1.3.24) or (1.3.22), both sweeps can be carried out in a matrix-free fashion, where in the forward sweep only contributions from elements with lower element number are taken into account and in the backward sweep only contributions from elements with higher element number.

On a general unstructured grid the contributions of the upper and lower triangular part of the Jacobian matrix can be easily obtained by splitting the set of neighbors $\mathcal{K}_i$ of a cell C_i into two subsets $\mathcal{K}_i^-$ and $\mathcal{K}_i^+$ with $\mathcal{K}_i = \mathcal{K}_i^- \cup \mathcal{K}_i^+$ so that elements $j \in \mathcal{K}_i^- < i$

and $j \in \mathcal{K}_i^+ > i$ as it is proposed in [138, 57, 143]. Consequently, the contribution of the linearized convective terms to the Jacobian matrix of the Newton method is split into three contributions denoted by

$$\mathcal{C} = \mathcal{C}^L + \mathcal{C}^D + \mathcal{C}^U. \tag{1.3.41}$$

In particular, in case of the semi-implicit Ducros flux is considered, the matrix-vector product (1.3.24) for a generic cell C_i is computed as the sum of the following contributions: the lower diagonal part of the matrix vector product which reads

$$\mathcal{C}_i^L \Delta\mathbf{w}^* = \frac{\Delta t}{|C_i|} \sum_{j \in \mathcal{K}_i^-} |\Gamma_{ij}| \frac{1}{2} \left(u_{ij}^n - \alpha_{ij}^d \right) \Delta\mathbf{w}_j^*, \tag{1.3.42}$$

the contribution to the upper diagonal part given by

$$\mathcal{C}_i^U \Delta\mathbf{w}^* = \frac{\Delta t}{|C_i|} \sum_{j \in \mathcal{K}_i^+} |\Gamma_{ij}| \frac{1}{2} \left(u_{ij}^n - \alpha_{ij}^d \right) \Delta\mathbf{w}_j^* \tag{1.3.43}$$

and the diagonal contribution

$$\mathcal{C}_i^D \Delta\mathbf{w}^* = \frac{\Delta t}{|C_i|} \sum_{j \in \mathcal{K}_i} |\Gamma_{ij}| \frac{1}{2} \left(u_{ij}^n + \alpha_{ij}^d \right) \Delta\mathbf{w}_i^*. \tag{1.3.44}$$

In the same way, also the stiffness matrix $\mathbf{K}$ has also been split into its diagonal part $\mathbf{K}^D$, an upper triangular matrix $\mathbf{K}^U$ and a lower triangular one $\mathbf{K}^L$. The matrix-vector products associated with $\mathbf{K}^L\Delta\mathbf{w}^*$ and $\mathbf{K}^U\Delta\mathbf{w}^*$ are again easily carried out at the aid of the sets $\mathcal{K}_i^-$ and $\mathcal{K}_i^+$, as for the convective terms. On the other hand, no operations are needed on the global mass matrix since it is naturally diagonal for $\mathbb{P}^1$ Crouzeix-Raviart elements in 2D and it has been diagonalized via mass-lumping when 3D problems are considered. Thus, the final Jacobian, including the viscous terms, is then formally given by

$$\mathbf{J}(\mathbf{w}_k^*) = \mathbf{M} + \mathbf{M} \left(\mathcal{C}^L + \mathcal{C}^D + \mathcal{C}^U \right) - \Delta t \mu \left(\mathbf{K}^L + \mathbf{K}^D + \mathbf{K}^U \right). \tag{1.3.45}$$

Note that the decomposition of the Jacobian itself is never needed in the preconditioner, but only the associated matrix-vector products.

The symmetric Gauss-Seidel method shown above cannot be directly parallelized, hence in the parallel implementation of our scheme we carry out the two sweeps (1.3.39) and (1.3.40) only over the elements contained in each CPU. However, in all numerical experiments run in parallel, we have found that this is not a problem, since in the proposed scheme the SGS method is only used as a preconditioner for a GMRES/BiCGStab algorithm, which instead can be properly parallelized by exchanging the norms of the residuals between all CPUs.

Mesh reordering The performance in the preconditioner step can be accelerated by nodal reordering. Reordering the elements of the mesh can bring a great improvement, making the preconditioner well suited for parallel computation and, thus, increasing the overall efficiency of the Newton-Krylov method. Essentially, the reordering leads to a reduction of the matrix bandwidth, so that more non-zero elements are present outside

the main diagonal, lowering the execution effort of the matrix-vector product. If the elements are reordered properly along the main flow direction, the combination of the forward and backward sweeps of the SGS preconditioner perform similar to a direct solver based on Gauss elimination, in particular for the Ducros flux. For the simple linear scalar advection equation in 1D based on the implicit upwind scheme, the SGS preconditioner even corresponds to the exact direct solver.

Performing an accurate and efficient reordering of elements for unstructured grids can be more challenging than in case structured collocated grids are considered. Since if in the second case quite simple reordering techniques, such as the chess board colouring [142], are available, in case of unstructured mesh the reordering of graphs, based on the local flow velocity and mesh connectivity, see e.g. [196, 56, 34], is, in general, required.

However, in this work we propose the use of a simpler algorithm, which even though may not provide the best possible reordering, it still considerably reduces the number of iterations needed to achieve convergence in the linear solver and it is compatible and easy to implement for parallel codes, since it does not need any extra communication between CPUs.

The approach presented here is a purely spatial reordering of the control volumes of the dual mesh based on an *a priori* defined main flow direction, say $\mathbf{v}_0$, that needs to be determined for each test problem. In the simplest case $\mathbf{v}_0$ corresponds to one of the main coordinate directions $\mathbf{e}_i$. Once the flow direction is set, we construct a total number N_B of equidistant one-dimensional bins of size $\Delta\lambda$ along the chosen unitary main flow direction $\mathbf{v}_0$ with $\|\mathbf{v}_0\| = 1$ and define a straight line starting in a point $\mathbf{x}_0 \in \Omega$ as

$$\mathbf{x} = \mathbf{x}_0 + \lambda \mathbf{v}_0, \qquad \lambda \in \mathbb{R}. \tag{1.3.46}$$

The uniform grid of bins of length $\Delta\lambda$ along $\mathbf{v}_0$ is defined as $\lambda_j = j\Delta\lambda$ with $j \in \mathbb{Z}$. For the mesh reordering we then run over the dual mesh, i.e. over the control volumes C_i, and compute the projection of the barycenter $\mathbf{x}_i$ of cell C_i onto the straight line $\mathbf{x}$ as

$$\xi_i = (\mathbf{x}_i - \mathbf{x}_0) \cdot \mathbf{v}_0. \tag{1.3.47}$$

The control volume C_i is then sorted into the bin number

$$j = \text{int}\left(\frac{\xi_i}{\Delta\lambda}\right). \tag{1.3.48}$$

On the other hand, when dealing with complex geometries, such as blood vessel trees, the choice of the main flow direction according to which elements are sorted may be not so straightforward. In such cases, e.g. for 3D networks of vessels, we assume the main flow direction $\mathbf{v}_0$ to be driven by the centerlines of the 3D volume meshes. Thus, the equidistant one-dimensional bins of size $\Delta\lambda$ are placed along the centerline from the inlet's network towards the outlets and the control volumes of the dual mesh are then sorted into bin numbers according to the concept of the Voronoi diagram. Hence, each bin λ_j is associated to a corresponding region of the domain constituted of all dual elements whose Euclidean distance to λ_j is not greater than their distance to the other bins.

In both cases, once all dual elements have been sorted into their corresponding bins, they are reordered by running over all bins in ascending order, i.e. along the flow direction $\mathbf{v}_0$. Within each bin the element order is simply determined by the order in which the

elements have been put into the bin following a first-in-first-out (FIFO) principle. In case MPI parallelization is used, each CPU simply performs the same type of reordering, but only for its own cells.

To illustrate the effects of the mesh reordering on a 3D domain, we report in Figure 1.2 the original dual cell index and the reordered one for a simple straight geometry in which the flow direction is supposed to coincide with one of the main coordinate directions and the simulation is carried out sequentially.

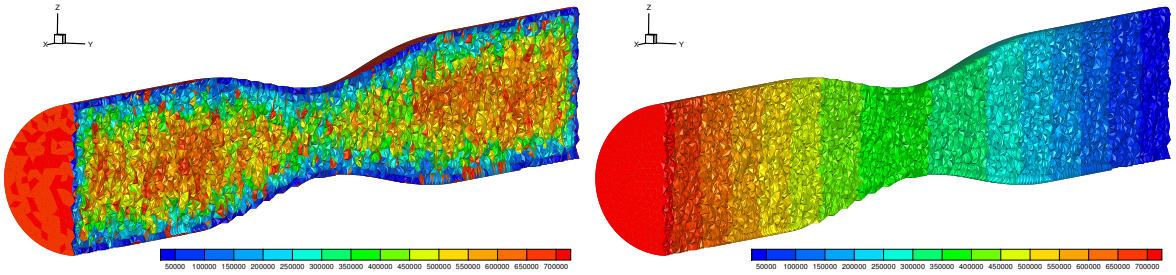

Figure 1.2: Ideal vessel with narrowing section. Dual cells inside the domain colored according to the original dual cell index (left) and according to the index after the reordering (right).

On the other hand, Figure 1.3 shows how the proposed reordering technique reorganizes the indexes of the control volumes in a more complex geometry in which MPI parallelization is performed. The dual elements are reordered in each CPU following the centerlines of the vessels composing the arterial tree, which correspond with the assumed main flow direction.

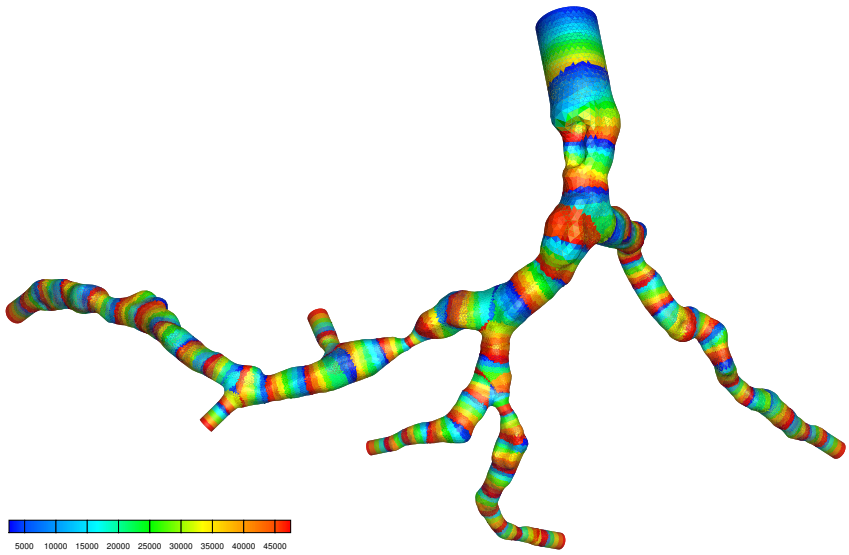

Figure 1.3: Arterial tree. Dual cells colored according to the index after the reordering applied in each of the 60 CPUs employed.

We remark that the presented algorithm is a very simple approach for the reordering of the grid elements. The main shortcoming of this approach is that the number of bins to be employed is not automatically computed but must be estimated taking into account the

size of the domain, the characteristic dual element size and the mesh distribution between CPUs. Furthermore, the choice of the main flow direction according to which elements are sorted depends on the test case and may not be unique for complex flows.

1.3.3 Discrete kinetic energy stability

As aforementioned, for an inviscid fluid under zero gravity effects system (1.1.1) admits an extra energy conservation law in terms of the kinetic energy density. Hence, when deriving a discretization of the Euler equations, it could be of interest to check if the obtained scheme is also kinetic energy stable. As demonstrated below, this property is verified for the proposed scheme when the Ducros numerical flux function is used.

Theorem 1.3.1. *Assuming constant density ($\rho = const.$), vanishing viscosity ($\mu = 0$), zero gravity ($\mathbf{g} = 0$), a divergence-free velocity field at time t^n*

$$\sum_{j\in\mathcal{K}_i} |\Gamma_{ij}| u_{ij}^n = 0, \qquad u_{ij}^n = \frac{1}{2}\left(\mathbf{u}_i^n + \mathbf{u}_j^n\right)\cdot \boldsymbol{n}_{ij} \tag{1.3.49}$$

and vanishing boundary fluxes ($u_{ij}^n = 0\ \forall \Gamma_{ij} \in \partial\Omega$) the finite volume scheme for the discretization of the nonlinear convective terms based on the semi-implicit Ducros flux function

$$\mathbf{u}_i^* = \mathbf{u}_i^n - \frac{\Delta t}{|C_i|}\sum_{j\in\mathcal{K}_i} |\Gamma_{ij}| \left(\frac{1}{2}u_{ij}^n\left(\mathbf{u}_i^* + \mathbf{u}_j^*\right) - \frac{1}{2}\alpha_{ij}^n\left(\mathbf{u}_j^* - \mathbf{u}_i^*\right)\right), \tag{1.3.50}$$

with $\alpha_{ij}^n = |u_{ij}^n| + c_\alpha \geq 0$ is kinetic energy stable in the sense

$$\int_\Omega \frac{1}{2}\left(\mathbf{u}^*\right)^2 d\mathbf{x} \leq \int_\Omega \frac{1}{2}\left(\mathbf{u}^n\right)^2 d\mathbf{x}. \tag{1.3.51}$$

Proof. Taking the dot product of $\mathbf{u}_i^*$ by (1.3.50) yields

$$\mathbf{u}_i^*\cdot\mathbf{u}_i^* = \mathbf{u}_i^*\cdot\mathbf{u}_i^n - \frac{\Delta t}{|C_i|}\sum_{j\in\mathcal{K}_i} |\Gamma_{ij}| \left(\frac{1}{2}u_{ij}^n\mathbf{u}_i^*\cdot\left(\mathbf{u}_i^* + \mathbf{u}_j^*\right) - \frac{1}{2}\alpha_{ij}^n\mathbf{u}_i^*\cdot\left(\mathbf{u}_j^* - \mathbf{u}_i^*\right)\right). \tag{1.3.52}$$

On the other hand, taking into account the divergence-free property of the velocity, (1.3.49), we have

$$\begin{aligned}\sum_{j\in\mathcal{K}_i} |\Gamma_{ij}|\frac{1}{2}u_{ij}^n\mathbf{u}_i^*\cdot\left(\mathbf{u}_i^* + \mathbf{u}_j^*\right) &= \sum_{j\in\mathcal{K}_i} |\Gamma_{ij}|\frac{1}{2}u_{ij}^n\left(\mathbf{u}_i^*\right)^2 + \sum_{j\in\mathcal{K}_i} |\Gamma_{ij}|\frac{1}{2}u_{ij}^n\mathbf{u}_i^*\cdot\mathbf{u}_j^* \\ = \frac{1}{2}\left(\mathbf{u}_i^*\right)^2\sum_{j\in\mathcal{K}_i} |\Gamma_{ij}| u_{ij}^n + \sum_{j\in\mathcal{K}_i} |\Gamma_{ij}|\frac{1}{2}u_{ij}^n\mathbf{u}_i^*\cdot\mathbf{u}_j^* &= \sum_{j\in\mathcal{K}_i} |\Gamma_{ij}|\frac{1}{2}u_{ij}^n\mathbf{u}_i^*\cdot\mathbf{u}_j^*,\end{aligned} \tag{1.3.53}$$

where the second equality comes from the fact that $\mathbf{u}_i^*$ does not depend on j. Applying the former relation to (1.3.52) and adding and subtracting

$$\frac{\Delta t}{|C_i|}\sum_{j\in\mathcal{K}_i} |\Gamma_{ij}|\frac{1}{2}\mathbf{u}_j^*\cdot\frac{1}{2}\alpha_{ij}^n\left(\mathbf{u}_j^* - \mathbf{u}_i^*\right)$$

and $\frac{1}{2}\mathbf{u}_i^n\cdot\mathbf{u}_i^n$ at the right hand side, lead to

$$\begin{aligned}\frac{1}{2}\mathbf{u}_i^*\cdot\mathbf{u}_i^*+\frac{1}{2}\mathbf{u}_i^*\cdot\mathbf{u}_i^* &= \frac{1}{2}\mathbf{u}_i^*\cdot\mathbf{u}_i^n+\frac{1}{2}\mathbf{u}_i^*\cdot\mathbf{u}_i^n-\frac{1}{2}\mathbf{u}_i^n\cdot\mathbf{u}_i^n+\frac{1}{2}\mathbf{u}_i^n\cdot\mathbf{u}_i^n\\ -\frac{\Delta t}{|C_i|}\sum_{j\in\mathcal{K}_i}|\Gamma_{ij}|\Big(u_{ij}^n\frac{1}{2}\mathbf{u}_i^*\cdot\mathbf{u}_j^*-\frac{1}{2}\alpha_{ij}^n\frac{1}{2}\mathbf{u}_i^*\cdot\left(\mathbf{u}_j^*-\mathbf{u}_i^*\right)-\frac{1}{2}\alpha_{ij}^n\frac{1}{2}\mathbf{u}_j^*\cdot\left(\mathbf{u}_j^*-\mathbf{u}_i^*\right)\\ -\frac{1}{2}\alpha_{ij}^n\frac{1}{2}\mathbf{u}_i^*\cdot\left(\mathbf{u}_j^*-\mathbf{u}_i^*\right)+\frac{1}{2}\alpha_{ij}^n\frac{1}{2}\mathbf{u}_j^*\cdot\left(\mathbf{u}_j^*-\mathbf{u}_i^*\right)\Big).\end{aligned}\tag{1.3.54}$$

Reordering terms, we get

$$\begin{aligned}\frac{1}{2}\mathbf{u}_i^*\cdot\mathbf{u}_i^* &= \frac{1}{2}\left(\mathbf{u}_i^*-\mathbf{u}_i^n\right)\cdot\left(\mathbf{u}_i^n-\mathbf{u}_i^*\right)+\frac{1}{2}\mathbf{u}_i^n\cdot\mathbf{u}_i^n\\ -\frac{\Delta t}{|C_i|}\sum_{j\in\mathcal{K}_i}|\Gamma_{ij}|\Big(u_{ij}^n\frac{1}{2}\mathbf{u}_i^*\cdot\mathbf{u}_j^*-\frac{1}{2}\alpha_{ij}^n\left(\frac{1}{2}\left(\mathbf{u}_j^*\right)^2-\frac{1}{2}\left(\mathbf{u}_i^*\right)^2\right)+\frac{1}{2}\alpha_{ij}^n\frac{1}{2}\left(\mathbf{u}_j^*-\mathbf{u}_i^*\right)^2\Big).\end{aligned}\tag{1.3.55}$$

Since $\alpha_{ij}^n\geq 0$, then

$$\begin{aligned}\frac{1}{2}\left(\mathbf{u}_i^*\right)^2 &= \frac{1}{2}\left(\mathbf{u}_i^n\right)^2-\frac{\Delta t}{|C_i|}\sum_{j\in\mathcal{K}_i}|\Gamma_{ij}|\Big(u_{ij}^n\frac{1}{2}\mathbf{u}_i^*\cdot\mathbf{u}_j^*-\frac{1}{2}\alpha_{ij}^n\left(\frac{1}{2}\left(\mathbf{u}_j^*\right)^2-\frac{1}{2}\left(\mathbf{u}_i^*\right)^2\right)\Big)\\ &\quad-\frac{1}{2}\left(\mathbf{u}_i^*-\mathbf{u}_i^n\right)^2-\frac{\Delta t}{|C_i|}\sum_{j\in\mathcal{K}_i}|\Gamma_{ij}|\left(\frac{1}{2}\alpha_{ij}^n\frac{1}{2}\left(\mathbf{u}_j^*-\mathbf{u}_i^*\right)^2\right)\\ &\leq \frac{1}{2}\left(\mathbf{u}_i^n\right)^2-\frac{\Delta t}{|C_i|}\sum_{j\in\mathcal{K}_i}|\Gamma_{ij}|\Big(u_{ij}^n\frac{1}{2}\mathbf{u}_i^*\cdot\mathbf{u}_j^*-\frac{1}{2}\alpha_{ij}^n\left(\frac{1}{2}\left(\mathbf{u}_j^*\right)^2-\frac{1}{2}\left(\mathbf{u}_i^*\right)^2\right)\Big)\end{aligned}\tag{1.3.56}$$

which corresponds to a discrete kinetic energy inequality in each cell C_i. Finally, integrating over the domain results

$$\int_\Omega\frac{1}{2}\left(\mathbf{u}^*\right)^2\mathrm{dV}\leq\int_\Omega\frac{1}{2}\left(\mathbf{u}^n\right)^2\mathrm{dV}-\Delta t\sum_{C_i}\sum_{j\in\mathcal{K}_i}|\Gamma_{ij}|\Big(u_{ij}^n\frac{1}{2}\mathbf{u}_i^*\cdot\mathbf{u}_j^*-\frac{1}{2}\alpha_{ij}^n\left(\frac{1}{2}\left(\mathbf{u}_j^*\right)^2-\frac{1}{2}\left(\mathbf{u}_i^*\right)^2\right)\Big).\tag{1.3.57}$$

Since $\boldsymbol{n}_{ij}=-\boldsymbol{n}_{ji}$ when summing the fluxes over all cells they cancel,

$$|\Gamma_{ij}|u_{ij}^n\frac{1}{2}\mathbf{u}_i^*\cdot\mathbf{u}_j^*=-|\Gamma_{ji}|u_{ji}^n\frac{1}{2}\mathbf{u}_j^*\cdot\mathbf{u}_i^*,$$

apart from the ones on the boundary of the domain. Thus, assuming vanishing boundary fluxes and taking into account that the last term in (1.3.57) is the dissipative kinetic energy flux, we obtain

$$\int_\Omega\frac{1}{2}\left(\mathbf{u}^*\right)^2\mathrm{dV}\leq\int_\Omega\frac{1}{2}\left(\mathbf{u}^n\right)^2\mathrm{dV},\tag{1.3.58}$$

hence the scheme is kinetic energy stable. □

1.4 Projection stage

Once we have computed the intermediate approximation of the velocity field $\mathbf{w}^*$, which includes the nonlinear convective and the viscous terms, the final velocity field and the new pressure can be obtained via a projection method. We discretize the pressure system using standard continuous finite elements following the methodology exploited in former semi-implicit hybrid FV/FE schemes, [24, 46, 185].

Let $\psi \in V_0$ be a test function, $V_0 = \{\psi \in \mathcal{H}^1 : \int_\Omega \psi dV = 0\}$. Multiplication of (1.2.4) by the gradient of a test function ψ and integration over the domain Ω yields

$$\int_\Omega \nabla(p^{n+1} - p^n) \cdot \nabla \psi \, = \frac{1}{\Delta t} \int_\Omega \mathbf{w}^* \cdot \nabla \psi \, \mathrm{dV} - \frac{1}{\Delta t} \int_\Omega \mathbf{w}^{n+1} \cdot \nabla \psi \, \mathrm{dV} \,. \tag{1.4.1}$$

Then, applying the Green formula to the last integral in the former equation and considering (1.2.5), we derive

$$\int_\Omega \mathbf{w}^{n+1} \cdot \nabla \psi \, \mathrm{dV} = \int_{\partial\Omega} \mathbf{w}^{n+1} \cdot \boldsymbol{n} \psi \, \mathrm{dS} - \int_\Omega \nabla \cdot \mathbf{w}^{n+1} \psi \, \mathrm{dV} = \int_{\partial\Omega} \mathbf{w}^{n+1} \cdot \boldsymbol{n} \psi \, \mathrm{dS} \,. \tag{1.4.2}$$

By introducing the notation for the pressure correction, $\delta p = p^{n+1} - p^n$, and taking into account relation (1.4.2) onto the variational formulation (1.4.1), we obtain the weak problem:
Find $\delta p = p^{n+1} - p^n \in V_0$ *satisfying*

$$\int_\Omega \nabla \, \delta p \cdot \nabla \psi \, \mathrm{dV} = \frac{1}{\Delta t} \int_\Omega \mathbf{w}^* \cdot \nabla \psi \, \mathrm{dV} - \frac{1}{\Delta t} \int_{\partial\Omega} \mathbf{w}^{n+1} \cdot \boldsymbol{n} \psi \, \mathrm{dS} \tag{1.4.3}$$

for all $z \in V_0$.
The weak problem (1.4.3) corresponds to the following Poisson problem for the unknown δp with Neumann boundary conditions

$$\nabla^2 \, \delta p = \frac{1}{\Delta t} \nabla \cdot \mathbf{w}^* \qquad \text{in } \Omega, \tag{1.4.4}$$

$$\frac{\partial \delta p}{\partial \boldsymbol{n}} = \frac{1}{\Delta t} \left(\mathbf{w}^* \cdot \boldsymbol{n} - \mathbf{w}^{n+1} \cdot \boldsymbol{n} \right) \qquad \text{on } \partial\Omega. \tag{1.4.5}$$

Problem (1.4.3) is discretized using $\mathbb{P}^1$ finite elements in a constrained setting leading to a symmetric positive definite system. Then, an optimized matrix-free conjugate gradient method is employed to solve the resulting algebraic system.

1.5 Post-projection stage

Once the pressure correction δp is obtained at the vertex of the primal grid, we can recover the pressure at the new time step as $p^{n+1} = p^n + \delta p$. Moreover, the corrected value for the linear momentum is computed on the dual mesh by updating $\mathbf{w}^*$ with $\nabla \, \delta p$ according to (1.2.2). The needed pressure gradient $\nabla \, \delta p$ is first approximated at each primal element by using the gradients of the classical basis function for $\mathbb{P}^1$ finite elements. Then, it is interpolated on the dual grid by considering the weighted average of the contributions of the two primal subelements used to build each dual cell.

This stage concludes the novel fully explicit hybrid FV/FE algorithm. In what follows, the methodology is carefully assessed through a set of classical benchmarks for fluid mechanics. Besides, we first introduce the different types of boundary conditions to be employed.

1.6 Boundary conditions

An important point that still needs to be addressed is the treatment of boundary conditions. In this section, we present the key points to treat the different types of boundary conditions to be employed in the test cases analyzed in the next section. In particular, we will consider periodic boundary conditions, velocity inlet, pressure inlet, pressure outlet, Dirichlet boundary conditions and viscous and inviscid walls. Note that the methodology proposed in the transport-diffusion stage requires the computation of a residual, matrix-vector products and a preconditioner so boundary conditions must be consistently imposed throughout the Newton-Krylov algorithm as well as for the pressure system.

- Periodic boundary conditions. In case a periodic boundary condition is considered, the neighboring dual elements through the periodic boundaries are identified and virtually merged providing a new interior cell, which could be a quadrilateral in 2D or a polyhedron of six faces in 3D. Within the transport-diffusion stage, we keep the computation of the convective and diffusive terms on the original dual cell, namely at a half of this theoretically merged element, and then a correction is performed to incorporate the contributions of the other periodic half. This approach leads to double the boundary elements when computing the residuals. Therefore, a weight is assigned to each of them so that they contribute only with half the weight of the original interior cells. On the other hand, the periodic primal vertices are merged leading to the final mesh employed to compute the pressure solution in the projection stage. Careful attention must be taken if periodic boundary conditions are imposed everywhere, since the pressure could freely change by an additive constant. Hence, the pressure problem would result singular. To avoid it, we simply fix one of the vertex to a predefined value that may be taken from a mean pressure, the exact solution, if available, or the initial data.

- Velocity inlet boundary conditions. The momentum at the boundary, $\rho\mathbf{u}_{BC}$, is weakly imposed by computing the convective fluxes within the residual considering a right state of the form:
$$\rho\mathbf{u}_j = 2\rho\mathbf{u}_{BC} - \rho\mathbf{u}_i, \tag{1.6.1}$$
with $\rho\mathbf{u}_i$ the linear momentum computed at the boundary cell. Regarding the computation of the linearized fluxes inside the matrix-vector product and the flux contribution in the preconditioner, we define the right state to be the opposite of the inner one. The given velocity is also employed to compute the boundary integral of the pressure system, i.e. the last term in (1.4.3).

- Dirichlet boundary conditions for the velocity field or viscous wall/no slip boundary conditions. The given momentum, $\rho\mathbf{u}_{BC}$, is strongly imposed in the finite volume

stage by overwritten the obtained value with the exact momentum. This correction is also performed after the post-projection stage. Furthermore, the exact velocity is taken into account also in the boundary integral to compute the pressure within the projection stage, as it has been done for velocity inlet boundaries.

- Inviscid wall boundary. In this case the velocity is weakly defined inside the momentum solver by considering the state:

$$\rho\mathbf{u}_j = \rho\mathbf{u}_i - 2\left(\rho\mathbf{u}_i \cdot \boldsymbol{n}\right)\boldsymbol{n}. \tag{1.6.2}$$

  For the matrix-vector products and the preconditioner the approach followed is the same than for the velocity inlet. Meanwhile, inside the pressure system the boundary integral contribution is set to zero.

- Pressure outlet boundary conditions. The given pressure is imposed in the pressure subsystem, while the velocity is left completely free in the momentum equations. In this case, the convective fluxes are computed using the inner state.

- Pressure inlet boundary conditions. They are a combination of a velocity inlet for the solution of the momentum equations and a pressure outlet boundary condition for the pressure system.

1.7 Numerical results

In this section, the proposed fully implicit hybrid FV/FE methodology is validated with the aid of several benchmarks taken from fluid mechanics. First, the Taylor-Green vortex test case and the ABC problem are considered to analyze the accuracy. Then, to study the ability of the scheme to reproduce the behavior of viscous flows, the first problem of Stokes as well as the lid driven cavity are addressed. Since the methodology has been developed having in mind applications to blood flow simulations in vessels, the flow over a backward-facing step and the flow over a cylinder for an inviscid fluid and a set of viscous flows are also analyzed. Moreover, we study the classical Hagen-Poiseuille and Womersley problems and the flow through an ideal artery with stenosis. Finally, a real 3D coronary tree geometry is considered. The results obtained with the proposed algorithm are validated against either analytical solutions, numerical reference solution or available experimental data. In addition, for the lid-driven cavity test, for the viscous flow over a cylinder problem and for the realistic test case, the computational efficiency of the new fully-implicit hybrid FV/FE method is compared with that of the former semi-implicit hybrid FV/FE scheme.

Unless stated otherwise, in this section, the density is set to $\rho = 1$ and the convective-diffusive subsystem is solved by employing the SGS preconditioned Newton-BiCGStab algorithm with the second order in space Ducros flux function and an artificial viscosity set to $c_\alpha = 0$.

1.7.1 Taylor-Green vortex test

As first test case, we consider the classical steady state Taylor-Green vortex benchmark. We define the computational domain to be $\Omega = [0, 2\pi] \times [0, 2\pi]$ in which holds the following

exact solution:

$$p(x_1, x_2, t) = \frac{1}{4}(\cos(2x_1) + \cos(2x_2)), \quad \rho(x_1, x_2, t) = 1,$$
$$u_1(x_1, x_2, t) = \sin(x_1)\cos(x_2), \quad u_2(x_1, x_2, t) = -\cos(x_1)\sin(x_2).$$

To perform the analysis of the error and order of accuracy, we employ the five meshes with decreasing cell number presented in Table 1.1. Six different schemes are used

Mesh	Primal elements	Vertices	Dual elements
M_1	512	289	800
M_2	2048	1089	3136
M_3	8192	4225	12416
M_4	32768	16129	49408
M_5	131072	66049	197120

Table 1.1: Taylor-Green vortex test. Mesh features.

to solve the problem: the SGS-preconditioned Newton-GMRES method as well as the preconditioned Newton-BiCGStab method employing a Ducros semi-implicit scheme of both first and second order and the Newton-BiCGStab-SGS method with the first and second order Rusanov scheme as numerical flux function. As initial condition we impose the exact solution and the simulation is run up to $t = 1$ with a fixed time step set to $\Delta t = 0.05$ for the coarser grid and then properly scaled according to the mesh refinement. Periodic boundary conditions are imposed on all sides. The obtained L_2 error norms at the final time and the corresponding convergence rates, computed for any variable q as

$$E(q)_{M_i} = ||q - q_{M_i}||_{L_2(\Omega)}, \qquad o_{q_{M_i/M_j}} = \frac{\log(E(q)_{M_i}/E(q)_{M_j})}{\log(h_{M_i}/h_{M_j})}, \tag{1.7.1}$$

are reported in Table 1.2. We observe that the sought order of accuracy is obtained for all cases considered. In addition, the performance of the different methods has been also analyzed and compared. Table 1.3 reports the total computational time, the computational time per dual element and time step, namely

$$t_e = \frac{\text{CPU time}}{\text{N. dual elements} \cdot \text{N. time steps}}, \tag{1.7.2}$$

and the number of time steps employed in each methodology analyzed. As expected, using the Ducros flux function, and thus avoiding Newton iterations, is less time consuming than employing the implicit Rusanov flux, which requires the Newton algorithm for the linearization of the convective terms. This difference can be observed better for the first order scheme due to the lower accuracy of the method which forces the Krylov and Newton methods to perform more iterations to attain the stop criteria tolerance than when using the more accurate second order scheme. This fact also justifies the smaller CPU time of the second order in space approach with respect to the first order scheme for fine grids. For instance, for mesh M_5, when running the Ducros flux function in the BiCGStab algorithm we need 2 iterations to reach the tolerance in each time step, while for the first order

	E_{M_1}	E_{M_2}	E_{M_3}	E_{M_4}	E_{M_5}	o_{M_1/M_2}	o_{M_2/M_3}	o_{M_3/M_4}	o_{M_4/M_5}
GMRES, Ducros, 1^{st} order									
p	0.639	0.327	0.151	7.1e-2	3.5e-2	0.96	1.12	1.09	1.03
W	0.798	0.45	0.246	0.131	6.8e-2	0.83	0.87	0.91	0.95
GMRES, Ducros, 2^{nd} order									
p	0.173	5.1e-2	1.3e-2	3.3e-3	8.2e-4	1.77	1.96	1.99	2.0
W	4.7e-2	9.3e-3	2.1e-3	5.2e-4	1.2e-4	2.32	2.13	2.03	2.17
BiCGStab, Ducros, 1^{st} order									
p	0.639	0.327	0.151	7.1e-2	3.5e-2	0.96	1.12	1.09	1.03
W	0.798	0.45	0.246	0.131	6.8e-2	0.83	0.87	0.91	0.95
BiCGStab, Ducros, 2^{nd} order									
p	0.173	5.1e-2	1.3e-2	3.3e-3	8.2e-4	1.77	1.96	1.99	2.0
W	4.7e-2	9.3e-3	2.1e-3	5.2e-4	1.2e-4	2.32	2.13	2.03	2.17
BiCGStab, Rusanov, 1^{st} order									
p	1.121	0.754	0.394	0.195	9.6e-2	0.57	0.93	1.01	1.02
W	1.124	0.646	0.356	0.19	9.9e-2	0.8	0.86	0.9	0.94
BiCGStab, Rusanov, 2^{nd} order									
p	0.145	4.7e-2	1.3e-2	3.2e-3	8.2e-4	1.63	1.89	1.96	1.98
W	4.5e-2	9.3e-3	2.2e-3	5.2e-4	1.2e-4	2.28	2.11	2.04	2.16

Table 1.2: Taylor-Green vortex test. Observed L_2 norm errors in space and time, E_{M_i}, and convergence rates, $o_{M_i/M_{i+1}}$.

scheme we perform 4 iterations of the Krylov algorithm per time step. Besides, the smaller CPU time required for the BiCGStab-Rusanov algorithm for the M_5 grid with respect to M_4 is due to the smaller error committed by the Krylov solver for M_5, which avoids the necessity of Newton iterations. Meanwhile, for M_4 or coarser grids, at least two iterations of the Newton loop are needed to reach the prescribed tolerance.

1.7.2 3D Arnold-Beltrami-Childress flow

The second academic test is performed to assess the accuracy of the proposed method also for problems defined in a three dimensional space. We consider the Arnold-Beltrami-Childress (ABC) flow originally introduced in [9, 58] and also studied in [209]. The exact solution for the inviscid incompressible Navier-Stokes equations in a periodic domain reads

$$
\begin{aligned}
u_1(x_1, x_2, x_3, t) &= (\sin(x_3) + \cos(x_2)),\\
u_2(x_1, x_2, x_3, t) &= (\sin(x_1) + \cos(x_3)),\\
u_3(x_1, x_2, x_3, t) &= (\sin(x_2) + \cos(x_1)),
\end{aligned}
$$

$$
p(x_1, x_2, x_3, t) = -(\cos(x_1)\sin(x_2) + \sin(x_1)\cos(x_3) + \sin(x_3)\cos(x_2)) + c, \tag{1.7.3}
$$

	M_1	M_2	M_3	M_4	M_5
GMRES, Ducros, 1^{st} order					
CPU time [s]	0.2085	1.8085	18.6728	234.1114	2818.3383
t_e [ms]	0.013	0.0144	0.0188	0.0296	0.0447
Time steps	20	40	80	160	320
GMRES, Ducros, 2^{nd} order					
CPU time [s]	0.2267	1.7674	17.142	196.3942	212.272
t_e [ms]	0.0142	0.0141	0.0173	0.0248	0.0034
Time steps	20	40	80	160	320
BiCGStab, Ducros, 1^{st} order					
CPU time [s]	3.6388	1.7925	18.7976	221.8836	2763.4684
t_e [ms]	0.2274	0.0143	0.0189	0.0281	0.0438
Time steps	20	40	80	160	320
BiCGStab, Ducros, 2^{nd} order					
CPU time [s]	4.6886	1.7353	17.5796	183.9679	205.1983
t_e [ms]	0.293	0.0138	0.0177	0.0233	0.0033
Time steps	20	40	80	160	320
BiCGStab, Rusanov, 1^{st} order					
CPU time [s]	0.9933	7.3803	48.1604	466.2547	4647.945
t_e [ms]	0.0621	0.0588	0.0485	0.059	0.0737
Time steps	20	40	80	160	320
BiCGStab, Rusanov, 2^{nd} order					
CPU time [s]	45.2971	6.0887	26.9274	260.3956	220.1567
t_e [ms]	2.8311	0.0485	0.0271	0.0329	0.0035
Time steps	20	40	80	160	320

Table 1.3: Taylor-Green vortex test. CPU time, CPU time per element, t_e, and number of time steps. All simulations have been carried out in serial on one single CPU core of an AMD Ryzen Threadripper 3990X workstation with 64 cores and 128 GB of RAM.

with $c \in \mathbb{R}$. The convergence study is performed using the implicit hybrid method with a preconditioned Newton-BiCGStab scheme and a Ducros semi-implicit scheme of both first and second order. An artificial viscosity coefficient of $c_\alpha = 1.0$ is set for the second order in space scheme. The computational domain is given by $\Omega = [-\pi, \pi]^3$ and a sequence of four successively refined meshes is used. The main features of those meshes are reported in Table 1.4. As initial condition we impose the exact solution and the simulations are run up to $t = 1$ with a time step set to $\Delta t = 0.05$ for the coarser grid and then properly scaled according to the mesh refinement. Since we impose periodic boundary conditions on all sides, we have a set of solutions for the pressure differing by a constant c. In order to test also the convergence rate of the pressure, we set the constant c in (1.7.3) a posteriori

Mesh	Primal elements	Vertices
M_1	8640	2197
M_2	69120	15625
M_3	552960	117649
M_4	4423680	912673

Table 1.4: ABC test. Mesh features.

equal to the mean value of the resulting numerical pressure, as done in [209].

The obtained pressure and the velocity streamlines for mesh M_3 are depicted in Figure 1.4 for a qualitative comparison with available reference data.

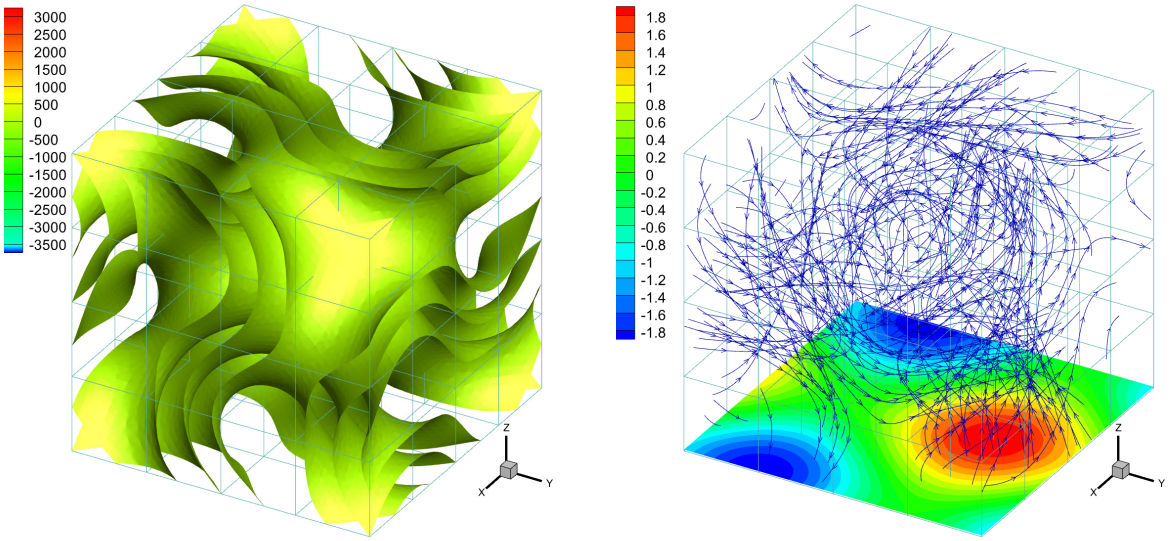

Figure 1.4: ABC test. Pressure isosurfaces at levels $p = [-0.8, 0.0, 0.8]$ (left) and velocity streamlines (right).

Meanwhile, the resulting L_2 error norms and convergence rates computed according to (1.7.1) are reported in Table 1.5. We observe that the first order scheme is slightly below the expected accuracy especially for the pressure variable, while the second order scheme achieves the sought order of accuracy.

In addition, Table 1.6 reports the computational time, the computational time per dual element and the number of time steps needed to reach the final time. As in the convergence study for the Taylor-Green vortex in 2D, Section 1.7.1, for fine grids we observe a smaller CPU time of the second order in space approach with respect to the first order scheme, justified by the fact that the use of a higher accuracy method requires less iterations to attain the tolerance of the stop criteria in the iterative method. Again, for mesh M_4, when running the second order scheme in the BiCGStab algorithm we need 2 iterations to reach the tolerance in each time step, while for the first order scheme we perform 4 iterations of the Krylov algorithm per time step.

	E_{M_1}	E_{M_2}	E_{M_3}	E_{M_4}	o_{M_1/M_2}	o_{M_2/M_3}	o_{M_3/M_4}
BiCGStab, Ducros, 1^{st} order							
p	2.9	1.739	0.939	0.522	0.74	0.89	0.85
W	4.346	2.265	1.176	0.603	0.94	0.95	0.96
BiCGStab, Ducros, 2^{nd} order							
p	0.79	0.227	5.1e-2	1.2e-2	1.8	2.15	2.05
W	0.807	0.198	4.6e-2	7.3e-3	2.02	2.11	2.67

Table 1.5: ABC test. Observed L_2 errors in space and time, E_{M_i}, and convergence rates, $o_{M_i/M_{i+1}}$.

	M_1	M_2	M_3	M_4
BiCGStab, Ducros, 1^{st} order				
CPU time [s]	3.187	15.0431	199.1015	2855.7914
t_e [ms]	0.0615	0.1451	0.1309	0.123
Time steps	20	40	80	160
BiCGStab, Ducros, 2^{nd} order				
CPU time [s]	8.3805	38.4215	233.7558	681.022
t_e [ms]	0.1617	0.3706	0.1537	0.0293
Time steps	20	40	80	160

Table 1.6: ABC test. CPU time, CPU time per element, t_e, and number of time steps.

1.7.3 First problem of Stokes

We now simulate the first problem of Stokes, [192]. This is one of the rare unsteady problems for which an exact solution of the incompressible Navier-Stokes equations is known. We consider the computational domain $\Omega = [-0.5, 0.5] \times [-0.05, 0.05]$, a mesh composed of 128000 primal elements and the following initial condition:

$$p(x_1, x_2, 0) = 0, \quad u_1(x_1, x_2, 0) = 0, \quad u_2(x_1, x_2, 0) = \begin{cases} 0.1, & \text{if } x_1 > 0, \\ -0.1, & \text{if } x_1 < 0. \end{cases}$$

To reproduce the classical 1D test case, periodic boundary conditions are set along x_2-direction, whereas the initial condition is imposed on the left and right boundaries of the domain. The fluid density is $\rho = 1$, while a sequence of viscosity values are considered $\mu \in \{10^{-2}, 10^{-3}, 10^{-4}\}$. The simulations are run using the BiCGStab-Newton algorithm with a second order semi-implicit Ducros numerical flux function. The fixed time step is $\Delta t = 0.01$ and we set a final time of $t = 1$. The numerical results for the velocity component u_2 are validated against the exact solution of the Navier-Stokes equations which is given by

$$u_2(x_1, x_2, t) = \frac{1}{10} \text{erf}\left(\frac{x_1}{2\sqrt{\mu t}}\right).$$

Figure 1.5 presents the comparison between the reference solution and the numerically obtained one-dimensional cut along the x_1-direction at $x_2 = 0$. An excellent agreement can be observed for all viscosities considered.

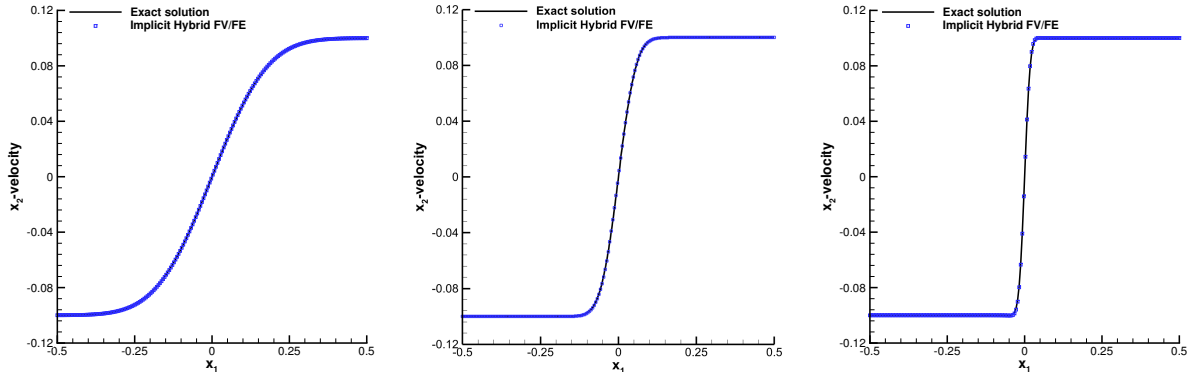

Figure 1.5: First problem of Stokes. Comparison between the exact solution and the numerical results computed with the implicit hybrid FV/FE scheme on the one-dimensional cut along the x_1-direction at $x_2 = 0$ at the final time $t = 1$. The viscosity values considered are: $\mu = 10^{-2}$ (left), $\mu = 10^{-3}$ (middle), $\mu = 10^{-4}$ (right).

1.7.4 Lid-driven cavity

The lid-driven cavity problem has widely been used as a validation test for incompressible flow solvers, [98, 5, 207, 185]. We discretize the square domain $\Omega = [0, 1] \times [0, 1]$ with a triangular grid made of 2906 primal elements. Dirichlet boundary conditions are imposed on all sides: no slip conditions are applied on lateral boundaries and at the bottom, while a fixed velocity field $\mathbf{u} = (1, 0)$ is imposed at top boundary. Moreover, the fluid density is set to $\rho = 1$ and the fluid viscosity is fixed to $\mu = 10^{-2}$, resulting in a Reynolds number of 100. To run the simulation, we consider an initial fluid at a rest with pressure $p = 1$ and we let the time step vary at each time iteration according to the CFL condition as

$$\Delta t = \min_{C_i} \{\Delta t_i\}, \qquad \Delta t_i = \mathrm{CFL} \frac{r_i^2}{(|\zeta|_{\max} + c_\alpha) r_i} \tag{1.7.4}$$

with $|\zeta|_{\max}$ the maximum absolute eigenvalue related to the convective terms, r_i the incircle diameter of each dual control volume and CFL= 100. The preconditioner inside the Newton-BiCGStab algorithm makes use of a reordering of the elements in x_1-direction. The obtained velocity profiles along the vertical and horizontal lines passing through the geometric center of the cavity are compared against the reference solution from Ghia et al. [98] in Figure 1.6. The contour plots of the velocity components together with the velocity vectors are also depicted.

We now analyze the computational cost of the implicit scheme with respect to the semi-implicit hybrid FV/FE methodology proposed in [185, 45]. To solve the convective part of the semi-implicit scheme, the second order in space explicit approach with the Rusanov flux function is used, while the counterpart of the fully implicit scheme employs the preconditioned Newton-BiCGStab method also with a second order in space Rusanov

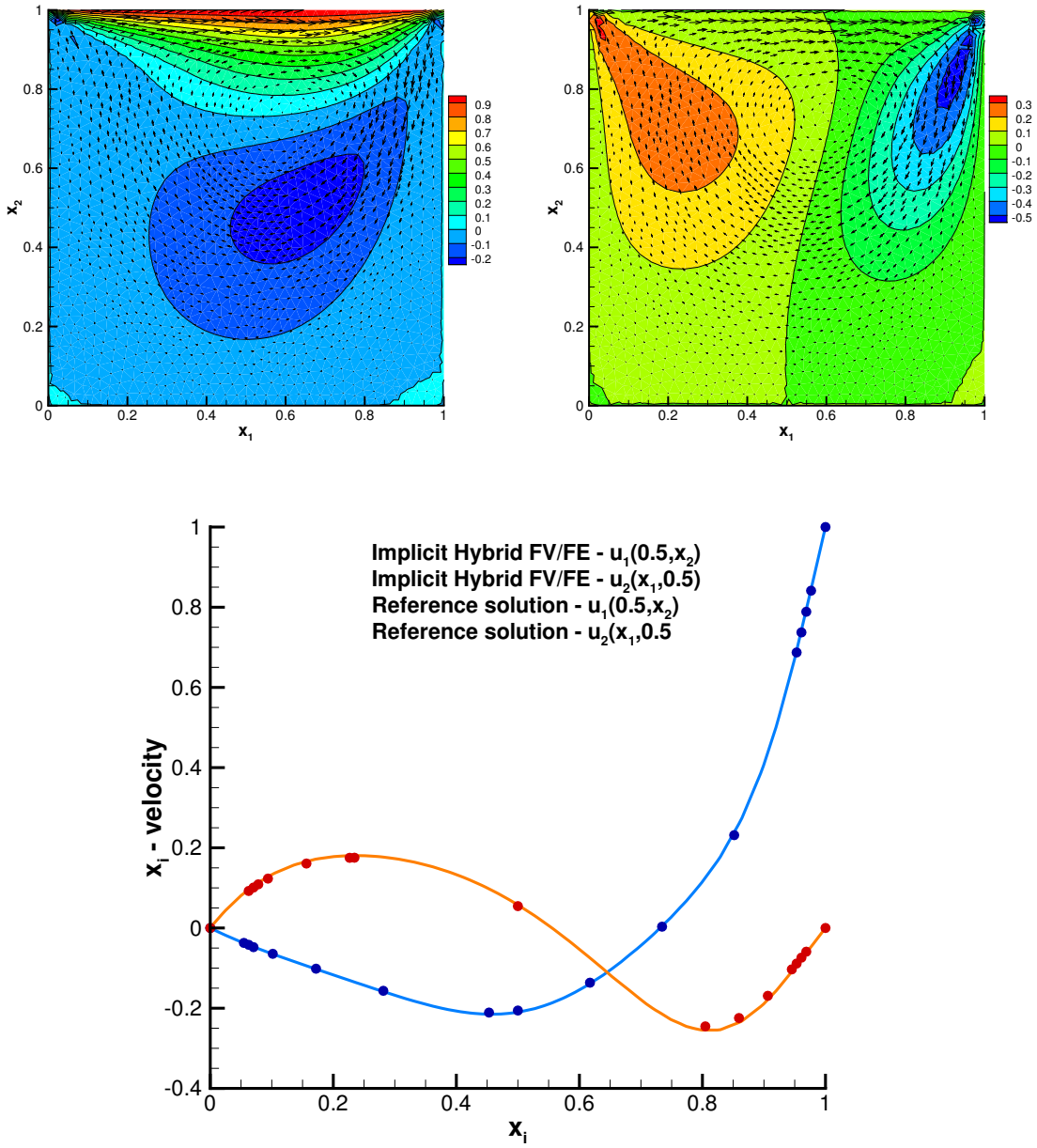

Figure 1.6: Lid driven cavity. Top: contour plot of the x_1-component of velocity vector, u_1, (left) and of x_2-component, u_2, (right) obtained using the implicit hybrid FV/FE scheme. Bottom: 1D cuts for u_1 and u_2 along the vertical and horizontal lines passing through the geometric center of the cavity . The reference solution for comparison is taken from [98].

flux function. The computational time for both tests is reported in Table 1.7. We can observe that for this test case the use of the new fully implicit scheme proposed in this thesis reduces the computational cost of the simulation by a factor of around 110 when using the Rusanov flux function and of about 145 in case the Ducros flux function is employed.

Numerical Flux	Semi-implicit FV/FE scheme	New implicit FV/FE scheme
Rusanov	4809.89 s	41.85 s
Ducros	4829.65 s	32.89 s

Table 1.7: Lid driven cavity. CPU times required by the novel fully implicit hybrid FV/FE scheme and the semi-implicit hybrid FV/FE method in [45]. The tests are run in parallel on 32 CPUs of an AMD Ryzen Threadripper 3990X.

1.7.5 Backward-facing step flow

We now study the fluid flow over a backward-facing step at different Reynolds numbers. The structure of the domain follows that reported in [74]. We choose a step of height $h = 0.097$. Then, the inlet boundary is located 20 step heights upstream the step, while the outlet boundary is chosen 300 step heights away from the step. The larger channel, downstream of the step, has a height of $H = 0.2$, i.e. we consider a expansion ratio, the ratio of the channel height H downstream of the step to the channel height h_i upstream of the step, equal to 1.942. At the inlet we impose the exact Poiseuille velocity profile, whereas a Neumann boundary condition is considered at the outlet. On all other boundaries, no-slip wall boundary conditions are imposed. For the current test the fluid density is set to $\rho = 1$ and the kinematic viscosity ν is chosen in order to obtain the desired Reynolds number, [7], which is given by $\text{Re}= \frac{DU}{\nu}$, with $D = 2h_i$ and U the mean inlet velocity. The time step is set to $\Delta t = 0.01$ and the simulation is run with the implicit hybrid FV/FE scheme until steady state is reached. Figure 1.7 depicts the x_1-component of the resulting velocity field and the streamlines at Re= 400. In addition, in Figure 1.8 we plot the resulting recirculation point X_1, normalized by the step height h, for different Reynolds numbers. Herein, we compare our results against the experimental data reported in [7], the numerical results obtained in [208] using a staggered semi-implicit discontinuous Galerkin scheme with polynomial approximation degree of order $N = 3$, and the explicit second-order upwind finite difference scheme presented in [74].

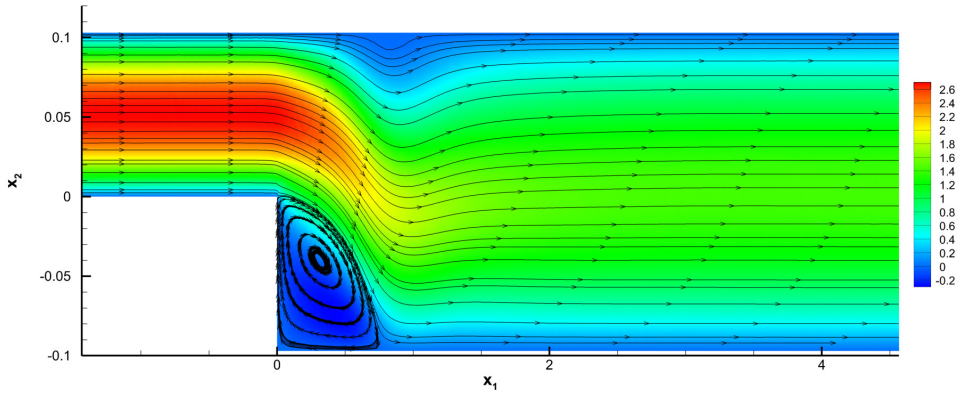

Figure 1.7: Backward-facing step flow. Contour plot of the velocity field obtained with the implicit hybrid FV/FE method at Re= 400 and resulting streamlines near the recirculation zone downstream the step.

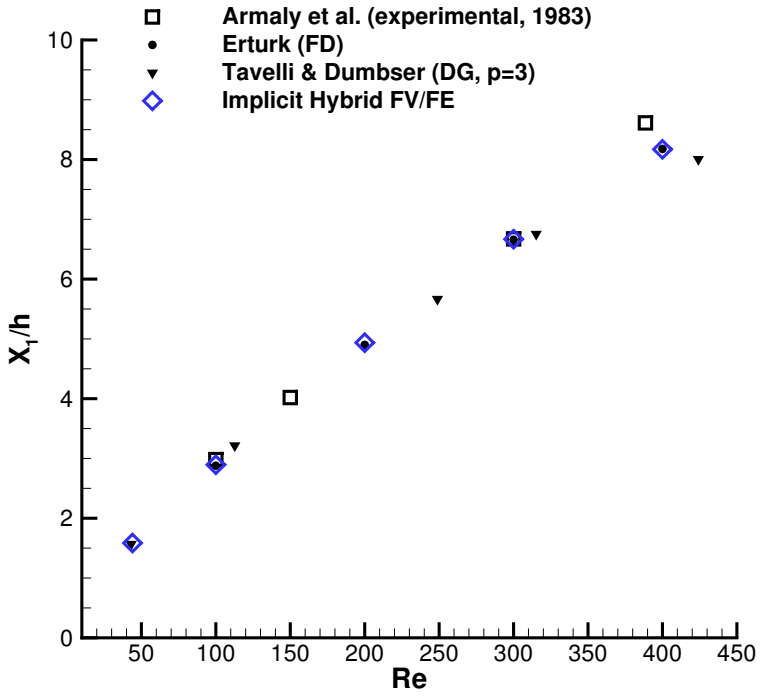

Figure 1.8: Backward-facing step flow. Normalized recirculation point X_1/h for different Reynolds numbers compared with the experimental data reported in [7], the numerical results obtained in [74] and those presented in [208].

1.7.6 Potential flow around a cylinder

The sixth test case analysed here consists in the inviscid flow around a circular cylinder, [208]. We consider the computational domain $\Omega = [-8, 8]^2 \backslash \{\mathbf{x} \in \mathbb{R}^2 \mid \|\mathbf{x}\| < 1\}$ discretized with 30384 primal triangular elements. The velocity field is strongly imposed at the left inflow boundary, making use of the known analytical potential flow solution:

$$u_r = u_m \left(1 - \frac{r_c^2}{r^2}\right) \cos(\phi), \qquad u_\theta = -u_m \left(1 + \frac{r_c^2}{r^2}\right) \sin(\phi), \qquad \tan(\phi) = \frac{x_2}{x_1},$$

where u_r, u_θ denote the radial and angular velocities, respectively, $u_m = 1$ is the mean flow velocity in the horizontal direction, $r_c = 1$ is the radius of the cylinder and r is the distance to the center of the cylinder of each spacial point $\mathbf{x}$. In the left boundary a pressure outlet boundary condition is defined using

$$p(r, \phi, t) = 1 + u_m^2 \frac{r_c^2}{r^2} \left(\cos(2\phi) - \frac{1}{2} \frac{r_c^2}{r^2}\right).$$

Finally at the top and bottom boundaries weak Dirichlet boundary conditions for the velocity field are employed. As initial condition we impose the constant velocity field $\mathbf{u} = (u_m, 0) = (1, 0)$ and $p = 1$. The results obtained with the second order implicit hybrid scheme with $c_\alpha = 0.5$ are reported in Figure 1.9.
We can observe that the obtained solution fits pretty well the known exact solution along the circumference of radius $r = 1.01$ centered at the origin.

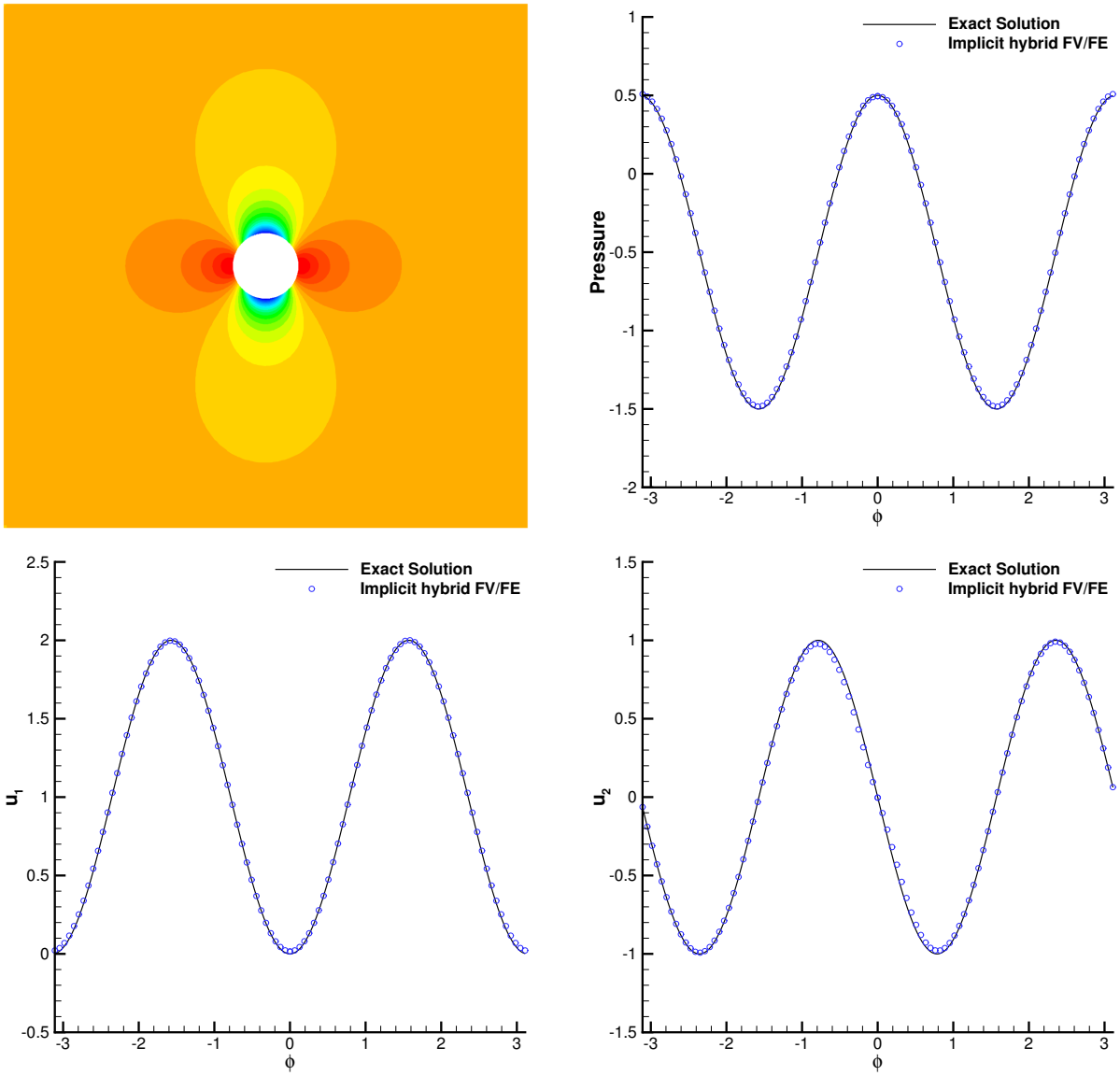

Figure 1.9: Inviscid flow passing around a cylinder. The top left figure depicts the contour plot of the pressure field obtained using the implicit hybrid FV/FE scheme at time $t = 1$. The 1D cuts of the pressure, horizontal and vertical velocities (from right top to left bottom, blue circles) along the cylinder of radius $r = 1.01$ centered at the origin are reported together with the exact known solution (black solid line).

1.7.7 Viscous flow around a cylinder

The next problem to be analyzed is the case of a viscous fluid flowing around a cylinder, [232, 44]. The geometry considered consists in a 2D channel of length 50 and height 20 pierced by an embedded cylinder of radius $R = 0.5$. At the inlet we set a constant velocity profile of value $\mathbf{u} = (1, 0)$, used also as initial condition. A pressure $p = 1$ is imposed at the outlet, while the cylinder boundary is assumed to be a viscous no-slip wall. We assume the top and bottom boundaries to be far enough away from the cylinder so that the velocity at infinity is recovered. Hence, it can be weakly imposed as a velocity boundary condition. A grid of 85050 primal triangular elements with 64 divisions along the cylinder is employed

to discretize the computational domain. To complete the test definition, the viscosity coefficient is calculated to get the desired Reynolds number, e.g. to have Re = 185 we have set the viscosity to $\mu = 5.4054054 \cdot 10^{-3}$. The results presented have been obtained using the second order implicit hybrid FV/FE scheme with the Ducros numerical flux function and an auxiliary artificial viscosity of $c_\alpha = 0.5$.

All simulations are run until the von Karman vortex street has been fully developed so that the vortex frequency can be computed. Since this benchmark is characterized by the Reynolds and Strouhal numbers, we plot in Figure 1.10 the value of $St = \frac{f_v D}{u_1}$ calculated for a set of different Reynolds numbers, $\mathrm{Re} \in \{50, 75, 100, 125, 150, 175, 185\}$. The results obtained using a semi-implicit DG scheme of order 4, [208], the experimental results of [232] and the so-called universal Strouhal curve are included for comparison. Furthermore,

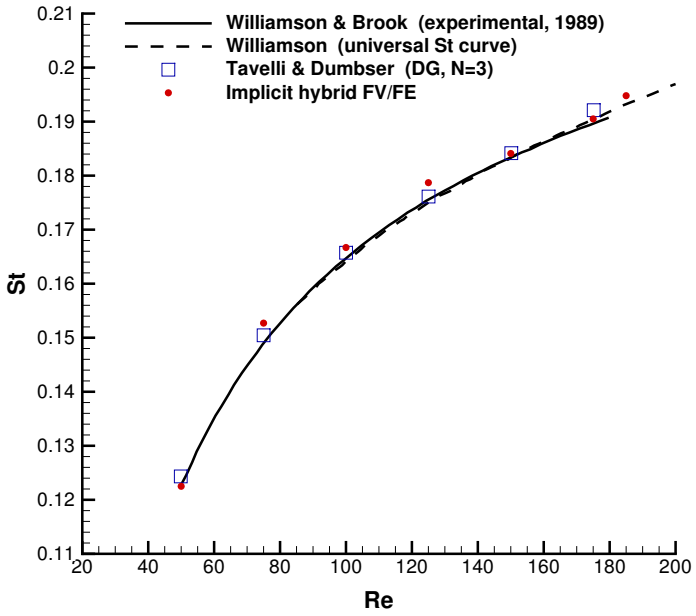

Figure 1.10: Viscous flow around a cylinder. Relationship of Reynolds and Strouhal numbers for the implicit hybrid FV/FE method (red dots), the semi-implicit DG proposed in [208] (blue squares), the experimental results of [232] (continuous black line) and the so-called universal Strouhal relation (dashed black line).

the time series of the drag and lift coefficients of the simulation for Re = 185, reported in Figure 1.11, are in agreement with the numerical results presented in [106, 44]. Also the contour plots of the vorticity field for different times along one periodic cycle are depicted in Figure 1.12 for a qualitative comparison with further references.

In this test case, the reordering of elements in x_2-direction results crucial for the preconditioner, otherwise the convergence of the method is much slower. The speed-up of the fully-implicit hybrid scheme with respect to the semi-implicit hybrid method presented in [45] is analyzed. The semi-implicit hybrid FV/FE scheme employed discretizes the nonlinear convective terms explicitly, while the viscous terms and the pressure system are treated implicitly. Accordingly, the CFL time step restriction, taken as CFL= 0.5, only depends on the eigenvalues of the transport subsystem. The Ducros and Rusanov numerical flux functions have been considered for both schemes. The computational cost

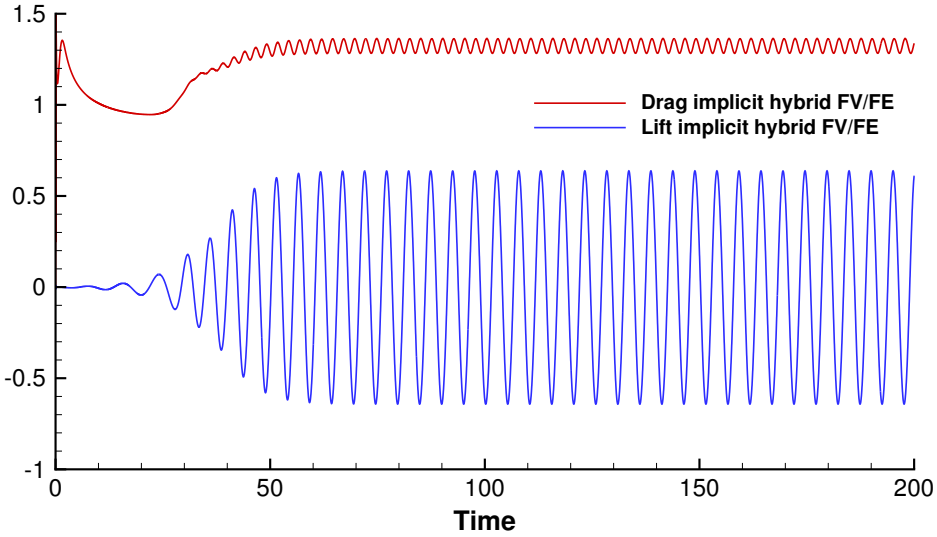

Figure 1.11: Viscous flow around a cylinder. Drag and lift coefficients for a flow of Re= 185 obtained using the implicit hybrid FV/FE scheme with the Ducros flux function, $c_\alpha = 0.5$ and $\Delta t = 10^{-2}$.

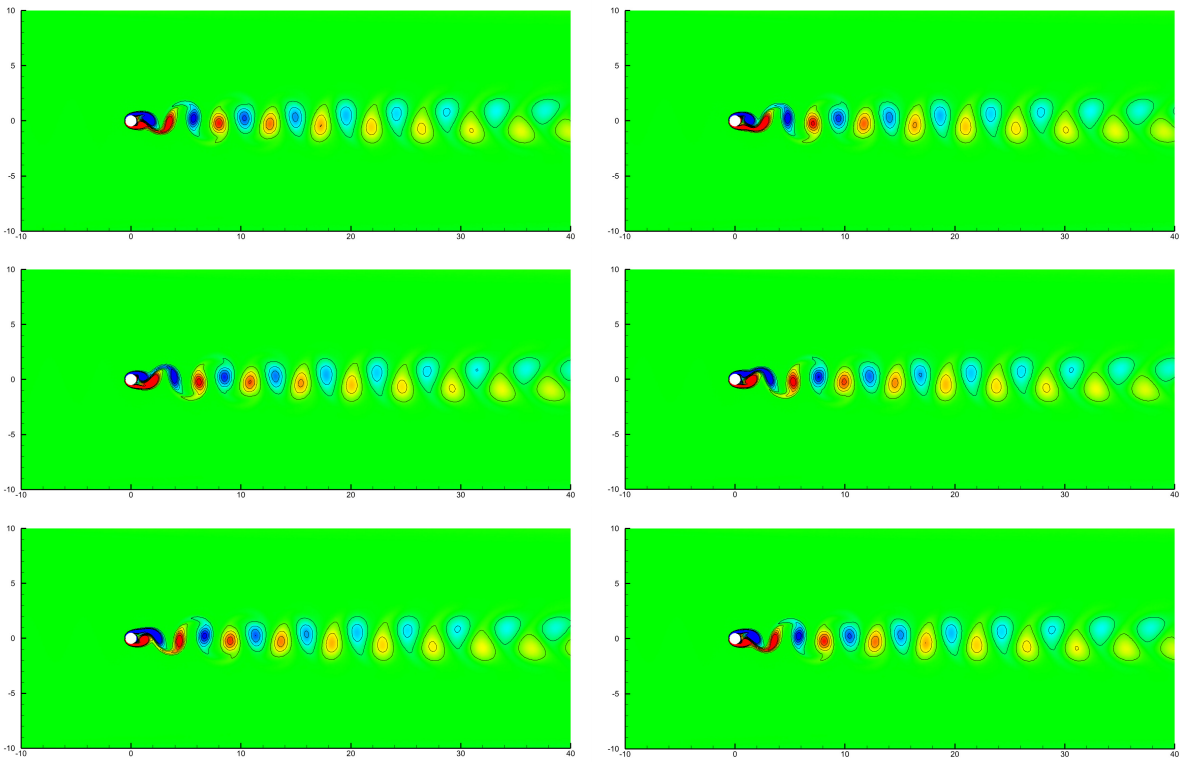

Figure 1.12: Viscous flow around a cylinder. Contour plots of the vorticity field for a flow of Re= 185 around a cylinder at times $100, 101, 102, 103, 104, 105$ (from top left to bottom right).

of the simulations for Re = 185 up to time 200 is reported in Table 1.8. We observe that the proposed implicit approach is around one order of magnitude cheaper than the semi-implicit method.

	Semi-implicit scheme	Implicit scheme
Rusanov	16120.12	1844.52
Ducros	16442.73	1412.57

Table 1.8: Viscous flow around a cylinder. CPU time (s) employed to run the simulation for Re = 185 up to time 200 using the novel fully implicit hybrid FV/FE scheme and the semi-implicit hybrid FV/FE method in [45]. All simulations have been carried out on 128 CPU cores of the Finisterrae III supercomputer (CESGA) which accounts for Intel® Xeon Ice Lake 8352Y processors with 32 cores at 2.2GHz.

1.7.8 Hagen-Poiseuille benchmark

Here, we test the proposed method in the context of a classical three-dimensional academic test for blood flow solvers. We consider a stationary fluid in a three-dimensional pipe of axis x_3, length $L = 1$ and radius $R = 0.1$. A constant pressure gradient $\Delta p < 0$ is imposed between its two ends, enforcing the fluid to flow in x_3-axis direction. This benchmark corresponds to a Hagen-Poiseuille flow whose exact solution is a parabolic velocity profile given by, see e.g. [191],

$$\mathbf{u} = \left(0, 0, \frac{1}{4}\frac{\Delta p}{L}\frac{\rho}{\mu}(r^2 - R^2)\right). \tag{1.7.5}$$

As initial condition we consider a fluid at rest. Moreover, we set $\rho = 1$ and $\mu = 0.1$. The pressure gradient imposed between the left inflow and the right outlet is $\Delta p = -4.8$, leading to a maximum velocity in x_3-axis direction of 0.12. The computational results at time $t = 10.13$ are shown in Figure 1.13, where we compare the sectional velocity across the flow at the mid section against the exact solution. The computed numerical solution excellently matches the exact one. In Figure 1.14 the velocity field in the $x_2 = 0$ plane is depicted.

1.7.9 Womersley problem

In this section the implicit hybrid FV/FE algorithm is validated against the exact solution for an oscillating flow of viscosity $\mu = 8.94 \cdot 10^{-4}$ passing between two flat parallel plates, [233, 134]. The unsteady flow is driven by a sinusoidal pressure gradient on the boundary given by

$$\frac{\partial p}{\partial x_1} = \frac{p_{out}(t) - p_{in}(t)}{l} = -Ae^{int}, \tag{1.7.6}$$

where $A = 1$ is the amplitude of the pressure gradient, n denotes the frequency of the oscillation, i represents the imaginary unit, l is the length of the plates and p_{in} and p_{out} are the pressure at the inlet and at the outlet, respectively. By imposing (1.7.6) at the two ends and a no-slip boundary condition on the upper and lower flat plates, the resulting velocity field can be expressed in complex form as

$$\mathbf{u}(x_1, x_2, t) = \left(\frac{A}{i\,\rho n}\left(1 - \frac{\cosh(\mathrm{Wo}\, i^{1/2}\frac{x_2}{a})}{\cosh(\mathrm{Wo}\, i^{1/2})}\right)e^{i\,nt}, 0\right),$$

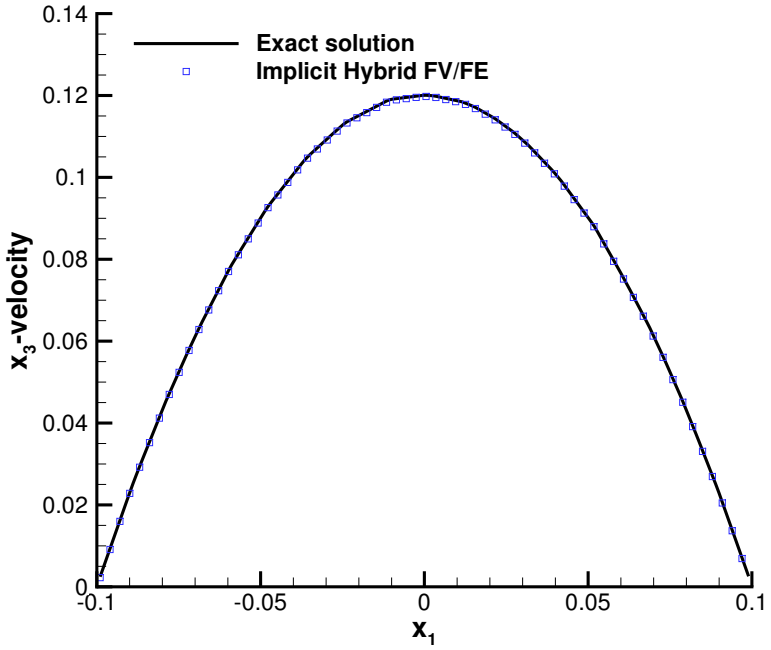

Figure 1.13: Steady laminar Hagen-Poiseuille flow in a cylinder. 1D cut along the x_1 axis at $x_2 = 0$ and $x_3 = L/2$.

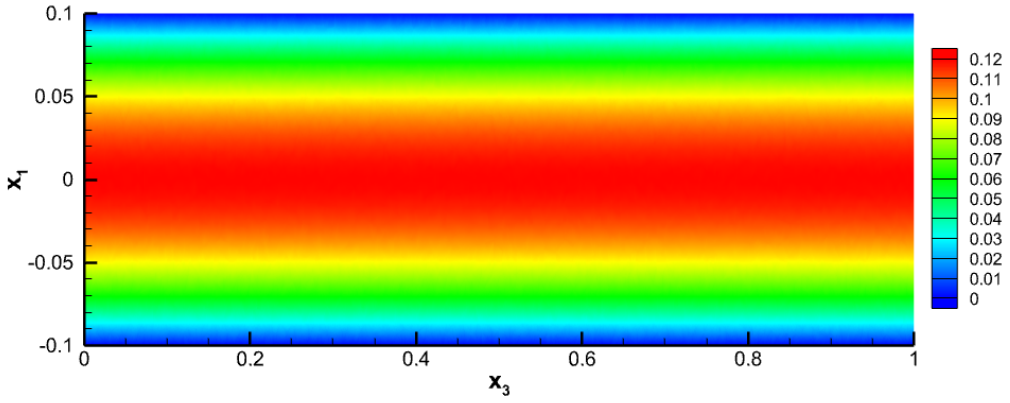

Figure 1.14: Steady laminar Hagen-Poiseuille flow in a cylinder. Velocity u_3 contour in the $x_2 = 0$ plane.

where the Womersley number, $\mathrm{Wo} = a\sqrt{\frac{n}{\nu}} = 10$, with ν the kinematic viscosity and $2a$ the distance between the plates, describes the nature of the unsteady flow. For the simulation we consider the computational domain $\Omega = [-0.5, 1] \times [-0.2, 0.2]$ discretized with a mesh of 228 primal elements. The time step is fixed during the whole simulation to $\Delta t = 2.5 \cdot 10^{-3}$ so that we properly follow the flow oscillations. The obtained velocity profile along the vertical cut $x_1 = 0$ is reported in Figure 1.15 for $t \in \{0.35, 0.7, 1.4, 2.1, 2.45\}$. A good agreement between exact and numerical solution is observed.

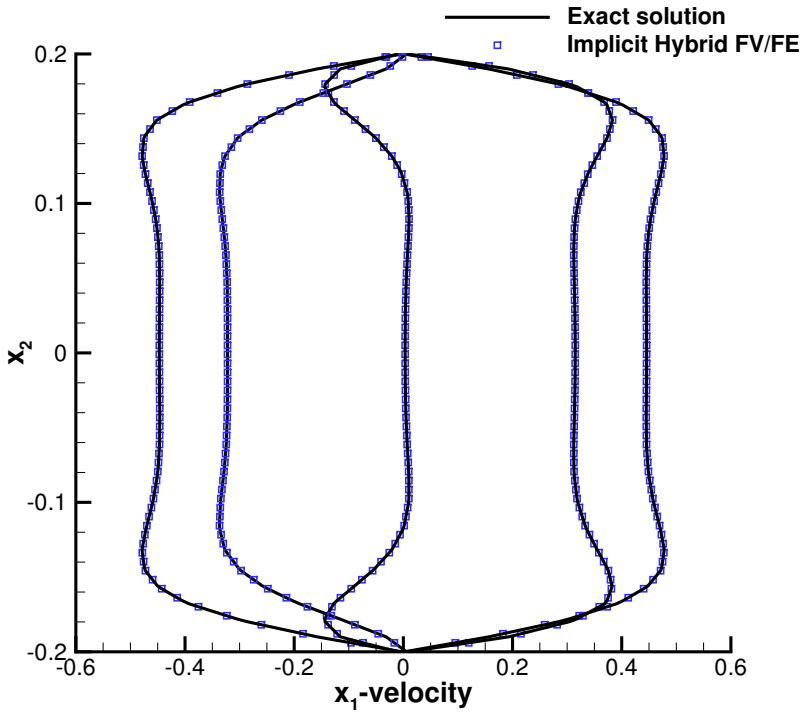

Figure 1.15: Womersley problem. Comparison between the exact and the numerical solution at times $t = 2.1$, $t = 2.45$, $t = 1.4$, $t = 0.35$, $t = 0.7$, from left to right.

1.7.10 Ideal artery with stenosis

To apply the presented algorithm to a more realistic test case in the context of blood flow dynamics, we propose the study of the flow inside an ideal stenotic artery. To this end, we consider a steady flow of a viscous fluid in a duct of length $L = 2$ with axis $x_1 = 0$ which has a shrinkage of 40% in diameter at the half length. The pressure gradient imposed between the left and right boundaries of the computational domain drives the fluid flow in the x_1-direction. On the lateral boundary, no-slip wall boundary conditions are imposed. Initially the flow is assumed to be at rest, the density and viscosity are set to $\rho = 1$, $\nu = 0.01$ and we define a fixed time step of $\Delta t = 0.5$. Four different simulations regarding the method employed are run: the GMRES-Newton method and the BiCGStab-Newton algorithm with both the first and second order approach for the convective terms. Figure 1.16 shows the velocity contour on a longitudinal clip of the domain together with the streamlines over its surface. Moreover, the velocity profiles of each of the four simulations on the section $x_1 = -0.5$, upstream the stenosis, and the section located at the maximal narrowing of the duct, $x_1 = 0$, are reported in Figure 1.17. We can observe that both methods provide numerical solutions in strict accordance using either the first or the second order in space scheme.

1.7.11 Realistic test case: a coronary tree

As last test, we present a blood flow simulation for a realistic three-dimensional configuration. The geometry is segmented from the coronary computed tomography

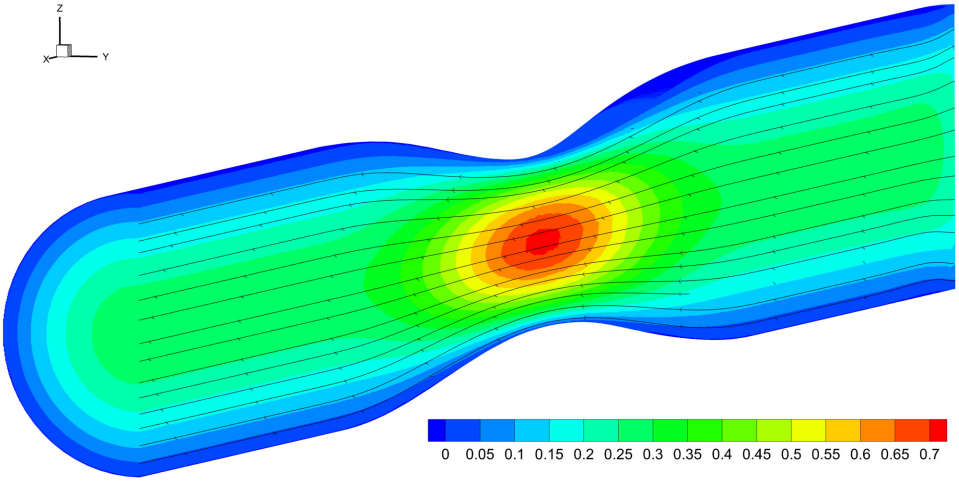

Figure 1.16: Ideal artery with stenosis test. Contours of the velocity field on a longitudinal clip of the domain and streamlines over its surface.

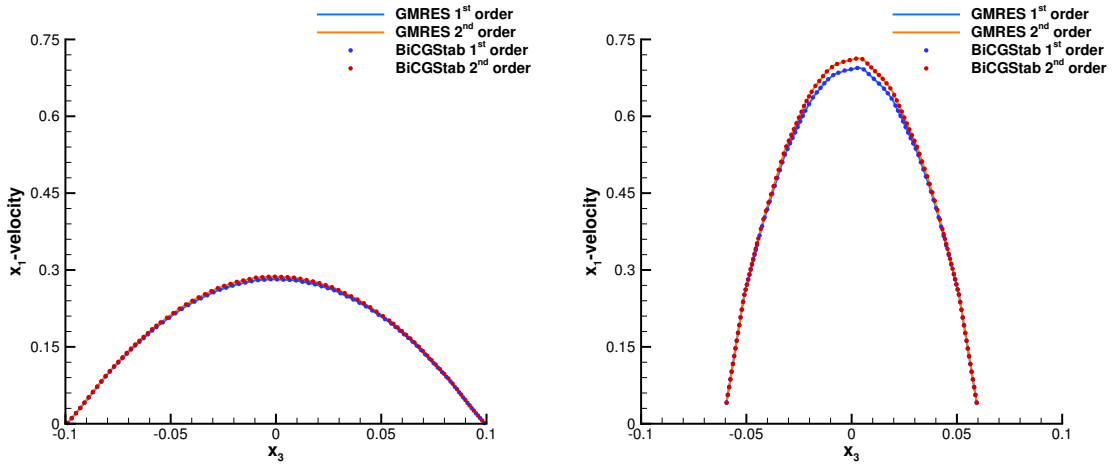

Figure 1.17: Ideal artery with stenosis test. Left: velocity profiles upstream the stenosis at $x_1 = -0.5$. Right: velocity profiles at the narrowest section $x_1 = 0$.

angiography image of a patient affected by a coronary artery disease. It represents a coronary tree, which includes the left main, the circumflex artery (LCX) and the left anterior descending artery (LAD) with the main diagonal branches. A severe stenosis of 85% occlusion is located at the mid LAD, while a minor lesion of 45% is located at mid LCX.

According to the modeling pipeline which will be described in the second part of this thesis, we simulate a hyperemic steady state flow through the entire coronary tree by prescribing a flow distribution among the vessels as outflow boundary condition and imposing a mean aortic pressure of 95.658 mmHg at the inlet section. The total flow passing through the coronary tree is 4.02 cm^3/s, the density is set to 1.05 g/cm^3 and the viscosity is 0.035 cm^2/s. The convective-diffusive system is solved by exploiting the preconditioned Newton-BiCGStab algorithm with the first order Ducros flux function and an auxiliary artificial viscosity of $c_\alpha = 50$.

The presence of a severe stenosis in a vessel causes a sharp drop in pressure, as we

can observe in Figure 1.18. Indeed, distal to the vessel's occlusion we record a pressure reduction of 47.53%. Moreover, Figure 1.19 highlights how a tortuous geometry with curvatures and sinus affects the shape of the sectional velocity profiles throughout the domain.

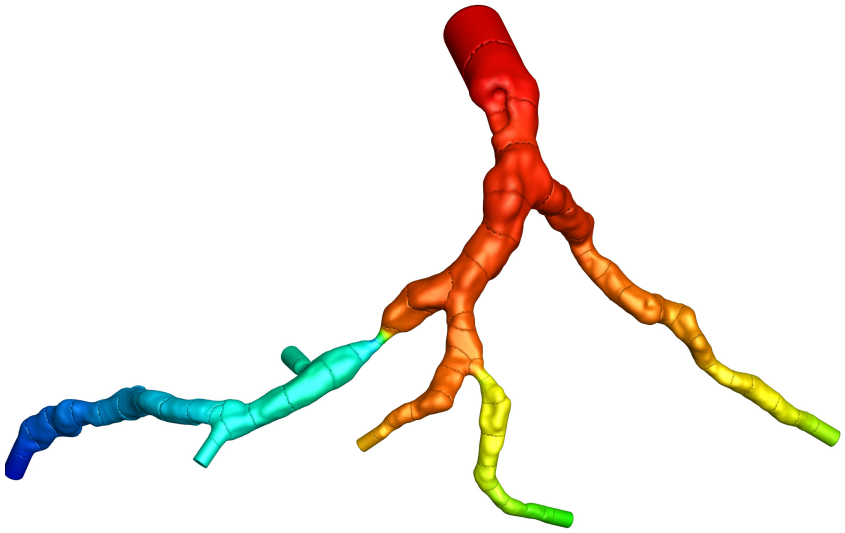

Figure 1.18: Coronary tree test. Pressure distribution among the entire domain.

In case of coronary artery disease, the gold standard for diagnosis of functional severity of ischemia-inducible coronary stenosis is the Fractional Flow Reserve (FFR) [172]. During catheterization, after having pharmacologically induced hyperemia, a guiding wire equipped with a pressure sensor is inserted into the coronary artery to record the pressure in the aorta (p_a) and the pressure approximately 2-3 cm distal to the lesion (p_d) to be investigated. FFR is then determined as a ratio between the mean values of p_d and p_a tracings, namely

$$FFR = \frac{p_d}{p_a},$$

and takes values between 0, standing for a complete occlusion of the vessel, and 1, corresponding to a healthy patient. According to the FFR value, the decision on whether to proceed with surgical intervention or if it is sufficient to treat the patient with Optimal Medical Therapy is taken. More precisely, trials evaluating the prognostic impact of the FFR have shown that a lesion is haemodynamically relevant if FFR < 0.75 and then revascularisation is recommended [171]. For the patient here considered, three FFR measurements at different locations are available. The first one is at the end of LCX, while the others are along the LAD after the stenosis. Table 1.9 reports the FFR values obtained using the proposed hybrid FV/FE methodology as well as the results obtained employing the open-source library CBCFLOW. In addition, the values invasively measured in clinical setting are also reported, [89]. The open-source library CBCFLOW [76] is based on FEniCS [133] and makes use of P1 and P2 FE for the computation of the velocity and pressure fields, respectively. The methodology employed to perform this simulation is further detailed in Chapter 3. The FFR values obtained along the LAD, namely FFR_2

Figure 1.19: Coronary tree test. Sectional velocity profiles through the domain.

	FFR_1	FFR_2	FFR_3
CBCFLOW	0.94	0.68	0.69
Implicit hybrid FV/FE	0.85	0.52	0.57
Clinical value	0.88	0.52	0.57

Table 1.9: Coronary tree test. FFR computationally predicted by the implicit hybrid FV/FE simulation and by the FEniCS simulation at three different locations of the coronary tree. In addition, the corresponding clinically measured values provided in [89] are also reported.

and FFR_3, indicate, for both methodologies, the presence of a stenosis able to induce myocardial ischemia, while the stenosis located at mid LCX associated to FFR_1 resulted to be not functionally significant. The findings are in agreement with conclusions based on the invasive FFR and anatomical measurements, [89, 149].

We would point out that the mismatch between FFR predicted by the two numerical methods can be explained by the fact that the same mesh has been used for both methodologies. However, the methods have different order of accuracy. Hence, mesh independent solutions can be obtained for differently refined meshes. Solving the problem with the implicit hybrid FV/FE methods using refiner meshes provides solutions which converge towards the numerical solution obtained with the FEniCS solver.

On the other hand, an accurate comparison between the proposed methodology and the employed open-source solver is beyond the objective of this test, which aims instead to show the potentiality of the new fully implicit hybrid FV/FE scheme compared to the semi-implicit hybrid method. Indeed, what is remarkable to note in this test is the advantage in terms of computational cost when using the new fully implicit hybrid approach rather than the semi-implicit hybrid method described in [185]. The new fully implicit hybrid FV/FE method employs 22262.63s to reach a final time of $t = 3$s. Meanwhile, solving

the convective part of the semi-implicit scheme with the first order semi-implicit hybrid FV/FE method, in which the time step is computed according to the convective CFL condition with CFL= 0.9, takes 260640s to reach only $t = 7.4472 \cdot 10^{-3}$s so more than one year would be needed to reach the final time of 3s. The measured speed-up factor of the new fully implicit hybrid FV/FE scheme compared to the previous semi-implicit FV/FE method is therefore approximately 4716 times, i.e. more than three orders of magnitude. Both simulations have been performed on 60 CPU cores of an Intel® Xeon-Gold 6140M cluster with 768 GB of RAM.

Chapter 2

A semi-implicit finite volume scheme for blood flow in elastic and viscoelastic vessels

In this second chapter, we propose a novel staggered semi-implicit finite volume method for the simulation of one-dimensional blood flow in networks of elastic and viscoelastic vessels. This is a natural step towards the development of a numerical strategy able to simulate a complete cardiovascular network since the use of a 3D approach for the whole domain would become computationally unaffordable. The one-dimensional blood flow model to be employed is derived from the incompressible Navier-Stokes equations, (1.1.1). As in that case, the explicit discretization of the whole system may yield to a severe CFL condition. A simple strategy to reduce the time step restriction, already employed in the previous chapter, may be the decoupling of the equations so that at least the corresponding pressure subsystem is discretized implicitly. Consequently, the CFL condition would depend only in the mean flow velocity allowing larger time steps. Following this idea, the system of governing equations is split into three subsystems: one containing the nonlinear convective terms, a second one for the viscoelastic terms and a final subsystem for the pressure-related terms. An explicit approach is then employed to discretize the convective subsystem, while the viscous and pressure terms are treated implicitly. This leads to a semi-implicit scheme which is characterized by a CFL-type time step restriction depending only on the bulk velocity of the flow and not on the speed of the pressure waves nor on viscoelasticity. The resulting method is thus computationally efficient in case of a low speed index problem, which is equivalent to have a low Mach regime for the Navier-Stokes equations.

To extend the methodology proposed for 1D vessels to the case of networks, a novel and very simple 3D approach for the treatment of junctions is introduced. Each junction is represented by a unique three-dimensional primal cell and the Euler equations are employed to approximate the velocity and pressure unknowns. A multidimensional numerical flux then takes into account the elementary information of the junction geometry, namely normal vectors and areas of the incident vessels, when approximating the blood flow at the cell interfaces embedded in the 3D cell. As such, the final scheme, based on guaranteeing mass and momentum conservation through the junction, is able to capture reflecting waves properly considering the effect of the different incident angles of vessels at a junction.

The chapter is organized as follows. Section 2.1 is devoted to the construction of the one-dimensional model for the cardiovascular system. The one-dimensional equations are derived and the employed vessel wall model is introduced. Then, the splitting of the equations into the convective, diffusive and pressure subsystems is detailed. Section 2.2 presents the numerical method to be applied for the discretization of the 1D blood flow model in a single vessel. The semi-discretization in time of the equations allows the introduction of the explicit convective and the implicit viscous and pressure stages in which the proposed semi-implicit finite volume algorithm is divided. Then, the staggered grid is described and each stage of the algorithm is carefully detailed. To improve the accuracy in time of the overall algorithm, the θ-method is employed. Next, the treatment of boundary conditions is described. In Section 2.3, we present the extension of the proposed methodology to networks of vessels. To this end, a new 3D junction approach is introduced based on the principles of mass and momentum conservation given by the Euler equations. As an alternative to the 3D the junction, also a classical 0D junction approach is recalled. Finally, the proposed methodology is validated in Section 1.7 by comparing the numerical results obtained with analytical, experimental and numerical data. Several tests are run both for single elastic and viscoelastic vessels and to assess the new 3D methodology proposed for junctions.

2.1 Mathematical model

This section is devoted to the construction of a one dimensional model which provides a simplified description of the flow in the cardiovascular system and of its interaction with the vessel-wall displacement.

2.1.1 Derivation of one dimensional blood flow equations

The derivation of 1D models for an incompressible fluid flowing in compliant tubes is a well covered and active topic that has yield to several approaches. Here we report some key points of the one advocated and described in [175, 114] which aims to develop a cross-sectional averaged model. The final 1D governing equations are derived from conservation principles making use of the three dimensional incompressible Navier-Stokes equations and the Reynolds' transport theorem.

We consider a compliant vessel whose longitudinal axis is assumed to be rectilinear and to coincide with the $x-$axis. To derive the corresponding one-dimensional blood flow model, we will start by obtaining the transport equation for a generic function f that will be then employed to get the mass and momentum conservation equations.

Let V_t be an arbitrary time-dependent control volume with boundary ∂V_t and outer normal $\boldsymbol{n}$, on which we apply the Reynolds' transport theorem for a continuous function $f = f(t, \mathbf{x})$, namely

$$\frac{d}{dt}\int_{V_t} f \ \mathrm{dV} = \int_{V_t} \frac{\partial f}{\partial t} \ \mathrm{dV} + \int_{\partial V_t} f \mathbf{u}_b \cdot \boldsymbol{n} \ \mathrm{dS}, \tag{2.1.1}$$

with $\mathbf{u}_b$ the velocity of the boundary ∂V_t. Note that ∂V_t is composed of the vessel wall $\partial V_{t,w}$, that defines its lumen, and two fixed plane surfaces orthogonal to the x-axis at coordinates $x = x_1$ and $x = x_2$, which correspond to the inlet and outlet sections S_1 and

S_2 of the tube. Since

$$\boldsymbol{n} = (-1, 0, 0) \text{ on } S_1 \quad \text{and} \quad \boldsymbol{n} = (1, 0, 0) \text{ on } S_2, \tag{2.1.2}$$

it follows that

$$\mathbf{u}_b \cdot \boldsymbol{n} = 0 \text{ on } S_1 \text{ and } S_2. \tag{2.1.3}$$

Hence, $\mathbf{u}_b \cdot \boldsymbol{n}$ is not null only on the arterial wall $\partial V_{t,w}$, where it coincides with the wall velocity $\mathbf{u}_w$. The last term in the right hand side of (2.1.1) can be thus rewritten as

$$\int_{\partial V_t} f\mathbf{u}_b \cdot \boldsymbol{n} \, \mathrm{dS} = \int_{\partial V_{t,w}} f\mathbf{u}_w \cdot \boldsymbol{n} \, \mathrm{dS}, \tag{2.1.4}$$

where $\mathbf{u}_w$ may differ from $\mathbf{u}$ in case of permeable vessel wall giving rise to a relative velocity between the vessel wall and the fluid, that is

$$\mathbf{u}_r = \mathbf{u}_w - \mathbf{u}. \tag{2.1.5}$$

Since we aim at a cross-sectional averaged model, we introduce the area-averaged value of f, denoted by $\overline{f}$ and given by

$$\overline{f} = \frac{1}{A} \int_S f \, \mathrm{dS}, \tag{2.1.6}$$

where $A = |S|$ is the area of a generic cross-section S. The former notation allows us to rewrite the left-hand side of (2.1.1) as

$$\frac{d}{dt} \int_{V_t} f \, \mathrm{dV} = \int_{x_1}^{x_2} \frac{\partial A\overline{f}}{\partial t} \, \mathrm{dx}\,. \tag{2.1.7}$$

Moreover, using (2.1.5) we get

$$\int_{\partial V_{t,w}} f\mathbf{u}_w \cdot \boldsymbol{n} \, \mathrm{dS} = \int_{\partial V_{t,w}} f\mathbf{u}_r \cdot \boldsymbol{n} \, \mathrm{dS} + \int_{\partial V_{t,w}} f\mathbf{u} \cdot \boldsymbol{n} \, \mathrm{dS}\,. \tag{2.1.8}$$

Then,

$$\int_{\partial V_{t,w}} f\mathbf{u} \cdot \boldsymbol{n} \, \mathrm{dS} = \int_{\partial V_t} f\mathbf{u} \cdot \boldsymbol{n} \, \mathrm{dS} - \int_{S_1} f\mathbf{u} \cdot \boldsymbol{n} \, \mathrm{dS} - \int_{S_2} f\mathbf{u} \cdot \boldsymbol{n} \, \mathrm{dS} \tag{2.1.9}$$

and, thanks to the assumption on S_1 and S_2 being transversal to the tube axis, we have

$$\int_{\partial V_{t,w}} f\mathbf{u} \cdot \boldsymbol{n} \, \mathrm{dS} = \int_{\partial V_t} f\mathbf{u} \cdot \boldsymbol{n} \, \mathrm{dS} + \int_{S_1} fu_1 \, \mathrm{dS} - \int_{S_2} fu_1 \, \mathrm{dS}, \tag{2.1.10}$$

where u_1 is the $x-$component of the velocity $\mathbf{u}$. Next, exploiting the Gauss' theorem and noting that

$$\int_{S_2} fu_1 \, \mathrm{dS} - \int_{S_1} fu_1 \, \mathrm{dS} = \int_{x_1}^{x_2} \frac{\partial A\overline{fu_1}}{\partial x} \, \mathrm{dx}, \tag{2.1.11}$$

we can write the above expression as

$$\int_{\partial V_{t,w}} f\mathbf{u}\cdot\boldsymbol{n}\ \mathrm{dS} = \int_{V_t} \nabla\cdot f\mathbf{u}\ \mathrm{dV} - \int_{x_1}^{x_2} \frac{\partial A\overline{fu_1}}{\partial x}\ \mathrm{dx}\,. \tag{2.1.12}$$

Hence,

$$\int_{\partial V_{t,w}} f\mathbf{u}_w\cdot\boldsymbol{n}\ \mathrm{dS} = \int_{\partial V_{t,w}} f\mathbf{u}_r\cdot\boldsymbol{n}\ \mathrm{dS} + \int_{V_t} \nabla\cdot f\mathbf{u}\ \mathrm{dV} - \int_{x_1}^{x_2} \frac{\partial A\overline{fu_1}}{\partial x}\ \mathrm{dx}\,. \tag{2.1.13}$$

Now, inserting (2.1.7) and (2.1.13) into (2.1.1) leads to

$$\int_{x_1}^{x_2} \frac{\partial A\overline{f}}{\partial t}\ \mathrm{dx} = \int_{V_t} \frac{\partial f}{\partial t}\ \mathrm{dV} + \int_{\partial V_{t,w}} f\mathbf{u}_r\cdot\boldsymbol{n}\ \mathrm{dS} + \int_{V_t} \nabla\cdot f\mathbf{u}\ \mathrm{dV} - \int_{x_1}^{x_2} \frac{\partial A\overline{fu_1}}{\partial x}\ \mathrm{dx}, \tag{2.1.14}$$

which, in alternative, can be expressed as

$$\int_{x_1}^{x_2} \frac{\partial A\overline{f}}{\partial t}\,\mathrm{dx} = \int_{x_1}^{x_2}\int_{S} \frac{\partial f}{\partial t}\,\mathrm{dS}\,\mathrm{dx} + \int_{x_1}^{x_2}\int_{\partial S} f\mathbf{u}_r\cdot\boldsymbol{n}\ \mathrm{dS}\,\mathrm{dx} + \int_{x_1}^{x_2}\int_{S} \nabla\cdot f\mathbf{u}\ \mathrm{dS}\,\mathrm{dx} - \int_{x_1}^{x_2} \frac{\partial A\overline{fu_1}}{\partial x}\,\mathrm{dx}\,. \tag{2.1.15}$$

Hence, the final form of the one dimensional transport theorem for a generic function f is

$$\frac{\partial A\overline{f}}{\partial t} + \frac{\partial A\overline{fu_1}}{\partial x} = \int_{S}\left(\frac{\partial f}{\partial t} + \nabla\cdot f\mathbf{u}\right)\mathrm{dS} + \int_{\partial S} f\mathbf{u}_r\cdot\boldsymbol{n}\ \mathrm{dS}\,. \tag{2.1.16}$$

Now, we will proceed to derive the governing equations for the 1D bloood flow model by invoking the principles of conservation of mass and balance of momentum expressed by the incompressible Navier-Stokes equations reported in (1.1.1).

Conservation of mass. Evaluating (2.1.16) with $f = 1$ results in

$$\frac{\partial A}{\partial t} + \frac{\partial A\overline{u_1}}{\partial x} = \int_{S} \nabla\cdot\mathbf{u}\ \mathrm{dS} + \int_{\partial S} \mathbf{u}_r\cdot\boldsymbol{n}\ \mathrm{dS}\,. \tag{2.1.17}$$

Then, recalling the divergence free condition of the velocity field, (1.1.1a), we get

$$\frac{\partial A}{\partial t} + \frac{\partial A\overline{u_1}}{\partial x} = \int_{\partial S} \mathbf{u}_r\cdot\boldsymbol{n}\ \mathrm{dS}, \tag{2.1.18}$$

which represents the conservation of mass in a one dimensional compliant tube.

Balance of momentum. The derivation of the momentum balance equation requires more care. We start by evaluating (2.1.16) with $f = u_1$ obtaining

$$\frac{\partial A\overline{u_1}}{\partial t} + \frac{\partial A\overline{u_1^2}}{\partial x} = \int_{S}\left(\frac{\partial u_1}{\partial t} + \mathbf{u}\cdot\nabla u_1\right)\mathrm{dS} + \int_{\partial S} u_1\mathbf{u}_r\cdot\boldsymbol{n}\ \mathrm{dS}, \tag{2.1.19}$$

which in terms of the material derivatives reads

$$\frac{\partial A\overline{u_1}}{\partial t} + \frac{\partial A\overline{u_1^2}}{\partial x} = \int\limits_S \frac{Du_1}{Dt}\ \mathrm{dS} + \int\limits_{\partial S} u_1 \mathbf{u}_r \cdot \boldsymbol{n}\ \mathrm{dS}\,. \tag{2.1.20}$$

To calculate the first term in the right-hand side of equation (2.1.20), we use the balance of momentum reported in Chapter 1 for the control volume V_t, (1.1.1b), which in integral form reads

$$\int\limits_{V_t} \left(\frac{D\rho\mathbf{u}}{Dt} + \nabla p - \nabla\cdot\boldsymbol{\tau} \right) \mathrm{dV} = \int\limits_{V_t} \rho\mathbf{g}\,\mathrm{dV}, \tag{2.1.21}$$

where we have employed again the definition of the material derivative. Now, assuming the density to be constant, it yields

$$\int\limits_{x_1}^{x_2}\int\limits_S \frac{D\mathbf{u}}{Dt}\ \mathrm{dS}\,\mathrm{dx} = \int\limits_{x_1}^{x_2}\int\limits_S \left[\mathbf{g} + \frac{1}{\rho}\left(-\nabla p + \nabla\cdot\boldsymbol{\tau}\right) \right] \mathrm{dS}\,\mathrm{dx} \tag{2.1.22}$$

and since x_1 and x_2 are arbitrarily chosen, we could write the $x-$component of the above equation as

$$\int\limits_S \frac{Du_1}{Dt}\ \mathrm{dS} = \int\limits_S \left[g_1 + \frac{1}{\rho}\left(-\frac{\partial p}{\partial x} + d_1 \right) \right] \mathrm{dS}, \tag{2.1.23}$$

where d_1 is the x-component of $\nabla\cdot\boldsymbol{\tau}$. Consequently, inserting the above equation into (2.1.20) gives

$$\frac{\partial A\overline{u_1}}{\partial t} + \frac{\partial A\overline{u_1^2}}{\partial x} = \int\limits_S \left[g_1 + \frac{1}{\rho}\left(-\frac{\partial p}{\partial x} + d_1 \right) \right] \mathrm{dS} + \int\limits_{\partial S} u_1 \mathbf{u}_r \cdot \boldsymbol{n}\ \mathrm{dS}\,. \tag{2.1.24}$$

Recalling that, for a constant viscosity coefficient, we have

$$\nabla\cdot\boldsymbol{\tau} = \nabla\cdot(\mu(\nabla\,\mathbf{u} + \nabla\,\mathbf{u}^t)) = \mu\,\nabla\cdot(\nabla\,\mathbf{u}) = \mu\,\nabla^2\,\mathbf{u}, \tag{2.1.25}$$

then

$$d_1 = \mu\left(\frac{\partial^2 u_1}{\partial x^2} + \frac{\partial^2 u_1}{\partial y^2} + \frac{\partial^2 u_1}{\partial z^2} \right). \tag{2.1.26}$$

At this point assuming that the radial velocity components are negligible with respect to the axial velocity component and writing the incompressible Navier-Stokes equations in component-wise form in terms of nondimensional quantities, it follows that the term involving the axial velocity component in (2.1.26) can be neglected and the pressure field can be assumed to be constant over a cross-section. Then, we have

$$\frac{\partial A\overline{u_1}}{\partial t} + \frac{\partial A\overline{u_1^2}}{\partial x} = \int\limits_S \left(g_1 + \frac{1}{\rho}\left(-\frac{\partial p}{\partial x} + \mu\left(\frac{\partial^2 u_1}{\partial y^2} + \frac{\partial^2 u_1}{\partial z^2} \right) \right) \right) \mathrm{dx} + \int\limits_{\partial S} u_1 \mathbf{u}_r \cdot \boldsymbol{n}\ \mathrm{dS}\,. \tag{2.1.27}$$

Moreover, we note that

$$\int\limits_S \left(\frac{\partial^2 u_1}{\partial y^2} + \frac{\partial^2 u_1}{\partial z^2} \right) \mathrm{dS} = \int\limits_{\partial S} \nabla_S u_1 \cdot \boldsymbol{n}_{\partial S}\ \mathrm{dS}, \tag{2.1.28}$$

where the subscript S denotes the fact that the operator acts on the cross section S, while $\boldsymbol{n}_{\partial S}$ is the vector normal to the surface boundary. In addition, the last assumption implies also that

$$\int_S \frac{\partial p}{\partial x}\ \mathrm{dS} = A\frac{\partial \overline{p}}{\partial x}. \tag{2.1.29}$$

Using (2.1.28) and (2.1.29), (2.1.24) reads

$$\frac{\partial A\overline{u_1}}{\partial t} + \frac{\partial A\overline{u_1^2}}{\partial x} = A\overline{g_1} - \frac{A}{\rho}\frac{\partial \overline{p}}{\partial x} - \frac{\mu}{\rho}\int_{\partial S} \nabla_S u_1 \cdot \boldsymbol{n}_{\partial S}\ \mathrm{dS} + \int_{\partial S} u_1 \mathbf{u}_r \cdot \boldsymbol{n}\ \mathrm{dS}\,. \tag{2.1.30}$$

We note that equation (2.1.30) requires the specification of the $x-$component of the velocity over the cross section of the vessel. At this aim, we define

$$u_1(\mathbf{x}, t) = s(y, z, t)\overline{u_1}(x, t) \tag{2.1.31}$$

where $s(y, z, t)$ is the velocity profile function which is assumed to be a known function over the cross-section. To simplify the notation, we introduce a momentum-flux correction coefficient α, also called the Coriolis coefficient, which is a function of the velocity profile, as

$$\alpha = \frac{1}{A\overline{u}_1^2}\int_S u_1^2\,\mathrm{dS} = \frac{1}{A}\int_S s^2\,\mathrm{dS} \tag{2.1.32}$$

and

$$K_R = \frac{\mu}{\rho}\int_{\partial S} \nabla_S\, s \cdot \boldsymbol{n}_{\partial S}\ \mathrm{dS}, \tag{2.1.33}$$

which accounts for the viscous losses. Hence, the final form of the balance momentum equation is

$$\frac{\partial A\overline{u_1}}{\partial t} + \frac{\partial \alpha\overline{u}_1^2}{\partial x} = A\overline{g_1} - \frac{A}{\rho}\frac{\partial \overline{p}}{\partial x} - K_R\overline{u}_1 + \int_{\partial S} u_1 \mathbf{u}_r \cdot \boldsymbol{n}\ \mathrm{dS}\,. \tag{2.1.34}$$

The unknowns in the system composed of (2.1.18) and (2.1.34) are $p(x, t)$, $A(x, t)$ and $\overline{u_1}(x, t)$, respectively the pressure, the vessel cross-sectional area and the averaged velocity at a cross section. Since their number exceeds by one that of the governing equations, a common way to close the system is to explicitly provide the relationship between the pressure of the vessel p and and the wall displacement via the cross-sectional area A, the so-called tube law. A simple model of wall mechanics is presented in the next section.

2.1.2 Tube laws

The definition of a constitutive law which correctly describes and models the interaction between blood flow and vessel wall mechanics may not be straightforward. Indeed, the vessel wall is comparable to a complex multi-layer viscoelastic structure which deforms under the action of pressure, [8, 222], and, in case of veins, it can even collapse if certain circumstances are verified, [218, 202]. In particular, when subjected to stress very slowly, the viscous behavior of the wall is not apparent and the wall acts as a purely elastic tissue. Meanwhile, if experienced a fast deformation then it shows an additional resistance. A simple viscoelastic model capturing these properties is embodied by the Kelvin-Voigt

model. It comprises a parallel arrangement of a purely elastic spring, defined by a Young modulus E, and a purely viscous damper, characterized by a viscosity coefficient η. In a Kelvin-Voigt material the stress σ and the strain ϵ are linked according to the following constitutive relationship

$$\sigma = E\epsilon + \eta \frac{\partial \epsilon}{\partial t}. \tag{2.1.35}$$

Furthermore, we define the strain of the vessel as

$$\epsilon = \left(\frac{A}{A_0}\right)^m - \left(\frac{A}{A_0}\right)^n, \tag{2.1.36}$$

where A_0 is the equilibrium cross-sectional area and m, n are specific parameters related to the behavior of the vessel wall, and thus vary for arteries and veins. The typical values for arteries, $m = 0.5$ and $n = 0$, are derived from a mechanical model for the vessel-wall displacement, considering a generalized string model, [174]. On the other hand, for veins, which can collapse and stiffen, these parameters are commonly set to $m = 10$ and $n = -3/2$, based on the study of the buckling behaviour of a thin-walled tube during collapse, [79, 40]. In addition, we assume the following relationship between stress and pressure

$$\sigma = W(p - p_e), \tag{2.1.37}$$

with p_e the external pressure and W a coefficient which depending on the type of vessel, can be either the ratio between the thickness h_0 and the equilibrium radius of the wall R_0, for arteries, or $W = 12\left(\frac{h0}{R_0}\right)^3$, for veins. In case of arteries (2.1.37) recovers the Barlow's law, while for veins it has been modified in order to account the potential collapsibility of the wall, [214]. Hence, inserting (2.1.37) and (2.1.36) in (2.1.35), the following viscoelastic tube law can be derived:

$$p = p_e + K(x)\left(\left(\frac{A}{A_0}\right)^m - \left(\frac{A}{A_0}\right)^n\right) + \frac{\Gamma}{A_0\sqrt{A}}\frac{\partial A}{\partial t}, \tag{2.1.38}$$

where K is the stiffness coefficient of the wall, defined as

$$K = \frac{E}{W}, \tag{2.1.39}$$

while Γ corresponds to the viscoelastic parameter and it is given by

$$\Gamma = \frac{\eta h_0 \sqrt{\pi}}{2}. \tag{2.1.40}$$

Note that setting $\Gamma = 0$, one obtains a widely adopted constitutive tube law, which assumes a static equilibrium between the vessel wall and the blood at every time instant, neglecting any viscoelastic effects.

2.1.3 Governing equations

As we have seen in the previous section, the main features of the flow of a hydrostatic, incompressible fluid in compliant vessels can be described by a system of two one-dimensional partial differential equations (2.1.18) and (2.1.34), representing mass

conservation and momentum balance, respectively. Now, neglecting the gravity force, dropping bars from the unknowns, simplifying the notation by naming the area-averaged axial velocity by u instead of u_1 and assuming an impermeable wall, i.e. $\mathbf{u}_r = 0$, we obtain the following system of equations

$$\frac{\partial A}{\partial t} + \frac{\partial Au}{\partial x} = 0, \tag{2.1.41a}$$

$$\frac{\partial Au}{\partial t} + \frac{\partial \alpha Au^2}{\partial x} + \frac{A}{\rho}\frac{\partial p}{\partial x} = -K_R u, \tag{2.1.41b}$$

where $x \in [x_L, x_R] \subset \mathbb{R}$ is the axial coordinate and t is the time, $A(x,t)$ is the cross-sectional area, $u(x,t)$ is the average flow velocity in the axial direction and $p(x,t)$ is the average fluid pressure over a cross-section. As already introduced in Section 2.1.1, α, the momentum correction factor, and K_R, the viscous resistance coefficient, depend on the assumed velocity profile. Throughout this work we assume the velocity profile s in (2.1.31) to be given by

$$s(r) = \frac{\xi + 2}{\xi}\left(1 - \left(\frac{r}{R}\right)^{\xi}\right), \tag{2.1.42}$$

with $r = [0, R]$ the radial coordinate and ξ an exponent that determines the shape of the velocity profile, potentially varying between a fully developed parabolic flow closed to a plug flow. In particular, for $\xi = 2$ we are in the case of a fully developed laminar flow, characterized by a parabolic velocity profile, while higher values generate blunter profiles. Consequently, taking into account (2.1.42) into (2.1.32), we can relate α to ξ according to

$$\alpha = \frac{2 + \xi}{1 + \xi}. \tag{2.1.43}$$

For simplicity, α will be set to $\alpha = 1$ throughout the entire thesis, which indicates a perfectly flat velocity profile. This choice is commonly used in literature, since it simplifies the analysis of the resulting 1D model. On the other hand, for the velocity profile chosen in (2.1.42), the viscous resistance per unit length of tube K_R, defined as (2.1.33), becomes

$$K_R = 2(\xi + 2)\pi\frac{\mu}{\rho}, \tag{2.1.44}$$

where ρ and μ are the constant blood flow density and viscosity, respectively.

As aforementioned, the system of PDEs (2.1.41) has more unknowns than equations; hence, an additional closure condition is required. We consider the viscoelstic tube law described in Section 2.1.2 to couple the internal blood flow distribution with the mechanical properties of the solid moving vessel wall considering a simplified fluid-structure interaction setting. Accordingly, the internal pressure p is linked to the vessel cross-sectional area A by

$$p(x,t) = p_e + \psi(A, A_0, K) + \varphi(A, A_0)\frac{\partial A}{\partial t}, \tag{2.1.45}$$

where ψ represents the elastic pressure component, modeled by

$$\psi(A, A_0, K) = K(x)\left(\left(\frac{A}{A_0}\right)^m - \left(\frac{A}{A_0}\right)^n\right), \tag{2.1.46}$$

and

$$\varphi(A, A_0) = \frac{\Gamma}{A_0\sqrt{A}} \tag{2.1.47}$$

accounts for the viscoelastic behavior of the vessel wall.

Exploiting the mass conservation equation, (2.1.41a), the time derivative of the cross-sectional area can be expressed in terms of a spatial derivative as

$$\frac{\partial A}{\partial t} = -\frac{\partial Au}{\partial x}. \tag{2.1.48}$$

Then, applying (2.1.48) within the tube law (2.1.45), the pressure gradient in (1.1.1b) can be computed as

$$\frac{\partial p}{\partial x} = \frac{\partial \hat{p}}{\partial x} - \frac{\partial}{\partial x}\left(\varphi \frac{\partial Au}{\partial x}\right), \tag{2.1.49}$$

where $\hat{p} = p_e + \psi(A, A_0, K)$ describes only the elastic deformation of the vessel wall with pressure variations.

Introducing the notation $q = Au$ for the mass flux, $F(q) = q^2/A$ for the convective flux and accounting for (2.1.49), we can rewrite system (2.1.41) as

$$\frac{\partial A}{\partial t} + \frac{\partial q}{\partial x} = 0, \tag{2.1.50a}$$

$$\frac{\partial q}{\partial t} + \frac{\partial F(q)}{\partial x} + \frac{A}{\rho}\frac{\partial \hat{p}}{\partial x} - \frac{A}{\rho}\frac{\partial}{\partial x}\left(\varphi \frac{\partial q}{\partial x}\right) = -K_R \frac{q}{A}. \tag{2.1.50b}$$

Adding and subtracting, in the momentum equation, the spatial derivative of the pressure multiplied by the area and divided by the density, $\frac{A}{\rho}\frac{\partial p}{\partial x}$, system (2.1.41) becomes

$$\frac{\partial A}{\partial t} + \frac{\partial q}{\partial x} = 0, \tag{2.1.51a}$$

$$\frac{\partial q}{\partial t} + \frac{\partial F(q)}{\partial x} + \frac{A}{\rho}\frac{\partial p}{\partial x} - \frac{A}{\rho}\frac{\partial}{\partial x}\left(\varphi \frac{\partial q}{\partial x}\right) - \frac{A}{\rho}\frac{\partial (p - \hat{p})}{\partial x} = -K_R \frac{q}{A}. \tag{2.1.51b}$$

The use of a viscoelastic tube law gives rise to a second order spatial derivative of the flow in the momentum balance equation, which turns the problem into a convection–diffusion–reaction system. Following the idea behind the methodology described in Chapter 1 to solve the three dimensional Navier-Stokes equations, we apply a flux-vector splitting to divide system (2.1.51) into a convective subsystem, which will be discretized explicitly in time, and two subsystems that will both be treated implicitly in time, one related to the pressure and one related to the viscoelasticity. The presented splitting strategy, based on the flux-vector splitting of the compressible Euler equations proposed by Toro and Vázquez-Cendón [219] and on previous works on semi-implicit schemes for 1D flows in compliant vessels [53, 72], leads to a methodology involving four stages:

- **Convective stage.** The convective subsystem, which in the case of the 1D blood flow model reduces to a single scalar equation, reads

$$\frac{\partial q}{\partial t} + \frac{\partial F(q)}{\partial x} = 0. \tag{2.1.52}$$

Since it is the only subsystem discretized explicitly, it is responsible for the CFL time step restriction of the resulting final semi-implicit scheme. As a consequence, the CFL number depends only on the bulk flow velocity and not on the fast wave speed. Indeed, the eigenvalue of system (2.1.52) is $\lambda = 2u$, where one notices the absence of the wave speed $c = \sqrt{\frac{A}{\rho}\frac{\partial p}{\partial x}}$ that arises when the eigenvalues of the full system (2.1.51) are considered (see Appendix A).

- **Diffusive stage.** The diffusive subsystem, again formed by a unique scalar equation, is

$$\frac{\partial q}{\partial t} - \frac{A}{\rho}\frac{\partial}{\partial x}\left(\varphi\frac{\partial q}{\partial x}\right) = -(1-\beta)K_R\frac{q}{A}. \tag{2.1.53}$$

  Note that this stage is necessary only if a viscoelastic vessel is considered. It will be discretized implicitly in time, thus it does not influence the CFL time step restriction of the overall method. As an alternative, which would affect the stability condition, the explicit forward-in-time centered-in-space scheme (FTCS) could also be employed. Furthermore, in this subsystem an auxiliary parameter β has been introduced as a coefficient of the source term. As further explained later, it will allow us to incorporate the contribution of the source in two different stages of the scheme, depending whether the viscoelasticity is considered, or not.

- **Pressure stage.** The pressure subsystem reads

$$\frac{\partial A}{\partial t} + \frac{\partial q}{\partial x} = 0, \tag{2.1.54a}$$

$$\frac{\partial q}{\partial t} + \frac{A}{\rho}\frac{\partial p}{\partial x} - \frac{A}{\rho}\frac{\partial (p-\hat{p})}{\partial x} = -\beta K_R\frac{q}{A}, \tag{2.1.54b}$$

  and will be discretized using an implicit finite volume method on a staggered mesh.

- **Correction stage.** Using (2.1.54) the new pressure is employed to correct the intermediate velocity previously computed at the convective and diffusive stages. Consequently, the velocity at the new time step is obtained.

In the former diffusive and pressure stages, we have introduced the auxiliary parameter β that controls in which subsystem the source term is discretized. As general principle, the source should be included in the first subsystem to be treated implicitly. Hence, we fix $\beta = 0$ in case the diffusive subsystem is present and implicitly discretized. Otherwise, we set $\beta = 1$, so the source term is incorporated directly in the pressure subsystem. Note that this election is mainly motivated by the potential use of Dirichlet boundary conditions for the velocity field. In this case, in the implicit subsystems, we need to impose the correct values including all terms already incorporated for the velocity update. Hence, defining the boundary condition becomes easier if we have already included the source terms. Otherwise their contribution would need to be subtracted from the exact boundary value imposed. As it will be explained in Section 2.2.7, a similar issue arises with the missing contribution of the pressure in the viscoelastic subsystem for which a different approach will be proposed.

2.2 Numerical discretization

In order to discretize system (2.1.51), the first step is to perform a semi-discretization in time that leads to the split of the equations into the three types of subsystems presented in the previous section. Then, the spatial derivatives are discretized employing staggered grids and different numerical methods are considered for each subsystem according to the nature of their equations. In particular, discretization only in time of system (2.1.51), while keeping space still continuous, yields the following semi-discrete scheme:

$$A(p^{n+1}) = A(p^n) - \Delta t \frac{\partial q^{n+1}}{\partial x}, \tag{2.2.1a}$$

$$\begin{aligned} q^{n+1} = q^n &- \Delta t \frac{\partial F(q^n)}{\partial x} + \Delta t \frac{A(p^n)}{\rho} \frac{\partial}{\partial x}\left(\varphi^n \frac{\partial q^{n+1}}{\partial x}\right) - \Delta t \frac{A(p^n)}{\rho} \frac{\partial p^{n+1}}{\partial x} \\ &+ \Delta t \frac{A(p^n)}{\rho} \frac{\partial (p-\hat{p})^n}{\partial x} - \beta \Delta t \frac{K_R}{A(p^n)} q^{n+1} - (1-\beta)\Delta t \frac{K_R}{A(p^n)} q^{n+1} \end{aligned} \tag{2.2.1b}$$

where p^n, q^n are the known discrete solutions at time t^n, while q^{n+1} and p^{n+1} are the approximations of the solutions at the new time. In (2.2.1) we employ the notation $A(p)$ to recall that the area can be computed from the pressure using the tube law (2.1.45). Indeed, the variables directly solved with the semi-implicit scheme are q and p while A is then obtained as a function of p.

We denote by

$$q^* = q^n - \Delta t \frac{\partial F(q^n)}{\partial x} \tag{2.2.2}$$

a first intermediate approximation of q, which includes only the convective terms and therefore corresponds to subsystem (2.1.52). Moreover, we use the notation

$$q^{**} = q^* + \Delta t \frac{A(p^n)}{\rho} \frac{\partial}{\partial x}\left(\varphi^n \frac{\partial q^{**}}{\partial x}\right) - (1-\beta)\Delta t \frac{K_R}{A(p^n)} q^{**} \tag{2.2.3}$$

for the second intermediate approximation of q, which accounts also for the diffusive contribution, related to equation (2.1.53). Introducing the above notations, (2.2.1) can be rewritten more compactly as

$$A(p^{n+1}) = A(p^n) - \Delta t \frac{\partial q^{n+1}}{\partial x}, \tag{2.2.4a}$$

$$q^{n+1} = \frac{1}{1+\beta \Delta t \gamma^n}\left(q^{**} - \Delta t \frac{A(p^n)}{\rho} \frac{\partial p^{n+1}}{\partial x} + \Delta t \frac{A(p^n)}{\rho} \frac{\partial (p-\hat{p})^n}{\partial x}\right), \tag{2.2.4b}$$

with $\gamma^n = \dfrac{K_R}{A^n} = \dfrac{K_R}{A(p^n)}$. Hence, once the intermediate velocity q^{**} is computed, the pressure can be obtained from solving the Poisson-type system associated to (2.2.4). Finally, the velocity at the new time step is calculated from (2.2.4b).

2.2.1 Staggered grid

Before detailing the spatial discretization, we introduce the staggered computational grids to be employed. A generic vessel of length L is divided into a set of non-overlapping

intervals following the procedure reported in [53, 210, 77], so that the resulting primal grid is composed by a total of N_p control volumes with, in general, a non-uniform length Δx_i, $i = 1, \dots, N_p$. Each cell C_i has two vertexes, one on the left and one on the right, identified by the indices $l(i) \equiv i - \frac{1}{2}$ and $r(i) \equiv i + \frac{1}{2}$, respectively.

On the other hand, the interior dual cells have as vertexes two subsequent barycenters of the primal grid, while boundary dual cells go from the domain boundary to the closest primal cell barycenter. That is, given x_i, x_{i+1} the barycenters of two neighbouring cells C_i, C_{i+1}, the dual volume associated to the vertex between them, $x_{i+\frac{1}{2}}$, is $D_{i+\frac{1}{2}} \equiv [x_i, x_{i+1}]$ and has length $\Delta x^D_{i+1} \equiv \Delta x_{i+\frac{1}{2}} = x_{i+1} - x_i = \frac{1}{2}\Delta x_i + \frac{1}{2}\Delta x_{i+1}$, while $\Delta x_i = x_{i+\frac{1}{2}} - x_{i-\frac{1}{2}}$. Consequently, the dual grid accounts for $N_d = N_p + 1$ control volumes. A sketch of the primal and dual grids is shown in Figure 2.1.

Regarding the location of the discretized unknowns of (2.2.4), the discrete pressure will be computed on the primal elements, while the discrete axial velocity u and the averaged momentum q are associated to the dual cells. By convention, the positive velocity direction is defined to be from $l(i)$ to $r(i)$.

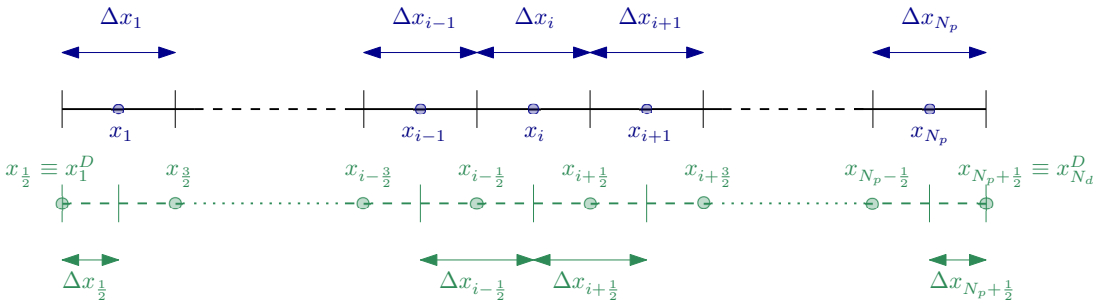

Figure 2.1: Sketch of the 1D staggered grids. Primal grid in blue and dual grid in green.

2.2.2 Convective stage

The first stage of the algorithm involves the spatial discretization of (2.2.2) employing an explicit finite volume method based on the Ducros numerical flux function [68, 70, 69]. Integration of (2.2.2) over a dual control volume $V_{i+\frac{1}{2}} = D_{i+\frac{1}{2}} \times [t^n, t^{n+1}]$, gives

$$\int_{x_i}^{x_{i+1}} q^*(x)\,\mathrm{dx} = \int_{x_i}^{x_{i+1}} q(x, t^n)\,\mathrm{dx} + \int_{t^n}^{t^{n+1}} \left[f(q(x_{i+1}, t)) - f(q(x_i, t))\right]\mathrm{dt}\,. \tag{2.2.5}$$

Then, a numerical method is constructed to find the solution of (2.2.2) by interpreting (2.2.5) in an approximate manner, that is by approximating the integrals involved in

(2.2.5). Introducing the notation

$$q^*_{i+\frac{1}{2}} \approx \frac{1}{\Delta x_{i+\frac{1}{2}}} \int_{x_i}^{x_{i+1}} q^*(x)\,\mathrm{dx}, \tag{2.2.6}$$

$$q^n_{i+\frac{1}{2}} \approx \frac{1}{\Delta x_{i+\frac{1}{2}}} \int_{x_i}^{x_{i+1}} q(x,t^n)\,\mathrm{dx}, \tag{2.2.7}$$

$$f^n_i \approx \frac{1}{\Delta t} \int_{t^n}^{t^{n+1}} f(q(x_i,t))\,\mathrm{dt}, \tag{2.2.8}$$

we arrive at the following relation:

$$q^*_{i+\frac{1}{2}} = q^n_{i+\frac{1}{2}} - \frac{\Delta t}{\Delta x_i}\left(f^n_{i+1} - f^n_i\right). \tag{2.2.9}$$

In (2.2.9) f^n_{i+1} and f^n_i represent the discrete fluxes at the cell boundaries, whose approximation is performed by means of a numerical flux function,

$$f^n_{i+1} = \phi\left(q^n_{i-\frac{j_1}{2}}, \ldots, q^n_{i+\frac{j_2}{2}}\right) \qquad f^n_i = \phi\left(q^n_{i-\frac{j_1-2}{2}}, \ldots, q^n_{i+\frac{j_2-2}{2}}\right) \tag{2.2.10}$$

with j_1, j_2 two non-negative integers. Assuming a piecewise constant solution, the computation of the numerical flux can be seen as classical Riemann problems at the dual finite volume boundaries. Depending on the choice of the discrete flux function different schemes can be derived. In this thesis, we employ a Ducros-type flux function which reads

$$f^n_i = \frac{1}{2}\left(u^n_{i+\frac{1}{2}} + u^n_{i-\frac{1}{2}}\right)\frac{1}{2}\left(q^n_{i+\frac{1}{2}} + q^n_{i-\frac{1}{2}}\right) - \frac{1}{2}\alpha^n_i\left(q^n_{i+\frac{1}{2}} - q^n_{i-\frac{1}{2}}\right) \tag{2.2.11}$$

where

$$\alpha^n_i = 2\max\left(|u^n_{i-\frac{1}{2}}|, |u^n_{i+\frac{1}{2}}|\right) \tag{2.2.12}$$

is the numerical viscosity. The former scheme is first order accurate in space and time and using the von Neumann stability analysis one can show that it is conditionally stable under the classical CFL condition

$$\Delta t \leq \mathrm{CFL} \min_{j\in\{1,\ldots,N_d\}} \left(\frac{\Delta x_{j-\frac{1}{2}}}{2|u^n_{j-\frac{1}{2}}|}\right) \tag{2.2.13}$$

with $\mathrm{CFL} \leq 1$.

To increase the accuracy in space a non linear high-order scheme has to be introduced. To this purpose, we employ a Kolgan-type methodology, [124, 215, 126], that makes use of limited slopes within the reconstruction step in order to circumvent Godunov's theorem. In particular, the CVC Kolgan-type approach is based on the idea of replacing the conservative variables $q^n_{i+\frac{1}{2}}$, $q^n_{i-\frac{1}{2}}$ in the numerical viscosity by improved interpolations given by the reconstructed polynomials $q^n_{i-\frac{1}{2},R}(x)$, $q^n_{i+\frac{1}{2},L}(x)$ evaluated at the cell interface x_i, namely,

$$q^n_{i-\frac{1}{2},R}(x_i) = q^n_{i-\frac{1}{2}} + (x_i - x_{i-\frac{1}{2}})\Delta q^n_{i-\frac{1}{2}}, \qquad q^n_{i+\frac{1}{2},L}(x_i) = q^n_{i+\frac{1}{2}} + (x_i - x_{i+\frac{1}{2}})\Delta q^n_{i+\frac{1}{2}} \tag{2.2.14}$$

where $\Delta q^n_{i-\frac{1}{2}}$ and $\Delta q^n_{i+\frac{1}{2}}$ are the left and right limited slopes at the cell interface. In order to avoid spurious oscillations, we select these slopes by employing a minmod-type limiter, that is,

$$\Delta q^n_{i+\frac{1}{2}} = \begin{cases} q^n_{i+\frac{1}{2}} - q^n_{i-\frac{1}{2}}, & \text{if } |q^n_{i+\frac{1}{2}} - q^n_{i-\frac{1}{2}}| < |q^n_{i+\frac{3}{2}} - q^n_{i+\frac{1}{2}}| \text{ and } (q^n_{i+\frac{1}{2}} - q^n_{i-\frac{1}{2}})(q^n_{i+\frac{3}{2}} - q^n_{i+\frac{1}{2}}) > 0, \\ q^n_{i+\frac{3}{2}} - q^n_{i+\frac{1}{2}}, & \text{if } |q^n_{i+\frac{1}{2}} - q^n_{i-\frac{1}{2}}| > |q^n_{i+\frac{3}{2}} - q^n_{i+\frac{1}{2}}| \text{ and } (q^n_{i+\frac{1}{2}} - q^n_{i-\frac{1}{2}})(q^n_{i+\frac{3}{2}} - q^n_{i+\frac{1}{2}}) > 0, \\ 0, & \text{if } (q^n_{i+\frac{1}{2}} - q^n_{i-\frac{1}{2}})(q^n_{i+\frac{3}{2}} - q^n_{i+\frac{1}{2}}) \leq 0. \end{cases} \tag{2.2.15}$$

This high-order extrapolation is used only in the upwind contribution of the numerical flux retaining the conservative variables in the centered part. Hence, the final numerical flux reads

$$f^n_i = \frac{1}{2}\left(u^n_{i+\frac{1}{2}} + u^n_{i-\frac{1}{2}}\right)\frac{1}{2}\left(q^n_{i+\frac{1}{2}} + q^n_{i-\frac{1}{2}}\right) - \frac{1}{2}\alpha^n_i(q^n_{i+\frac{1}{2},L} - q^n_{i-\frac{1}{2},R}), \tag{2.2.16}$$

with

$$\alpha^n_i = 2\max(|u^n_{i+\frac{1}{2},L}|, |u^n_{i-\frac{1}{2},R}|). \tag{2.2.17}$$

In this case, the stability condition requires CFL$\leq \frac{1}{2}$.

2.2.3 Diffusive stage

In order to treat the diffusion term we adopt the following strategy. Once the first intermediate solution of the conservative variable q^* is obtained within the convective stage, we can solve (2.2.3) following an implicit finite volume approach. The discretization of the diffusive equation based on the backward in time centered in space scheme (BTCS) yields

$$q^{**}_{i+\frac{1}{2}} = q^*_{i+\frac{1}{2}} + \frac{\Delta t}{\Delta x_{i+\frac{1}{2}}}\frac{A^n_{i+\frac{1}{2}}}{\rho}\left(\varphi^n_+\frac{q^{**}_{i+\frac{3}{2}} - q^{**}_{i+\frac{1}{2}}}{\Delta x_{i+1}} - \varphi^n_-\frac{q^{**}_{i+\frac{1}{2}} - q^{**}_{i-\frac{1}{2}}}{\Delta x_i}\right) - (1-\beta)\Delta t\gamma^n_{i+\frac{1}{2}}q^{**}_{i+\frac{1}{2}}, \tag{2.2.18}$$

with

$$A^n_{i+\frac{1}{2}} = \frac{A(p^n_i) + A(p^n_{i+1})}{2} \tag{2.2.19}$$

and

$$\varphi^n_- = \frac{\varphi(A^n_{i+\frac{1}{2}}) + \varphi(A^n_{i-\frac{1}{2}})}{2}, \quad \varphi^n_+ = \frac{\varphi(A^n_{i+\frac{3}{2}}) + \varphi(A^n_{i+\frac{1}{2}})}{2}. \tag{2.2.20}$$

Thus, equation (2.2.18) can be rearranged as

$$\left[-\frac{\Delta t}{\rho}\frac{\varphi^n_-}{\Delta x_i}\right]q^{**}_{i-\frac{1}{2}} + \left[\frac{\Delta x_{i+\frac{1}{2}}}{A^n_{i+\frac{1}{2}}}\left[1 + (1-\beta)\Delta t\gamma^n_{i+\frac{1}{2}}\right] + \frac{\Delta t}{\rho}\left(\frac{\varphi^n_+}{\Delta x_{i+1}} + \frac{\varphi^n_-}{\Delta x_i}\right)\right]q^{**}_{i+\frac{1}{2}} + \left[-\frac{\Delta t}{\rho}\frac{\varphi^n_+}{\Delta x_{i+1}}\right]q^{**}_{i+\frac{3}{2}} = q^*_{i+\frac{1}{2}}, \tag{2.2.21}$$

and written more compactly using the following matrix-vector notation:

$$\mathbf{D}\mathbf{q}^{**} = \mathbf{v} \tag{2.2.22}$$

where

- $\mathbf{D}$ is a matrix whose non-zero entries are

$$
\begin{aligned}
d_{i,i-1} &= -\frac{\Delta t}{\rho}\frac{\varphi_-^n}{\Delta x_i}, \\
d_{i,i} &= \frac{\Delta x_{i+\frac{1}{2}}}{A^n_{i+\frac{1}{2}}}\left[1+(1-\beta)\Delta t\gamma^n_{i+\frac{1}{2}}\right] + \frac{\Delta t}{\rho}\left(\frac{\varphi_+^n}{\Delta x_{i+1}} + \frac{\varphi_-^n}{\Delta x_i}\right), \\
d_{i,i+1} &= -\frac{\Delta t}{\rho}\frac{\varphi_+^n}{\Delta x_{i+1}}.
\end{aligned}
$$

- $\mathbf{q}^{**}$ is the vector containing the second intermediate approximation of the conservative variable q at each dual cell at time t^{n+1}.

- $\mathbf{v}$ is the known right-hand side term.

Since matrix $\mathbf{D}$ is symmetric-positive-definite, system (2.2.22) can be efficiently solved using a matrix-free conjugate gradient algorithm. Hence, the proposed scheme for the diffusive subsystem is unconditionally stable, first order accurate in time and second order accurate in space.

As an alternative to (2.2.22), equation (2.2.3) could be solved explicitly according to

$$
q^{**}_{i+\frac{1}{2}} = q^{*}_{i+\frac{1}{2}} + \frac{\Delta t}{\Delta x_{i+\frac{1}{2}}}\frac{A^n_{i+\frac{1}{2}}}{\rho}\left(\varphi_+^n\frac{q^*_{i+\frac{3}{2}}-q^*_{i+\frac{1}{2}}}{\Delta x_{i+1}} - \varphi_-^n\frac{q^*_{i+\frac{1}{2}}-q^*_{i-\frac{1}{2}}}{\Delta x_i}\right), \tag{2.2.23}
$$

which corresponds to the classical forward in time central in space method (FTCS). In this second case, we avoid the use of an iterative method, needed to solve the system resulting from the implicit discretization, which reduces the cost of performing a time step. However, the stability of (2.2.23) would be characterized by a restrictive CFL number. Thus, the overall algorithm would have to satisfy the following additional stability condition

$$
2\max_{j\in\{1,\dots,N_d\}}\left(\frac{A_{j-\frac{1}{2}}}{\rho\Delta x^2_{j-\frac{1}{2}}}\varphi_{j-\frac{1}{2}}\right)\Delta t < \mathrm{CFL}, \tag{2.2.24}
$$

with $\mathrm{CFL} \leq 1$. This would potentially lead to a larger number of time steps, hence increasing the overall computational cost of the simulation. Therefore, this explicit approach might be convenient only if the flow regime is dominated by pressure and convective terms, so that diffusive terms have less influence and barely affect the time step size.

2.2.4 Pressure and correction stages

The third stage of the algorithm involves the solution of the pressure subsystem (2.2.4). The implicit discretization of the continuity equation yields

$$
M(p_i^{n+1}) = M(p_i^n) - \Delta t\left(q^{n+1}_{i+\frac{1}{2}} - q^{n+1}_{i-\frac{1}{2}}\right), \tag{2.2.25}
$$

where $M(p_i) = A(p_i)\Delta x_i$ is the fluid mass contained in the $i-$th cell. At the same time, the discrete momentum equation reads

$$q_{i+\frac{1}{2}}^{n+1} = \frac{1}{1+\beta\Delta t\gamma_{i+\frac{1}{2}}^{n}}\left[q_{i+\frac{1}{2}}^{**} - \frac{\Delta t}{\Delta x_{i+\frac{1}{2}}}\frac{A_{i+\frac{1}{2}}^{n}}{\rho}\left(p_{i+1}^{n+1} - p_i^{n+1}\right)\right] + \frac{1}{1+\beta\Delta t\gamma_{i+\frac{1}{2}}^{n}}\left[\frac{\Delta t}{\Delta x_{i+\frac{1}{2}}}\frac{A_{i+\frac{1}{2}}^{n}}{\rho}\left((p-\hat{p})_{i+1}^{n} - (p-\hat{p})_i^{n}\right)\right]. \quad (2.2.26)$$

Substitution of (2.2.26) into (2.2.25) leads to

$$\begin{aligned} M(p_i^{n+1}) - \frac{\Delta t^2}{\Delta x_{i+\frac{1}{2}}}\frac{A_{i+\frac{1}{2}}^{n}}{\rho(1+\beta\Delta t\gamma_{i+\frac{1}{2}}^{n})}(p_{i+1}^{n+1} - p_i^{n+1}) - \frac{\Delta t^2}{\Delta x_{i-\frac{1}{2}}}\frac{A_{i-\frac{1}{2}}^{n}}{\rho(1+\beta\Delta t\gamma_{i-\frac{1}{2}}^{n})}(p_i^{n+1} - p_{i-1}^{n+1}) \\ = M(p_i^n) - \Delta t\left[\left(\frac{q_{i+\frac{1}{2}}^{**}}{1+\beta\Delta t\gamma_{i+\frac{1}{2}}^{n}}\right) - \left(\frac{q_{i-\frac{1}{2}}^{**}}{1+\beta\Delta t\gamma_{i-\frac{1}{2}}^{n}}\right)\right] \\ - \frac{\Delta t^2}{\Delta x_{i+\frac{1}{2}}}\frac{A_{i+\frac{1}{2}}^{n}}{\rho(1+\beta\Delta t\gamma_{i+\frac{1}{2}}^{n})}\left((p-\hat{p})_{i+1}^{n} - (p-\hat{p})_i^{n}\right) \\ + \frac{\Delta t^2}{\Delta x_{i-\frac{1}{2}}}\frac{A_{i-\frac{1}{2}}^{n}}{\rho(1+\beta\Delta t\gamma_{i-\frac{1}{2}}^{n})}\left((p-\hat{p})_i^{n} - (p-\hat{p})_{i-1}^{n}\right) \end{aligned}$$

which can be rearranged as

$$\begin{aligned} M(p_i^{n+1}) - \frac{\Delta t^2}{\Delta x_{i-\frac{1}{2}}}\frac{A_{i-\frac{1}{2}}^{n}}{\rho\left(1+\beta\Delta t\gamma_{i-\frac{1}{2}}^{n}\right)}p_{i-1}^{n+1} - \frac{\Delta t^2}{\Delta x_{i+\frac{1}{2}}}\frac{A_{i+\frac{1}{2}}^{n}}{\rho\left(1+\beta\Delta t\gamma_{i+\frac{1}{2}}^{n}\right)}p_{i+1}^{n+1} \\ + \Delta t^2\left[\frac{1}{\Delta x_{i+\frac{1}{2}}}\frac{A_{i+\frac{1}{2}}^{n}}{\rho\left(1+\beta\Delta t\gamma_{i+\frac{1}{2}}^{n}\right)} + \frac{1}{\Delta x_{i-\frac{1}{2}}}\frac{A_{i-\frac{1}{2}}^{n}}{\rho\left(1+\beta\Delta t\gamma_{i-\frac{1}{2}}^{n}\right)}\right]p_i^{n+1} \\ = M(p_i^n) - \Delta t\left(\frac{q_{i+\frac{1}{2}}^{**}}{1+\beta\Delta t\gamma_{i+\frac{1}{2}}^{n}} - \frac{q_{i-\frac{1}{2}}^{**}}{1+\beta\Delta t\gamma_{i-\frac{1}{2}}^{n}}\right) \\ - \Delta t^2\left[\frac{1}{\Delta x_{i+\frac{1}{2}}}\frac{A_{i+\frac{1}{2}}^{n}}{\rho\left(1+\beta\Delta t\gamma_{i+\frac{1}{2}}^{n}\right)}\left((p-\hat{p})_{i+1}^{n} - (p-\hat{p})_i^{n}\right)\right] \\ - \Delta t^2\left[\frac{1}{\Delta x_{i-\frac{1}{2}}}\frac{A_{i-\frac{1}{2}}^{n}}{\rho\left(1+\beta\Delta t\gamma_{i-\frac{1}{2}}^{n}\right)}\left((p-\hat{p})_i^{n} - (p-\hat{p})_{i-1}^{n}\right)\right]. \end{aligned} \quad (2.2.27)$$

The former scheme can be rewritten more compactly using a matrix-vector notation,

$$\mathbf{M}(\mathbf{p}^{n+1}) + \mathbf{T}\,\mathbf{p}^{n+1} = \mathbf{b}^n \quad (2.2.28)$$

where

- $\mathbf{M} = \mathrm{diag}(M(p_i^{n+1}))$ is a vector function which contains the non linearity, which has not always a non-decreasing derivative;
- $\mathbf{T}$ is a symmetric-positive-definite matrix, whose entries are

$$T_{i,i-1} = -\frac{\Delta t^{\,2}}{\Delta x_{i-\frac{1}{2}}} \frac{A^n_{i-\frac{1}{2}}}{\rho\left(1+\beta\Delta t\,\gamma^n_{i-\frac{1}{2}}\right)},$$
$$T_{i,i} = \frac{\Delta t^{\,2}}{\Delta x_{i+\frac{1}{2}}} \frac{A^n_{i+\frac{1}{2}}}{\rho\left(1+\beta\Delta t\,\gamma^n_{i+\frac{1}{2}}\right)} + \frac{\Delta t^{\,2}}{\Delta x_{i-\frac{1}{2}}} \frac{A^n_{i-\frac{1}{2}}}{\rho\left(1+\beta\Delta t\gamma^n_{i-\frac{1}{2}}\right)},$$
$$T_{i,i+1} = -\frac{\Delta t^{\,2}}{\Delta x_{i+\frac{1}{2}}} \frac{A^n_{i+\frac{1}{2}}}{\rho\left(1+\beta\Delta t\,\gamma^n_{i+\frac{1}{2}}\right)};$$

- $\mathbf{p}^{n+1}$ is the vector of the new pressure at the primal vertex;
- $\mathbf{b}^n$ is the known right hand side term.

An iterative method is employed in order to solve the system (2.2.28). However, due to the kind of non-linearity appearing in $\mathbf{M}(\mathbf{p})$ careful must be taken when veins are considered. To get a closer idea on the kind of non linearity arising in $\mathbf{M}(\mathbf{p})$, we report in Figure 2.2 the non-dimensional cross-sectional area as a function of the pressure for two different sets of model parameters: $\Gamma = 0$, $p_e = 0$, $K = 5 \cdot 10^4$, $m = 0.5$ and $n = 0$, which correspond to an artery; and $\Gamma = 0$, $p_e = 66.6$, $K = 1 \cdot 10^2$, $m = 10$ and $n = -1.5$, representing an elastic vein. As ones can note in Figure 2.2, the fluid mass function, if applied to veins, has not always a non-descreasing derivative, hence a direct application of Newton-type methods may, in general, fail to converge unless the initial guess is sufficiently accurate, [42]. Otherwise, the nested Newton-type algorithm, proposed in [54, 55], combined with the conjugate gradient method provides an efficient iterative methodology to solve the weakly non-linear system (2.2.28). The proposed strategy is first to split properly the diagonal nonlinear terms and then to linearize the nonlinear contributions in sequence to derive a nested iterative method. The splitting of the first derivative of $\mathbf{M}(\mathbf{p}^{n+1})$ is based on the Jordan decomposition, which assumes $\mathbf{M}(\mathbf{p}^{n+1})$ to be a function of bounded variations, as the difference of two nonnegative, nondecreasing bounded functions. In particular, defining $c_i(p) = \dfrac{dM_i(p)}{dp}$, then there exist $s_i(p)$ and $r_i(p)$ such that

$$c_i(p) = s_i(p) - r_i(p) \geq 0 \quad \text{and} \quad 0 \leq r_i(p) \leq s_i(p) \quad \forall\, p \in \mathbb{R}. \tag{2.2.29}$$

Hence

$$\begin{cases} s_i(p) = c_i(p), \quad r_i(p) = 0 & \text{if } \; p \leq p_v, \\ s_i(p) = c_i(p_v), \quad r_i(p) = s_i(p) - c_i(p) & \text{if } \; p > p_v, \end{cases} \tag{2.2.30}$$

with p_v such that $c_i(p)$ is strictly positive and non-decreasing in $(-\infty, p_v)$ and non-increasing in $(p_v, +\infty)$. Then, $\mathbf{M}(\mathbf{p}^{n+1})$ can be decomposed in two functions $\mathbf{M}_1(\mathbf{p}^{n+1})$ and $\mathbf{M}_2(\mathbf{p}^{n+1})$ with non-decreasing first derivatives. Thus system (2.2.28) is rewritten as

$$\mathbf{M}_1(\mathbf{p}^{n+1}) - \mathbf{M}_2(\mathbf{p}^{n+1}) + \mathbf{T}\,\mathbf{p}^{n+1} = \mathbf{b}^n, \tag{2.2.31}$$

where $\mathbf{M}_1(\mathbf{p}^{n+1})$ and $\mathbf{M}_2(\mathbf{p}^{n+1})$ are given by

$$\mathbf{M}_1(p) = \begin{cases} \mathbf{M}(p) & \text{if } \ p \le p_v, \\ \mathbf{M}(p_v) + \mathbf{M}'(p_v)(p - p_v) & \text{if } \ p > p_v, \end{cases} \qquad \mathbf{M}'(p) = \frac{d\mathbf{M}(p)}{dp}, \tag{2.2.32}$$

and

$$\mathbf{M}_2(p) = \mathbf{M}_1(p) - \mathbf{M}(p).$$

In the outer Newton iteration only the second function $\mathbf{M}_2(\mathbf{p}^{n+1})$ is linearized and the resulting nonlinear system is then solved in the inner Newton iterations by linearizing also the first function $\mathbf{M}_1(\mathbf{p}^{n+1})$. In what follows, we further detail the nested Newton-type algorithm employed.

Nested iteration. Let $\mathbf{C}(\mathbf{p})$, $\mathbf{S}(\mathbf{p})$ and $\mathbf{R}(\mathbf{p})$ denote the diagonal matrices whose entries are $c_i(p)$, $s_i(p)$ and $r_i(p)$, respectively. Hence, $\mathbf{C}(\mathbf{p}) = \mathbf{S}(\mathbf{p}) - \mathbf{R}(\mathbf{p})$ represents the Jacobian of $\mathbf{M}(\mathbf{p})$, $\mathbf{S}(\mathbf{p})$ is almost everywhere the Jacobian of $\mathbf{M}_1(\mathbf{p})$ and $\mathbf{R}(\mathbf{p})$ is almost everywhere the Jacobian of $\mathbf{M}_2(\mathbf{p})$.

As we have said, a nested Newton-type method for solving (2.2.31) is derived linearizing separately $\mathbf{M}_1(\mathbf{p})$ and $\mathbf{M}_2(\mathbf{p})$. Thus, first, by choosing $\mathbf{p}^0 \le \mathbf{p}_v$, a sequence of outer iterates $\mathbf{p}^k$ is derived from (2.2.31) by linearizing $\mathbf{M}_2(\mathbf{p})$ as follows

$$\mathbf{M}_1(\mathbf{p}^k) - \left[\mathbf{M}_2(\mathbf{p}^{k-1}) + \mathbf{R}(\mathbf{p}^{k-1})(\mathbf{p}^k - \mathbf{p}^{k-1})\right] + \mathbf{T}\,\mathbf{p}^k = \mathbf{b}, \tag{2.2.33}$$

so that the outer iteration is the solution of the mildly nonlinear systems

$$\mathbf{M}_1(\mathbf{p}^k) + \left(\mathbf{T} - \mathbf{R}^{k-1}\right)\mathbf{p}^k = \mathbf{d}^{k-1} \tag{2.2.34}$$

where $\mathbf{R}^{k-1} = \mathbf{R}(\mathbf{p}^{k-1})$ and $\mathbf{d}^{k-1} = \mathbf{b} + \mathbf{M}_2(\mathbf{p}^{k-1}) - \mathbf{R}^{k-1}\mathbf{p}^{k-1}$.
Next, for all $k \in \mathbb{N}$, by setting $\mathbf{p}^{k,0} = \mathbf{p}^{k-1}$, a sequence of inner iterates is derived from (2.2.34) by linearizing $\mathbf{M}_1(\mathbf{p})$ as follows

$$\left[\mathbf{M}_1(\mathbf{p}^{k,l-1}) + \mathbf{S}(\mathbf{p}^{k,l-1})(\mathbf{p}^{k,l} - \mathbf{p}^{k,l-1})\right] + \left(\mathbf{T} - \mathbf{R}^{k-1}\right)\mathbf{p}^{k,l} = \mathbf{d}^{k-1} \tag{2.2.35}$$

so that the inner iterates are determined from the following linear system

$$(\mathbf{S}^{k,l-1} + \mathbf{T} - \mathbf{R}^{k-1})\mathbf{p}^{k,l} = \mathbf{f}^{k,l-1} \tag{2.2.36}$$

where $\mathbf{S}^{k,l-1} = \mathbf{S}(\mathbf{p}^{k,l-1})$ and $\mathbf{f}^{k,l-1} = \mathbf{d}^{k-1} - \mathbf{M}_1(\mathbf{p}^{k,l-1}) + \mathbf{S}^{k,l-1}\mathbf{p}^{k,l-1}$. We stop the outer and inner iterations when, respectively, the norm of k-th outer residual,

$$\mathbf{r}^k = \mathbf{M}(\mathbf{p}^k) + \mathbf{T}\,\mathbf{p}^k - \mathbf{b},$$

derived from (2.2.34) and the norm of the (k,l)-th inner residual,

$$\mathbf{r}^{k,l} = \mathbf{M}_1(\mathbf{p}^{k,l}) + (\mathbf{T} - \mathbf{R}^{k-1})\mathbf{p}^{k,l} - \mathbf{d}^{k-1},$$

are less than a small prefixed tolerance $\epsilon \in \mathbb{R}^+$ which represents the maximum mass balance error allowed.

In general, fast convergence could be attained by taking as initial guess for the iterative procedure the solution of the outer iteration loop computed at the previous time step. Therefore, in order to comply with the requirement $\mathbf{p}^0 \leq \mathbf{p}_v$, we choose $\mathbf{p}^0$ to be

$$\mathbf{p}^0 = \min\left(\mathbf{p}_v, \mathbf{p}^{k,l-1}\right). \tag{2.2.37}$$

As shown in [55], it can be proven that the sequence of outer iterations of the pressure is bounded from above and monotonically increasing, whereas the sequence of inner iterations is bounded from below and it is monotonically decreasing. Thus, the convergence of the nested Newton method is guaranteed. The expression for p_v depends on the tube law and, in case an elastic vessel is considered, it is given by

$$p_v = p_e + K\left\{\left[\left(\frac{n(n-1)}{m(m-1)}\right)^{\frac{1}{m-n}}\right]^m - \left[\left(\frac{n(n-1)}{m(m-1)}\right)^{\frac{1}{m-n}}\right]^n\right\}. \tag{2.2.38}$$

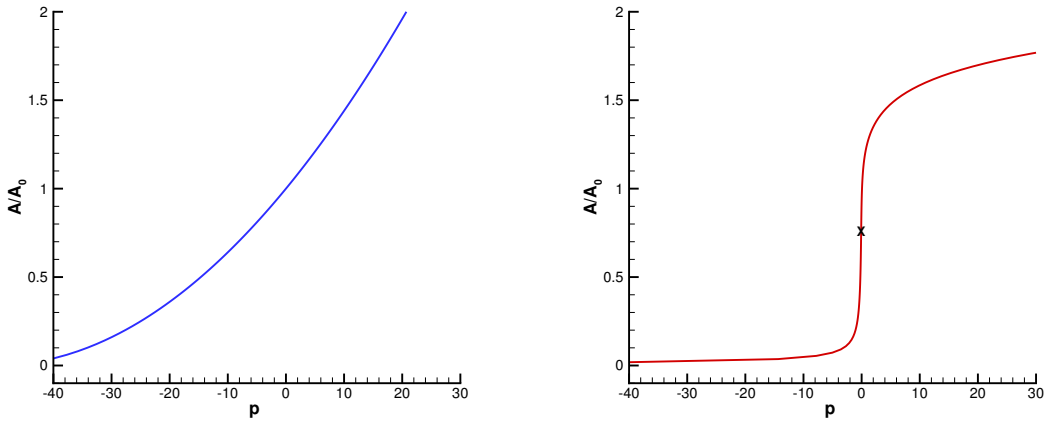

Figure 2.2: Non-dimensional cross-sectional area as a function of pressure in case of both elastic arteries (left) and veins (right) are considered. In the right plot it is also highlighted the point p_v (black cross) in which the non-dimensional cross-sectional area function changes its concavity.

Correction stage. Once the pressure at the new time step $\mathbf{p}^{n+1}$ is known, $\mathbf{q}^{n+1}$ is updated according to (2.2.26). Besides, the averaged area at each primal cell, A_i^{n+1}, is computed from the obtained pressure, p_i^{n+1}, and, if needed, the area at the previous time step, A_i^n. The complexity of the tube law makes it difficult to get a general analytical expression for the area as a function of the pressure. Therefore, we employ a Newton algorithm in order to solve the implicit function (2.1.45). If $\Gamma \neq 0$, the time derivative of the area is approximated using backward finite differences. In case an elastic artery is considered, i.e. for $m = 0.5$, $n = 0$ and $\Gamma = 0$, then the analytical expression

$$A_i^{n+1} = A_0\left(1 + \frac{p_i^{n+1} - p_e}{K}\right)^2 \tag{2.2.39}$$

is employed. Finally, the area at the dual cells is approximated as a weighted average of the areas in the two related primal subcells.

2.2.5 The θ-method

It is well known that, one major drawback of splitting strategies is that the order of accuracy in time of the overall algorithm gets reduced to one. Hence, we employ the θ-method to improve the accuracy in time of the overall scheme, while formally remaining first order accurate due to the employed splitting. Accordingly, we assume the main variables, q and p to be decomposed into two contributions by introducing an implicitness parameter θ to be taken in the range $\frac{1}{2} < \theta \leq 1$. Thus, we have the approximations at $t^{n+\theta}$ defined as

$$q^{n+\theta} = \theta q^{n+1} + (1-\theta)q^n, \tag{2.2.40}$$

$$p^{n+\theta} = \theta p^{n+1} + (1-\theta)p^n. \tag{2.2.41}$$

Now, replacing (2.2.40) in (2.2.3) and in (2.2.4a) and (2.2.41) in (2.2.4b), we get the modified equations for q^{**},

$$q^{**} = q^* + (1-\theta)\Delta t \frac{A(p^n)}{\rho}\frac{\partial}{\partial x}\left(\varphi^n \frac{\partial q^n}{\partial x}\right) + \theta \Delta t \frac{A(p^n)}{\rho}\frac{\partial}{\partial x}\left(\varphi^n \frac{\partial q^{**}}{\partial x}\right), \tag{2.2.42}$$

and for the computation of the cross-sectional area and the flow at the new time step,

$$A(p^{n+1}) = A(p^n) - (1-\theta)\Delta t \frac{\partial q^n}{\partial x} - \theta \Delta t \frac{\partial q^{n+1}}{\partial x}, \tag{2.2.43}$$

$$q^{n+1} = \frac{1}{1+\beta\Delta t\gamma^n}\left(q^{**} - (1-\theta)\Delta t \frac{A(p^n)}{\rho}\frac{\partial p^n}{\partial x} - \theta\Delta t \frac{A(p^n)}{\rho}\frac{\partial p^{n+1}}{\partial x} + \Delta t \frac{A(p^n)}{\rho}\frac{\partial (p-\hat{p})^n}{\partial x}\right). \tag{2.2.44}$$

Then, the methodology presented in Sections 2.2.3 and 2.2.4 is applied to compute the solution at the new time step. Let us note that, when choosing $\theta = 1$, we simply recover the first-order-in-time scheme already presented. Meanwhile, setting $\theta = \frac{1}{2}$ results in the second order Crank-Nicolson method. However, since the Crank-Nicolson method is well-known to produce spurious oscillations in the presence of discontinuities, in practical applications the θ parameter should be chosen strictly greater than $\frac{1}{2}$. Nevertheless, most blood flow dynamics problems are not expected to present strong discontinuities and it is well-known that the θ-method with $\theta \approx 0.5$ yields better results for smooth wave propagation problems than the implicit Euler scheme making this approach potentially useful for the study of cardiovascular flows.

2.2.6 Well-balanced property of the scheme

An important property of a numerical scheme is to be well-balanced, i.e., it should preserve the equilibria of balance laws. Although it may seem quite obvious from a physical point of view, verifying this property at the discrete level may not be trivial and a great effort has been dedicated to this topic in the last decades. Some examples of numerical methods designed to satisfy the so-called C-property can be found in [26, 95, 49, 152, 154, 120, 94, 173] and references therein. A particular and very interesting property of the numerical scheme proposed in this thesis is that it is already well-balanced by construction. For blood flow dynamics, the well balanced property corresponds with the dead man at eternal rest, i.e. in mathematical terms, if $q^n = 0$ and $p^n = const.$ then $p^{n+1} = p^n$ and $q^{n+1} = q^n = 0$. A proof of this property is reported below:

Proposition 2.2.1 (C-property)**.** *The scheme* (2.2.9), (2.2.21), (2.2.26) *and* (2.2.27) *is well balanced, that is, given* $q^n = 0$ *and* $p^n = const.$ *then* $p^{n+1} = p^n$ *and* $q^{n+1} = q^n = 0$.

Proof. Let us assume a fluid at rest with initial conditions of the form $A^n = A_0(x)$, $p^n = const.$ and $q^n = 0$ for all cells. Then, from (2.2.9) we have $q_j^* = q_j^n$, with both a Ducros-type, (2.2.16), or a Rusanov-type numerical flux in the discretization of the nonlinear convective terms, since any numerical dissipation in the numerical fluxes associated with the advective term $\dfrac{\partial F(q^n)}{\partial x}$ will vanish for $q^n = 0$. Then, since $q_j^* = q_j^n = 0$ and considering $K_R = 0$, there is no contribution of the diffusive term in (2.2.18) and we get $q_j^{**} = q_j^* = q_j^n = 0$. Next, we observe that (2.2.27) has $p_i^{n+1} = p_i^n = const.$ as solution. Finally, since the discrete gradient of a constant is zero, from (2.2.26) we have $q_j^{n+1} = q_j^{**} = q_j^* = q_j^n = 0$ which corresponds to the well-known C-property for homogenous stationary solutions of system (2.1.41). □

Let us note that the former result also holds in case the θ-method is employed. The new contributions in (2.2.42), (2.2.43) and (2.2.44) with respect to (2.2.3)-(2.2.4) depend on $q^n = 0$ and on the spatial derivative of the old constant pressure, to be discretized using central finite differences, so they are zero.

2.2.7 Boundary conditions

This section is devoted to illustrate the major key points to treat the different boundary conditions to be employed in the test cases analyzed in Section 1.7. In particular, we consider periodic boundary conditions, Dirichlet boundary conditions for the velocity, Dirichlet boundary conditions for the pressure and Windkessel boundary conditions.

- Periodic boundary conditions. In case periodic boundary conditions are prescribed, the left and right boundaries virtually coincide. Hence, the first primal cell is set to be the right neighbor of the last primal cell and vice-versa. Moreover, a unique dual cell at the periodic boundary is built merging the original boundary dual cells at both sides of the periodic boundary. Then, the solution can be approximated as for any interior cell.

- Strong Dirichlet boundary conditions for the mass flux. In the purely elastic case, we simply impose the given value at the corresponding dual cell at the end of the explicit stage which is then substituted in the pressure subsystem (2.2.25). In particular, focusing on the right boundary, identifying with index i the last primal cell and denoting q_e^{n+1} the exact mass flux at the boundary at time t^{n+1}, the continuity equation (2.2.25) reads

$$M(p_i^{n+1}) = M(p_i^n) - \Delta t(q_e^{n+1} - q_{i-\frac{1}{2}}^{n+1}) \tag{2.2.45}$$

  where $q_{i-\frac{1}{2}}^{n+1}$ is given by the discrete momentum equation (2.2.26). On the other hand, in case a viscoelastic vessel is considered, the value to be imposed as exact solution of the viscous subsystem, (2.2.22), should not contain the contribution due to the pressure terms that will be accounted for in the next stage. Hence, an approximation of the pressure term is computed employing finite differences and subtracted to the

given mass flux. Consequently, the mass flux to impose as exact solution of (2.2.22) is

$$q_{e,v}^{n+1} = q_e^{n+1} + \frac{\Delta t}{\Delta x_{i-\frac{1}{2}}} \frac{A_{i-\frac{1}{2}}^n}{\rho} (\hat{p}_i^n - \hat{p}_{i-1}^n). \tag{2.2.46}$$

Finally, as for the elastic case, the exact mass flow q_e^{n+1} is employed within the pressure stage.

- Pressure boundary conditions. Neumann boundary conditions are assumed for the velocity field and zero viscous fluxes are set through the boundary. Next, the pressure is weakly imposed in (2.2.25), i.e. the value of the pressure at the boundary is employed to define the corresponding pressure term in the momentum equation (2.2.26) and then the pressure system is solved providing also the value at the primal boundary cell. For instance, focusing on the right boundary, identifying with index i the last primal cell and denoting p_e^n the exact pressure at the boundary at time t^n, we set

$$\begin{aligned} q_{i+\frac{1}{2}}^{n+1} = \frac{1}{1+\beta\Delta t\gamma_{i+\frac{1}{2}}^n} \left[q_{i+\frac{1}{2}}^{**} - \frac{2\Delta t}{\Delta x_{i+\frac{1}{2}}} \frac{A_{i+\frac{1}{2}}^n}{\rho} \left(p_e^n - p_i^{n+1} \right) \right] \\ + \frac{1}{1+\beta\Delta t\gamma_{i+\frac{1}{2}}^n} \left[\frac{2\Delta t}{\Delta x_{i+\frac{1}{2}}} \frac{A_{i+\frac{1}{2}}^n}{\rho} \left(\left(p_e^n - \hat{p}_{i+\frac{1}{2}} \right) - (p - \hat{p})_i^n \right) \right]. \end{aligned} \tag{2.2.47}$$

Finally, the intermediate velocity is updated taking into account the new pressure.

- Lumped parameters, or Windkessel, model as terminal boundary condition. In order to provide boundary conditions which reflect as much as possible a physiological situation, the effect of the cardiovascular system distal to generic one-dimensional computational domain is taken into account by coupling it to a Windkessel model [177, 228, 230]. The Windkessel model is based on the observation that the blood flow in the peripheral arteries is relatively smooth, despite the pulsatile action of the heart, and on the idea that the interaction between the heart and the arteries has similarity with a working principle of a fire hose, in which the pulsatile action of the pump is damped by an air chamber. The simplest model, first introduced in [90], consists in a two element Windkessel composed of two building blocks: the peripheral resistance, R, representing the peripheral arterioles and capillaries, and the total arterial compliance C, which accounts for the elasticity of the larger conduit vessels. It relates the volumetric inflow q to the volume V stored in the capacitive element and to the resistive element R through the following relationship

$$q = \frac{\partial V}{\partial t} + \frac{p - p_{out}}{R} \tag{2.2.48}$$

where the compartment volume V is itself related to the pressure via the compliance as $V = Cp$ and p_{out} is the pressure at which the flow at the microcirculation ceases. Following [35], we consider the three element lumped parameter model depicted in Figure 2.3 which improves on the two-element model by incorporating another resistive element to simulate resistance to blood flow due to the characteristic resistance of major arteries. In this way, identifying with index i the last primal cell

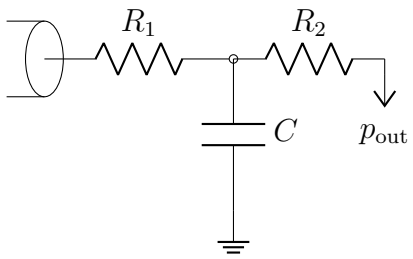

Figure 2.3: The three element lumped parameter model (RCR) coupled to terminal one-dimensional vessels.

and with subscript w an undetermined but distal position to the one dimensional domain before reaching microcirculation, the pressure drop between these two locations is given by

$$p_i - p_w = R_1 q. \tag{2.2.49}$$

On the other hand, q is related to p_w according to (2.2.48) when p_w is substituted for p. Hence, the pressure and the flow in the lumped parameter model and at the end point of a terminal vessel is then related through

$$\frac{\partial V(p_w)}{\partial t} = \frac{p_i - p_w}{R_1} - \frac{p_w - p_{out}}{R_2} \tag{2.2.50}$$

where $V(p_w) = Cp_w$. In order to integrate the Windkessel model with the proposed semi-implicit method in a rigorous way, we perform an implicit coupling solving the ODE (2.2.50) in an unique step within the pressure subsystem (2.2.25), thus adopting a monolithic approach. Accordingly, at the end of each vessel coupled to a Windkessel model, a pressure point, which represents the pressure p_w inside the lumped parameter model, is added. Then, the vector of the unknowns in (2.2.28) is augmented with one additional element p_w^{n+1} becoming $\bar{\mathbf{p}}^{n+1} = [\mathbf{p}^{n+1}, p_w^{n+1}]$ and $\mathbf{M}$, $\mathbf{T}$ matrices, as well as the right hand side vector, $\mathbf{b}$, in (2.2.28), are properly modified. In particular, taking into account the relation (2.2.49) the continuity equation (2.2.9) added for the last primal cell reads

$$M(p_i^{n+1}) = M(p_i^n) - \Delta t \left(\frac{p_i^{n+1} - p_w^{n+1}}{R_1} - q_{i-\frac{1}{2}}^{n+1} \right), \tag{2.2.51}$$

where $q_{i-\frac{1}{2}}^{n+1}$ has the same expression as for an interior cell, that is (2.2.26). As a consequence, the $i-$th row non-zero entries of the $\mathbf{T}$ matrix and the right-hand side

vector become

$$T_{i,i-1} = -\frac{\Delta t^{\,2}}{\Delta x_{i-\frac{1}{2}}} \frac{A^n_{i-\frac{1}{2}}}{\rho\left(1+\beta\Delta t\,\gamma^n_{i-\frac{1}{2}}\right)},$$

$$T_{i,i} = \frac{\Delta t^{\,2}}{\Delta x_{i-\frac{1}{2}}} \frac{A^n_{i-\frac{1}{2}}}{\rho\left(1+\beta\Delta t\gamma^n_{i-\frac{1}{2}}\right)} + \frac{\Delta t}{R_1},$$

$$T_{i,i+1} = -\frac{\Delta t}{R_1},$$

$$b_i = M(p^n_i) + \Delta t \frac{q^{**}_{i-\frac{1}{2}}}{1+\beta\Delta t\gamma^n_{i-\frac{1}{2}}} - \frac{\Delta t^2}{\Delta x_{i-\frac{1}{2}}} \frac{A^n_{i-\frac{1}{2}}}{\rho\left(1+\beta\Delta t\gamma^n_{i-\frac{1}{2}}\right)} \left((p-\hat{p})^n_i - (p-\hat{p})^n_{i-1}\right).$$

On the other hand, the evolution of the added pressure point is governed by (2.2.50) whose implicit discretization reads

$$V(p^{n+1}_w) - \frac{\Delta t}{R_1} p^{n+1}_i + \Delta t\left(\frac{1}{R_1}+\frac{1}{R_2}\right) p^{n+1}_w = V(p^n_w) + \Delta t \frac{p_{out}}{R_2}. \tag{2.2.52}$$

Consequently, the $i+1$-th entries of the new row of $\mathbf{M}$, $\mathbf{T}$ and $\mathbf{b}$ result

$$\begin{aligned} M_{i+1,i+1} &= V(p^{n+1}_w), \\ T_{i+1,i} &= -\frac{\Delta t}{R_1}, \\ T_{i+1,i+1} &= \Delta t\left(\frac{1}{R_1}+\frac{1}{R_2}\right), \\ b_{i+1} &= V(p^n_w) + \Delta t \frac{p_{out}}{R_2}. \end{aligned}$$

The $\mathbf{M}$ matrix is still a diagonal matrix, while $\mathbf{T}$ preserves the symmetric-positive-definite property, so the resulting monolithic system can be solved exploiting the same procedure as described in Section 2.2.4. In this way, the coupling with the lumped parameter model does not affect the time step of the semi-implicit scheme. For further details and a recent revision on different lumped parameter 0D models we refer to [100].

2.3 Junctions and extension to networks

The above section was devoted to the numerical solution of the blood flow model in a single branch. However, this type of models are rarely applied to model a single tube. In most cases one has to deal with a network of vessels. To simulate blood flows in such networks, a simple approach assumes that the cardiovascular system consists in a set of one-dimensional vessels which are connected through nodes, so-called junctions, where several vessels meet. The underlying idea on the novel methodology proposed in this thesis is to see the junction as a sort of three-dimensional container to which the blood arriving from the ingoing vessels is mixed and then distributed among all the vessels in the junction

fulfilling the principle of conservation of mass and balance of momentum expressed by the Euler equations.

Whilst each single vessel is simultaneously discretized as described in Section 2.2.1, a proper discretization for junction elements has to be introduced. In this framework, the 3D cell corresponds to a primal element whose inlet and outlet boundaries are located at the extrema of the corresponding 1D vessel geometries, while the remaining boundaries, which correspond to vessel walls, are considered to be of wall type and thus it is assumed that no fluxes can go through them. Besides, the 3D cell can be virtually divided into as many subcells as vessels intersect in the junction, each of them going from the corresponding 1D vessel boundary to the center of the junction. Each of those subcells are glued with the boundary dual cell of the corresponding vessel resulting on dual mixed 3D-1D cells related to the junction. Consequently, the 3D junction and the 1D vessels are completely coupled, see Figure 2.4 for a sketch of the mesh structure. Due to the staggered mesh arrangement, the junction itself is a pressure point. As such, mass conservation is solved on the primary control volume around the pressure point, see left panel of Figure 2.4. On the other hand, as we can observe in the right panel of Figure 2.4, the discretization of the nonlinear convective terms on the dual control volumes needs the computation of a numerical flux in the junction point, where several vessels meet. In this work we propose to use a very simple but genuinely multi-dimensional Riemann solver in order to compute the numerical flux for the convective subsystem in the junction point, following the ideas of Abgrall, see [1] and references therein. The multi-dimensional flux relies on the computation of an appropriate 3D velocity and momentum average in the junction point, in combination with a suitable multi-dimensional numerical dissipation term, both accounting for the minimum set of essential geometrical features that describe the junction, namely the normal vectors of all incident vessels and their respective cross-sectional areas. The pressure, given at the primal cells, is approximated implicitly at a unique step, solving a monolithic system that contains all the degrees of freedom of both the 1D vessels and the 3D junctions, see [53].

As a simpler alternative to the new 3D junction approach to be presented in Section 2.3.1, we may employ the classical 0D junction model proposed in [197, 83, 141, 158]. Note that one major advantage of the 3D model, with respect to the 0D simplified approach, is that it takes into account the real geometry of the junction which may greatly influence the flow behavior. Moreover, the classical 0D junction approach to be employed is based on the use of Riemann Invariants and thus can not correctly deal with shock waves. In that case, an alternative 0D model accounting for shocks hitting junctions should be designed, [61]. Besides, the 0D approach requires the solution of an additional system which may not be computationally cheaper than the proposed 3D junction approach.

Before detailing the proposed methodology at junctions, we introduce some further notations. Let us focus on a single junction whose corresponding primal cell is denoted by C_i and that connects the 1D vessels V_j, $j \in S_i$ where S_i is the set of indexes corresponding to the primal neighbors of C_i which are 1D boundary cells in V_j identified by C_j. Hence, S_i has as many elements as vessels are connected through that junction, i.e., for a junction of n branches we have n neighbors saved in the set S_i. Moreover, we denote $D_{ij} \equiv D_k$ each of the mixed 3D-1D dual cells with one part belonging to C_i and the remaining part in C_j. Since C_i is a 3D cell and C_j is a 1D cell, their boundaries could be initially seen as a surface and a point, respectively. Note however that the 1D vessel geometry arises as a simplification of the 3D model so it is possible to identify also the real boundary

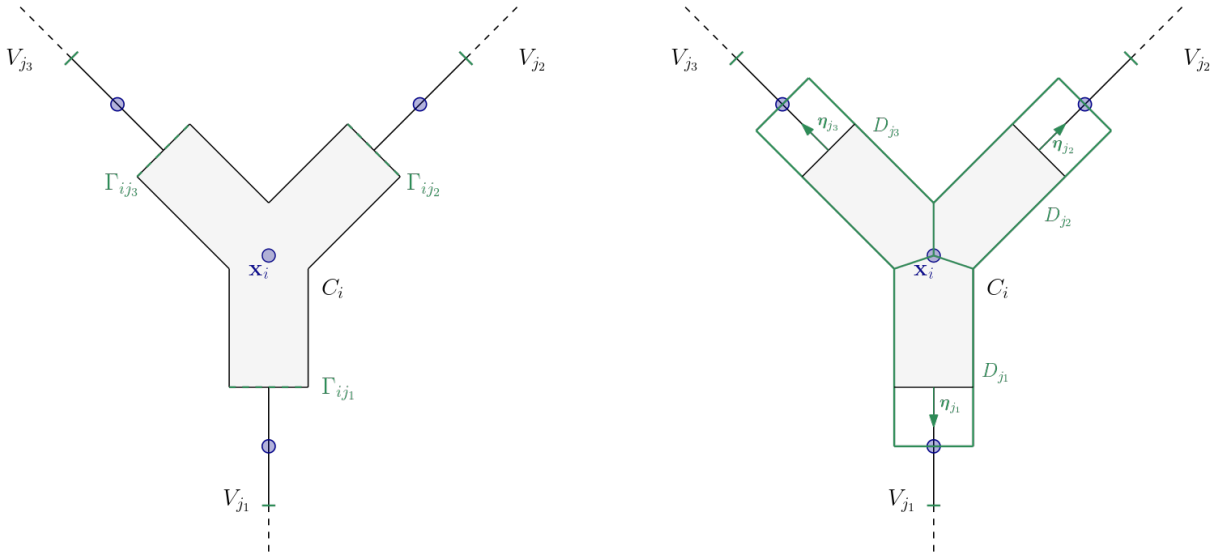

Figure 2.4: Sketch of the primal and dual grid structures in the neighbouring of a junction i with center $\mathbf{x}_i$ for the 3D junction approach. C_i denotes the primal junction cell with neighbouring elements of index $S_i = \{j_1, j_2, j_3\}$, V_{j_k}, $k \in S_i$ the vessels related to the junction, Γ_{ij_k} the corresponding interfaces between the 3D primal cell and each 1D vessel and D_{j_k} the mixed 3D-1D dual cells related to the junction.

corresponding to the 1D cell as being that of the 3D cell. We write $\Gamma_{ij} \equiv \Gamma_k$ to identify such boundary between cells C_i and C_j whose unit normal vector, outward to the 3D cell, is $\boldsymbol{\eta}_{ij} \equiv \boldsymbol{\eta}_k$. In Figure 2.4 a sketch of the grid structure and the main notation related to a junction is depicted.

2.3.1 3D junction

As aforementioned, a semi-implicit approach is employed to approximate the pressure and velocity unknowns related to a junction, that is, the pressure at the junction primal cell, p_i^{n+1}, and the weighted velocity at the mixed 3D-1D dual cells, q_j^{n+1}, $j \in S_i$, see Figure 2.5. In particular, the incompressible Euler equations,

$$\nabla \cdot \rho \mathbf{u} = 0, \tag{2.3.1}$$

$$\frac{\partial \rho \mathbf{u}}{\partial t} + \nabla \mathcal{F}(\mathbf{u}) + \nabla p = 0, \qquad \mathcal{F}(\mathbf{u}) = \rho \mathbf{u} \otimes \mathbf{u}, \tag{2.3.2}$$

are discretized in the junction applying a splitting strategy which provides two subsystems: one related to the pressure and a transport subsystem for the velocity field. Hence, the transport equations are solved using explicit finite volumes providing an intermediate velocity at the junction dual cells, u_j^*, $j \in S_i$, which does not include the pressure gradient at the new time step. Regarding the pressure subsystem, we recall that vessels can be deformed over time and, consequently, the boundary of the 3D cell changes. Denoting by R the radius of the vessel, which is time-dependent, $R^2 = \frac{A}{\pi}$, u the axial component of the velocity field, and r the radial direction from the vessel centerline, we can integrate the continuity equation in the radial direction and apply a kinematic boundary condition at

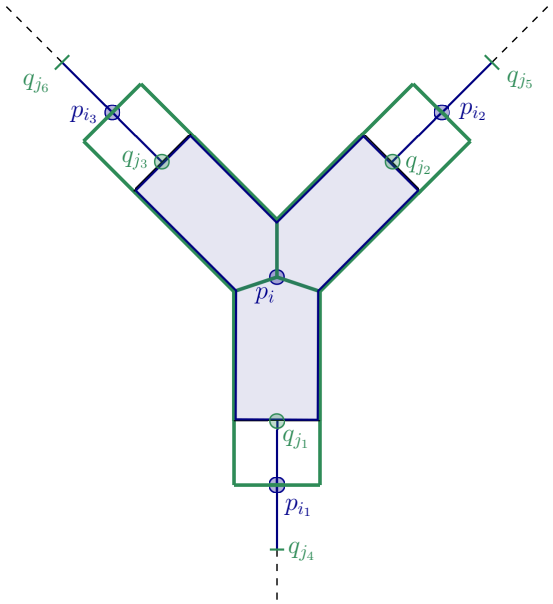

Figure 2.5: Sketch of the location of the main variables of the blood flow model in the vicinity of a 3D junction. The indices j_m correspond to dual cells (in green) while the indices i_n refer to primal cells (in blue). Moreover, i identifies the primal 3D cell of the junction (shadowed in blue) and j_m with $m \in \{1, 2, 3\}$ correspond to mixed 3D-1D dual cells.

the vessel wall obtaining the following equation of the moving vessel boundary:

$$\frac{\partial A(p)}{\partial t} + 2\pi \frac{\partial}{\partial x} \left(\int_0^{R(p)} u \, r dr \right) = 0 \tag{2.3.3}$$

that is discretized with the aid of an implicit finite volume scheme. Then, the obtained equations for the pressure are coupled with the discrete pressure equations for the 1D vessels thus enlarging the pressure system, (2.2.28). Note that the proposed approach is monolithic, that is, it completely integrates the computations related to the junction in the overall scheme. As a consequence, we will get a unique mildly non-linear pressure system including the cells of all vessels and junctions. Finally the new pressure is employed to correct the intermediate velocities.

Computation of the intermediate velocity Following the methodology presented in Section 2.2, the intermediate velocity in a junction related cell is explicitly computed solving the corresponding convective subsystem according to (2.2.9). It is important to remark that the only fluxes needed to be accounted for are those at faces between two cells since the remaining boundaries are walls with zero flux. Therefore, in the following description of the algorithm we will omit the wall-type boundaries. Let us focus on a particular junction with a dual cell D_j. Integrating the convective subsystem over D_j and applying Gauss theorem, we obtain

$$\rho u_j^* = \rho u_j^n - \Delta t \, \frac{1}{|D_j|} \sum_{i \in K_j} \int_{\Gamma_{ij}} \mathcal{F}(\mathbf{u}^n) \cdot \boldsymbol{\eta}_{ij} \, \mathrm{dS} \tag{2.3.4}$$

where Γ_{ij} identifies the dual cell boundaries with outward unit normal $\boldsymbol{\eta}_{ij}$ and K_j the primal cells used to build D_j. It is important to note that the dual cell is of a hybrid type, i.e. a part of the staggered cell lives in the one-dimensional domain while the other part belongs to the junction volume. Hence, the fluxes in (2.3.4) have different dimensional nature at each cell interface. Consequently, at the face located inside the 1D vessel the flux term is simply computed following (2.2.11). Meanwhile, for the boundary contained in the 3D cell we employ a multidimensional approach inspired by [1]. Then, the multi-dimensional numerical flux is projected along the centerline of vessel V_j, involved in the $i-$th junction, and incorporated into the discrete scalar equation used to approximate the intermediate velocity in the dual cell. In this way, the velocity is affected by the shape of the junction through the multidimensional normal vectors, while the exact shape and the precise volume of the dual cell D_j are not necessary. The final numerical flux that is needed at the junction point and which corresponds to the projected multidimensional flux of the 3D boundary Γ_{ij} onto the normal direction $\boldsymbol{\eta}_j$ is approximated as

$$\left(\int_{\Gamma_{ij}} \mathcal{F}(\mathbf{u}^n) \cdot \boldsymbol{\eta}_{ij} \, \mathrm{dS} \right) \cdot \boldsymbol{\eta}_j \approx \left(\mathbf{u}_i^n \cdot \boldsymbol{\eta}_j \right) \left(\mathbf{q}_i^n \cdot \boldsymbol{\eta}_j \right) + \alpha_i^n (q_j^n - \mathbf{q}_i^n \cdot \boldsymbol{\eta}_j), \tag{2.3.5}$$

where $\boldsymbol{\eta}_j$ is the unit vector defined from the vessel centerline of D_j and α_i denotes the artificial viscosity computed as the maximum absolute eigenvalue for all neighboring cells through the junction,

$$\alpha_i^n = \max_{j \in S_i} \left(2|u_j^n| \right). \tag{2.3.6}$$

In addition, we define the needed three-dimensional physical flux at the junction, $\mathbf{f}_i^n$, as the weighted average of the 3D physical fluxes computed at the related dual cells, $\mathbf{f}_j^n$, that is

$$\mathbf{f}_i^n = \frac{\sum\limits_{j \in S_i} A_j^n \mathbf{f}_j^n}{\sum\limits_{j \in S_i} A_j^n}. \tag{2.3.7}$$

The auxiliary multidimensional velocity $\mathbf{u}_i^n$ at the junction is then defined in order to satisfy the flux compatibility condition in the junction, which states that the sum of the fluctuations on a cell must equal the boundary integral of the normal flux, i.e.,

$$\sum_{j \in S_i} A_j^n \boldsymbol{\eta}_j \cdot (\mathbf{f}_i^n - \mathbf{f}_j^n) + \sum_{j \in S_i} A_j^n \alpha_i^n (\mathbf{u}_j^n - \mathbf{u}_i^n) = - \sum_{j \in S_i} A_j^n \boldsymbol{\eta}_j \cdot \mathbf{f}_j, \qquad \mathbf{u}_j^n = u_j^n \boldsymbol{\eta}_j. \tag{2.3.8}$$

Assuming closed areas, namely,

$$\sum_{j \in S_i} A_j^n \boldsymbol{\eta}_j = 0, \tag{2.3.9}$$

we have

$$\sum_{j \in S_i} A_j^n \boldsymbol{\eta}_j \cdot \mathbf{f}_i^n = \left(\sum_{j \in S_i} A_j^n \boldsymbol{\eta}_j \right) \cdot \mathbf{f}_i^n = 0 \tag{2.3.10}$$

and (2.3.8) is thus rewritten as

$$\sum_{j \in S_i} A_j^n \mathbf{u}_i^n = \sum_{j \in S_i} A_j^n \mathbf{u}_j^n. \tag{2.3.11}$$

Hence, the compatible velocity at the junction reads

$$\mathbf{u}_i^n = \frac{\sum\limits_{j\in S_i} A_j^n \mathbf{u}_j^n}{\sum\limits_{j\in S_i} A_j^n}. \tag{2.3.12}$$

Similarly, we compute the auxiliary vector

$$\mathbf{q}_i^n = \frac{\sum\limits_{j\in S_i} A_j^n \mathbf{q}_j^n}{\sum\limits_{j\in S_i} A_j^n}, \qquad \mathbf{q}_j^n = q_j^n \boldsymbol{\eta}_j, \tag{2.3.13}$$

which provides the needed approximated multidimensional value related to q at the junction point $\mathbf{x}_i$. Let us remark that (2.3.7), (2.3.12) and (2.3.13) depend on the areas of the vessels and on $\boldsymbol{\eta}_j$, $j \in S_i$, so the junction deformation is taken into account, not only through the moving vessel boundary equation used to derive the pressure system, (2.3.3), but, also, when solving the momentum equation.

Approximation of the pressure field Following [53], at junctions the mass conservation equation must be considered over the three-dimensional primal cell with a dynamic boundary. More precisely, we allow simple deformations of the junctions analogous to the variable cross-sectional areas in the 1D vessels domains. Hence, the discrete pressure p_i^n, in the primal junction cell C_i, is evolved according to an implicit finite volume scheme discretizing the moving boundary equation (2.3.3). Accordingly, we have,

$$M(p_i^{n+1}) = M(p_i^n) - \Delta t \sum_{j\in S_i} \sigma_{ij} q_j^{n+1}, \tag{2.3.14}$$

where $M(p)$ is a non-linear function depending on the pressure, p_i, which represents the fluid volume associated to the primal cell C_i. It is computed using a simple sum of the half-volumes given by the tube laws of all vessels joining at the junction,

$$M(p_i) = \frac{1}{2} \sum_{j\in S_i} \Delta x_j A_j(p_i), \tag{2.3.15}$$

with $A_j(p_i)$ the area of the $j-$th vessel, V_j, at the boundary with the 3D junction, $\frac{1}{2}\Delta x_j$ the distance between that boundary and the center of the junction. Moreover, q_j denotes the flow approximated at the dual 3D-1D cell related to the vessel V_j, that can be computed according to (2.2.26), and σ_{ij} corresponds to the sign function

$$\sigma_{ij} = \frac{r(j) - 2i + l(j)}{r(j) - l(j)}, \tag{2.3.16}$$

which ensures that the inflow/outflow momentum to the junction has the right sign according to the convention employed for the 1D vessels. Note that (2.3.14) reduces to (2.2.25) if only two neighbouring vessels are considered, consistently with the fact that the 1D model is derived from the incompressible Navier-Stokes equations.

Overall methodology In what follows, we summarize the main stages of the proposed semi-implicit method for a network of vessels when using the proposed 3D junction approach:

- Convective stage. The first intermediate velocity, q^*, at the fully 1D dual vessel cells is computed explicitly using (2.2.9) with the Ducros flux function (2.2.16). In case a dual cell D_j is a 3D-1D dual cell, i.e. if it is the first/last cell of the 1D vessel after/before a junction, the flux on the boundary embedded in the 3D primal cell is computed using (2.3.5), with (2.3.12) and (2.3.13), and then substituted into (2.2.9) to get q_j^*. We note that, since the other boundary of the 3D-1D dual cell belongs to a 1D domain, it is simply computed using the 1D numerical flux function (2.2.16).

- Diffusive stage. If viscoelastic vessels are considered then, system (2.2.22) is solved using a conjugate gradient algorithm to get q^{**}. Otherwise, i.e. if a pure elastic vessel is assumed, we set $q^{**} = q^*$.

- Pressure stage. The weakly non-linear pressure system, defined by using (2.2.27) for the 1D primal vessel cells and (2.3.14) with (2.2.26) for the junction primal cells, is solved employing the nested Newton algorithm.

- Correction stage. The new pressure, p^{n+1}, is substituted in (2.2.4b) to correct the intermediate values q^{**} thus obtaining q^{n+1}.

2.3.2 0D junction

In contrast to the three-dimensional approach, a common choice in the literature for treating junctions is the use of a 0D model in which junctions have no spatial representation, i.e., they are treated as points, [83]. In this case, to handle the arterial tree, a domain splitting technique is adopted and suitable boundary conditions at the junction points of the network are applied. In what follows we briefly recall this approach.

Suppose we have $n = n_{\text{in}} + n_{\text{out}}$ vessels involved in a junction, where n_{in} and n_{out} are number of the ingoing and outgoing vessels, respectively. Since the one-dimensional model does not include information of vessel orientation, we are in fact considering that all vessels share the same direction. Therefore, this approach clearly does not account for the fact that vessels converging to a junction might do so with different angles. As a consequence, the complex three-dimensional configuration is represented by n one-dimensional parallel vessels and the fully multidimensional problem is replaced by n one-dimensional problems connected through algebraic relations. These algebraic relations are based on strong physical assumptions and provide the junction matching conditions to be imposed at the interface of the vessels involved in the junction. In particular, the continuity of mass is enforced across the junction leading to

$$\sum_{i=1}^{n_{\text{in}}} q_{i,BC} - \sum_{j=1}^{n_{\text{out}}} q_{j,BC} = 0. \tag{2.3.17}$$

Similarly, the continuity of total pressure is imposed, i.e., taken a j-vessel involved in the

junction, we get

$$p(A_{j,BC}) + 0.5\rho\left(\frac{q_{j,BC}}{A_{j,BC}}\right)^2 = p(A_{i,BC}) + 0.5\rho\left(\frac{q_{i,BC}}{A_{i,BC}}\right)^2, \qquad i = 1,\dots,n, \;\; i \neq j. \tag{2.3.18}$$

In addition, to close the system and find the $2n$ unknowns $(A_{j,BC}, q_{j,BC})$, $j = 1,\dots,n$, the constancy of generalized Riemann invariants assuming external rarefaction waves at each boundary is enforced, providing the remaining n relations that read

$$\int_{A_{i,N_d-1}}^{A_{i,BC}} \frac{c(\tau)}{\tau} d\tau + \frac{q_{i,BC}}{A_{i,BC}} - \frac{q_{i,N_d-1}}{A_{i,N_d-1}} = 0, \qquad i = 1,\dots,n_{\text{in}}, \tag{2.3.19}$$

$$\int_{A_{j,BC}}^{A_{j,2}} \frac{c(\tau)}{\tau} d\tau + \frac{q_{j,BC}}{A_{j,BC}} - \frac{q_{j,2}}{A_{j,2}} = 0, \qquad j = 1,\dots,n_{\text{out}}, \tag{2.3.20}$$

where $c(A)$ is the sound speed function given by $c(A) = \sqrt{\frac{A}{\rho}\frac{\partial p}{\partial A}}$. Note that the use of Riemann invariants (2.3.20) assumes subcritical flow. The $2n$ equations given by (2.3.17), (2.3.18) and (2.3.20) define a non-linear system of $2n$ algebraic equations which allow to determine the values of $(A_{j,BC}, q_{j,BC})$, $j = 1,\dots,n$, at the junction. Indeed, the resulting non-linear system is solved exploiting an iterative Newton method. Then, the obtained values are used to impose Dirichlet boundary conditions at the boundary of the cells involved in the junction. In particular, $q_{j,BC}$ is imposed in the diffusive and convective stages as a strong Dirichlet boundary condition, while $A_{j,BC}$ is used to recover $p_{j,BC}$ and thus impose this value in the pressure subsystem. In this way, each cell adjoining a junction is treated as a boundary cell and the implicit subsystems for the different vessels could be solved independently.

2.4 Numerical results

This section aims at assessing the proposed methodology and it is organized in two main subsections. In the first one, Section 2.4.1, the proposed 1D semi-implicit methodology is validated with the aid of several classical benchmarks applied to single straight vessels. Next, in Section 2.4.2, we address several test cases for networks of vessels.

Unless stated otherwise, the international system of units (SI) is employed throughout all test cases, the blood density is set to $\rho = 1050$ and the fluid viscosity is assumed to be $\mu = 0$. Besides, the convective terms are solved employing the second order approach presented in Section 2.2.2, while the diffusive subsystem is discretized implicitly according to the BTCS scheme.

Note that when convective terms are neglected and diffusive terms are treated implicitly, the resulting semi-implicit scheme is unconditionally stable. Otherwise, the method has to obey a CFL stability condition based on the flow speed, u. Hence, when an implicit scheme is employed for the discretization of the diffusive subsystem, the time step has to obey only the mild stability condition

$$\max_{j\in\{1,\dots,N_d\}} \left(\frac{2|u^n_{j-\frac{1}{2}}|}{\Delta x_{j-\frac{1}{2}}}\right)\Delta t \leq \text{CFL}. \tag{2.4.1}$$

If the explicit FTCS approach is used for the discretization of the diffusive subsystem, then the time step is selected in order to satisfy the CFL condition

$$\max_{j\in\{1,\dots,N_d\}} \left(\frac{2|u^n_{j-\frac{1}{2}}|}{\Delta x_{j-\frac{1}{2}}} + \frac{2A^n_{j-\frac{1}{2}}\varphi_{j-\frac{1}{2}}}{\rho \Delta x^2_{j-\frac{1}{2}}} \right) \Delta t \leq \text{CFL}. \tag{2.4.2}$$

In the former expressions, CFL indicates the standard Courant number satisfying $0 < \text{CFL} \leq 1$ in case of a first order scheme or $0 < \text{CFL} \leq \frac{1}{2}$ if a second order scheme is used.

2.4.1 Single vessel test cases

To validate the semi-implicit methodology proposed to simulate the blood flow within a vessel, we first analyze its accuracy, thanks to two manufactured problems, and the well-balanced property of the scheme, then we study four Riemann problems, chosen to resemble possible physiological scenarios both for veins and arteries. Besides, the case of a travelling pulse in a viscoelastic vessel and the blood flow in the human common carotid artery and in the upper thoracic aorta are also presented.

Convergence studies

The first test cases to be posed are obtained by using the method of manufactured solutions and aim at assessing the accuracy of the proposed semi-implicit methodology. The first problem consists in a stationary test, while in the second one the cross-sectional area, $A(x,t)$, is described by a function varying in time and in space which is necessary to take into account the viscous terms arising in the tube law (2.1.45). For both test cases, we report the absolute errors computed at the final time step using the L^2 norm in space. More precisely, given a mesh M_i, the error in space for any variable Q is computed according to

$$E_{M_i}(Q) = ||Q_{\text{exact}} - Q_{M_i}||_{L_2(\Omega)}. \tag{2.4.3}$$

Meanwhile, the convergence rate between two consecutive increasingly refined meshes, M_1 and M_2 with characteristic lengths h_{M_1} and h_{M_2}, respectively, is obtained as

$$\mathcal{O}_{M_2/M_1}(Q) = \frac{\log(E_{M_1}(Q)/E_{M_2}(Q))}{\log(h_{M_2}/h_{M_1})}. \tag{2.4.4}$$

Stationary test To introduce a manufactured solution test, system (2.1.41) needs to be modified by adding an extra source term to guarantee that the sought solution is verified. Consequently, assuming an exact solution given by

$$A(x,t) = (\sin(2\pi x) + u_c)^{-1}, \tag{2.4.5a}$$

$$q(x,t) = 1, \tag{2.4.5b}$$

with $u_c = 4$, we perform a convergence study by solving a modification of (2.1.41) reading

$$\frac{\partial A}{\partial t} + \frac{\partial Au}{\partial x} = 0, \tag{2.4.6a}$$

$$\frac{\partial Au}{\partial t} + \frac{\partial \alpha Au^2}{\partial x} + \frac{A}{\rho}\frac{\partial p}{\partial x} = -K_R u + \hat{s}, \tag{2.4.6b}$$

where $\hat{s}$ contains non-zero terms resulting from replacing (2.4.5) in (2.1.41). Note that (2.4.5) satisfies (1.1.1a), so that no additional source terms are needed in the mass conservation equation. The convergence test is performed on a vessel of length $L = 1$ discretized using a set of increasingly refined meshes at the ends of which periodic boundary conditions are applied. The reference parameters are set as $\rho = 1050$, $p_e = 0$, $A_0 = 3.1416 \cdot 10^{-4}$, $K = 80$, $m = 0.5$, $n = 0$ and $\mu = 0$. Since the test is stationary, viscoelasticity does not play any role in this test. The final time for the simulation is $t = 0.1$ and the time step is fixed within each simulation. The L^2 absolute errors for the three variables of interest, A, q and p, are reported in Table 2.1 together with the empirical convergence orders of the proposed method in which the convective terms are discretized using the second order scheme. We can observe that the expected second order is achieved for all the quantities of interest.

	L^2 errors					Numerical convergence order			
Δt	$5.00{\cdot}10^{-3}$	$2.50{\cdot}10^{-3}$	$1.25{\cdot}10^{-3}$	$6.25{\cdot}10^{-4}$	$3.13{\cdot}10^{-4}$				
N_s	10	20	40	80	160				
A	$4.20{\cdot}10^{-3}$	$1.12{\cdot}10^{-3}$	$2.84{\cdot}10^{-4}$	$7.12{\cdot}10^{-5}$	$1.78{\cdot}10^{-5}$	1.90	1.98	2.00	2.00
q	$9.70{\cdot}10^{-3}$	$2.70{\cdot}10^{-3}$	$6.95{\cdot}10^{-4}$	$1.75{\cdot}10^{-4}$	$4.39{\cdot}10^{-5}$	1.84	1.96	1.99	2.00
p	$3.88{\cdot}10^{2}$	$1.06{\cdot}10^{2}$	$2.70{\cdot}10^{1}$	$6.76{\cdot}10^{0}$	$1.69{\cdot}10^{0}$	1.87	1.97	2.00	2.00

Table 2.1: Stationary manufactured solution test for an elastic vessel. Absolute errors in L^2 norm for A, q and p and corresponding empirical convergence rates for the new semi-implicit finite volume scheme. Δt defines the fixed time step for each grid and N_p is the number of primal cells in which the vessel has been subdivided.

Unsteady test The second manufactured test to be considered is a modification of the previous problem to account for the viscoelasticity of the vessel wall. In this case, we let the cross-sectional area change in time, so that the viscoelastic behaviour of the vessel wall is active. We consider the solution

$$A(x,t) = t\sin(2\pi x) + u_c, \tag{2.4.7a}$$

$$q(x) = \frac{\cos(2\pi x)}{2\pi}, \tag{2.4.7b}$$

with $u_c = 4$. As in the steady test, we perform a numerical convergence study by solving (2.4.6), where $\hat{s}$ contains the non-zero terms resulting from replacing (2.4.7) in (2.1.41). Note that, again, (2.4.7) satisfies (1.1.1a), so that no additional source terms are needed in the mass conservation equation. The convergence test is performed exploiting the same computational domain and the same reference parameters of the steady test except for the viscoelastic parameter that now takes the value $\Gamma = 1$. The numerical simulation is run until a final time of $t = 0.1$, when the errors for the three variables of interest, A, q and p, are computed. Table 2.2 reports the absolute errors in norm L^2 and the empirical convergence orders obtained for the proposed semi-implicit numerical scheme in which a second order discretization is used for the convective terms, while the diffusive terms are treated explicitly. We can observe that the expected convergence order is achieved for all variables.

	L^2 errors					Numerical convergence order			
Δt	$5.00{\cdot}10^{-3}$	$2.50{\cdot}10^{-3}$	$1.25{\cdot}10^{-3}$	$6.25{\cdot}10^{-4}$	$3.13{\cdot}10^{-4}$				
N_p	10	20	40	80	160				
A	$1.08{\cdot}10^{-3}$	$2.67{\cdot}10^{-4}$	$6.67{\cdot}10^{-5}$	$1.67{\cdot}10^{-5}$	$4.16{\cdot}10^{-6}$	2.01	2.00	2.00	2.00
q	$3.58{\cdot}10^{-3}$	$9.06{\cdot}10^{-4}$	$2.29{\cdot}10^{-4}$	$5.75{\cdot}10^{-5}$	$1.44{\cdot}10^{-5}$	1.98	1.99	1.99	2.00
p	$1.99{\cdot}10^{1}$	$4.94{\cdot}10^{0}$	$1.23{\cdot}10^{0}$	$3.08{\cdot}10^{-1}$	$7.70{\cdot}10^{-2}$	2.01	2.00	2.00	2.00

Table 2.2: Unsteady manufactured solution test for a viscoelastic vessel. Absolute errors in L^2 norm for A, q and p and empirical convergence rates for the new semi-implicit scheme. Δt defines the fixed time step and N_p is the number of primal cells in which the vessel has been subdivided.

Numerical verification of the well-balanced property

The C-property characterizes the capability of numerical schemes to exactly preserve stationary equilibrium solutions of the system. The numerical method proposed in this thesis is well balanced by construction, as demonstrated in Section 2.2. To check this property also numerically, we consider a stationary blood-at-rest solution on a computational domain $[0, L]$ discretized using a uniform mesh with $\Delta x = 0.005$. We define the initial flow $q(\mathbf{x}, 0) = 0$ and a cross-sectional area of the form

$$A(\mathbf{x}, 0) = \begin{cases} A_0(\mathbf{x}) + \epsilon & 0.4\,L \leq \mathbf{x} \leq 0.6\,L, \\ A_0(\mathbf{x}) & \text{otherwise.} \end{cases} \tag{2.4.8}$$

from which the initial pressure is computed according to (2.1.45) by setting $p_e = 1.0$, $K(x) = \frac{1}{A_0(x)}$, $m = 0.5$, $n = 0$ and $\Gamma = 1.0$. The reference cross-sectional area $A_0(\mathbf{x})$ descends linearly along the vessel from an inlet radius given by $r_{in} = 0.442$ to an outlet radius of $r_{out} = 0.339$. Homogeneous Dirichlet boundary conditions are imposed at both vessel boundaries. If no perturbation is defined, i.e. $\epsilon = 0$, the initial solution is perfectly preserved along time. Therefore, to check the C-property, we introduce a small perturbation of the order of machine precision on the initial cross-sectional area. In particular, we consider single, double and quadruple machine precision and define $\epsilon \sim \{10^{-6}, 10^{-12}, 10^{-24}\}$ in (2.4.8). The errors in L^2 norm computed at the final time $t = 2.481$ are reported in Table 2.3. The obtained results confirm the ability of the proposed scheme to preserve the fluid at rest solution up to machine precision.

Precision	Perturbation ϵ	$L^2(A)$	$L^2(q)$	$L^2(p)$
Single	10^{-6}	$1.1084179 \cdot 10^{-6}$	$3.6971045 \cdot 10^{-8}$	$1.6950896 \cdot 10^{-6}$
Double	10^{-12}	$4.4717764 \cdot 10^{-13}$	$3.4168353 \cdot 10^{-14}$	$6.7595882 \cdot 10^{-13}$
Quadruple	10^{-24}	$4.4721359 \cdot 10^{-25}$	$3.4173954 \cdot 10^{-26}$	$6.7601137 \cdot 10^{-25}$

Table 2.3: Well-balanced test. L^2 errors obtained for single, double and quadruple machine precision at time $t = 2.481$.

Riemann problems

We now compare the novel semi-implicit FV algorithm against the exact solution of four Riemann problems in a straight elastic vessel. The reference solutions are computed using the exact Riemann solver put forward in [218]. Meanwhile, the numerical solution is computed making use of the semi-implicit method in which the convective terms are discretized according to the second order approach. The tests are designed choosing parameters reported in applications regarding cardiovascular mathematics, [154, 218, 201]. In all cases the blood is assumed to have density $\rho = 1050$ and we consider a tube of length $L = 0.2$, except for the last Riemann problem in which the vessel has length $L = 0.5$. The mechanical properties and geometrical characteristics of each test are reported in Table 2.4, while the initial conditions are specified in Table 2.5. Besides the third case,

Test	K_{ref}	m	n	A_{ref}	p_{ref}
1	$2.0005{\cdot}10^4$	0.5	0	$3.14{\cdot}10^{-4}$	0
2	$9.999{\cdot}10^3$	10	-1.5	$2.9688{\cdot}10^{-5}$	66.66
3	$5.8725{\cdot}10^4$	0.5	0	$3.1353{\cdot}10^{-4}$	0
4	$9.999{\cdot}10^3$	10	-1.5	$2.9688{\cdot}10^{-5}$	66.66

Table 2.4: Parameters used for the Riemann problems: K_{ref} reference stiffness; m and n exponents for the elastic part in the tube law; reference cross-sectional area A_{ref}; reference external pressure p_{ref}. Values are reported in international units.

Test	A_L	$A_{0,L}$	u_L	K_L	pe_L	A_R	$A_{0,R}$	u_R	K_R	$p_{e,R}$
1	$1.6A_{ref}$	A_{ref}	1	K_{ref}	p_{ref}	$1.05A_{ref}$	A_{ref}	2	K_{ref}	p_{ref}
2	$3.1{\cdot}10^{-5}$	A_{ref}	-0.2	K_{ref}	p_{ref}	$3.1{\cdot}10^{-5}$	A_{ref}	2	K_{ref}	p_{ref}
3	$1.6A_{ref}$	$0.5A_{ref}$	1	K_{ref}	3999.66	$1.05A_{ref}$	A_{ref}	0	$10K_{ref}$	0
4	$1.6A_{ref}$	A_{ref}	0	K_{ref}	p_{ref}	$0.05A_{ref}$	A_{ref}	0	K_{ref}	p_{ref}

Table 2.5: Left and right initial conditions for the Riemann problems. The values are reported in international units.

the remaining Riemann problems have constant mechanical and geometrical parameters and present an initial jump placed at the midpoint of the vessel. Figures 2.6-2.9 report the numerical profile of the non-dimensional cross-sectional area, the mass flow and the pressure waveform obtained along the domain as well as the corresponding exact solution. In what follows we further study each test case.

Riemann problem 1. The first test presents a left rarefaction and a right shock in an artery. The numerical results at time $t = 0.013$ obtained with the proposed scheme using a grid composed of 800 primal cells and a fixed time step of $\Delta t = 10^{-4}$ are reported in Figure 2.6. We can observe a good agreement between the numerical results and the exact solution.

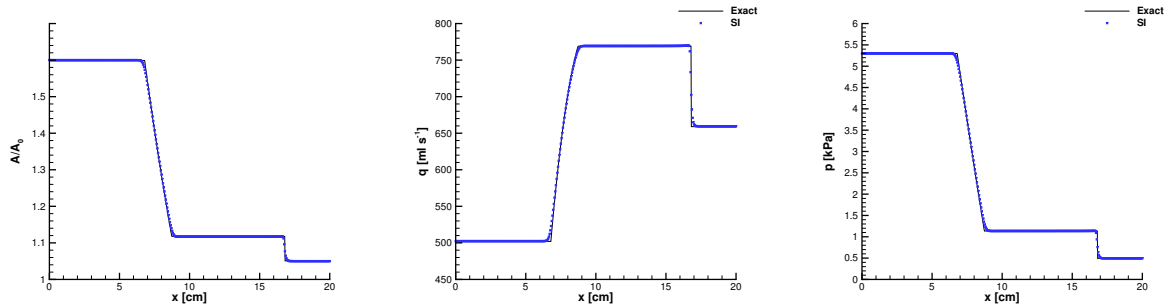

Figure 2.6: Riemann problem 1. Non-dimensional cross-sectional area, mass flow and pressure waveform obtained for RP 1 using the new semi-implicit FV scheme (blue squares) and exact solution (black solid line) at time $t = 0.013$.

Riemann problem 2. The second test corresponds to two rarefaction waves travelling in opposite directions along a vein. The simulation is run until time $t = 7 \cdot 10^{-3}$ with a fixed time step of $\Delta t = 10^{-4}$ on a grid composed of 1600 primal cells. The numerical results together with the exact solution are reported in Figure 2.7. Again, we observe a good agreement between the computational results obtained with the new semi-implicit scheme and the exact solution.

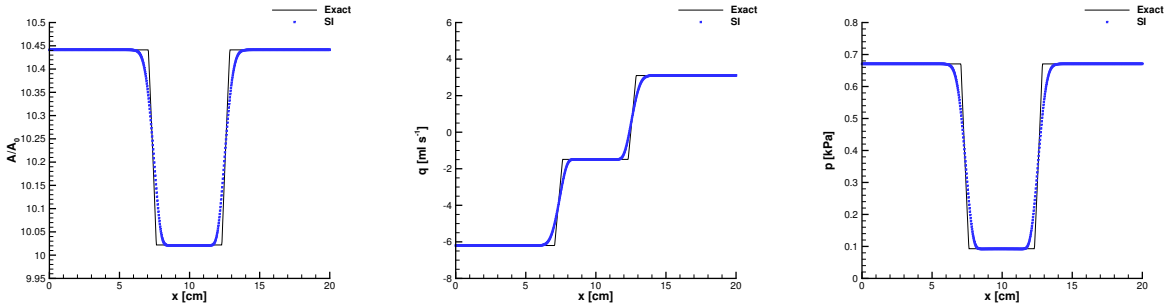

Figure 2.7: Riemann problem 2. Non-dimensional cross-sectional area, mass flow and pressure waveform obtained for RP 2 using the new semi-implicit FV scheme (blue squares) and exact solution (black solid line) at time $t = 7 \cdot 10^{-3}$.

Riemann problem 3. The third test has been introduced in [154, 201] and describes an idealized problem of a systolic pressure and flow peak arriving to a certain region of the thoracic aorta. In addition, the problem presents variations in the geometrical and mechanical vessel parameters across the initial discontinuity which is localized in a third of the vessel length. In particular, the left side of the aorta, that is the part already reached by the systolic peak, has been compressed, while the vessel wall of the right portion of the aorta is 10 times stiffer than the portion to the left of the initial discontinuity. Figure 2.8 shows the numerical results, obtained at time $t = 6 \cdot 10^{-3}$ on a grid characterized by a spatial step of $\Delta x = 1.25 \cdot 10^{-4}$ with a fixed time step given by $\Delta t = 2.5 \cdot 10^{-5}$, as well as the known exact solution. We can observe a good agreement between the solutions for the two shocks moving in opposite directions and the contact discontinuity centered at $x = 0.06$.

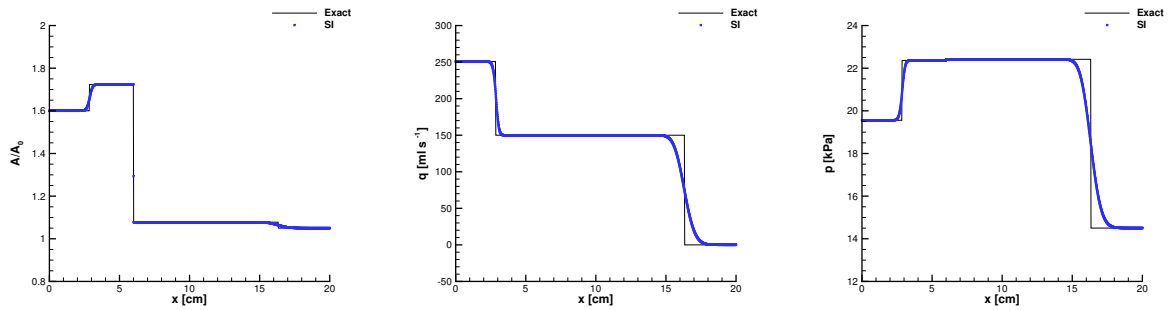

Figure 2.8: Riemann problem 3. Non-dimensional cross-sectional area, mass flow and pressure waveform obtained for RP 3 using the new semi-implicit FV scheme (blue squares) and exact solution (black solid line) at time $t = 6 \cdot 10^{-3}$.

Riemann problem 4. The venous system has particular features, among which it is important to highlight the possibility to collapse if certain conditions are satisfied, [218, 202]. When the pressure is raised the vessel wall is extended, while if the pressure decreases the system collapses. Hence, the vein section results very deformable in a highly non-linear way representing a challenge from the mathematical modeling point of view. This last Riemann problem aims at assessing precisely this case reporting an almost complete vein collapse. The numerical results obtained at time $t = 5.1 \cdot 10^{-3}$ on a primal grid made of 500 elements with $\Delta t = 10^{-5}$ are reported in Figure 2.9. A good agreement is observed with the reference solution even if, in this case, a spurious small wave is present left to the shock.

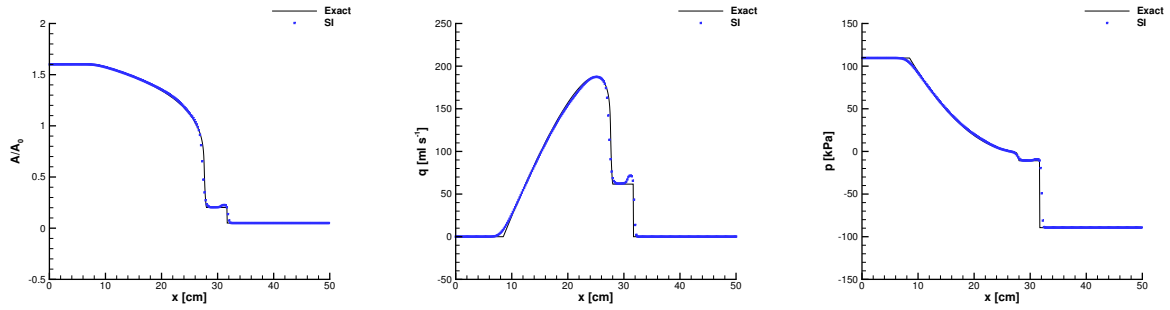

Figure 2.9: Riemann problem 4. Non-dimensional cross-sectional area, mass flow and pressure waveform obtained for RP 4 using the new semi-implicit FV scheme (blue squares) and exact solution (black solid line) at time $t = 5 \cdot 10^{-3}$.

Pulse flow in a viscoelastic vessel

In this test, we consider a stationary state along a vessel perturbed by an incoming Gaussian wave. The computational domain of length 0.4 is composed of 800 primal control volumes. The model parameters are set as $\rho = 1050$, $p_e = 1.0675 \cdot 10^4$, $A_0 = 3.1416 \cdot 10^{-4}$, $K = 80$, $m = 0.5$, $n = 0$, $\mu = 0$, $\Gamma = 1$. As initial condition blood at rest is imposed together with a constant pressure equal to the external pressure, p_e. The stationary state

is then perturbed prescribing the following flow at the left boundary:

$$q(t) = \hat{q} \exp\left(-10000(t - 0.025)^2\right), \tag{2.4.9}$$

where $\hat{q} = 10^{-4}$. The simulation is run with fixed time step $\Delta t = 6.25 \cdot 10^{-4}$ up to a final time of $t = 0.075$. To analyze the importance of the increase of accuracy due to the use of the θ-method, the problem is solved twice, first using a backward Euler scheme by setting $\theta = 1$, and then imposing $\theta = 0.6$. The resulting axial waveforms of pressure and flow along the vessel obtained at the final time are illustrated in Figure 2.10. To make a qualitative comparison with a reference solution, we also depict the numerical results on the same computational grid obtained using the explicit method described in Appendix A. The explicit scheme employed discretizes the governing equation according to a FORCE method combined with the Muscl-Hancock scheme (FORCE-MH) to achieve second order of accuracy [215]. In Figure 2.10, we can observe that both methods are in

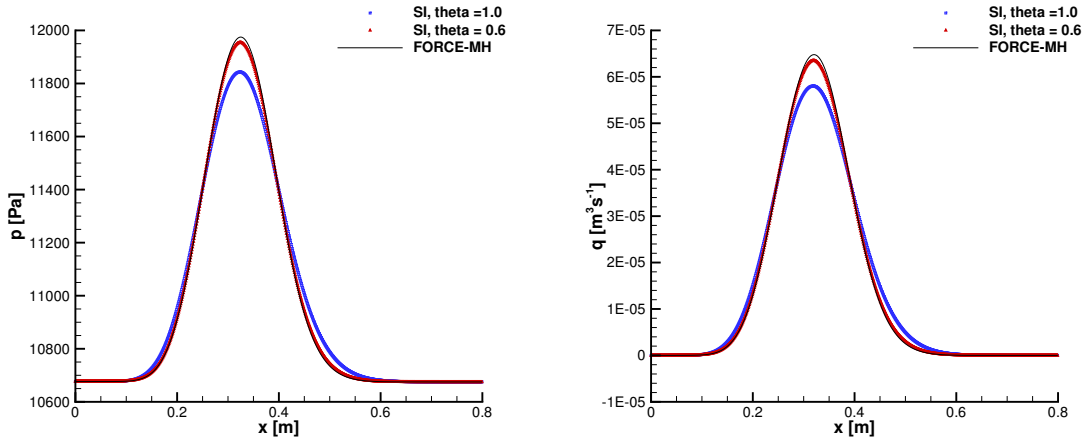

Figure 2.10: Pulse flow in the viscoelastic vessel. Comparison of the pressure and mass flow obtained for the pulse flow in the viscoelastic vessel using the new semi-implicit FV scheme with $\theta = 1$ (blue squares) and $\theta = 0.6$ (red triangles) and a reference solution obtained an explicit FORCE-MH scheme (black solid line).

good agreement. We moreover observe that the use of the θ-method is crucial to gain in accuracy and to deliver a less dissipative solution within the semi-implicit methodology, avoiding the need of increasing the resolution of the spatial grid. Besides, in Table 2.6 we also analyze the speed-up of the semi-implicit hybrid scheme with respect to the fully explicit method. The computational cost of the simulations is reduced by more than a half when employing the semi-implicit approach.

Benchmarks of physiological tests

The following two tests simulate blood flow in the human common carotid artery and in the upper thoracic aorta. The tests were proposed in [35, 234]. In both cases the artery is modeled as a single vessel with uniform wall properties. As inflow boundary conditions an in-vivo signal $q_{in}(t)$ taken from [234] is prescribed, while at the outlet the vessel is coupled to a three-element lumped parameter model to simulate the system circulation distal to

	Semi-implicit scheme	Explicit scheme
CPU time	61.035	143.625

Table 2.6: Pulse flow in the viscoelastic vessel. CPU time (s) employed to run the simulation up to time 0.075s using the novel semi-implicit scheme with $\theta = 0.6$ and the explicit FORCE-MH approach. Both simulations has been carried out in serial on a computer which accounts for Intel® Core i9-10980XE CPU processors at 3.0GHz.

the branch taken into account. For each test case, we provide a graphical comparison of the solution obtained with the novel semi-implicit FV scheme with a 3D reference solution of the Navier-Stokes provided in [234] and a set of 1D numerical solutions reported in [35]. The three-dimensional solution in [234] is computed on an ideal three-dimensional domain with compatible geometrical and mechanical properties to the 1D simulations. When comparing the obtained results, it is important to recall that the 1D model discretized using the novel semi-implicit scheme is a simplification of the fully 3D model, therefore some discrepancies between the solutions for both models are expected. The central goal of a 1D model is to capture the main features of the flow greatly reducing the cost of solving a more accurate 3D model. The 1D plots are also supported by tabulated calculations of the relative errors of pressure and flow computed with respect to the 3D solution and, for the sake of comparison, also the errors obtained with other six different methods described in [35] are included. For further details about the time step, the characteristic spatial discretisation, the CFL number and specific numerical approach of each reference solution, we refer to [35].

The obtained pressure and volumetric flow over a single cardiac cycle are compared between the one-dimensional and three-dimensional models by using the following relative error metrics:

$$E_p^{\mathrm{RMS}} = \sqrt{\frac{1}{n}\sum_{i=1}^{n}\left(\frac{p_i - \mathcal{P}_i}{\mathcal{P}_i}\right)^2}, \quad E_q^{\mathrm{RMS}} = \sqrt{\frac{1}{n}\sum_{i=1}^{n}\left(\frac{q_i - \mathcal{Q}_i}{\max_j(\mathcal{Q}_j)}\right)^2}, \tag{2.4.10}$$

$$E_p^{\mathrm{MAX}} = \max_i\left|\frac{p_i - \mathcal{P}_i}{\mathcal{P}_i}\right|, \quad E_q^{\mathrm{MAX}} = \max_i\left|\frac{q_i - \mathcal{Q}_i}{\max_j(\mathcal{Q}_j)}\right|, \tag{2.4.11}$$

$$E_p^{\mathrm{SYS}} = \frac{\max_i(p_i) - \max_i(\mathcal{P}_i)}{\max_i(\mathcal{P}_i)}, \quad E_q^{\mathrm{SYS}} = \frac{\max_i(q_i) - \max_i(\mathcal{Q}_i)}{\max_i(\mathcal{Q}_i)}, \tag{2.4.12}$$

$$E_p^{\mathrm{DIAS}} = \frac{\min_i(p_i) - \min_i(\mathcal{P}_i)}{\min_i(\mathcal{P}_i)}, \quad E_q^{\mathrm{DIAS}} = \frac{\min_i(q_i) - \min_i(\mathcal{Q}_i)}{\max_i(\mathcal{Q}_i)} \tag{2.4.13}$$

where $\mathcal{P}_i$ and $\mathcal{Q}_i$ are the cross-sectional averaged pressure and flow from the 3D reference solution at a given spatial location $\mathbf{x}_i$ and time instant. The number of time points n is determined by the 3D solution. E_p^{RMS} and E_q^{RMS} are the root mean square relative errors for pressure and flow, E_p^{MAX} and E_q^{MAX} are the maximum relative errors in pressure and flow, E_p^{SYS} and E_q^{SYS} are the errors in systolic pressure and flow and E_p^{DIAS} and E_q^{DIAS} are the errors in diastolic pressure and flow, respectively.

Common carotid artery. We start simulating the common carotid artery. The numerical results are obtained using the second order semi-implicit scheme characterized by a grid spacing of $\Delta x = 10^{-3}$ and evolved in time according to an adaptive time step computed at each iteration to satisfy the mild stability condition (2.4.1) with $CFL = 0.6$. Figure 2.11 shows the pressure, the flow, the luminal radius variations with time at the midpoint of the vessel *dr*, as well as *dp*, the pressure drop (difference between inlet and outlet pressures) obtained with the proposed semi-implicit FV scheme as well as with the second order explicit FORCE-MH method. These waveforms show a good match between the results obtained with the reference one-dimensional methods and are in agreement with the waveforms calculated by solving the corresponding three-dimensional problem with identical inflow and outflow boundary conditions. The relative errors determined with respect to the 3D solution over a single cardiac cycle once both numerical solutions have achieved a periodic behavior are presented in Table 2.7. Analogous error metrics to the flow rate are used for *dp* and *dr*. Besides, we also analyze the speed-up of the

	Semi-implicit	Explicit	DCG	LCG	FEM	FVM	McC	STM
E_p^{RMS}	0.28	0.31	0.20	0.24	0.23	0.28	0.24	0.24
E_q^{RMS}	0.32	0.34	0.39	0.26	0.28	0.29	0.30	0.29
E_{dr}^{RMS}	1.05	1.08	0.96	1.00	1.00	1.07	1.01	0.98
E_{dp}^{RMS}	4.35	4.34	4.42	4.35	4.27	4.21	4.47	4.47
E_p^{MAX}	0.65	0.75	0.34	0.52	0.5	0.66	0.52	0.53
E_q^{MAX}	1.22	1.22	1.23	1.02	1.12	1.07	1.2	1.13
E_{dr}^{MAX}	2.24	2.47	1.75	1.93	1.88	2.28	1.93	1.96
E_{dp}^{MAX}	15.82	16.19	16.69	16.17	15.88	15.6	16.58	16.9
E_p^{SYS}	-0.25	-0.24	-0.27	-0.27	-0.26	-0.29	-0.27	-0.26
E_q^{SYS}	-0.47	-0.46	-0.55	-0.46	-0.54	-0.58	-0.62	-0.55
E_{dr}^{SYS}	-1.59	-1.56	-1.65	-1.63	-1.61	-1.68	-1.63	-1.63
E_{dp}^{SYS}	-15.65	-15.84	-15.05	-15.37	-15.16	-14.83	-15.73	-15.76
E_p^{DIAS}	0.24	0.28	0.28	0.28	0.27	0.29	0.28	0.27
E_q^{DIAS}	0.28	0.24	0.25	0.22	0.26	0.24	0.23	0.27
E_{dr}^{DIAS}	0.02	0.10	0.08	0.11	0.08	0.12	0.09	0.08
E_{dp}^{DIAS}	5.21	5.05	4.99	4.76	5.03	4.91	4.45	4.85

Table 2.7: Common carotid artery. Relative errors (in per cent) respect to the reference 3D solution computed according to (2.4.10), (2.4.11), (2.4.12), (2.4.13). Both the semi-implicit method and the FORCE-MH scheme are applied in a mesh characterized by a uniform grid spacing of $\Delta x = 0.001$. The relative errors obtained with several numerical schemes and reported in [35] are also recalled for comparison: DCG: discontinuous Galerkin; LCG: locally conservative Galerkin; FEM: finite element method; FVM: finite volume method; McC: McCormack; STM: simplified trapezium rule method.

semi-implicit scheme with respect to the explicit method. The explicit scheme employed discretizes (2.1.41) according to the FORCE-MH scheme. Consequently, the CFL time

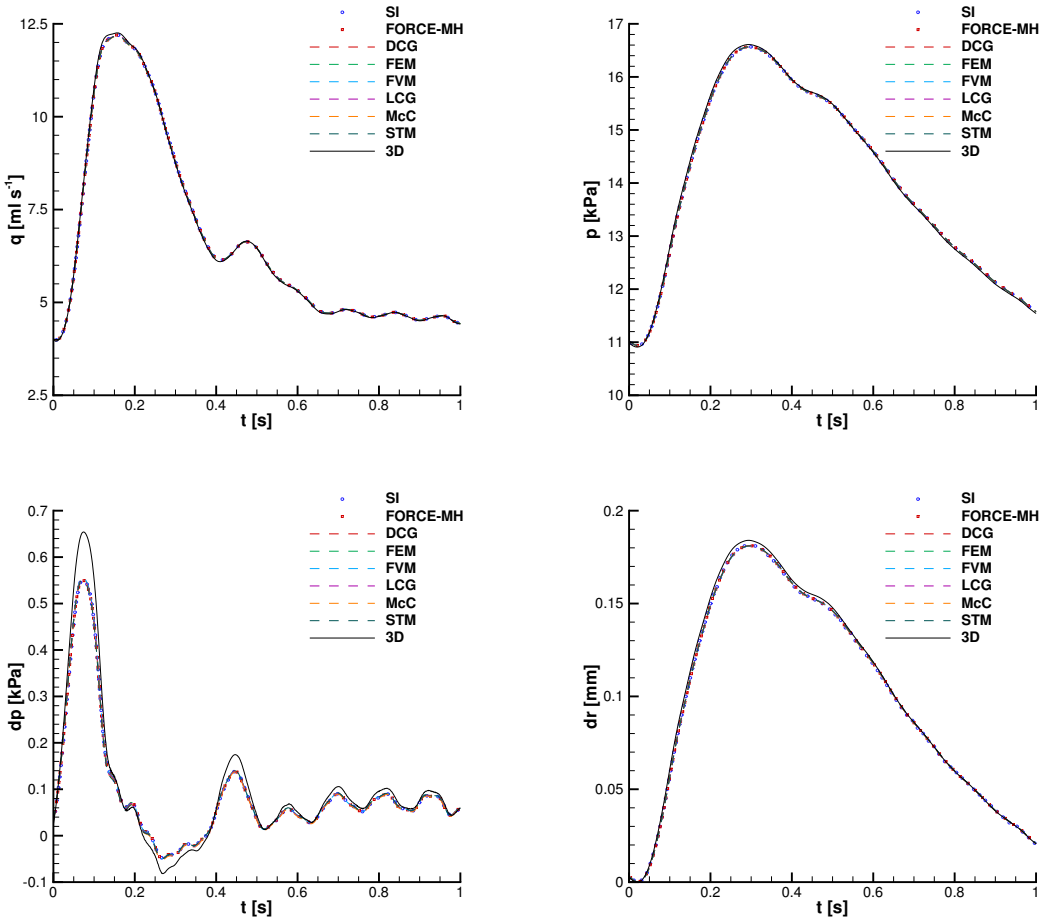

Figure 2.11: Common carotid artery. Top: flow and pressure variations with time at the midpoint of the vessel. Bottom: radius variation in time at the midpoint of the vessel and pressure drop variation in time. The numerical results obtained with the novel semi-implicit approach are reported using blue circles while the FORCE-MH scheme is represented using red squares. The solutions in [35] obtained employing a wide range of numerical approaches are also reported for the sake of comparison. 3D: three dimensional solution of the Navier-Stokes equations (black solid line), DCG: discontinuous Galerkin (red dashed line); LCG: locally conservative Galerkin (purple dashed line); FEM: finite element method (light green dashed line); FVM: finite volume method (light blue dashed line); McC: McCormack (orange dashed line); STM: simplified trapezium rule method (dark green dashed line).

step restriction, taken as CFL=0.5, depends on the eigenvalues of the full system. The computational cost of the simulations to compute 10 cardiac cycles reaching the final time of 11.055 is reported in Table 2.8 showing a speed-up factor of 4 between the semi-implicit and the explicit approaches.

Upper thoracic aorta. The second physiological benchmark addresses the haemodynamics in the thoracic aorta from the aortic root to the descending aorta. The simulation is performed exploiting the second order semi-implicit scheme with $\theta = 0.6$ as well as the

	Semi-implicit scheme	Explicit scheme
CPU time	30.8828	121.16

Table 2.8: Common carotid artery. CPU time (s) employed to run the simulation up to time 11.055s using the novel semi-implicit scheme and the fully explicit FORCE-MH method. Both simulations has been carried out in serial on a computer which accounts for Intel® Core i9-10980XE CPU processor at 3.0GHz.

second order explicit method. The computational domain is composed of uniform cells of length $2.5 \cdot 10^{-4}$, the solution is evolved in time according to a time step computed adaptively at each time iteration, in order to satisfy the corresponding CFL condition with $CFL = 0.6$. Figure 2.12 shows the pressure, the flow and the luminal radius variations with time at the midpoint of the vessel as well as the pressure drop obtained with both schemes. The obtained waveforms present a good agreement between the results obtained using the one-dimensional methods reported in [35] and with the waveforms calculated by solving the corresponding three-dimensional problem. The relative errors determined with respect to the 3D solution over a single cardiac cycle, computed once both numerical solutions have achieved a periodic behaviour, are reported in Table 2.9. Besides, we also analyze the speed-up of the semi-implicit scheme with respect to the explicit method. Again, the explicit scheme employed discretizes (2.1.41) according to the aforementioned second order FORCE-MH scheme. Consequently, its CFL time step restriction, with CFL=0.5, depends on the eigenvalues of the full system. On the other hand, the semi-implicit scheme must satisfy the mild stability condition (2.4.1) which depends only on the bulk velocity. The computational cost of both schemes when simulating 21 cardiac cycles, reaching a final time of 20.055, is reported in Table 2.10. In this test, the advantage of the semi-implicit scheme with respect to the explicit one in terms of computational cost is reduced if compared to that obtained in the previous test case, see Table 2.8. This is attributable to the fact that the velocity of the pressure waves is not as strongly dominant in the limitation of the time step, thus the CFL restriction results anyway demanding due to the major contribution of the bulk velocity.

2.4.2 Junctions

A first simple network composed of two vessels connected by a junction with a set of different angles between the vessels is proposed to validate the new simple 3D junction model, previously introduced, and to show its capability to properly capture multi-dimensional effects related to the basic geometry of the junction. Then, we study the case of Y junction connecting three arteries and the case of a complex junction linking five vessels in a three dimensional spatial configuration. Finally, as show cases for realistic networks, the blood flow in the aortic bifurcation as well as in a large network composed of 37 arteries is simulated.

Junction of two vessels

As a first test to validate the methodology proposed to address junctions, we consider a single junction connecting two vessels. In particular, we define two vessels of length

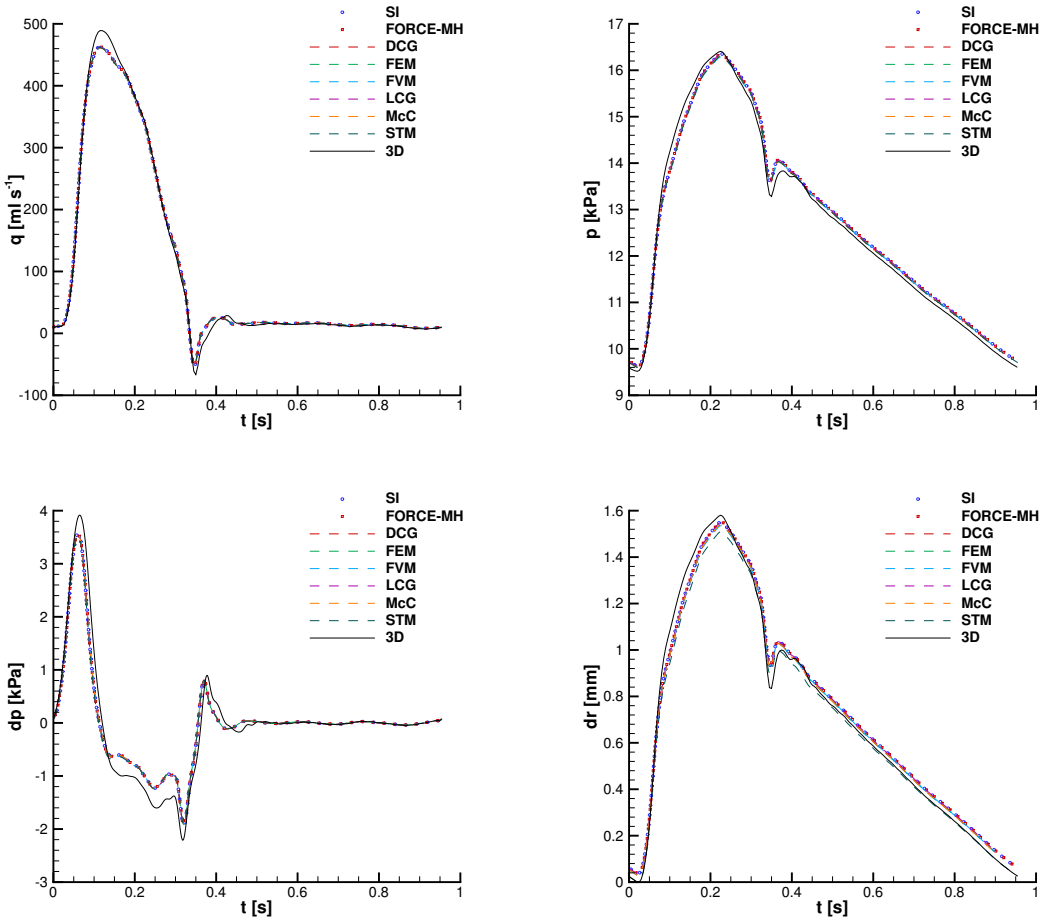

Figure 2.12: Upper thoracic aorta. Top: flow and pressure variations with time at the midpoint of the vessel. Bottom: radius variation in time at the midpoint of the vessel and pressure drop variation in time. The numerical results obtained with the novel semi-implicit approach are reported using blue circles while the FORCE-MH scheme is represented using red squares. The solutions in [35] obtained employing a wide range of numerical approaches are also reported for the sake of comparison. 3D: three dimensional solution of the Navier-Stokes equations (black solid line), DCG: discontinuous Galerkin (red dashed line); LCG: locally conservative Galerkin (purple dashed line); FEM: finite element method (light green dashed line); FVM: finite volume method (light blue dashed line); McC: MacCormack (orange dashed line); STM: simplified trapezium rule method (dark green dashed line).

$L = 1$ contained in the XY plane with junction at $\mathbf{x}_{\text{jun}} = (0, 0)$ and a set of angles $\omega \in \left\{0, \frac{\pi}{6}, \frac{\pi}{4}, \frac{\pi}{3}, \frac{\pi}{2}, \frac{3\pi}{4}, \pi\right\}$ between the vessels. As initial conditions we set an homogeneous velocity and a cross-sectional area jump in the first vessel leading to a Riemann problem of the form

$$\mathbf{u}(\mathbf{x}, 0) = \mathbf{0}, \qquad A(\mathbf{x}, 0) = \begin{cases} 1.6 & \mathbf{x} \leq \mathbf{x}_0, \\ 1.05 & \mathbf{x} > \mathbf{x}_0, \end{cases} \qquad p(\mathbf{x}, 0) = \begin{cases} 5299.5458 & \mathbf{x} \leq \mathbf{x}_0, \\ 494.025 & \mathbf{x} > \mathbf{x}_0, \end{cases} \tag{2.4.14}$$

	Semi-implicit	Explicit	DCG	LCG	FEM	FVM	McC	STM
E_p^{RMS}	1.10	1.31	1.09	1.21	1.09	1.14	1.08	1.12
E_q^{RMS}	1.79	1.75	2.55	2.19	2.23	2.17	2.22	2.28
E_{dr}^{RMS}	2.44	2.63	2.32	2.41	2.33	2.44	2.33	2.9
E_{dp}^{RMS}	6.58	6.47	7.7	7.23	7.23	7.14	7.23	7.52
E_p^{MAX}	3.10	3.02	3.54	3.55	3.26	3.18	3.27	3.3
E_q^{MAX}	5.60	5.68	9.13	7.2	7.04	7.07	7.04	7.4
E_{dr}^{MAX}	6.75	6.91	7.8	7.67	7.32	7.2	7.09	8.04
E_{dp}^{MAX}	24.16	24.26	31.83	29.31	29.15	29.13	29.31	31.19
E_p^{SYS}	-0.56	-0.31	-0.57	-0.32	-0.56	-0.71	-0.55	-0.59
E_q^{SYS}	-5.39	-5.36	-5.56	-5.36	-5.63	-5.29	-5.58	-5.56
E_{dr}^{SYS}	-2.40	-1.82	-2.54	-1.93	-2.50	-2.86	-2.49	6-4.48
E_{dp}^{SYS}	-9.06	-8.92	-8.92	-8.89	-9.29	-8.53	-9.04	-9.70
E_p^{DIAS}	0.57	1.11	0.85	1.12	0.88	0.99	0.87	0.85
E_q^{DIAS}	2.78	2.68	2.75	2.67	3.09	3.48	2.67	12.95
E_{dr}^{DIAS}	1.57	2.30	1.85	2.24	1.89	2.05	1.89	0
E_{dp}^{DIAS}	7.22	7.25	7.32	7.24	7.6	6.37	7.32	7.47

Table 2.9: Upper thoracic aorta. Relative errors (in per cent) respect to the reference 3D solution computed according to (2.4.10),(2.4.11),(2.4.12),(2.4.13) are reported for both semi-implicit method and the FORCE-MH scheme for a mesh characterized by a grid spacing of 0.001. Moreover, relative errors obtained with several numerical schemes and reported in [35] are also listed for the sake of comparison. DCG: discontinuous Galerkin; LCG: locally conservative Galerkin; FEM: finite element method; FVM: finite volume method; McC: MacCormack; STM: simplified trapezium rule method.

	Semi-implicit scheme	Explicit scheme
CPU time	3196.93	3700.30

Table 2.10: Upper thoracic aorta. CPU time (s) employed to run the simulation up to time 20.055s using the novel semi-implicit scheme and the fully explicit FORCE method. Both simulations has been carried out in serial on a computer which accounts for Intel® Core i9-10980XE CPU processor at 3.0GHz.

with $\mathbf{x}_0 = (-0.5, 0)$ the mean point of the first vessel and the pressure computed employing the tube law. Meanwhile, in the second vessel the initial condition is given as

$$\mathbf{u}(\mathbf{x}, 0) = \mathbf{0}, \qquad A(\mathbf{x}, 0) = 1.05, \qquad p(\mathbf{x}, 0) = 494.025. \tag{2.4.15}$$

The density and fluid viscosity are assumed to be $\rho = 1050$, $\mu = 0$. Moreover, the parameters of the tube law are set as $m = \frac{1}{2}$, $n = 0$ and $\Gamma = 0$, so a purely elastic vessel is considered. The simulation is run up to time $t = 0.2$ on a mesh with uniform grid spacing $\Delta x = 10^{-3}$ and a fixed time step of $\Delta t = 10^{-4}$ using the first order scheme.

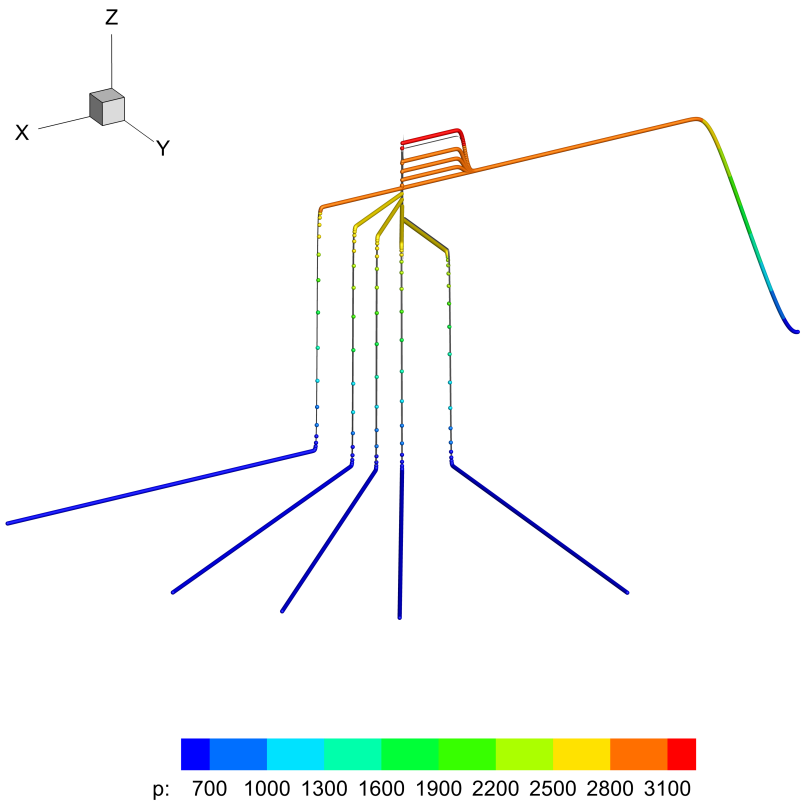

Figure 2.13: Junction of two vessels. Pressure obtained before and after the junction using the proposed 1D methodology with 3D junctions (pressure-coloured spheres). The reference solution (grey lines) is obtained with the explicit 2D code for barotropic Euler equations.

Figure 2.13 shows the 3D elevated pressure obtained at the end time for angles $\omega \in \left\{0, \frac{\pi}{6}, \frac{\pi}{4}, \frac{\pi}{3}, \frac{\pi}{2}\right\}$. We can clearly observe the influence of the angle in the flow propagation. Moreover, the 1D plot in Figure 2.14 depicts the pressure obtained for the different angles when the geometry is projected into a straight line, i.e., the x-axis corresponds to the distance of each grid point to the center of the junction.

To analyse the capability of the proposed approach to capture the influence of the angle, the results are compared against the solution of the barotropic Euler equations in 2D computed employing a classical second order accurate MUSCL-Hancock-type finite volume method based on the Barth and Jespersen limiter [12]. Also the numerical results obtained using the 0D junction model are reported. A very good agreement between the proposed 1D methodology with 3D junctions and the 2D simulation is observed for the 0 degrees junction where the shock wave passes through the junction matching the reference solution obtained by considering a unique vessel of length 2. A nice agreement is also observed with the 0D junction approach even if, in this case, a spurious small wave is propagated in the opposite direction to the shock.

On the other hand, for increasing non-zero angles, the pressure wave is increasingly reflected backwards in the first vessel so that the transmitted wave amplitude decreases. The reported results clearly demonstrate the importance of taking into account the 3D

geometry in the junction. We observe that the novel simplified 3D junction approach proposed in this thesis provides a nice agreement with respect to the 2D reference solution, properly capturing the reflected and transmitted waves, which cannot be done by the 0D junction model. To ease the comparison of the different approaches, Figure 2.15 reports the pressure values at the reflected and transmitted waves plateaus obtained for the complete set of angles. The greater discrepancy of the 3D junction that results with respect to the 2D solution for large angles is related to the more complex flow patterns present in the junction which may even generate recirculation zones which, to be captured, would require for a fully three-dimensional simulation of the flow within the junction.

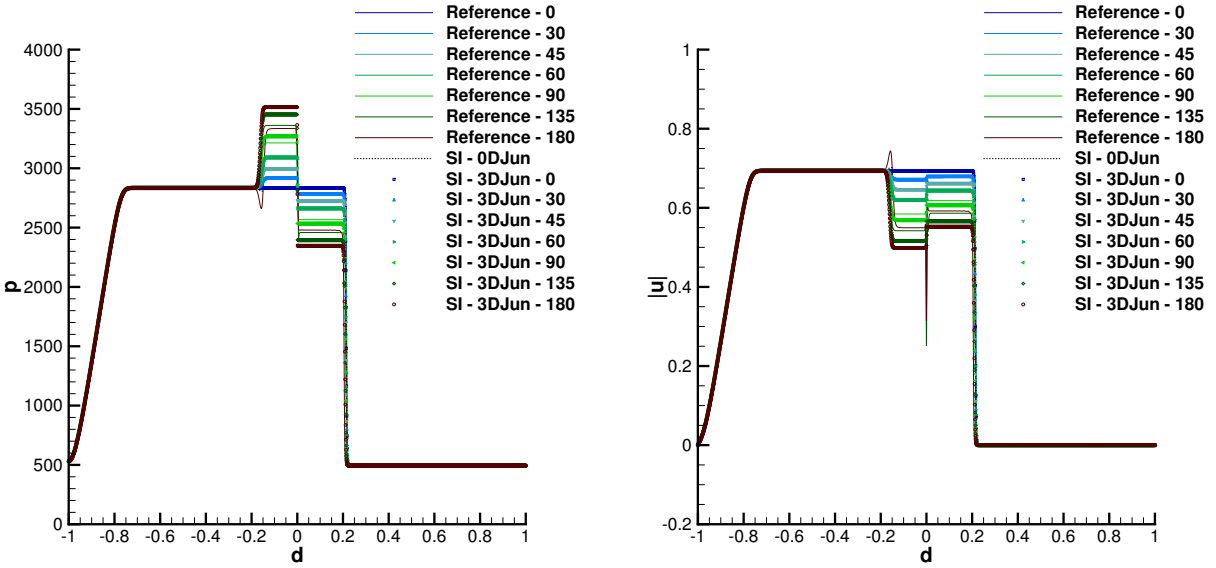

Figure 2.14: Junction of two vessels. Pressure (left) and velocity (right) cuts along the center line of the networks for angles $\omega \in \left\{0, \frac{\pi}{6}, \frac{\pi}{4}, \frac{\pi}{3}, \frac{\pi}{2}, \frac{3\pi}{4}, \pi\right\}$. The solution computed using the proposed 1D methodology with the 3D junction approach is depicted using symbols. The solution obtained using the 0D junction model is indicated via a pointed line. Continuous lines report the reference 2D solution of the Barotropic Euler equations.

Junction of three vessels

We extend the previous case to a network of three arteries. In particular, we consider three vessels of length 1 contained in the XY plane connected by a Y junction located at $\mathbf{x}_{\text{jun}} = (0, 0)$ and with bifurcation angle 90°. As previous case, the initial condition consists on a Riemann problem with homogeneous velocity and a cross-sectional area jump in the first vessel given by (2.4.14) with $\mathbf{x}_0 = (-0.5, 0)$ and in the remaining two vessels we set the main variables according to (2.4.15). The vessel parameters are also set as in the former test case.

We run two simulations employing the first order version of the novel semi-implicit FV scheme, one combined with the proposed 3D junction approach and the second one with the 0D junction model. In both cases the problem has been solved on a grid characterized by a uniform spatial length of $\Delta x = 10^{-3}$ and evolved in time with fixed time step of

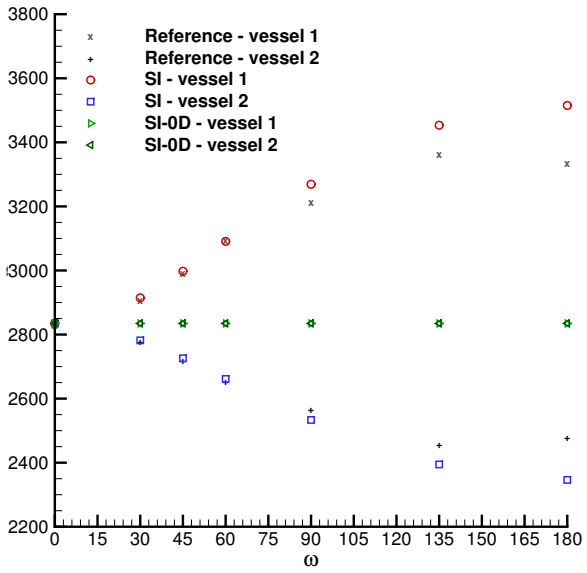

Figure 2.15: Junction of two vessels. Pressure value at the plateaux of the reflected (red circles) and transmitted (blue squares) waves in the neighbouring of the junction using the proposed 1D methodology with 3D junctions. The reference solution (reflected wave: grey cross; transmitted wave: black plus) has been obtained using an explicit FV 2D code for the barotropic Euler equations.

$\Delta t = 10^{-4}$ up to $t = 0.2$. The resulting 3D elevated pressure obtained at the end time for both methodologies is depicted in Figure 2.16.

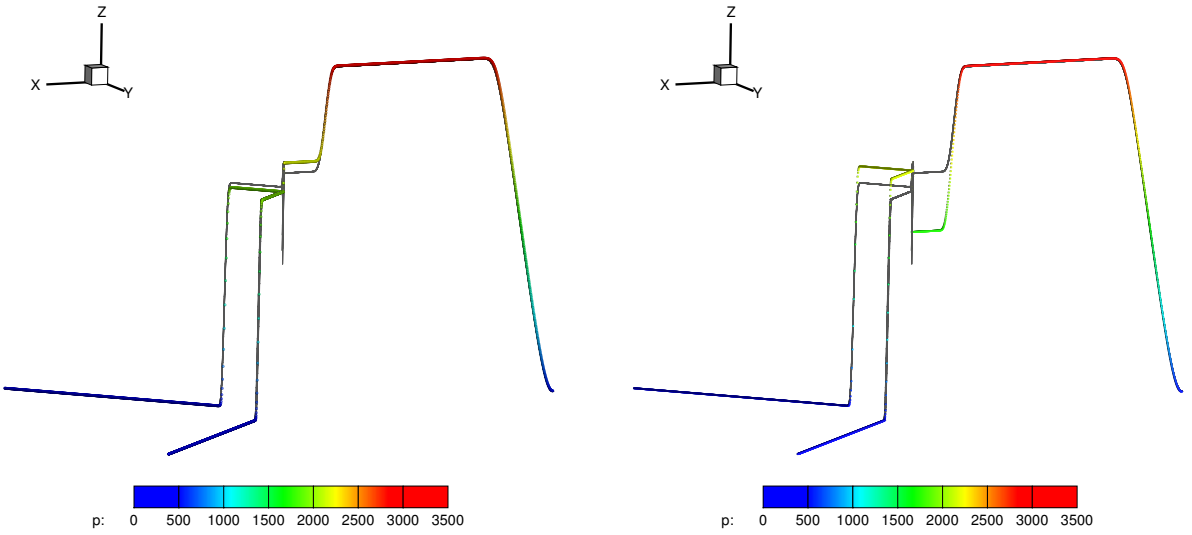

Figure 2.16: Junction of three vessels. Pressure obtained before and after the junction using the proposed 1D semi-implicit methodology with 3D junctions (left) and coupled to the 0D junction model (right). The grey surface reports the reference solution obtained solving the 2D barotropic Euler equations using an explicit FV method.

Besides, to appreciate better the discrepancies between the solutions provided by the two methodologies, in Figure 2.17, we report the resulting pressure and velocity after projecting the solution into a straight line given by the distance of each vessel point to the junction. For comparison, we also report a reference solution obtained with the explicit 2D FV method solving the barotropic Euler equations on a grid made of 31972 elements. We observe that the new simplified 3D junction approach is able to capture the reflecting wave going backwards in the ongoing vessel to the junction. It thus provides a closer solution to the reference 2D simulation than the 0D junction approach, that does not account for the geometry of the junction.

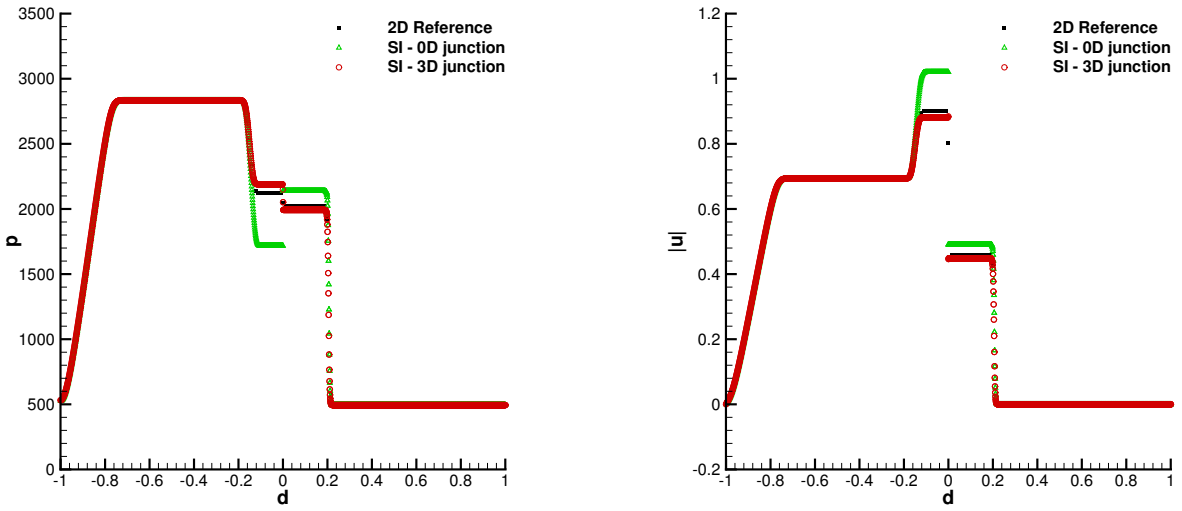

Figure 2.17: Junction of three vessels. Pressure (left) and velocity (right) cuts along the center line of the networks. The solution computed using the proposed 1D methodology with the 3D junction approach is depicted using red circles, while the solution obtained using the 0D junction model is indicated via green triangles. Black squares report the reference 2D solution of the Barotropic Euler equations.

Junction of five vessels

To show the behavior of the proposed 3D junction model when handling more complex configurations, we now address the case of a Y junction of 90° contained in the XY plane combined with a T junction, 180°, contained in the XZ plane. More precisely, the corresponding 3D geometry, shown in Figure 2.18, consists on a junction located at $\mathbf{x}_{\text{jun}} = (0, 0)$ which links a vessel of length 1, with centerline on the negative part of the x-axis, to the three-dimensional branching of four vessels, also of length 1. All vessels are assumed to be straight pure elastic arteries.

The test is built using the same parameters of the previous two tests. In particular, as initial condition, we consider the fluid at rest and a cross-sectional area jump in the vessel with centerline on the x-axis using the Riemann problem (2.4.14) with $\mathbf{x}_0 = (-0.5, 0)$ and the pressure computed employing the tube law. In all other vessels the initial condition is given by (2.4.15). The 1D computational domain is discretized using uniform cells of length $\Delta x = 10^{-3}$, the solution is then evolved in time according to a fixed time step

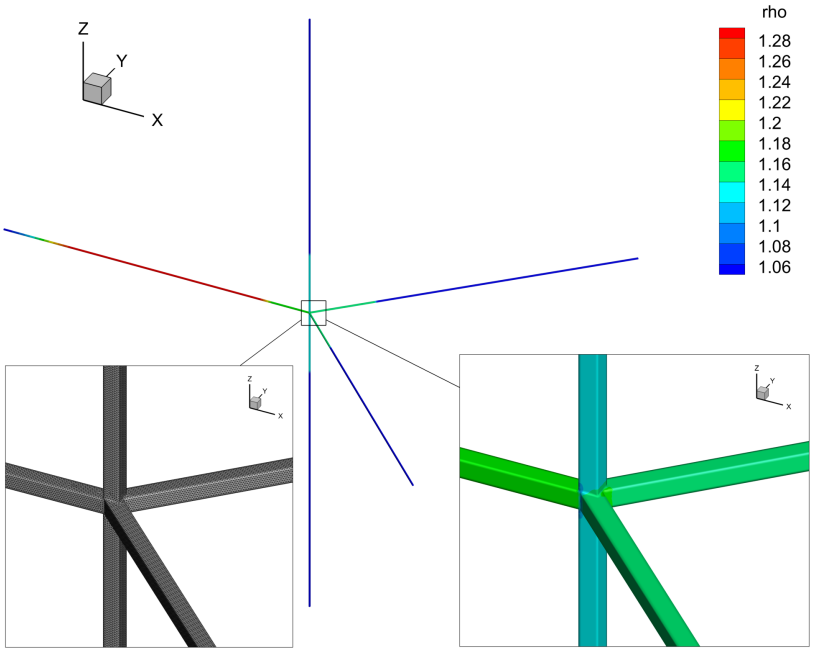

Figure 2.18: Sketch of the five vessels junction in 3D. The main plot and the right subfigure are coloured using the density contour lines at the end time of the simulation while de left subplot corresponds to a zoom in the junction and depicts the 3D grid employed for the reference 3D simulation.

given by $\Delta t = 10^{-4}$ up to $t = 0.2$. The problem has been solved twice, first employing the first order scheme combined with the proposed 3D junction approach and then coupling the semi-implicit FV scheme with the 0D junction. The resulting 3D elevated pressure obtained at the end time for both methodologies is illustrated in Figure 2.19. This 3D plot is constructed by looking at the xz plane as base plane and then the third axis component is given by the pressure value at each xz-point of the network. Besides, the 1D plot in Figure 2.20 depicts the pressure and the velocity obtained for both methodologies when the distance to the junction is projected into a straight line, i.e. the x-axis corresponds to the distance of each grid point to the center of the junction. We observe that the proposed 3D junction approach is able to capture the reflected pressure wave backward in the first vessel and, consequently, predicts a different decreasing transmitted wave amplitude among the vessels placed after the junction depending on the bifurcation angle. On the other hand, the 0D junction model, which is not informed of the junction geometry, provides a complete different solution. Indeed, not capturing the reflected wave, it estimates a higher transmitted wave amplitude equal for all four vessels. In both Figures 2.19-2.20, we also plot a reference solution obtained solving the 3D barotropic Euler equations using a finite volume scheme on the 3D domain depicted in Figure 2.18 discretized employing 2592291 tetrahedral cells. As for the previous junction test cases, the obtained results demonstrate the importance of incorporating, in the numerical approach, at least some basic information about the geometry of the junction.

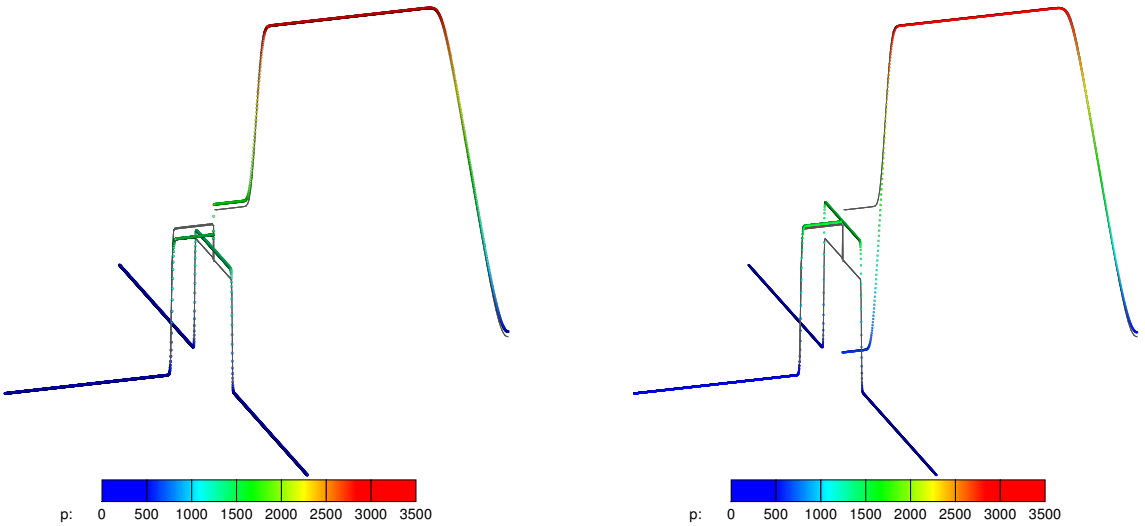

Figure 2.19: Junction of five vessels. Elevated pressure over the xz plane obtained using the proposed 1D methodology with a 3D junction (left) and with the 0D junction (right). The grey surface reports the reference solution obtained solving the 3D barotropic Euler equations using an explicit FV method.

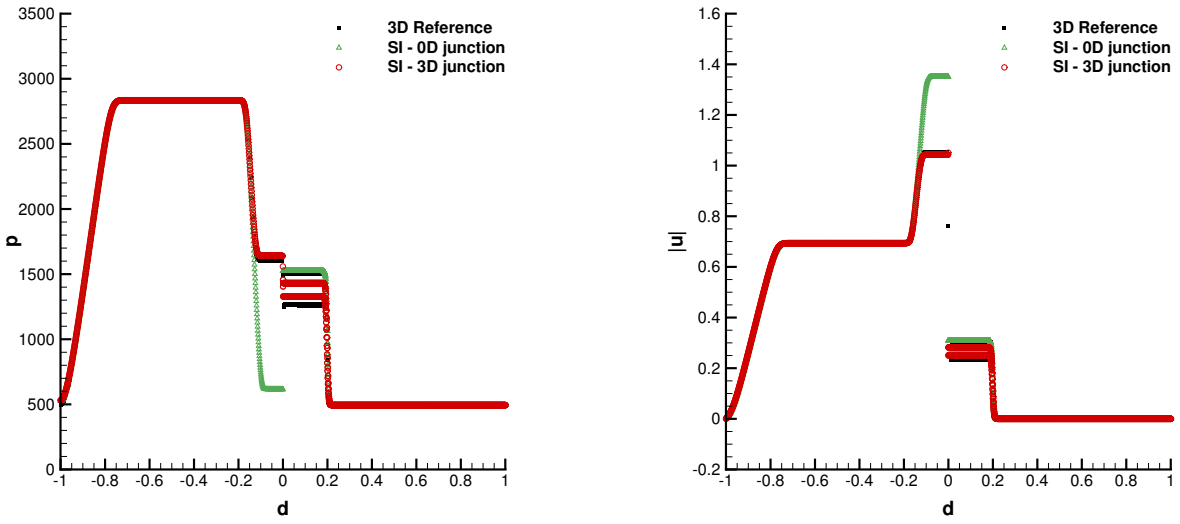

Figure 2.20: Junction of five vessels. Pressure (left) and velocity (right) along the center line of the networks. The solution computed using the proposed 1D methodology with the 3D junction approach is depicted using red circles while the one obtained using the 0D junction model is indicated via green triangles. Black squares report the reference 3D solution of the Barotropic Euler equations.

Aortic bifurcation

As last test case, we present a blood flow simulation in a physiological network of vessels. In particular, we simulate the aortic bifurcation containing a single parent vessel, representing the abdominal aorta, and two branches, representing the iliac arteries, placed

in a way to form a bifurcation angle of 47.9 degrees. The configuration of the problem is reported in [234, 35]. The blood density is set to $\rho = 1060$, the fluid viscosity is assumed to be $\mu = 0.004$. Moreover, the velocity profile order ξ in the friction force is set as $\xi = 9$. The values of parameters to define the state equations together with the vessel length are reported in Table 2.11 for each type of branch assembling the network. A time varying

Parameter	Aorta	Iliac
Length	0.086	0.085
External pressure, p_{ex}	$9.46 \cdot 10^3$	$9.46 \cdot 10^3$
Reference area, A_0	$2.3235 \cdot 10^{-4}$	$1.1310 \cdot 10^{-4}$
Stiffness parameter, K	$8.0 \cdot 10^4$	$1.12 \cdot 10^5$
m	0.5	0.5
n	0	0

Table 2.11: Aortic bifurcation. Model parameters taken from [35] used to define the network and the state equations of the branches taken into account in the aortic bifurcation network.

inflow function given by an in-vivo signal is prescribed at the inlet of the network, while the outlets are coupled to a three element lumped parameter model of the same type as that depicted in Figure 2.3 which embodies the peripheral vasculature. The two resistances are set to be $R_1 = 6.8123 \cdot 10^7$ and $R_2 = 3.1013 \cdot 10^9$, respectively, and are connected in series by a compliance given by $C = 3.6664 \cdot 10^{-10}$. Besides, a zero outflow pressure is assumed. The simulation is performed on a grid with uniform cell length $\Delta x = 5 \cdot 10^{-4}$ and it is advanced in time according to a time step given by (2.4.1) with CFL= 0.6.

The proposed semi-implicit method is employed to solve the aortic bifurcation using the first order Ducros-type flux function. Both the 3D and 0D junction approaches are considered for comparison. In addition, the test is also run using the second order explicit FORCE-MH methodology for the 1D model combined with the 0D junction approach. The obtained results are compared with the solutions reported in [35] that have been obtained with a set of different high order numerical methods. More precisely, Figure 2.21 displays the waveforms of the pressure, the flow rate and the variations of the luminal radius at three points of the network: the midpoint of the aorta, the end point of the aorta and the midpoint of either iliac artery. All these waveforms are similar among the different numerical schemes and compare well with the corresponding 3D model waveforms. The relative errors with respect to the 3D solution, shown in Tables 2.12-2.13, are calculated according to (2.4.10)-(2.4.13).

We observe that the new simplified three-dimensional junction model that accounts for the bifurcation angle provides a more efficient methodology with respect to the 0D junction approach. Indeed, the numerical solutions obtained for both methodologies on the same computational grid provide relative errors determined with respect to the 3D solution with no significant differences between the two schemes, as we can see in Table 2.12. However, by employing the semi-implicit scheme, we record a reduction in the computational cost, as reported in Table 2.14. Hence, avoiding an additional non linear system for the computation of the solution at the 0D junction at each time step shows to be an important factor for the speed-up of the method.

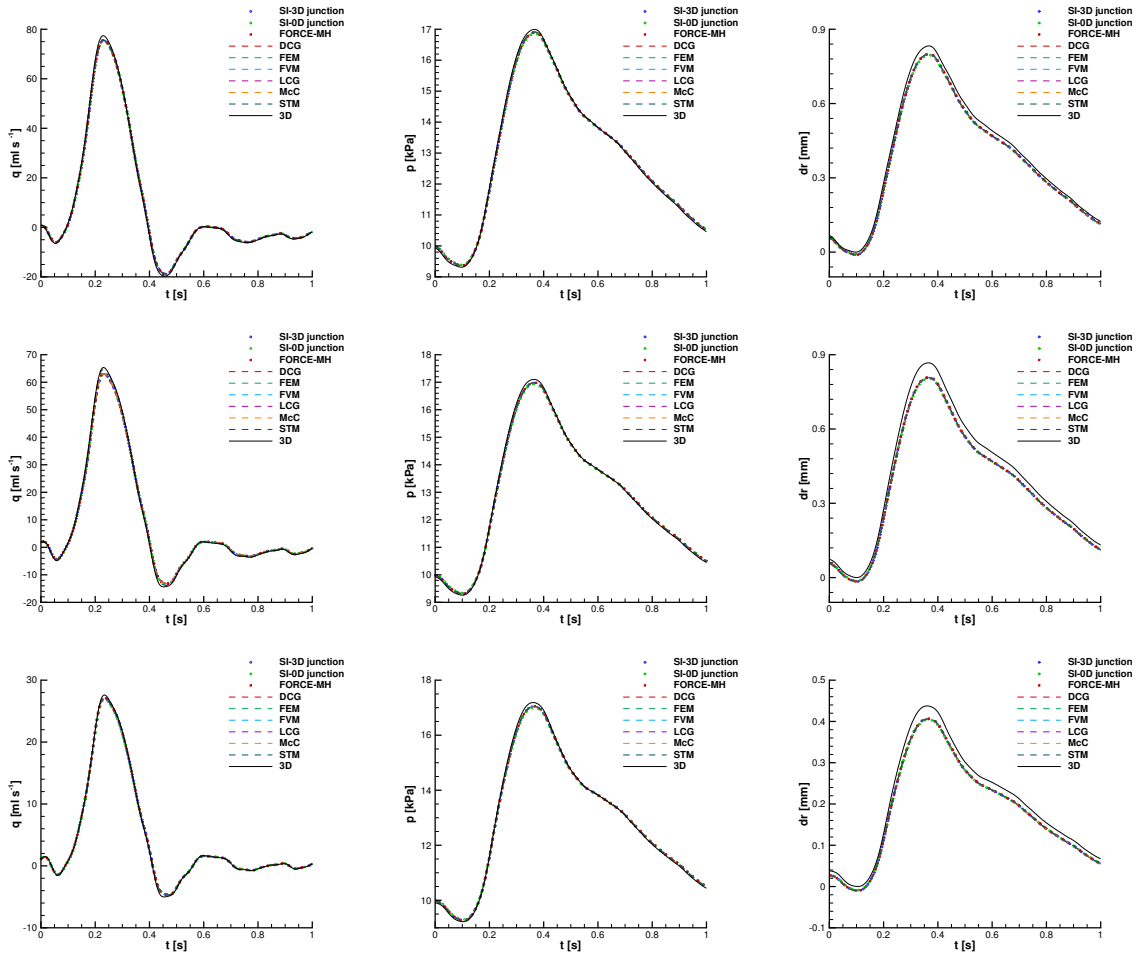

Figure 2.21: Aortic bifurcation. Flow, pressure and radius variation in time at three different points along the network: midpoint of the aorta (top), end point of the aorta (middle), midpoint of either iliac artery (bottom). The numerical results obtained with the novel semi-implicit approach with the 3D junction approach are reported using blue circles while those with the 0D approach are reported using green circles. The FORCE-MH scheme is represented using red squares. The solutions in [35] are denoted as: 3D: three dimensional solution of the Navier-Stokes equations (black solid line), DCG: discontinuous Galerkin (red dashed line); LCG: locally conservative Galerkin (purple dashed line); FEM: finite element method (light green dashed line); FVM: finite volume method (light blue dashed line); McC: MacCormack (orange dashed line); STM: simplified trapezium rule method (dark green dashed line).

37-artery network

In order to assess the performance of the proposed methodology on a large network of vessels, we consider the in-vitro model of the human arterial system first presented in [141, 3] and further studied in [35]. This arterial tree is composed of 37 silicone vessels representing the largest central systemic arteries. Following [35], at the inlet of the ascending aorta, the flow rate measured in-vitro is prescribed as a periodic inflow boundary condition. In the remaining boundaries, outflow boundary conditions are set

		Semi-implicit		Explicit	DCG	LCG	FEM	FVM	McC	STM
		3D jun.	0D jun.							
Mid aorta	E_p^{RMS}	0.45	0.59	0.45	0.37	0.39	0.37	0.4	0.38	0.38
	E_q^{RMS}	0.88	0.83	0.88	0.89	0.71	0.82	0.81	0.83	0.82
	E_{dr}^{RMS}	2.48	2.59	2.47	2.48	2.43	2.55	2.49	2.48	2.45
	E_p^{MAX}	0.78	0.99	0.81	0.61	0.67	0.65	0.68	0.66	0.66
	E_q^{MAX}	2.68	2.53	2.61	2.51	2.24	2.53	2.44	2.56	2.52
	E_{dr}^{MAX}	4.15	4.59	4.17	4.05	3.9	4.03	4.01	3.98	3.94
	E_p^{SYS}	-0.62	-0.79	-0.55	-0.53	-0.54	-0.51	-0.55	-0.53	-0.51
	E_q^{SYS}	-2.25	-2.26	-2.39	-2.47	-2.23	-2.52	-2.44	-2.55	-2.52
	E_{dr}^{SYS}	-4.07	-4.43	-3.90	-3.96	-3.86	-3.99	-4.00	-3.94	-3.93
	E_p^{DIAS}	0.51	0.77	0.45	0.5	0.51	0.47	0.53	0.49	0.48
	E_q^{DIAS}	1.08	1.01	1.12	1.16	1.03	1.16	1.16	1.17	1.17
	E_{dr}^{DIAS}	-1.29	-0.98	-1.36	-1.39	-1.37	-1.49	-1.35	-1.40	-1.41
End aorta	E_p^{RMS}	0.49	0.62	0.47	0.42	0.43	0.41	0.44	0.42	0.42
	E_q^{RMS}	1.15	1.03	1.11	1.2	1.13	1.12	1.08	1.12	0.46
	E_{dr}^{RMS}	4.06	4.15	4.05	4.07	4.02	4.14	4.08	4.08	4.05
	E_p^{MAX}	0.94	1.10	0.90	0.73	0.75	0.72	0.8	0.74	0.73
	E_q^{MAX}	3.59	3.26	3.41	3.55	3.54	3.53	3.28	3.53	1.48
	E_{dr}^{MAX}	7.01	7.41	6.95	6.87	6.76	6.89	6.95	6.85	6.98
	E_p^{SYS}	-0.76	-0.95	-0.71	-0.71	-0.70	-0.69	-0.72	-0.70	-0.69
	E_q^{SYS}	-3.41	-3.14	-3.35	-3.47	-3.53	-3.52	-3.26	-3.52	-1.08
	E_{dr}^{SYS}	-6.86	-7.27	-6.77	-6.84	-6.73	-6.87	-6.88	-6.83	-6.9
	E_p^{DIAS}	0.55	0.81	0.50	0.54	0.55	0.53	0.57	0.54	0.53
	E_q^{DIAS}	1.69	1.54	1.71	1.76	1.78	1.76	1.74	1.77	0.69
	E_{dr}^{DIAS}	-1.83	-1.54	-1.90	-1.93	-1.92	-2.02	-1.89	-1.94	-1.88

Table 2.12: Aortic bifurcation. Relative errors (in per cent) respect to the reference 3D solution computed according to (2.4.10)-(2.4.13) reported for the semi-implicit scheme using 3D and 0D junction and the explicit FORCE method for a mesh with $\Delta x = 5 \cdot 10^{-4}$ computed at the mid aorta and the end aorta. Relative errors reported in [35] are added comparison.

by coupling terminal vessels to single-resistance models, that characterize the peripheral resistance to flow. The computational network has been created in order to reproduce the topology of the simulated arteries reported in [141, 3] and the vessels are linearly tapered. Hence, each vessel is characterized by constant parameters along its length except for the cross-sectional reference area, $A_0(x)$, and the stiffness parameter, $K(x)$, which vary along the vessel. General parameters of this model are given in Table 2.15. For a complete set of parameters, we refer the reader to [141, 3] and to the supplementary information in [35].

The 1D governing equations are solved using the proposed semi-implicit methodology

		Semi-implicit		Explicit	DCG	LCG	FEM	FVM	McC	STM
		3D jun.	0D jun.							
Mid illiac	E_p^{RMS}	0.49	0.63	0.47	0.45	0.45	0.44	0.47	0.45	0.44
	E_q^{RMS}	0.59	0.76	0.53	0.92	0.66	0.65	0.68	0.67	0.66
	E_{dr}^{RMS}	4.26	4.34	4.25	4.29	4.3	4.35	4.31	4.31	4.26
	E_p^{MAX}	0.96	1.16	0.94	0.84	0.86	0.84	0.92	0.86	0.85
	E_q^{MAX}	2.16	2.35	2.01	2.33	2	2.01	1.8	2.01	2.02
	E_{dr}^{MAX}	7.43	7.85	7.36	7.29	7.36	7.37	7.48	7.35	7.34
	E_p^{SYS}	-0.86	-1.06	-0.82	-0.83	-0.83	-0.81	-0.85	-0.82	-0.81
	E_q^{SYS}	-1.80	-2.32	-1.63	-1.68	-1.84	-1.81	-1.58	-1.89	-1.79
	E_{dr}^{SYS}	-7.23	-7.65	-7.15	-7.25	-7.26	-7.27	-7.31	-7.25	-7.22
	E_p^{DIAS}	0.56	0.82	0.51	0.55	0.55	0.54	0.57	0.54	0.54
	E_q^{DIAS}	1.15	1.37	1.12	1.17	1.19	1.17	1.18	1.19	1.18
	E_{dr}^{DIAS}	-2.28	-1.98	-2.34	-2.36	-2.37	-2.45	-2.35	-2.38	-2.41

Table 2.13: Aortic bifurcation. Relative errors (in per cent) respect to the reference 3D solution computed according to (2.4.10)-(2.4.13) reported for the semi-implicit scheme using 3D and 0D junction and the explicit FORCE method for a mesh with $\Delta x = 5 \cdot 10^{-4}$ computed at the mid illiac. Relative errors reported in [35] are added comparison.

	Semi-implicit scheme		Explicit scheme
	3D junction	0D junction	
CPU time	2889.95	4472.29	3853.73

Table 2.14: Aortic bifurcation. CPU time (s) employed to run the simulation up to time 34.1s using the novel semi-implicit scheme combined with the 3D and 0D junction approaches and with the explicit FORCE-MH scheme with the 0D junction approach. All simulations have been carried out in serial on a computer which accounts for Intel® Core i9-10980XE CPU processors at 3.0GHz.

combined with both 0D and 3D junction model exploiting a first order scheme to treat the convective terms and setting $\theta = 0.55$. The computational domain is discretized according to a uniform grid with characteristic mesh size given by $\Delta x = 0.00125$. The initial condition, defined as $(A_0(x,0), q(x,0), p(x,0)) = (A_0(x), 0, 0)$ on all segments, is evolved in time according to a time step adaptively computed at each time iteration, in order to satisfy the CFL restriction given by (2.4.1) with CFL= 0.9. An upper bound of $dt_{\max} = 0.01$ is imposed in order to avoid larger time steps.

In what follows, the obtained numerical results are analyzed for two aortic segments (aortic arch II and thoracic aorta II), two vessels of the first generation of bifurcations (left subclavian I and right iliac-femoral II), two of the second generation (left ulnar and right anterior tibial) and two of the third generation (right ulnar and splenic). Qualitative comparisons between the time evolution of the experimental and numerical pressure and flow waveforms are shown in Figures 2.22-2.25, while Tables 2.17-2.20 show the relative

Parameter	Value
Blood density, ρ	1050
Blood viscosity, μ	0.0025
Velocity profile order, ψ	9
Young's modulus, E	$1.2 \cdot 10^7$
External pressure, p_{ext}	0
Outflow pressure, p_{out}	432.6

Table 2.15: 37-artery network. General model parameters of the 37-artery model taken from [35].

errors calculated with respect to in vitro measurements at the eight arterial vessels under study according to the following relative error metrics (2.4.10)-(2.4.13). For the sake of comparison, we also recall the solutions and errors reported in [35] for other six different numerical methods. We observe that the proposed semi-implicit scheme is able to capture the main features of in vitro pressure and flow waveforms at the eight arterial sites investigated. Besides, it provides numerical predictions comparable with the solutions obtained using high order schemes in [35]. Observing Tables 2.17-2.20, we note that, when a 3D junction model is employed within the semi-implicit scheme, the obtained relative root mean square errors are on average 2.73% (maximum value 3.72%, minimum value 1.77%) for pressure and 14.17% (maximum value 23.85%, minimum value 8.54%) for flow. Whereas, if the proposed semi-implicit scheme is combined with the 0D junction model, the obtained relative root mean square errors result on average 2.77% (maximum value 3.83%, minimum value 1.76%) for pressure and 15.16% (maximum value 25.79%, minimum value 9.46%) for flow. The new simplified three-dimensional junction model that accounts for the bifurcation angle provides errors comparable to those obtained with the widespread 0D junction approach in most of the cases analyzed. In particular, the use of the 3D junction approach results to be more accurate in predicting flow waves rather than the use of the 0D junction model, providing numerical solutions closer to experimental data. Among the vessels analyzed, the cases where we compute a higher difference between the errors provided by the two junction models are the thoracic aorta II (aortic segment), the right illiac-femoral II (first generation of bifurcations) and the right anterior tibial (second generation of bifurcations). In Table 2.21 we report these differences for the selected cases. The best gain is achieved in the computation of the maximum error in flow in the right illiac-femoral artery. Here, the proposed semi-implicit scheme combined with the 3D junction model provides a reduction of more than 15 percentage points in the maximum error respect to the corresponding error obtained if the scheme is combined with the 0D junction model. On the other hand, in the thoracic aorta II the use of the 3D junction model implies a reduction of 13 and almost 7 percentage points in systolic and diastolic flow error, respectively. To have a clearer qualitative assessment, in Figure 2.26 we repropose for the selected cases the resulting flow waveforms where we compare the numerical results obtained with the semi-implicit methods combined with both junction models and the available experimental data. In addition, in Table 2.16 we report the computational cost of both methods in performing one single cardiac cycle. Having an additional non linear system to solve at each 0D junction and at each time step makes

each cardiac cycle 7.83% more demanding.

	Semi-implicit scheme	
	3D junction	0D junction
CPU time	717.29	773.47

Table 2.16: 37-artery network. CPU time (s) employed to perform one cardiac cycle of 0.827s using the novel semi-implicit scheme combined with the 3D and 0D junction approaches. All simulations have been carried out in serial on a computer which accounts for Intel® Core i9-10980XE CPU processors at 3.0GHz.

Offering a complete view of the results, Figure 2.27 features the pressure and flow distribution along the entire network for time $t = 10$s, which corresponds to a nearly maximum flow rate at the root of the aorta. Meanwhile, Figures 2.28-2.29 report the pressure and flow rate along two selected arterial paths. One of them goes from the aorta throughout the left lower limb, while the other follows the left upper limb. In these latter cases, the solution is projected into a straight line given by the distance of each vessel point to the inlet of the network placed at $d = 0$.

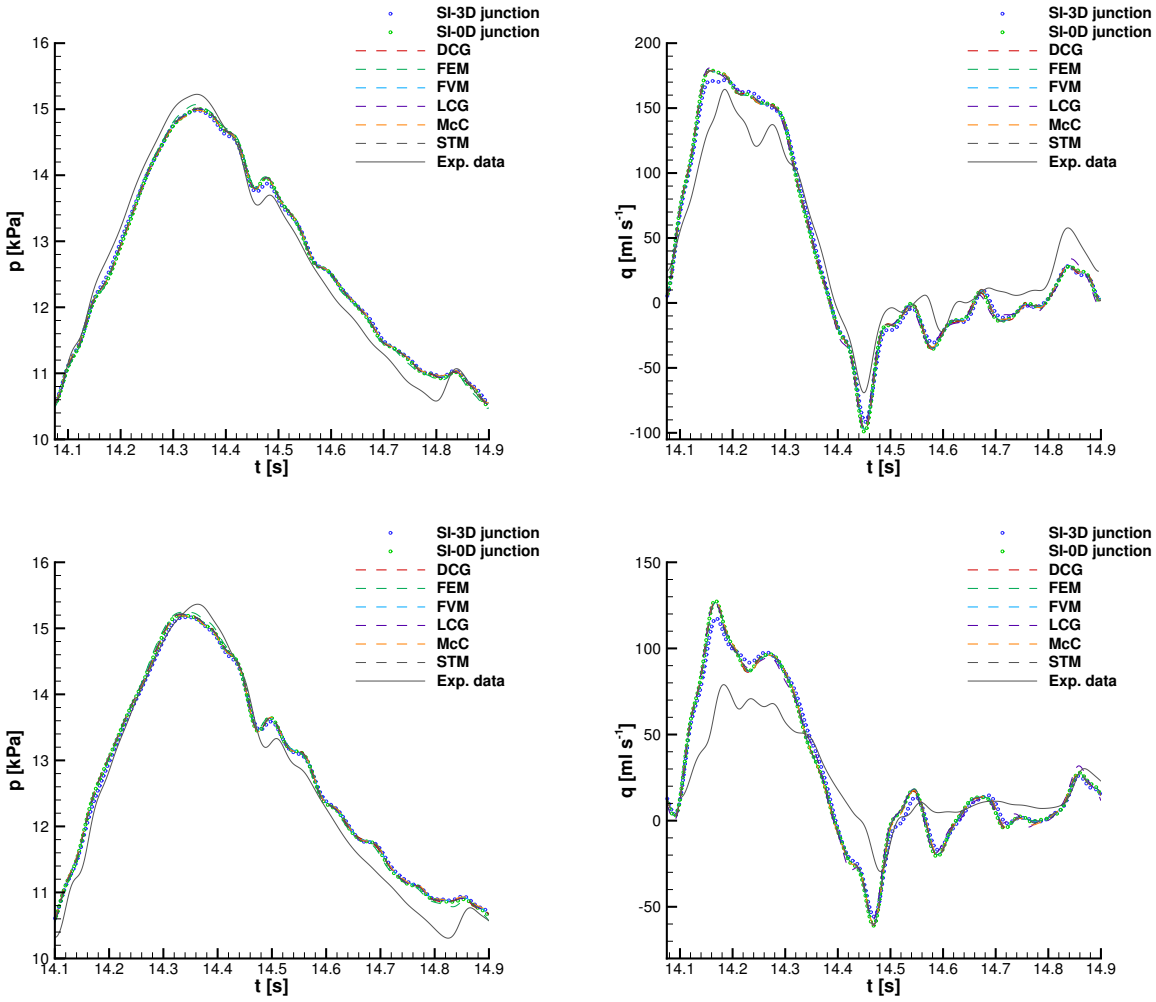

Figure 2.22: 37-artery network. Pressure (left) and flow (right) waveforms in the midpoint of two aortic segments: aortic arch II (top) and thoracic aorta II (bottom). The numerical results obtained with the novel semi-implicit approach using the 3D and 0D junction approach are reported employing blue and green circles, while the solutions in [35] are denoted as: Exp. data: in-vitro data (black solid line); DCG: discontinuous Galerkin (red dashed line); LCG: locally conservative Galerkin (purple dashed line); FEM: finite element method (light green dashed line); FVM: finite volume method (light blue dashed line); McC: MacCormack (orange dashed line); STM: simplified trapezium rule method (dark green dashed line).

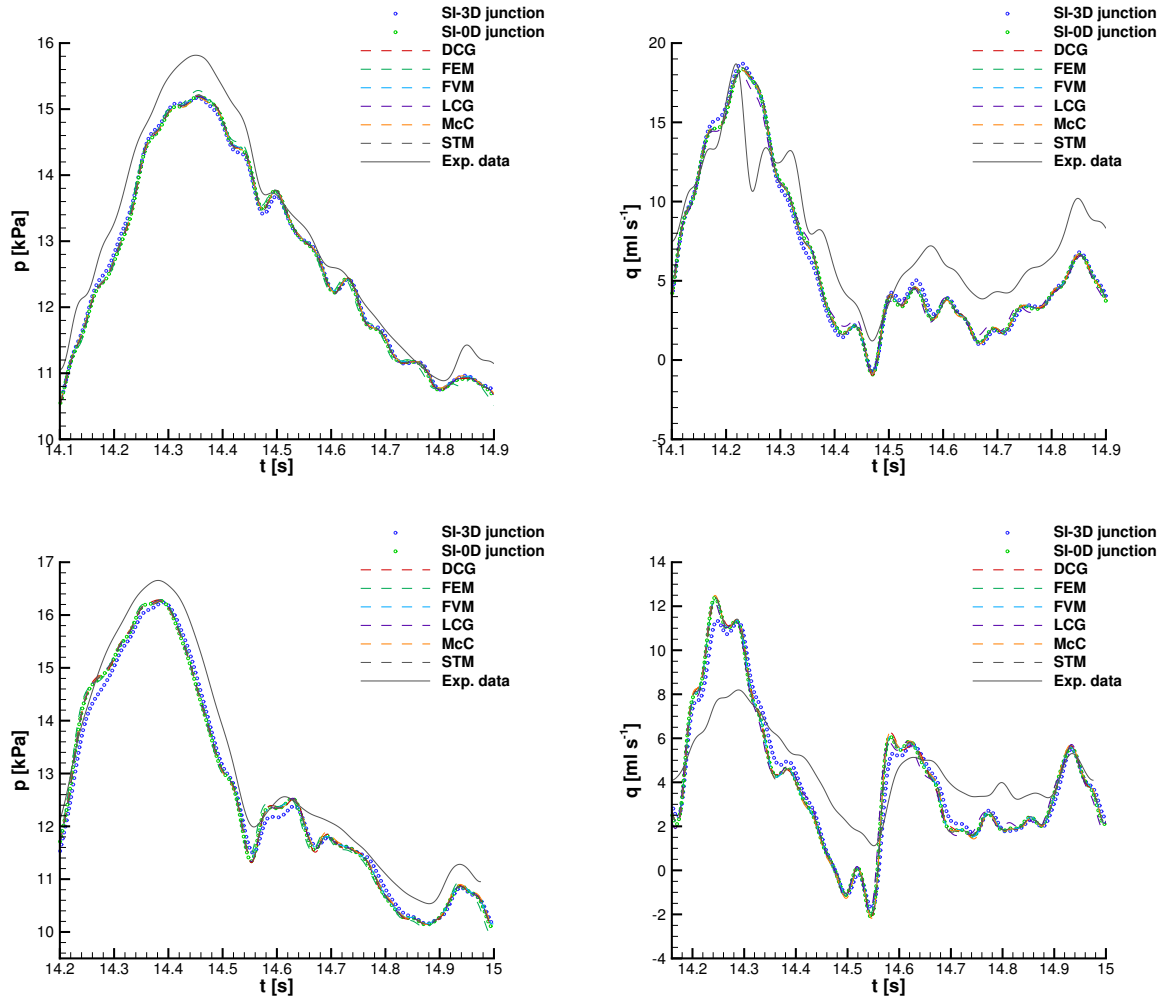

Figure 2.23: 37-artery network. Pressure (left) and flow (right) waveforms in the midpoint of the first generation of bifurcations: left subclavian I (topo) and right iliac-femoral II (bottom). The numerical results obtained with the novel semi-implicit approach using the 3D and 0D junction approach are reported employing blue and green circles, while the solutions in [35] are denoted as: Exp. data: in-vitro data (black solid line); DCG: discontinuous Galerkin (red dashed line); LCG: locally conservative Galerkin (purple dashed line); FEM: finite element method (light green dashed line); FVM: finite volume method (light blue dashed line); McC: MacCormack (orange dashed line); STM: simplified trapezium rule method (dark green dashed line).

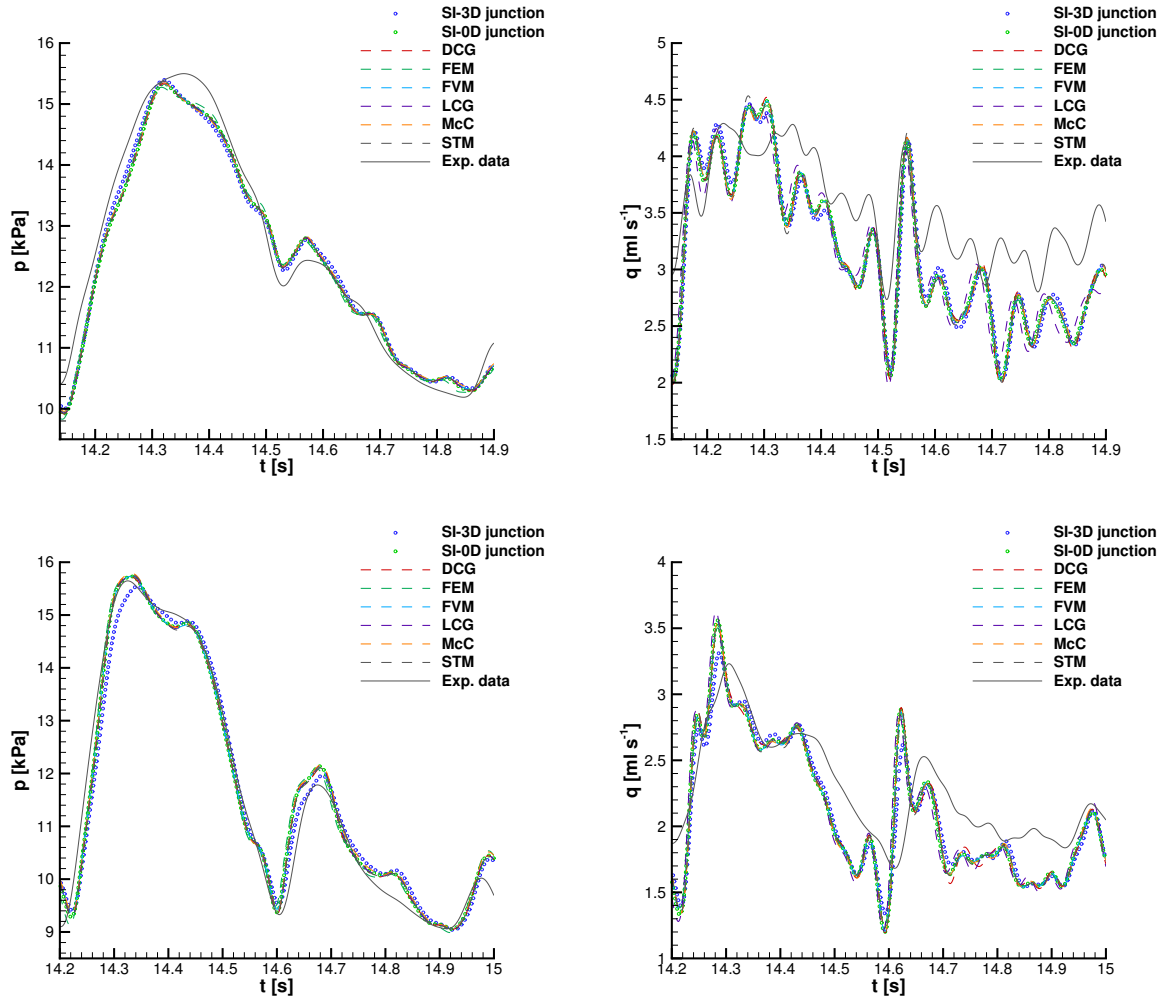

Figure 2.24: 37-artery network. Pressure (left) and flow (right) waveforms in the midpoint of the second generation of bifurcations: left ulnar (top) and right anterior tibial (bottom).The numerical results obtained with the novel semi-implicit approach using the 3D and 0D junction approach are reported employing blue and green circles, while the solutions in [35] are denoted as: Exp. data: in-vitro data (black solid line); DCG: discontinuous Galerkin (red dashed line); LCG: locally conservative Galerkin (purple dashed line); FEM: finite element method (light green dashed line); FVM: finite volume method (light blue dashed line); McC: MacCormack (orange dashed line); STM: simplified trapezium rule method (dark green dashed line).

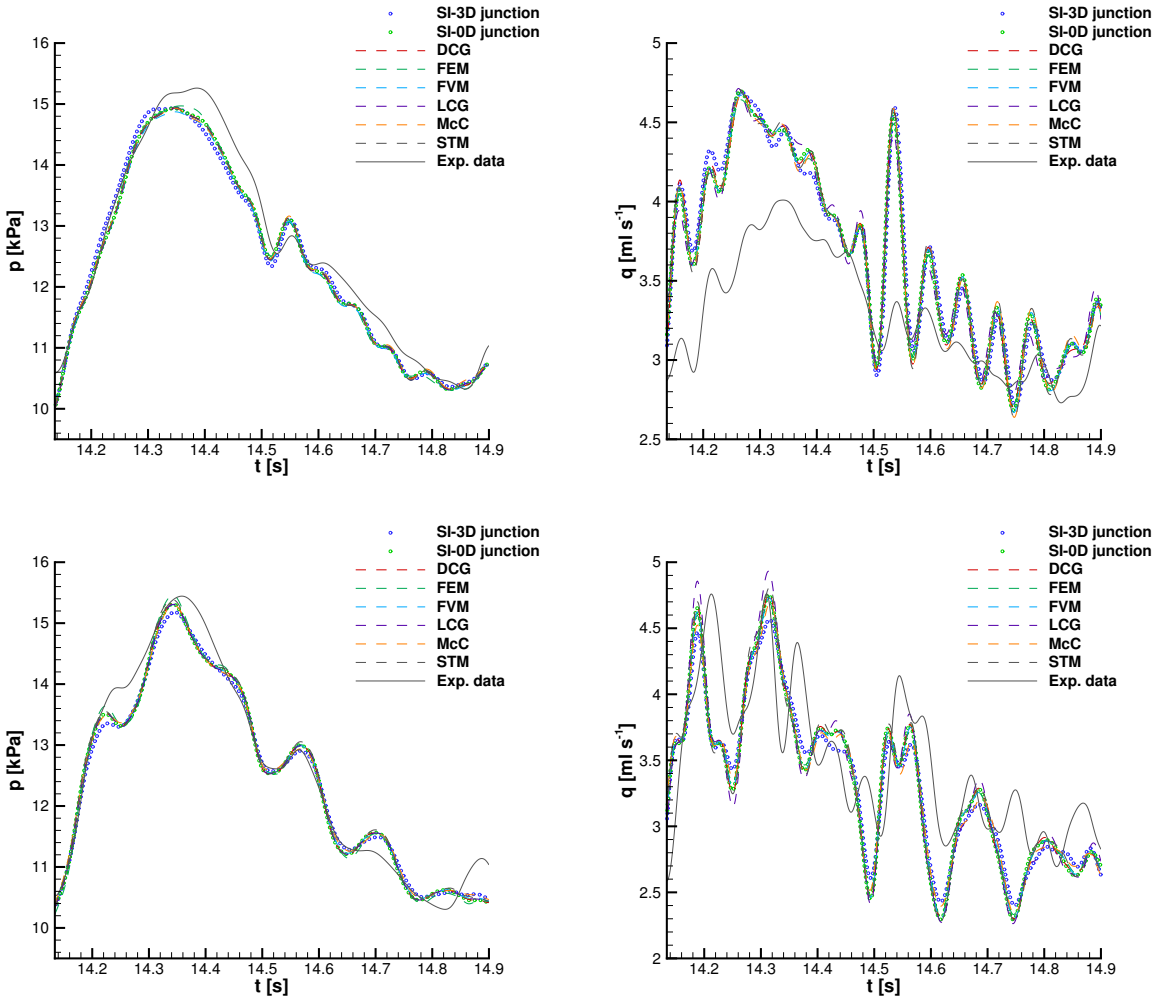

Figure 2.25: 37-artery network. Pressure (left) and flow (right) waveforms in the midpoint of the third generation of bifurcations: right ulnar (top) and splenic (bottom). The numerical results obtained with the novel semi-implicit approach using the 3D and 0D junction approach are reported employing blue and green circles, while the solutions in [35] are denoted as: Exp. data: in-vitro data (black solid line); DCG: discontinuous Galerkin (red dashed line); LCG: locally conservative Galerkin (purple dashed line); FEM: finite element method (light green dashed line); FVM: finite volume method (light blue dashed line); McC: MacCormack (orange dashed line); STM: simplified trapezium rule method (dark green dashed line).

		Semi-implicit		DCG	LCG	FEM	FVM	McC	STM
		3D jun.	0D jun.						
Aortic arch II	E_p^{RMS}	2.13	1.76	1.78	1.68	1.89	1.87	1.94	1.84
	E_q^{RMS}	11.05	12.53	12.32	12.34	12.02	12.11	12.11	12.19
	E_p^{MAX}	4.47	3.36	3.59	3.21	3.78	3.72	3.97	3.76
	E_q^{MAX}	23.67	31.52	29.58	31.83	29.00	29.13	29.40	29.45
	E_p^{SYS}	-2.42	-1.45	-1.40	-1.02	-1.40	-1.46	-1.60	-1.39
	E_q^{SYS}	4.44	9.55	8.78	10.02	8.81	8.75	8.81	8.75
	E_p^{DIAS}	1.06	-0.55	-0.42	-0.93	-0.17	-0.30	-0.12	-0.36
	E_q^{DIAS}	-11.93	-17.55	-17.95	-16.93	-17.08	-17.93	-17.74	-17.99
Thoracic aorta II	E_p^{RMS}	2.86	2.28	2.36	2.17	2.49	2.44	2.53	2.41
	E_q^{RMS}	23.45	25.53	25.59	25.36	25.26	25.43	25.62	25.37
	E_p^{MAX}	6.38	5.44	5.29	5.03	5.66	5.57	5.70	5.58
	E_q^{MAX}	49.05	70.46	67.52	70.75	64.93	65.69	66.22	65.32
	E_p^{SYS}	-1.85	-1.25	-0.96	-0.79	-0.97	-1.03	-1.13	-0.98
	E_q^{SYS}	48.02	60.80	60.70	61.59	60.39	61.59	62.24	61.16
	E_p^{DIAS}	3.14	1.69	1.66	1.13	1.97	1.81	1.98	1.69
	E_q^{DIAS}	-33.44	-37.99	-39.65	-35.47	-38.29	-39.26	-38.74	-38.77

Table 2.17: 37-artery network. Relative errors (in per cent) with respect to in vitro measurements computed according to (2.4.10), (2.4.11), (2.4.12) and (2.4.13). The semi-implicit scheme combined with the 3D and 0D junctions approach is run on a uniform mesh of $\Delta x = 0.00125$. The relative errors reported in [35] are also included for the sake of comparison. The different schemes considered are denoted as: DCG: discontinuous Galerkin; LCG: locally conservative Galerkin; FEM: finite element method; FVM: finite volume method; McC: MacCormack; STM: simplified trapezium rule method.

		Semi-implicit		DCG	LCG	FEM	FVM	McC	STM
		3D jun.	0D jun.						
Left subclavian I	E_p^{RMS}	3.02	3.18	3.09	3.12	3.05	3.12	3.11	3.11
	E_q^{RMS}	14.03	14.31	14.31	13.87	14.17	14.24	14.31	14.45
	E_p^{MAX}	5.52	5.92	6.13	6.06	6.10	6.29	6.35	6.13
	E_q^{MAX}	37.505	38.00	38.39	34.76	37.89	38.12	38.25	38.96
	E_p^{SYS}	-4.94	-3.85	-3.92	-3.38	-3.91	-3.96	-4.09	-3.80
	E_q^{SYS}	-2.65	-1.33	-2.11	-2.92	-2.53	-2.25	-2.08	-1.18
	E_p^{DIAS}	-2.25	-4.11	-3.97	-4.63	-3.72	-3.93	-3.69	-3.97
	E_q^{DIAS}	-9.80	-10.85	-11.57	-11.33	-10.86	-11.05	-10.92	-10.83
Right iliac femoral II	E_p^{RMS}	3.66	3.85	3.82	3.97	3.69	3.75	3.65	3.75
	E_q^{RMS}	20.12	24.26	24.49	24.17	23.90	24.19	24.80	24.12
	E_p^{MAX}	8.92	8.45	9.00	9.69	8.66	9.09	8.95	9.32
	E_q^{MAX}	41.25	61.70	59.63	61.14	59.28	60.61	61.61	60.41
	E_p^{SYS}	-3.18	-2.53	-2.20	-2.19	-2.32	-2.26	-2.33	-2.37
	E_q^{SYS}	36.24	49.71	50.20	49.23	49.99	51.42	52.41	51.29
	E_p^{DIAS}	-3.09	-4.33	-4.13	-5.57	-3.67	-4.04	-3.73	-4.17
	E_q^{DIAS}	-31.74	-37.83	-39.72	-36.92	-37.18	-39.06	-40.21	-38.26

Table 2.18: 37-artery network. Relative errors (in per cent) with respect to in vitro measurements computed according to (2.4.10), (2.4.11), (2.4.12) and (2.4.13). The semi-implicit scheme combined with the 3D and 0D junctions approach is run on a uniform mesh of $\Delta x = 0.00125$. The relative errors reported in [35] are also included for the sake of comparison. The different schemes considered are denoted as: DCG: discontinuous Galerkin; LCG: locally conservative Galerkin; FEM: finite element method; FVM: finite volume method; McC: MacCormack; STM: simplified trapezium rule method.

		Semi-implicit		DCG	LCG	FEM	FVM	McC	STM
		3D jun.	0D jun.						
Left ulnar	E_p^{RMS}	2.66	2.63	2.65	2.57	2.70	2.74	2.75	2.74
	E_q^{RMS}	12.16	12.46	12.74	12.42	12.43	12.70	12.78	12.91
	E_p^{MAX}	6.68	6.58	7.18	6.51	7.29	7.51	7.42	7.46
	E_q^{MAX}	25.72	28.63	30.14	25.91	27.75	29.30	29.19	29.55
	E_p^{SYS}	-1.59	-1.24	-0.99	-1.45	-1.13	-1.09	-1.07	-0.81
	E_q^{SYS}	2.69	4.32	5.37	4.30	3.63	4.60	4.43	5.68
	E_p^{DIAS}	-0.21	-2.86	-2.68	-3.54	-2.34	-2.54	-2.27	-2.63
	E_q^{DIAS}	-13.76	-16.65	-17.48	-17.93	-16.14	-17.1	-16.80	-17.02
Right anterior tibial	E_p^{RMS}	3.66	3.61	3.25	3.43	3.21	3.30	3.41	3.27
	E_q^{RMS}	7.86	10.60	10.49	11.05	9.88	10.22	10.24	10.24
	E_p^{MAX}	8.92	12.31	9.87	12.24	9.12	9.42	10.33	9.22
	E_q^{MAX}	16.87	34.96	35.07	35.80	31.16	33.57	34.38	34.54
	E_p^{SYS}	-3.18	-0.15	0.57	0.57	0.55	0.66	0.89	0.72
	E_q^{SYS}	0.83	10.27	8.37	12.37	8.40	9.79	9.76	10.32
	E_p^{DIAS}	-3.09	0.50	-2.68	-3.54	-2.34	-2.54	-2.27	-2.63
	E_q^{DIAS}	-9.37	-14.55	-15.09	-14.59	-13.25	-14.75	-14.43	-14.07

Table 2.19: 37-artery network. Relative errors (in per cent) with respect to in vitro measurements computed according to (2.4.10), (2.4.11), (2.4.12) and (2.4.13). The semi-implicit scheme combined with the 3D and 0D junctions approach is run on a uniform mesh of $\Delta x = 0.00125$. The relative errors reported in [35] are also included for the sake of comparison. The different schemes considered are denoted as: DCG: discontinuous Galerkin; LCG: locally conservative Galerkin; FEM: finite element method; FVM: finite volume method; McC: MacCormack; STM: simplified trapezium rule method.

		Semi-implicit		DCG	LCG	FEM	FVM	McC	STM
		3D jun.	0D jun.						
Right ulnar	E_p^{RMS}	2.61	2.47	2.54	2.58	2.66	2.49	2.42	2.50
	E_q^{RMS}	11.55	11.59	11.67	11.47	11.22	11.62	11.63	11.73
	E_p^{MAX}	5.82	6.22	6.32	6.88	6.36	6.32	6.06	6.50
	E_q^{MAX}	30.11	28.65	31.30	28.19	29.28	30.93	31.09	31.58
	E_p^{SYS}	-2.88	-2.31	-2.18	-1.92	-2.55	-2.20	-2.15	-2.06
	E_q^{SYS}	14.43	17.37	16.89	17.56	15.77	16.50	16.58	17.40
	E_p^{DIAS}	-1.66	-3.74	-3.91	-4.33	-3.96	-3.92	-3.66	-4.09
	E_q^{DIAS}	-0.56	–5.77	3.47	-7.48	-4.08	-4.60	-4.39	-5.34
Splenic	E_p^{RMS}	2.31	2.45	2.35	2.34	2.28	2.33	2.22	2.36
	E_q^{RMS}	7.91	9.65	9.44	9.79	9.02	9.22	9.04	9.56
	E_p^{MAX}	4.41	6.22	6.25	6.23	5.95	6.12	5.57	5.96
	E_q^{MAX}	23.25	24.48	23.74	22.82	22.83	23.20	23.30	24.47
	E_p^{SYS}	-2.37	-1.15	-0.79	0.09	-0.90	-0.87	-0.97	-0.38
	E_q^{SYS}	-6.75	-0.33	0.09	3.59	-1.32	-0.58	-1.47	1.05
	E_p^{DIAS}	0.25	-0.29	-0.14	-0.77	0.04	-0.04	-0.19	-0.03
	E_q^{DIAS}	-1.90	-5.87	-5.97	-6.75	-5.46	-5.95	-5.21	-6.40

Table 2.20: 37-artery network. Relative errors (in per cent) with respect to in vitro measurements computed according to (2.4.10), (2.4.11), (2.4.12) and (2.4.13). The semi-implicit scheme combined with the 3D and 0D junctions approach is run on a uniform mesh of $\Delta x = 0.00125$. The relative errors reported in [35] are also included for the sake of comparison. The different schemes considered are denoted as: DCG: discontinuous Galerkin; LCG: locally conservative Galerkin; FEM: finite element method; FVM: finite volume method; McC: MacCormack; STM: simplified trapezium rule method.

$\lvert E_q(\text{3D jun.}) - E_q(\text{0D jun.})\rvert$	Thoracic aorta II	Right illiac-femoral II	Right anterior tibial
RMS	1.94	2.97	1.48
MAX	14.45	15.49	10.39
SYS	13.09	12.84	7.67
DIAS	6.77	4.95	4.34

Table 2.21: 37-artery network. Difference between the relative errors (in percentage) with respect to in vitro measurements computed according to (2.4.10), (2.4.11), (2.4.12) and (2.4.13) obtained using the 3D and 0D junction model, respectively, within the proposed semi-implicit methodology.

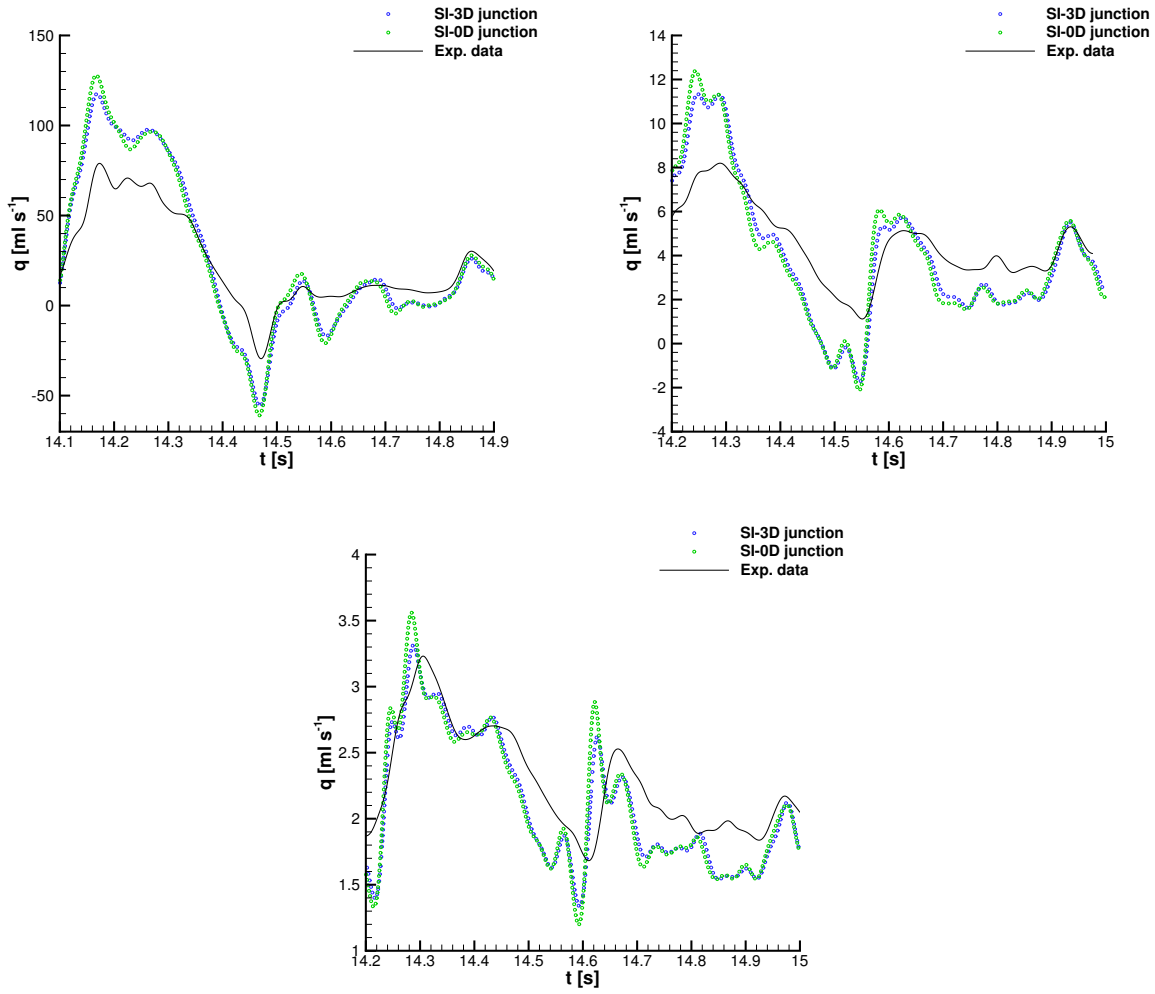

Figure 2.26: 37-artery network. Flow waveforms in the midpoint of the thoracic aorta II, the right illiac-femoral II and the right anterior tibial. The numerical results obtained with the novel semi-implicit approach using the 3D and 0D junction approach are reported employing blue and green circles, respectively. While the experimental data are reported in black line.

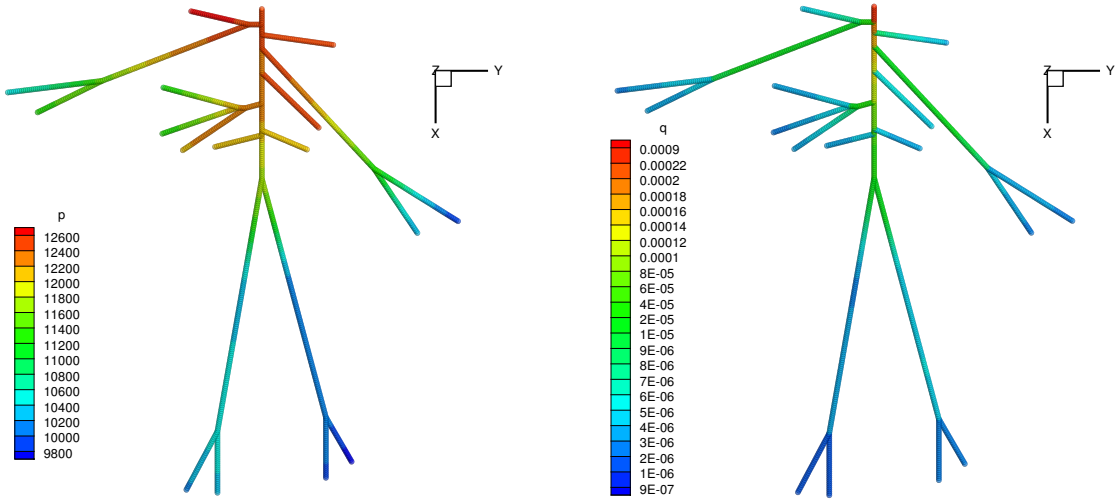

Figure 2.27: 37-artery network. Pressure (left) and flow (right) distribution for the entire network obtained with the new semi-implicit scheme combined with the 3D junction approach; time $t = 10$s.

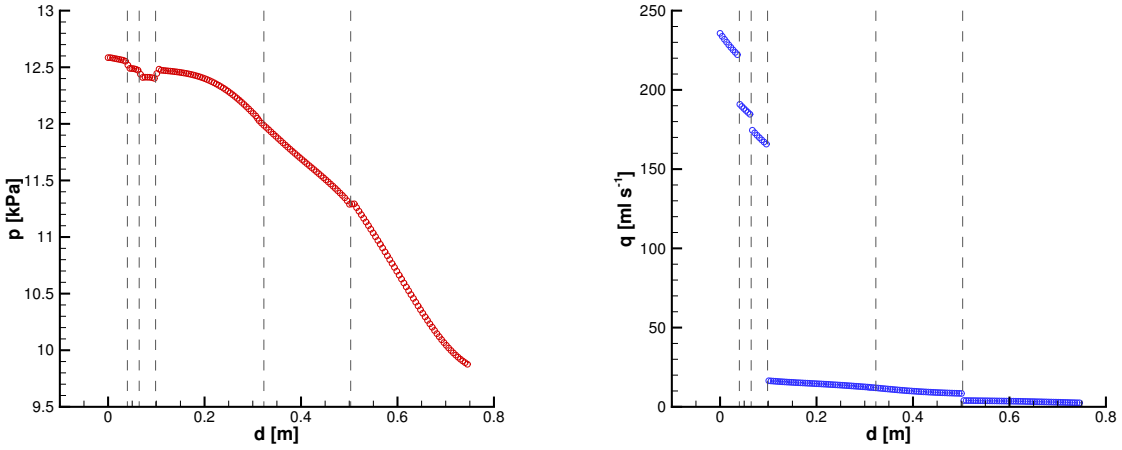

Figure 2.28: 37-artery network. Pressure (left) and flow (right) rate along the aorta and left upper limb obtained with the new semi-implicit scheme combined with the 3D junction approach; time $t = 10$s. Vertical lines indicate the location of bifurcations. The solutions are projected onto a straight line given by the distance of each vessel point to the network's inlet placed at $d = 0$.

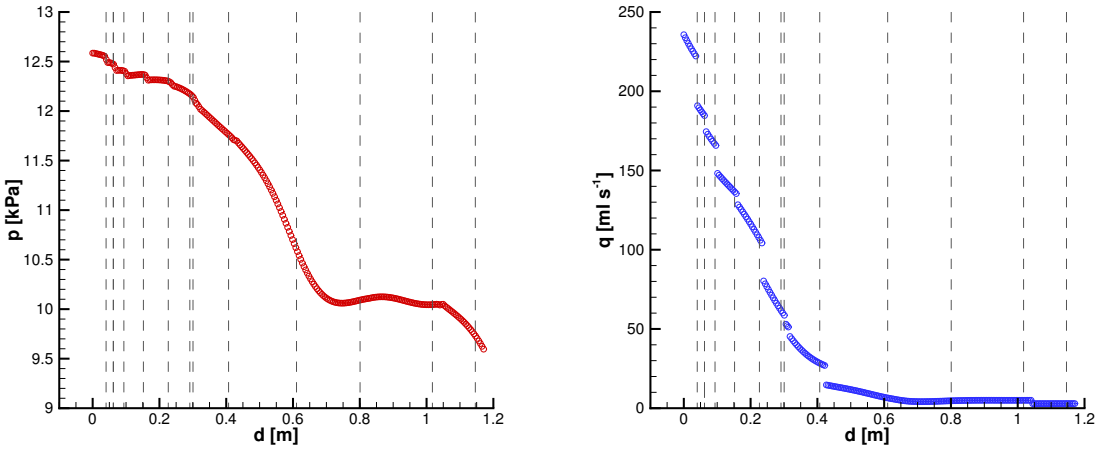

Figure 2.29: 37-artery network. Pressure (left) and flow (right) rate along the aorta and left lower limb obtained with the new semi-implicit scheme combined with the 3D junction approach; time $t = 10$s. Vertical lines indicate the location of bifurcations. The solutions are projected onto a straight line given by the distance of each vessel point to the network's inlet placed at $d = 0$.

Conclusions

In this part of the thesis, we have constructed novel numerical schemes for solving mathematical models able to capture the main features of blood flow dynamics. In particular, having in mind to apply the proposed methods as a tool to investigate haemodynamic features of the cardiovascular system, we have focused on the incompressible Navier-Stokes equations in multiple dimensions and on a reduced one dimensional model.

In particular, a novel fully implicit hybrid FV/FE algorithm for the solution of the incompressible Navier-Stokes equations in two and three dimensions has been presented. The splitting of the equations allows the decoupling of the pressure and momentum subsystems. Consequently, the convective-diffusion subsystem is solved with the aid of Crouzeix-Raviart elements for the viscous terms combined with an implicit finite volume discretization for the nonlinear convective terms, which, being unconditionally stable, allows larger time steps that the explicit approach employed in the former algorithm. This feature results to be crucial to perform blood flow simulations in complex 3D geometries for trees of vessels. To solve the corresponding nonlinear system an inexact Newton method has been used combined with an SGS-preconditioned BiCGStab or GMRES algorithm. As a consequence, linearised numerical flux functions have been introduced. To gain in computational efficiency it has also been proposed a simple but effective strategy for the reordering of the dual elements compatible with an MPI parallelization. Regarding the projection stage, classical $\mathbb{P}^1$ finite elements are employed and the result obtained is used to correct the intermediate momentum obtained as the solution of the transport-diffusion subsystem. In addition, the code has been tested against a set of classical fluid dynamic benchmarks and validated using a real test case for the simulation of the flow in a coronary tree.

Although the design of a fully implicit method has allowed us to considerably reduce the computational cost when addressing haemodynamics problems, if larger networks of vessels are considered the time consumption could still result unaffordable. Thus, a simplified mathematical model for solving the one dimensional blood flow equations has been developed. We have proposed a novel semi-implicit finite volume approach for the numerical simulation of blood flow in networks of elastic and viscoelastic vessels. The use of a splitting technique based on [219] leads to three subsystems: a convective subsystem, which has been discretized using explicit finite volume methods with a Ducros-type flux function and a Kolgan approach to achieve second order in space; a diffusive subsystem, needed only in case a viscoelastic vessel is considered and which is solved implicitly using BTCS; and a pressure subsystem, also treated using an implicit finite volume method on a staggered grid. One main advantage of this approach, with respect to more classical fully explicit schemes, is that the CFL condition of the final algorithm depends only on the flow velocity and not on the wave speed nor on the viscous terms which leads to an

efficient methodology both in case of low speed index and in case viscoelastic vessels are studied. In addition, to increase the time accuracy of the overall scheme a θ-method has been introduced.

To extend the algorithm to networks, a new approach able to deal with junctions of vessels taking into account their incidence angles has been introduced. We have proposed a novel semi-implicit methodology considering a unique 3D primal cell in each junction where the pressure is implicitly computed and which employs a multidimensional flux function in order to explicitly approximate the fluxes at the interfaces of the 3D-1D dual cells contained in the three dimensional primal cell. Consequently, the solution of junctions and 1D vessels is fully coupled, a unique pressure system is defined for the whole network including the degrees of freedom of both the 1D and 3D cells. Moreover, the geometry of the junctions is taken into account in the flux computation so that the effect of the angles among the vessels can be captured. Finally, the behaviour of the proposed methodology has been numerically investigated both, for single vessels with constant and variable parameters, and in the case of networks containing junctions and defined using realistic data.

Part II

Model-based FFR Prediction

Introduction

The heart is a muscular organ responsible for pumping oxygen and nutrient-rich blood throughout the body to sustain life. As all other organs, it must be supplied with nutrients and oxygen via the circulatory system. Indeed, its continuous activity creates a large demand for nutrients to be delivered to the cardiac tissue and produces waste that needs to be removed. Although its chambers are full of blood, it is not feasible for the tissue to obtain nourishment directly from this blood, since the organ is made of three layers and presents a thickness of almost 10 millimeters. Therefore, in order to maintain optimal cardiac performance and homeostasis, the heart receives the needed sustenance from specific arteries, the coronary arteries, that depart from the aorta and encircle the heart branching throughout the tissue. The coronary vascular network is closed, tortuous, with multi-generation systems of branching and merging junctions of deformable vessels with widely different diameters and lengths. All the larger vessels that run over the epicardial surface of the heart are called epicardial arteries and are of primary importance for the correct function of the coronary circulatory system. The two main coronary arteries are the left coronary artery (LCA) and the right coronary artery (RCA) which originate from the left side of the heart at the root of the aorta, just after the aorta exits the left ventricle. In particular, the LCA divides into the circumflex (LCX), following the coronary sulcus to the left, and the left anterior descending artery (LAD), following the anterior interventricular sulcus around the pulmonary trunk, and feeds the left ventricle and the interventricular septum. On the other hand, the RCA passes anteriorly and slightly to the right between the right atrial auricle and the pulmonary trunk and supplies the right ventricle and various atrial branches that reach the atria and the interatrial septum. The anatomy of the coronary artery system is schematically represented in Figure 2.30 in anterior and posteroinferior views.

In 70-80% of subjects, the posterior descending artery (PDA) originates from the RCA and then runs in the posterior interventricular sulcus to the apex of the heart where it meets with the left anterior descending artery. In this case the heart circulation is defined to be right dominant. Alternatively, as in the 5-10% of population, the PDA can depart from circumflex coronary artery giving rise to a left dominance subject. Finally, when the PDA is supplied by both the left circumflex and the right coronary artery then, the heart circulation is known as co-dominant [195]. As we can note in Figure 2.31, coronary arterial dominance influences the amount and anatomic location of myocardium perfused by the right or left coronary circulation and might also have an impact on the coronary blood flow volume entering the coronary circulation. In particular, as far as the population considered in Sakamoto's study [189] is concerned, coronary blood flow in the LCX is about 56% higher in left dominant or balanced circulations than in right-dominant ones, while flow in the RCA is roughly twice as high in right-dominant circulations with respect

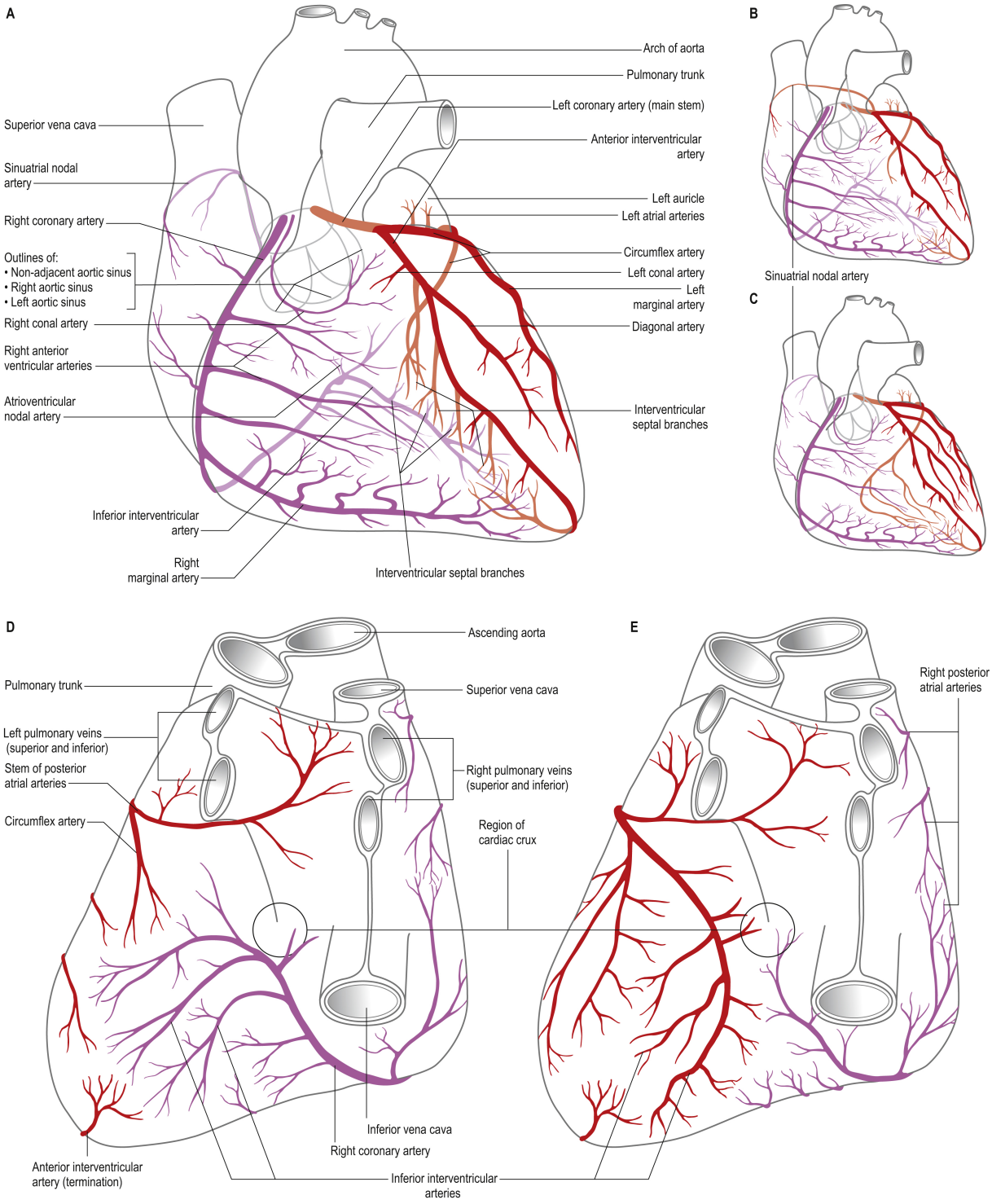

Figure 2.30: Coronary artery anatomy. The right coronary arterial tree is shown in purple, while the left coronary arterial tree is coloured in red. Panels A–C correspond to an anterior view of the coronary tree, whereas panels D–E represent its posteroinferior view. Figure reproduced with permission from [203].

to that found in left or co-dominant.

Coronary blood flow in healthy people at rest usually averages about 225 ml/min, which

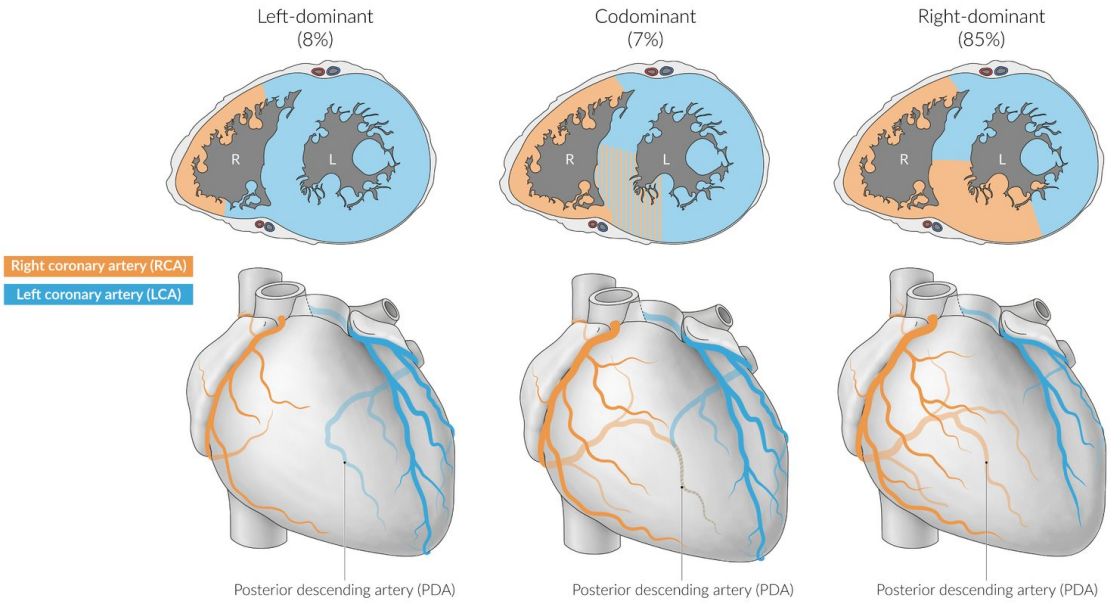

Figure 2.31: Myocardial perfusion according to coronary arterial dominance. Taken from [101].

corresponds to 4-5% of the total cardiac output, and arterial oxygen extraction is about 70-80%, [180]. Its regulation is understood to be dictated through multiple mechanisms which collectively modulate coronary vascular resistance and act to ensure an overall balance between the myocardial requirements for oxygen and substrates and metabolism, [102]. Small arteries, which branch from epicardial vessels, play the role of resistive vessels which are able to modulate the vascular resistance under physiological or pharmacological stress in order to match the myocardial blood flow to variable energy requirements. Since these vessels dive into the wall where they branch off to form the microcirculation of the myocardium, they are affected by the contractions of myocardium. This results in a particular waveform of the coronary blood flow as a function of time. During contraction of the ventricular myocardium, the intramural coronary vessels are compressed due to the intramyocardial pressure. This compression leads to momentary stop or even retrograde blood flow which further inhibits perfusion of myocardium during systole. As a result, in contrast to all other organs, most myocardial perfusion occurs during diastole, when the intramural coronary vessels are open and under lower pressure. The specifics of this metabolism-perfusion matching are unique compared to those in other systemic circulations. They are dictated by variations in pressure that arise, both, proximally at the level of the aorta and distally from an active compression and decompression of the coronary microcirculation caused by the rhythmic contraction and relaxation of the myocardium.

Owing to the limited ability of the myocardium to contract anaerobically, a correct coronary blood flow is crucial for the regular function of the heart. Among the main factors that can lead to a dysfunction of this mechanism, we focus on the presence of a stenosis in the main coronary arteries. This abnormal narrowing causes an impaired coronary blood flow and consequently a mismatch between oxygen delivery to the myocardium and its metabolic needs.

The most common manifestation of cardiovascular disease, related to stenosis, is the coronary artery disease (CAD) which represents one of the main mortality causes worldwide, accounting in 2019 for 16% of total deaths [165], and confirms itself at the top of the list of the main causes of death in the USA in 2020, registering an increase of 5% compared to the previous year [2]. CAD occurs when, within arteries walls, a buildup of atherosclerotic plaque, composed of fatty material including cholesterol, connective tissue, white blood cells, and some smooth muscle cells, is formed. This leads to the creation of a stricture, and, consequently, an obstruction of blood flow, and in a decrease of the flexibility or compliance of the vessels (see Figure 2.32). Accordingly, the heart does not receive enough oxygen and vital nutrients resulting in its damage, the potential scarring of the heart muscle without regrowth of cells constituting the tissue and, ultimately, the death. However, when the blood flow supply tends to decrease due to the presence of a narrowing in the coronary arteries, the system reacts by reducing the resistance of the microvasculature to balance the increased proximal resistance. In addition, as the size of the blockage in a coronary artery increases, the narrowed artery may develop collateral circulation developing new blood vessels that reroute blood flow around the blockage. However, during times of increased exertion or stress, arteries may not be able to vasodilate sufficiently to supply the needed oxygen-rich blood to the heart muscle, since part of its vasodilatory capacity was used to guarantee flow in baseline conditions. In order to prevent this condition, it is often necessary to perform medical interventions.

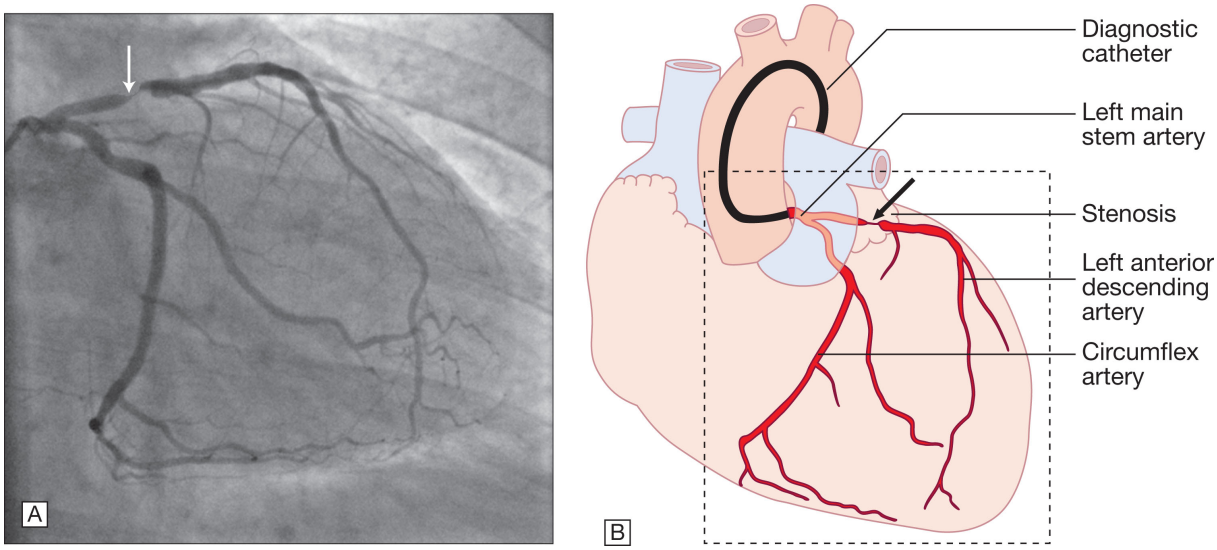

Figure 2.32: Coronary artery angiography (Panel A) and schematic view (Panel B) of a coronary tree which presents a stenosis. The stenosis is indicated with a arrow, colored in white on the left and in black on the right). Figure reproduced with permission from [178].)

As explained in [112], various pharmacological and surgical treatments are then available. The opportunity of performing one or another procedure at the level of a particular lesion is evaluated based on its severity degree identified during angiography or through other non-invasive techniques and on the measurement of haemodynamic indices. In case of stable CAD, the most recent guidelines recommend deciding whether a surgical procedure is needed or if patients can just be treated with optimal medical therapy, after evaluating

not only the anatomical location and size of a stenosis, but also its functional significance, i.e., the actual extent of coronary blood flow restriction caused by the lesion, [161, 123]. In fact, the Fractional Flow Reserve (FFR), defined as the ratio of the maximal achievable flow in a stenotic coronary artery to the hypothetical maximal achievable flow in the same artery in the absence of stenosis, becomes the gold standard for diagnosis of functional severity of ischemia-inducible coronary stenosis, [172]. Since at maximum vasodilation blood flow to the myocardium is proportional to myocardial perfusion pressure, the ratio of two flows can be equivalently expressed as the ratio of two pressures, which, unlike flows, can be easily measured thanks to the use of a pressure wire and a guiding catheter. Clinically, the FFR of a given lesion is assessed during invasive coronary angiography under drug-induced hyperemia, i.e. maximal blood flow is induced by administration of vasodilatory drugs, such as adenosine or papaverine. During transfemoral or transradical catherization, a guiding wire equipped with a miniaturised pressure sensor is inserted into the coronary artery to record simultaneously the pressure in the aorta, p_a, and the pressure approximately 2-3 cm distal to the lesion, p_d, that is to be investigated. FFR is then determined as a ratio of cardiac-cycle averaged pressure distal to a coronary stenosis to mean aortic pressure [190], namely

$$\mathrm{FFR} = \frac{\dfrac{1}{T}\displaystyle\int_T p_d(t)\,\mathrm{dt}}{\dfrac{1}{T}\displaystyle\int_T p_a(t)\,\mathrm{dt}}, \tag{2.4.16}$$

where T denotes the duration of one cardiac cycle. FFR can take values between 0 and 1: the smaller it is, the lower is the flow distal to the stenosis and the bigger is the probability to develop a myocardial ischaemia. In particular, FFR thresholds are defined in order to guide therapy for stable CAD. Trials evaluating the prognostic impact of the FFR have shown that revascularization can be safely deferred if FFR is greater than 0.80, while a lesion is considered to be ischemic-inducible if FFR < 0.75, [190]. When FFR is in the gray zone (0.75-0.80), sound clinical judgments should balance the final decision.

Although clinical and economical benefits of using FFR to evaluate the necessity of a revascularization procedure have been demonstrated, FFR remains underused. Indeed, it proves to be a costly procedure which requires trained interventionalists to be performed. Besides, its invasive nature is associated with the risk of perforation or dissection due to the insertion of the wire and of adverse effects related to adenosine administration, [15]. These considerations have motivated the scientific community to search non-invasive diagnostic techniques that can hypothetically act as an effective gatekeeper for the cardiac revascularization in patients with CAD suspicion.

Among the developed diagnostic techniques, Coronary Computed Tomography Angiography (CCTA) has emerged as a valid non-invasive tool to quantify the geometrical significance of a lesion producing detailed 3D images of the arteries. Studies have shown that it is characterized by high diagnostic accuracy and high negative predictive value [116]. As a consequence, current guidelines recommend it as an initial test to rule out obstructive CAD in patients whose disease can not be excluded based only on clinical evaluation. Its non-invasive nature makes it a low-risk procedure with significantly lower economical costs compared to coronary angiography. In addition, technological advancement and innovative post-processing techniques have led to greater anatomical detail of the coronary plaques.

However, CCTA-based CAD evaluation has shown to overestimate the severity of the disease in many cases, resulting in false positives and consequently in a low specificity, [187].

The search for an optimal non-invasive test, that can therefore characterize both the functional and the anatomical significance of a coronary lesion, has then led to the development of CCTA-based FFR analysis [65]. CCTA-based FFR methods combine non-invasive subject-specific clinical data (CCTA, cardiac output, heart rate, dominance, diastolic and systolic pressure, etc.) and mathematical models to reproduce the fluid mechanics in coronary vessels and so non-invasively estimate FFR. In this context, computational models offer a powerful and non-invasive tool to perform an accurate investigation of physiology characterising the cardiovascular system, both in healthy and pathological conditions.

CCTA-based FFR models allows to predict FFR using only CCTA scans and non-invasive subject-specific clinical data. Fully physics-based models, relying on solving the incompressible Navier-Stokes equations in complex, three-dimensional domains, and also reduced models, based on one-dimensional blood flow equations, have shown a high diagnostic performance, [89, 88, 31]. CCTA-derived FFR has proved to complement the anatomical information provided by CCTA to aid diagnosis and reduce the number of unnecessary invasive procedures conducted in patients who turn out to have non-flow-limiting coronary artery stenoses.

Most CCTA-derived FFR models neglect the presence of the guidewire. However, some studies conducted both in vitro, [10], and computationally, on idealized geometries and in a patient-specific domain, [235], have shown that the haemodynamic alteration caused by the presence of the guidewire, may lead to an underestimation of the predicted FFR. It is then relevant to further analyze this configuration and develop efficient mathematical tools able to account for the presence of a guidewire. Therefore, this second part of the thesis, devoted to our medical applied work, aims at estimating, in a non invasive way, the FFR and at investigating if the small dimension of the guidewire is effectively negligible or if its presence crucially influences the resulting FFR value.

Chapter 3

Impact of a pressure guidewire on model-based FFR prediction in 3D

As we have already mentioned, Fractional Flow Reserve (FFR) is used to characterize the functional significance of coronary artery stenosis. FFR is classically assessed under hyperemic conditions by invasive measurements of trans-stenotic pressure thanks to the insertion of a pressure guidewire across the coronary stenosis during catheterization. In order to overcome the potential risk related to the invasive procedure and to reduce the associated high costs, blood flow simulations that incorporate clinical imaging and patient-specific characteristics have been proposed.

To deliver non-invasive FFR predictions, we need to perform some steps allowing the combination of clinical non-invasive data with mathematical models. Following the modeling pipeline depicted in Figure 3.1, the first step consists on acquiring an accurate geometry of the coronary tree. Among the available imaging modalities, CCTA is the most commonly used technique for coronary artery disease. In the CCTA images, distinct tissues have different attenuation characteristics and the coronary artery lumen can be made visible thanks to the injection of a contrast agent in the blood. Therefore, coronary arteries of interest can be isolated and thus segmented (Step 1, Figure 3.1). Then, after applying image processing techniques, a 3D anatomical model that represents the patient specific coronary artery anatomy is generated (Step 2, Figure 3.1). In the next step, assumptions related to the coronary physiology and clinical patient-specific information are used to define a mathematical model including boundary conditions at the inlet and outlet sections (Step 3, Figure 3.1). The resulting physiological model is then numerically solved using computational fluid dynamics (Step 4, Figure 3.1). Finally, based on the predicted pressure and flow distribution throughout the computational domain, non-invasive FFR predictions can be computed (Step 5, Figure 3.1).

Along this chapter, each step is carefully addressed and a detailed description is provided. In addition, even if most CCTA-derived FFR models neglect the potential influence of the guidewire, which is present during clinical FFR measurements, on flow and pressure distribution, we conduct a study aimed to quantify the impact of considering its presence in FFR prediction for a wide range of FFR values and several patients.

The chapter is structured as follows. In Section 3.1, we provide a summary of the main characteristics of the patients involved in the study, the acquisition of patient-specific data and the definition of computational domains. Section 3.2 illustrates the modeling

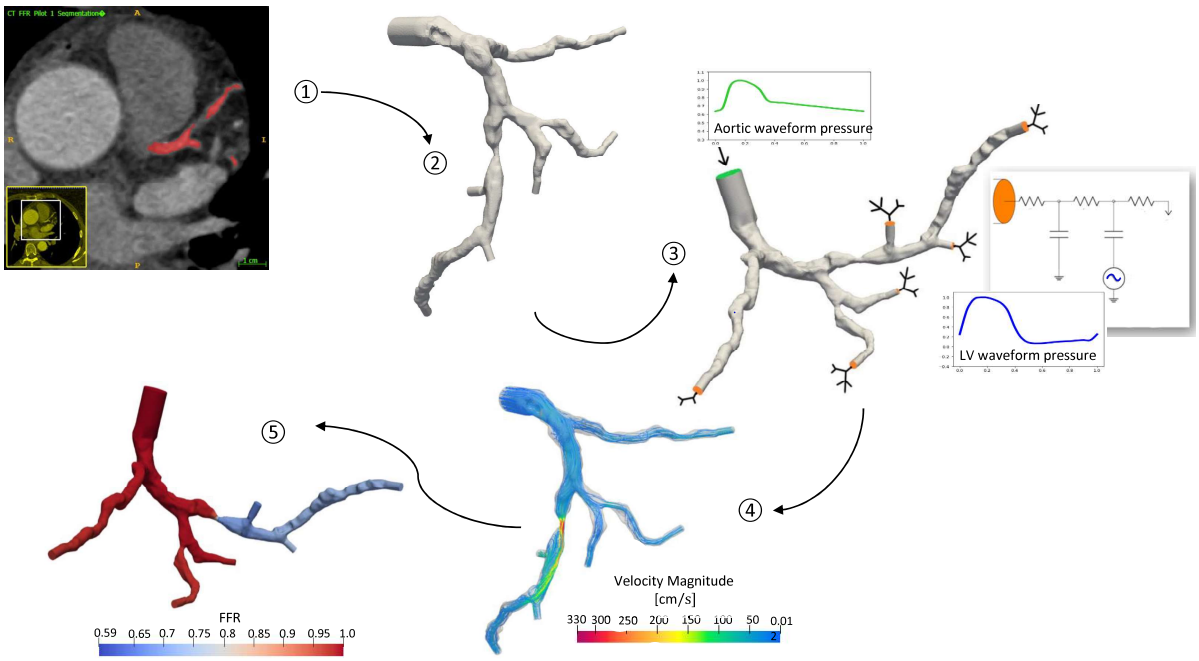

Figure 3.1: Overview of the non-invasive FFR prediction pipeline: (1) image processing and segmentation, (2) anatomical model, (3) physiological model, (4) CFD analysis, (5) extraction of computational FFR.

framework used to computationally solve blood flow dynamics in coronary artery trees, the adopted microcirculatory model, the strategy to predict a hyperemic state and to define relevant model patient-specific parameters. Finally, Section 3.3 provides results on the impact of the explored modeling feature to include the presence of the pressure guidewire on FFR predictions.

3.1 Data collection and processing

We start describing the sample population involved in this study as well as the acquisition of clinical data used to define the model. Then, we focus on coronary artery segmentation and meshing, which are the fundamental steps required to derive, from clinical images, the computational domains.

3.1.1 Patient population

We consider a population of 18 patients recruited as part of a clinical trial at St. Olavs hospital, Trondheim, Norway [38]. The subjects included in this study had undergone invasive angiography and FFR measurements after the clinical and coronary computed

tomography angiography (CCTA) examinations had indicated stable CAD. Exclusion criteria that disqualified patients from participation comprised:

- Unstable CAD. It has a similar anatomical background to stable CAD. However, stable CAD is a condition in which there is regional myocardial ischaemia caused by inadequate coronary perfusion and it is usually induced by increases in myocardial oxygen requirements. The chest pain that can be characterized as chronic stable angina is typically produced with physical exertion and relieved by rest or after taking medication. In contrast, if chest pain occurs at rest, it is usually indicative of unstable disease, such as acute coronary syndrome that is often caused by a coronary plaque rupture and the subsequent intracoronary thrombosis formation, it worsens quickly and it does not subside after medication or rest.
- Previous percutaneous coronary intervention or bypass surgery.
- Renal insufficiency.
- Contraindication to use vasodilator agents and non diagnostic quality of the CCTA.

The recruited patients present at least one suspected lesion, resulting in a set of 24 FFR measurements. Besides, the patients are selected from a larger patient pool in order to obtain a homogeneous distribution of invasive FFR values. The FFR measurements have a mean of 0.69 and a standard deviation of 0.03, with a positive FFR prevalence of 66.67% for a cutoff value of FFR$<$ 0.80. Tables 3.1 and 3.2 provide an overview of general patient characteristics and invasive FFR measurements, while a 3D visualization of the corresponding anatomical models is reported in Figure 3.2.

3.1.2 Medical data acquisition

As we have introduced at the beginning of this part of the thesis, CCTA is an anatomical test suggested as diagnostic tool in CAD intermediate-risk patients. CCTA scans are performed to visualize epicardial coronary arteries, which are moving structures typically characterized by diameters in millimeters. Due to their small vessel size and their motion in space, CCTA requires both good spatial and temporal resolution to accurately identify them. Spatial resolution refers to the smallest distance across which two points can be differentiated, while temporal resolution refers to how quickly images of a moving stricture can be acquired, [181]. Since epicardial vessels move in space according to the contraction and relaxation of the heart, image acquisition synchronized with cardiac motion by simultaneous electrocardiogram (ECG) recording is essential to limit the motion artifacts. In particular, synchronisation of data acquisition with the ECG signal of the patient enables the selection of the cardiac resting period, characterized by the least cardiac motion, to perform an optimal data acquisition, [97]. Moreover, if patients are not hypotense, nitroglycerin is administered sublingually shortly before image acquisition in order to dilate the coronary arteries and, consequently, to allow an easier image visualisation and analysis. Additionally, a iodinate contrast medium is administered intravenously during CCTA to opacify the vessel lumen. This makes possible to differentiate the vessel lumen from both, calcifications and the surrounding structures, allowing an accurate detection of lesions.

Patient IDs	MAP(mmHg)	CO (L min^{-1})	Dominance
1	93.33	6.0	right
2	95.67	3.8	right
3	92.67	6.2	right
4	97.67	6.5	right
5	84.33	4.4	right
6	99.33	5.2	right
7	95.33	3.6	right
8	100.33	6.3	left
9	98.67	3.4	right
10	100.67	5.4	left
11	115.33	6.4	right
12	92.33	4.9	right
13	88.67	6.0	right
14	99.33	3.97	right
15	90.0	4.3	right
16	105.33	4.66	right
17	99.0	3.88	right
18	100.0	5.25	right

Table 3.1: Patient-specific data for the 18 patients considered in this work. Mean aortic pressure (MAP), cardiac output (CO) and dominance are reported.

For the patients under study, CCTA was performed using two CT scanners with 2×128 detector rows (Siemens dual source Definition Flash) following a standardized protocol, [89]. The exam consists of three main scans performed during patient breath hold. The first acquired image is an anterior-posterior scout image that allows the determination of the scan range. Afterwards, non-contrast-enhanced images are acquired in order to evaluate the extent of the coronary artery calcification based on calcium deposits identified as regions with high attenuation characteristics. Finally, contrast-enhanced images ECG synchronized are obtained, [181].

FFR was measured in-vivo using Verrata Plus (Philips Volcano, San Diego, USA) pressure wires according to standard practice. Prior to inserting the pressure wire into the coronary artery, intracoronary nitroglycerin was administered and hyperemia was induced by continuous intravenous infusion of adenosine. Pressure at the ostium and approximately 2-3 cm distal to the lesion under examination were recorded over several cycles and FFR, defined as (2.4.16), was taken equal to the lowest observed value.

Standard non-invasive diastolic and systolic pressure measurements were performed on both arms as a part of clinical routine, while cardiac output (CO) was calculated on the basis of the cross-sectional area of the left ventricle outflow tract and of the velocity time integral derived from Pulse Wave Doppler.

FFR IDs	Patient IDs	Lesion location	FFR
1	1	mLAD	0.68
2	2	mLAD	0.52
3	2	dLAD	0.46
4	2	pLCX	0.88
5	3	mLAD	0.87
6	4	pLAD	0.5
7	4	2^{nd} diagonalLAD	0.51
8	5	LCX	0.71
9	6	pLAD	0.6
10	7	mLAD	0.59
11	8	LCX	0.38
12	9	mLAD	0.92
13	10	pRCA	0.74
14	11	pLAD	0.7
15	12	mLAD	0.8
16	13	mLAD	0.77
17	13	LCX	0.72
18	14	mRCA	0.96
19	15	mLAD	0.44
20	16	mLAD	0.78
21	16	LCX	0.52
22	17	mLAD	0.83
23	17	1^{st} diagonalLAD	0.89
24	18	dRCA	0.84

Table 3.2: Data for invasive FFR measurements. Location of the lesion and FFR clinically measured are reported. Prefixes p, m, d represent the proximal, the mid and the distal tract of the coronary artery to which they are related. Nomenclature according to [128].

3.1.3 Coronary vessel segmentation and volume meshing

Besides the numerical model, another feature that is of primary importance in simulating blood flow in patient-specific setting is the reconstruction of accurate anatomic models on which the numerical methods can be applied. In the following section, we describe the definition of the computational domains for patient-specific haemodynamic modeling starting from CCTA scans. At this aim, the first step to be performed is the segmentation of anatomical structures in the available medical images. Segmentation allows the separation of information from the required target region of the image. There are different techniques used for segmentation of pixels of interest from the image. In this study, the geometry representing the vascular lumen of the coronary tracts of interest is segmented from

Figure 3.2: Visualization of the 3D computational domain for the patients included in the study.

the CCTA scans using the open-source software ITK-SNAP, [118]. ITK-SNAP provides semi-automatic segmentation exploiting active contour methods which can be defined as use of energy forces and constraints for segregation of the pixels of interest from the image

for further processing and analysis [111].

In particular, ITK-SNAP formulates the problem of segmentation in terms of active contour evolution, i.e. the evolving estimate of the structure of interest is represented by one or more contours, where the user specifies the initial contour, balances the various forces which act on it and monitors the evolution. As reported in [238], the contours are closed surfaces dependent on space and time $C(t, u, v)$ parameterized by variable u, v which evolve in time according to the partial differential equation:

$$\frac{\partial c(t, u, v)}{\partial t} = F\mathbf{n} \tag{3.1.1}$$

where $\mathbf{n}$ is the unit normal to the contour and F denotes the sum of internal and external forces acting on it in the normal direction. The internal forces derive from the contour's geometry, while the external ones are derived either from the gradient magnitude of image intensity or from voxel probability maps. Further details can be found in [238] and references therein.

The workflow of semi-automatic segmentation through ITK-SNAP is divided into three main suggested steps as described in [118, 238]. Initially, contrast should be adjusted to improve structure visualization; in general, in the case of coronary arteries, linear contrast should be between -200 and 1200. In the first stage, the user chooses thresholds which are used by the algorithm to estimate the probability that a voxel belongs to the structure of interest or is part of the background. To our purpose, the lower threshold is set to distinguish between the opacified vessel lumen and the surrounding region, while the upper threshold is set to exclude calcium deposits from the segmented vessel lumen. In the second stage, the user initializes the segmentation by placing one or more spherical seeds in the structure to be extracted. It is common to place several seeds within one structure, with an increased density near vessel bifurcations, in order to avoid gaps in the segmented image, and then let them merge into a single contour over the course of evolution. In the last stage the user can modify the parameters in the active contour evolution equation (3.1.1) and running the evolution interactively.

At this point, through a 3D view of the segmentation, it is possible to check for disconnected vessel segments and leaks. Disconnected segments should be merged by increasing the number of seeds corresponding to the gap location or lowering the lower threshold, while excessive leaks can be removed through the use of a brush tool. Once the segmentation is completed, a surface mesh in VTK format [193] can be exported for further image processing and analysis.

The polygonal surface resulting from segmentation is, in general, not directly usable for generating a computational mesh. Hence, once the lumen surface of the coronary tree of interest is available, surface processing and volume meshing are performed using the open-source library Vascular Modeling ToolKit (VMTK), [212, 6]. This open-source constitutes a collection of libraries and tools for 3D reconstruction, geometric analysis, mesh generation and surface data analysis for image-based modeling of blood vessels which allows us to generate a 3D volume mesh partitioned into tetrahedral elements.

The procedure involves some steps. The first part regards operations on the lumen surface in order to finalize the shape of the model, while the second one is devoted to the generation of a computational mesh.

As first step, the obtained lumen surface is smoothed in order to eliminate the contour leaks that may arise during segmentation due to poor image quality. Then, since inlet

and outlet sections are typically not flat, endcaps of the surface are cut reflecting the orientation of the vessel, both interactively or by using centerlines to define the cutting planes. The obtained sections are then connected to cylindrical flow extensions. In this way, circular sections are generated a few diameters upstream or downstream the region of interest, which are necessary in case of fully developed Dirichlet boundary conditions to impose velocity profile analytically.

Once the anatomical model is defined, a computational mesh is generated for the numerical solution of the partial differential equations describing blood flow. VMTK proposes an approach for automated mesh generation which plans first on forming a high quality triangulated surface mesh and then on filling the volume with tetrahedral elements. During volume meshing, sizing of the tetrahedral mesh can be provided through the specification of target tetrahedron edge size. We employ a radius-adaptive mesh in which we define the average ratio between a tetrahedra edge length and the radius of the vessel at a given location. Further details on the surface mesh processing and volume mesh generation can be found in [6].

Furthermore, since the aim of the presented study is to investigate the influence of the physical presence of a pressure wire in the clinical measurements of FFR, it is necessary to reproduce the fluid dynamics situation also in its presence. The guidewire is modeled as a curvilinear tube of given diameter (0.036 cm, according to the diameter of the pressure guidewire used in the clinical setting: Verrata Plus, Philips Volcano), created starting from the centerline of the branches in which the pressure guidewire has been inserted.

In particular, inspecting the angiography image, we can identify the route taken by the pressure guidewire inside the coronary tree under examination. Then, the corresponding path inside the anatomical model is assumed to be the centerline of the vessels in which the wire has been inserted. The centerline is then extracted using a dedicated command in VMTK. As described in [6], centerlines are determined as the weighted shortest paths traced between two external points, the source point and the target point. Then, in order to ensure that the generated lines are centered with respect to vessel cross-sections, the paths of such lines are bounded to run along the Voronoi diagram of the vessel model, that is, the place where the centers of maximal inscribed spheres are defined. In our case, the source point is taken to be the center of the inlet section of the coronary tree, whereas the target point is defined to be the the center of the outlet section where the pressure guidewire leaves the domain of interest.

The presence of the wire in the computational domain is then reproduced by performing a Boolean difference between the mere anatomical model and the resulting tube representing the catheter. This step is performed using the open source software Blender [33] under the assumption that the guidewire is always positioned along the centerline, even if it is improbable in real practice.

The last stage involves the meshing process performed using Gmsh© software [96], a three-dimensional mesh generator. Once the surface file is imported in Gmsh©, it is possible to fill that volume defined by a set of tetrahedral elements, obtaining a 3D volume mesh. Moreover, the software allows us to recognize and assign a label to the inlet and outlet sections and to the two wall surfaces, i.e., the external surface defining the lumen area and the internal wall between the blood and wire's wall.

In this way, at the end of the process, for each patient involved in the study, we produce two computational domains. The first of them represents the coronary tree

that, in whichever part it is transversely cut, has a full section. Meanwhile, the second stands for the configuration which accounts of the presence of the pressure wire, hence the cross-sections along the vessels in which the catheter has been inserted result to be perforated sections.

A schematic representation of the meshing process for the insertion of the pressure guidewire into the stenotic branch is reported in Figure 3.3.

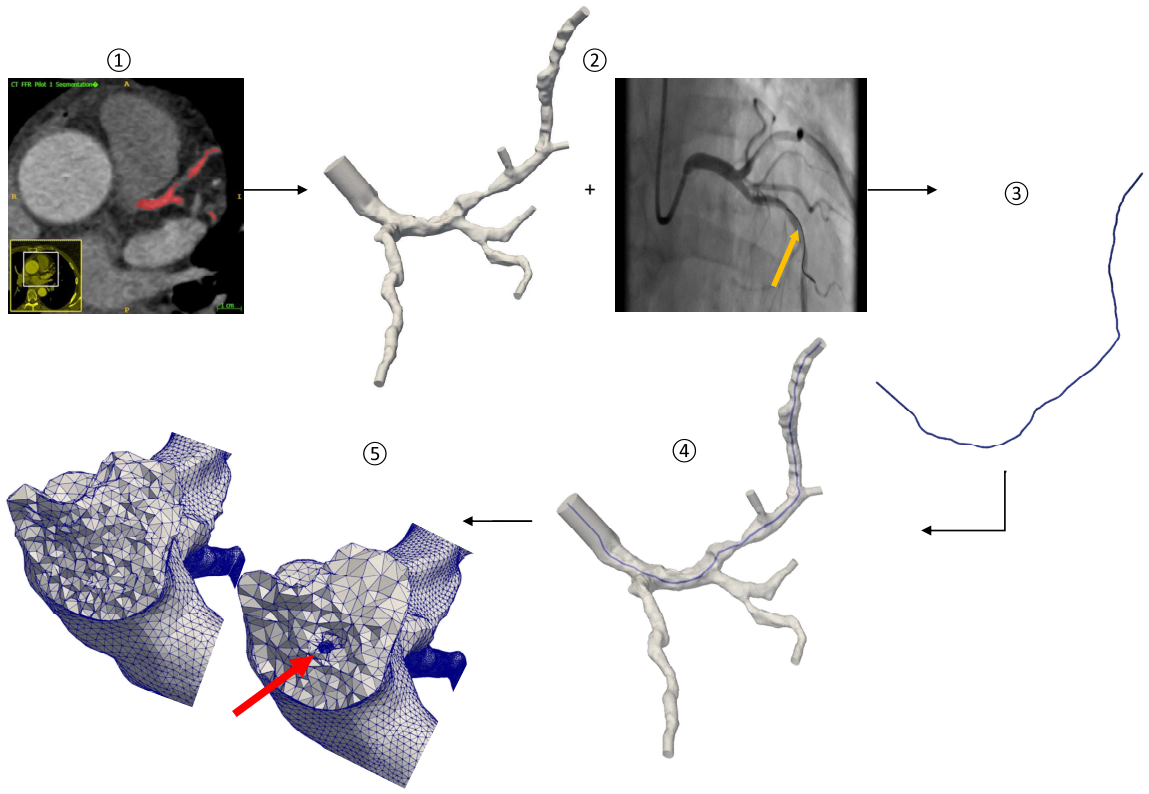

Figure 3.3: Illustration of the segmentation and meshing process: (1) coronary artery segmentation; (2) use of the anatomical model and clinical image information on the path of the guidewire to model and place the pressure guidewire inside the computational domain; (3) creation of the guidewire from the stenotic branch centerline, (4) Boolean difference between the mere coronary tree and the tube; (5) sections of both meshes, with and without the guidewire, along the vessel where the guidewire has been inserted. The red arrow highlights the region where the pressure guidewire is located.

3.2 Computational model for blood flow

Once the computational domain has been delineated, the mathematical model has to be defined. This section is devoted to outline the model employed in this chapter to reproduce blood flow within the coronary arteries, the micro-circulatory model to embody the coronary bed distal to the computational domain in order to provide physiologically sound boundary conditions and the procedure to compute the desired output.

3.2.1 Mathematical model

Mathematical modeling of the cardiovascular system features tremendous challenges, due to the amazing complexity of the cardiocirculatory system. Moreover, the blood flow in the lumen vessel is intimately connected with the vessel wall and its deformation. Hence, modeling the problem accounting for all physical features and fluid-structure interaction between blood flow and vessel wall leads to really complex models, the numerical resolution of which carries enormous computational cost. This feature does not match properly with the aim of a clinical applicability which instead requires fast and accurate prediction. For this reason, in order to provide a suitable modelization of our problem, we need to make some assumptions about blood rheology.

As stated in Chapter 1, the flow is assumed to be laminar and blood is modeled as a homogeneous incompressible Newtonian fluid with constant density 1.05 g cm^{-3} and viscosity 0.035 g cm^{-1} s^{-1}. In addition, although some works consider compliant vessels for numerical simulations in stenotic coronaries (see e.g. [179, 104]), in this work the segmented coronary tree is considered as a rigid domain, whose boundary is decomposed into the inlet section, the surface delimiting the vessel lumen jointly with the interface between the surface of the wire and the blood and N outlet sections, with $N \in \mathbb{N}$ depending on the patient, see Figure 3.4.

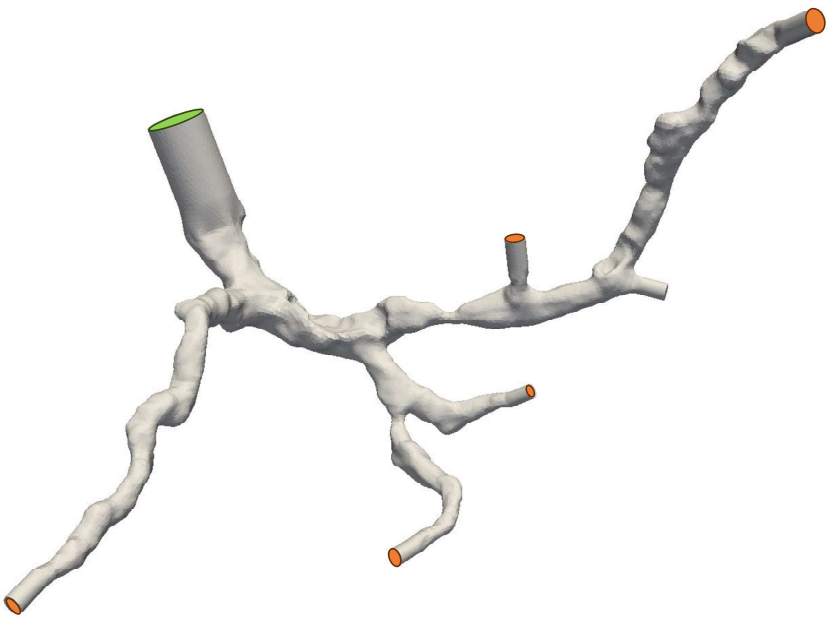

Figure 3.4: An example of 3D computational domain. The surface in gray is considered a wall-type boundary, while the inlet section and the outlet sections are colored in green and orange, respectively.

To describe the fluid dynamics, we consider the Navier-Stokes equations for incompressible flows, (1.1.1), supplemented with the initial conditions of the fluid velocity and with appropriate boundary conditions. The resulting governing equations are numerically solved exploiting the open source library CBCFLOW [76] based on the FEniCS solver [133]. In particular, CBCFLOW provides a highly efficient incompressible Navier-Stokes solver which makes use of the incremental pressure correction scheme described in [199]. The

spatial discretization is thus based on a finite element method. The velocity field is approximated using piecewise-quadratic polynomials, while linear polynomials are employed for the pressure. On the other hand, discretization in time is performed with finite differences. The solver implementation follows very closely the one reported in [147].

3.2.2 Micro-circulatory model

In recent years, remarkable efforts have been made in simulating blood flow in realistic anatomical models obtained from three dimensional medical imaging data, since accurate anatomic models are of primary importance in patient-specific blood flow simulations. Besides, it has been demonstrated that imposing physiologically sound boundary conditions plays an equally crucial role in predicting correctly velocity and pressure fields throughout the computational domain in this type of application, [228, 227, 200].

As we have done in case of the one dimensional blood blow model (see Section 2.2.7), in order to take into account the presence of micro-circulation excluded from the anatomic model, a model for the coronary bed, based on the analogy between electrical and hydraulic networks, has been adopted. In particular, the Windkessel model here considered is an improvement of that presented in Section 2.2.7, which is extended in order to reproduce some typical characteristics of the coronary bed.

The lumped parameter model we adopt is derived from the original work of Mantero et al. [140] and is depicted in Figure 3.5. In particular, it embodies the coronary bed by a single arterial path, composed of R_a, C_a, $R_{a-micro}$, and a single venous path, represented only by a resistance R_v. Specifically, R_a is the coronary arterial resistance, C_a denotes the coronary arterial compliance and $R_{a-micro}$ identifies the coronary arterial micro-circulation resistance. The two paths are then connected by the myocardial compliance C_{myo} which is affected by the time-varying left ventricular pressure p_{LV}, linked to the compliance as an additional pressure source. In this way, the increase of impedance experienced by coronary arteries due to the contraction of myocardium is replicated by the model.

The variation of volume V of the two Windkessel compartments is governed by the following ordinary differential equations

$$\begin{cases} \dfrac{dV_a}{dt} = q_{out} - \dfrac{p_a - p_{a-micro}}{R_{a-micro}}, \\ \dfrac{dV_v}{dt} = \dfrac{p_a - p_{a-micro}}{R_{a-micro}} - \dfrac{p_{a-micro} - p_v}{R_v}, \end{cases} \tag{3.2.1}$$

where p and R represent the pressure and resistance of different elements of the lumped model. Moreover, volumes relate to pressure via compliance according to

$$\begin{cases} p_a = \dfrac{V_a}{C_a}, \\ p_{a-micro} = \dfrac{V_v}{C_{myo}} + p_{LV}. \end{cases} \tag{3.2.2}$$

To numerically solve the ODE system (3.2.1) and to couple it to the three dimensional model, we follow the scheme and procedure reported in [89]. In particular, an explicit Euler scheme is used to discretize system (3.2.1) and a Python script allows CBCFLOW

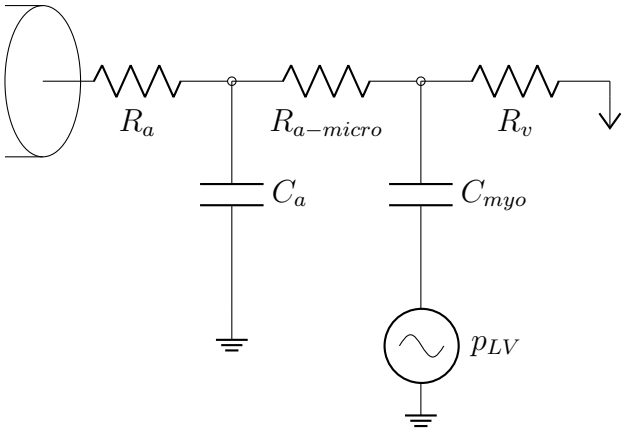

Figure 3.5: Schematic representation of the coronary bed model coupled to 3D domain outlets. R_a is the coronary arterial resistance, C_a denotes the coronary arterial compliance and $R_{a-micro}$ identifies the coronary arterial micro-circulation resistance. Additionally, C_{myo} is the myocardial compliance and R_v the coronary venous resistance. p_{LV} represents the time-varying left ventricular pressure.

to interact with the lumped parameter model and to prescribe the needed boundary conditions. At each time step, the Windkessel model receives as input the flow $q_{out,k}$ for the $k-$th outlet, which is computed as

$$q_{out,k} = \int_{\Gamma_{out,k}} \mathbf{u} \cdot \boldsymbol{n}_{out,k} \, \mathrm{dS}, \tag{3.2.3}$$

where $\boldsymbol{n}_{out,j}$ is the exterior unit-vector normal for the outlet section $\Gamma_{out,j}$. Consequently, after updated, it provides $p_{out,k}$ as

$$p_{out,k} = p_{a,k} + R_{a,k} q_{out,k} \tag{3.2.4}$$

to be imposed at the $k-$th outlet as boundary condition.

How to model hyperemia. As we have already mentioned, FFR measurements are performed during hyperemia. Maximal hyperemia is necessary to ensure the negligibility of the impact of the micro-circulatory haemodynamics on intracoronary resistance variations and it is achieved through pharmacological induction of epicardial arteries and micro-vasculature dilatation. Accordingly, the resistances in Windkessel models coupled to the three dimensional model need to be tuned in order to reproduce this condition. To extract the value of peripheral resistances in this status, two stages are involved. The first of them consists in predicting a baseline state of resting coronary haemodynamics using non-invasive clinical measurements and data. Then, the resulting pressure and flow distribution are used to compute the hyperemic peripheral resistances to be utilized in the adapted micro-circulatory models.

The modeling pipeline was first introduced by Müller et al. in [149] and involves the following steps:

- Define total baseline flow that enters the coronary tree. A total baseline flow is predicted from patient-specific cardiac output (CO) clinically measured and it is assumed to be a portion of it: $q_{tot} = 0.045$ CO, [189].

- Distribute the total baseline flow defined in the previous step among the N outlets of the coronary tree. As it is shown in [149], the flow distribution strategy results to be one of the main determinant factors to deliver a prediction in agreement with invasive measurements. Here, we exploit two different distribution flow methods. The first of them is the distal Murray method, which assumes a proportionality between the flow and outlets' vessel diameters [157],

$$q \propto d^{\xi}, \tag{3.2.5}$$

  where $\xi = 3$ from theoretical considerations on minimum work. On the other hand, in the vessel length-based method the flow is distributed among all outlets using a stem-and-crown model, which is based on allometric scaling between length of coronary arterial tree and myocardial mass [122, 115]. Noteworthy, several flow distribution criteria are available in the literature [149]. In particular, we would like to mention a method recently developed in the context of FFR prediction which splits the flow proportionally to the myocardial mass suspending the outlet vessel [59]. In this latter case, information about the volume of the left ventricle is also included. The left ventricle is segmented from CCTA scans and each selected voxel is associated to the nearest outlet according to the concept of the Voronoi diagram. Hence, the flow that leaves each outlet vessel of the coronary tree under examination is assumed to be proportional to the mass of the portion of left ventricle to which it has been associated.

- Perform a baseline steady state simulation. A steady state for the entire domain is obtained by imposing a constant pressure as inflow boundary condition and by prescribing the flow distribution obtained in the previous step as outflow Dirichlet boundary conditions. We prescribe a parabolic velocity profile, while the pressure value imposed at the inlet is taken equal to the mean aortic pressure (MAP). As suggested by [186], MAP is computed as a linear combination of diastolic blood pressure (DBP) and systolic blood pressure (SBP), both clinically measured, namely,

$$\mathrm{MAP} = \frac{2}{3}\mathrm{DBP} + \frac{1}{3}\mathrm{SBP}. \tag{3.2.6}$$

- Compute baseline peripheral coronary resistances according to the pressure and flow distribution of the resting simulation

$$R_k^{bln} = \frac{p_{out,k}^{bln} - p_v}{q_{out,k}^{bln}}, \qquad k = 1, \dots, N, \tag{3.2.7}$$

  where $p_{out,k}^{bln}$ and $q_{out,k}^{bln}$ are the pressure and flow at the k-th boundary of a total of N outlets resulting from the baseline simulation performed in the previous step and p_v is a reference venous pressure set to $p_v = 5$ mmHg.

- Compute hyperemic peripheral coronary resistances

$$R_k^{hyp} = \frac{R_k^{bln}}{\mathrm{TCRI}} \quad \text{for} \quad k = 1, \dots, N. \tag{3.2.8}$$

The Total Coronary Resistance Index (TCRI) is the factor by which peripheral coronary resistance drops from its value at baseline condition to its value in hyperemia, accounting for the effect of the drug on peripheral coronary arteries vasodilation, required to clinically measure FFR. In case of a change in resistance of normal coronary arteries, a TCRI $\backsimeq$ 4 is well suited. Hence, it represents a commonly used value for the maximal change that can be achieved in patients affected by coronary artery diseases. However, previous studies indicate that the capacity to vasodilate the coronary microcirculation is typically reduced in populations with stable coronary artery disease [119]. The explanation of this might be the fact that part of this vasodilatory capacity has been used at rest condition in order to balance the increased proximal resistance due to the lumen restriction, compensating a suffering state. The adopted pipeline assumes TCRI= 3 which results in coronary flow reserve values close to those measured on average on a population of patients with stable coronary artery disease [89].

On the other hand, the compliance to be used in the Windkessel models is derived from the total peripheral compliance, which characterizes the micro-vasculature distal to the coronary tree under examination. Total peripheral compliance is computed as a portion of the systemic arterial compliance of 1.7 mL mmHg^{-1} according to

$$C_{tot} = \frac{q_{tot}}{CO} 1.7 \tag{3.2.9}$$

and then it is distributed among outlets taking into account Murray's law, namely,

$$C_k = \frac{r_k^3}{\sum_{j=1}^{N} r_j^3} C_{tot} \quad \text{for} \quad k = 1, \dots, N. \tag{3.2.10}$$

This modelling choice is related to the fact that peripheral vascular compliance distribution is assumed to be directly proportional to flow distribution, as adopted in many modelling works, [155, 130, 159].

As depicted in Figure 3.5, each k-th Windkessel model, with $k = 1, \dots, N$, comprises three resistances, R_a, $R_{a-micro}$, R_v, and two compliances, C_a, C_{myo}. Hence, the resulting R_k^{hyp} and C_k computed in (3.2.8) and (3.2.10), respectively, must be subsequently distributed among the different components of the lumped parameter model. The fractions for distributing R_k^{hyp} among R_a, $R_{a-micro}$, R_v are 0.01, 0.84 and 0.15, respectively. In the same way, C_k is distributed among C_a and C_{myo} according to fractions 0.025 and 0.975, as reported in [89].

3.2.3 FFR prediction modeling

Computational FFR during hyperemia is calculated based on the results of a transient simulation as the ratio between the time averaged pressure at a given cross-section over the mean aortic pressure (MAP). To perform the transient simulation, we follow the methodology described in [89] and [149]. At the inlet section a properly scaled aortic pressure waveform is prescribed, while outlets are coupled to the lumped parameters models presented in Section 3.2.2, with the involved parameters tuned in order to model a hyperemic state following the reported pipeline. In addition, a no-slip condition is imposed

at the lumen surface and on the interface between the guidewire surface and the blood. The normalized aortic and left ventricle characteristic waveforms used for patient-specific simulations are shown in Figure 3.6. All the parameters required to perform hyperemic simulations are extracted from patient-specific clinical data. In particular, MAP, pulse pressure and cardiac cycle duration, extracted from clinical tracings, are used to scale the prescribed aortic and left ventricle pressure waveforms at the inlet section and in lumped parameter models coupled at the outlets, respectively.

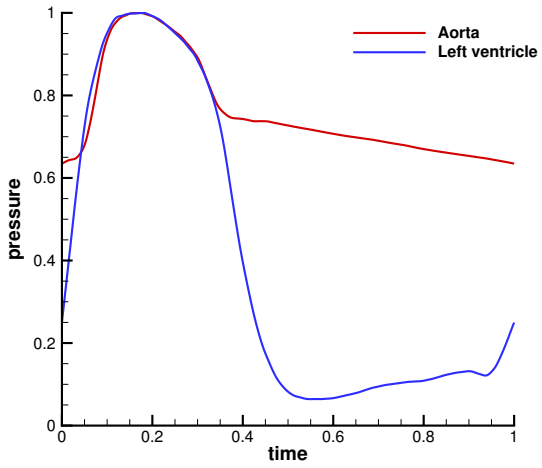

Figure 3.6: Aortic and left ventricle characteristic waveforms used for patient-specific simulations. Pressure and time are normalized values. The waveform shape is taken from [121].

We perform transient simulations considering two different settings. The first of them is called the Murray's flow setup and corresponds to a hyperemic simulation setting in which peripheral coronary resistances are extracted from baseline simulation's results with the flow distributed according Murray's law. Meanwhile, the vessel length-based flow setup refers to a hyperemic simulation setting in which peripheral coronary resistances are extracted from baseline simulation's results with the flow distributed according to the vessel length-based method. Moreover, each hyperemic simulation setting is performed twice: first on the computational domain representing the mere coronary tree and then on the computational domain which accounts of the presence of the pressure guidewire.

The flow dynamics starts from a rest condition, given by $u = 0$ and $p = 86$mmHg, and evolves in time according to a fixed time step of $\Delta t = 0.001$s. As already mentioned in Section 3.1.3, the computational meshes are composed of tetrahedral elements. The average ratio between a tetrahedral edge length and the radius of the vessel at a given location is set to 0.21 for the wire-absent configuration and to 0.18 for the wire-included configuration resulting in meshes that have on average 985181 elements. A mesh independence study was performed on two geometries with and without guidewire to verify that the adopted meshing parameter, which in turn defines the mesh elements density, yields mesh independent solutions in terms of FFR prediction. In particular, we ensure a relative error respect to solution obtained with the finest mesh to be below 10^{-2}.

Finally, the approach for non-invasive FFR prediction proposed in this study is sum-

marized as follows:

1. Define the 3D domain via ITK-SNAP segmentation of CCTA images.
2. Prepare the computational domain through surface and volume meshing.
3. Execute a baseline steady state simulation with prescribed inlet pressure and outlet flows according to the methodology described in Section 3.2.2 in order to compute hyperemic peripheral coronary resistances.
4. Perform a hyperemic transient simulation prescribing at the inlet a properly scaled aortic pressure waveform (the normalized curve is reported in Figure 3.6) and coupling, at the outlets, lumped parameter models (depicted in Figure 3.5) with the resistances computed in the previous step.
5. Estimate the FFR from the results of the hyperemic simulation performed in the fourth step.

3.3 Results and discussion

The effects of guidewire insertion on coronary haemodynamics are studied and presented for a population of 18 patients whose characteristics are reported in Table 3.1. The 24 FFR measurements collected are distributed among four different ranges of values: 0.38-0.52, 0.52-0.72, 0.72-0.84, 0.84-1. Each FFR range defines a class, we refer to class 1 as the group of the most severe stenoses, while class 4 represents the group of the less severe stenoses.

The numerical results obtained in the wire-absent and in the wire-included configuration are compared and analysed in terms of the reduction in the mean coronary hyperemic flow rate, of the difference in trans-stenotic pressure drop and of the resulting effect on computational FFR. The predicted FFR are then evaluated against the invasive FFR clinically measured. Moreover, the resulting pressure distribution and velocity field for selected patients are shown in Figures 3.7-3.8.

Guidewire insertion effect on flow discharge. To observe the guidewire flow-obstruction effects, the pulsatile flow rate is calculated at the inlet section in both conditions: with and without insertion of guidewire into the stenotic branch of each coronary tree. The presence of the pressure guidewire is reflected in a reduction of the mean total flow rate with respect to the condition without the guidewire for both flow distribution setups and for all FFR classes. In particular, the average flow reduction observed after the inclusion of the guidewire is of 4.58% ($\pm$3.23 in per cent) for Murray's flow setup and of 6.98% ($\pm$5.32 in per cent) for the vessel length-based flow setup. The average values for each FFR classes are reported in Table 3.3.

The flow discharge is intimately connected with the coronary vascular resistance. Indeed, flow across a blood vessel is governed by Ohm's Law, which states that flow equals the pressure gradient across the vessel divided by vascular resistance. As far as the blood flow entering a coronary tree is concerned, the pressure gradient is calculated as the difference between the mean pressure in the artery supplying the network minus

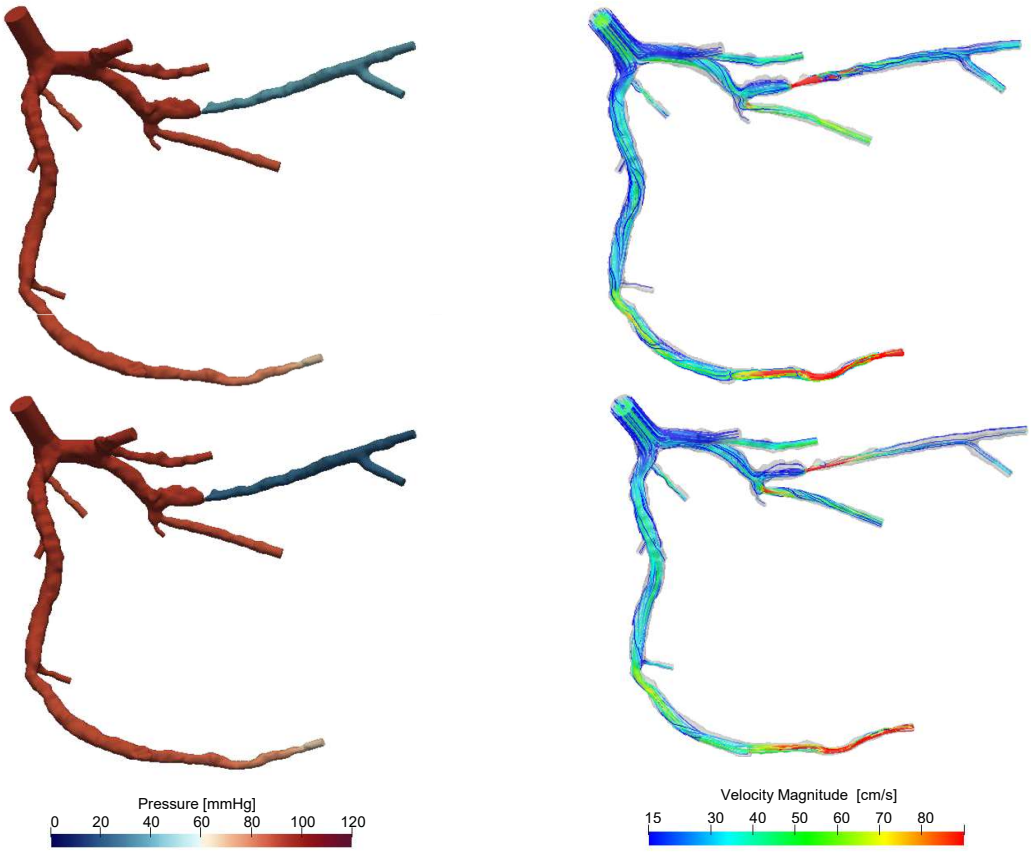

Figure 3.7: Pressure distribution (left) and velocity field (right) for patient 15 in the wire-absent configuration (top panels) and in the wire-included configuration (bottom panels).

the mean pressure at level of veins circulation. Therefore flow and resistance are inversely related. In particular, when the pressure gradient across a vascular segment remains constant, flow is reduced proportionally to an increase in resistance, and vice versa. In particular, for Murray's flow setup, the resulted total resistance rises from an average value of 26218.28 $\text{gcm}^{-4}\text{s}^{-1}$ in the wire-absent configuration to 27826.53 $\text{gcm}^{-4}\text{s}^{-1}$ when the guidewire is included in the model, leading to a percentage increase of 4.91% (±3.81 in per cent). Whereas, for the vessel length-based flow setup, the total resistance results to be on averaged equal to 27462.11417 $\text{gcm}^{-4}\text{s}^{-1}$ in the wire-absent configuration and to 30536.04169 $\text{gcm}^{-4}\text{s}^{-1}$ in the wire-included configuration with a percentage increase of 7.92% (±7.49 in per cent).

Guidewire insertion effect on trans-stenotic pressure drop. We compute the trans-stenotic pressure drop for both conditions, observing, as expected, that a reduction of the lumen contributes to increase the pressure drop. Moreover, the insertion of the pressure guidewire in the simulations enhances this drop. In the wire-included configuration we note an average increase of pressure drop of 42.23% (±9.57 in per cent) across all FFR classes in the Murray's flow setup and of 19.16% (±5.41 in per cent) using the vessel

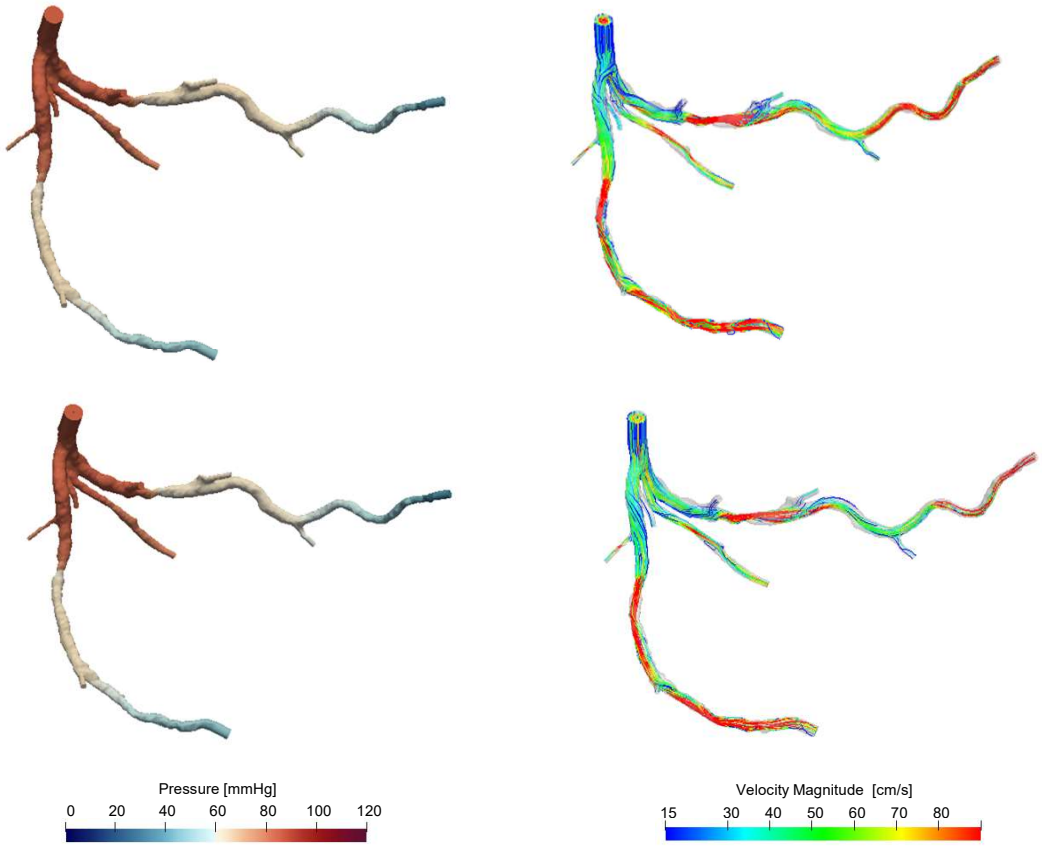

Figure 3.8: Pressure distribution (left) and velocity field (right) for patient 27 in the wire-absent configuration (top panels) and in the wire-included configuration (bottom panels).

length-based flow setup.

Guidewire insertion effect on FFR measurements. As already stated, FFR is calculated as the ratio of the pressure distal to the stenosis p_d, computed at the same location where it was clinically measured, to the pressure computed at the ostium of the coronary tree p_a. p_d and p_a are obtained as average values of the cross-sectional pressure over one cardiac cycle. We refer to FFR_{pred} as the computational FFR predicted using the wire-absent condition, while gFFR_{pred} is the computational FFR predicted using the wire-included condition. Figure 3.9 compares gFFR_{pred} against FFR_{pred} and shows the FFR_{pred}-gFFR_{pred} characteristics for all stenoses under pulsatile hyperemic flow for both flow distribution setups. We observe that the difference between FFR_{pred} and gFFR_{pred} increases as the stenosis severity increases. Furthermore, in the Murray's flow setup the value of predicted gFFR_{pred} decreases on average by 2.2%, 6.7%, 9.4%, 11.7% for class 4, class 3, class 2, class 1, respectively. The same trend is recorded also for the predicted gFFR_{pred} with the vessel length-based flow setup. In this configuration, the FFR reduction for the four ordered class after the inclusion of the wire are, respectively, 2.7%, 5.3%, 10.7% and 11.4%. The average values are reported in Table 3.3. On the other hand,

Figure 3.10 compares $gFFR_{pred}$ and FFR_{pred} against the invasive FFR and shows the FFR_{pred}-$gFFR_{pred}$ characteristics for all stenoses under pulsatile hyperemic flow for both flow distribution setups.

	Murray's flow setup		
FFR class	drop in FFR	rise in ΔP	drop in inflow
class 4	-2.18%	+39.06%	-3.21%
class 3	-6.70%	+44.34%	-5.94%
class 2	-9.40%	+47.50%	-4.47%
class 1	-11.70%	+38.00%	-4.69%
	vessel length-based flow setup		
FFR class	drop in FFR	rise in ΔP	drop in inflow
class 4	-2.71%	+19.00%	-5.56%
class 3	-5.34%	+21.84%	-5.48%
class 2	-10.73%	+19.64%	-9.94%
class 1	-11.38%	+15.24%	-6.94%

Table 3.3: For each FFR class here considered we report the mean percentage of predicted FFR drop, increase of trans-stenotic pressure drop and decrease of hyperemic flow rate which we recorded when we move from the wire-absent model to the wire-included model.

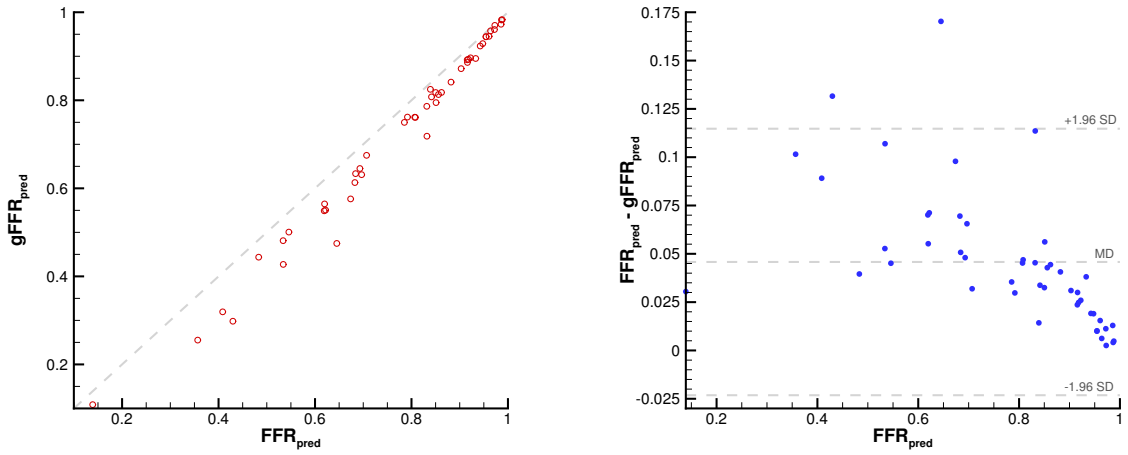

Figure 3.9: Comparison of FFR_{pred} and $gFFR_{pred}$ for both flow distribution setups. Scatter plot (left) and Bland-Altman plot (right).

The aim of providing the medical community with a diagnostic tool to guide doctor's decisions of medical treatment in case of stable CAD, makes the accuracy an essential feature of the proposed model. Sensitivity, specificity and accuracy are widely used statistics to assess the efficiency of a model as a diagnostic test, [239, 224]. If a disease is proven present in a patient and the diagnostic test indicates the presence of the disease,

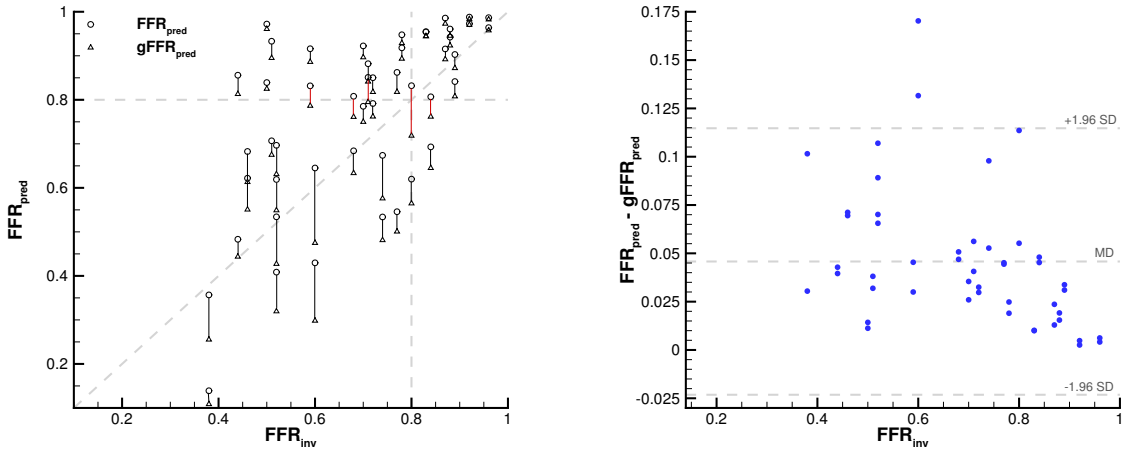

Figure 3.10: Comparison of predicted FFR in both models, wire-absent and wire-included model, and for both flow distribution setups against invasive FFR_{inv}. Scatter plot (left) and Bland-Altman plot (right). In the scatter plot the corresponding FFR_{pred} and gFFR_{pred} are connected by a line, which is colored in red in cases presenting different classification ($\mathrm{FFR} \leq 0.8$) depending on the presence, or not, of the guidewire.

then the result of the diagnostic test is considered true positive (TP). Similarly, if a disease is proven absent in a patient and the diagnostic test suggested the absence of the disease, then the test result is true negative (TN). On the other hand, if the diagnostic test indicates the presence of the disease in a patient who is healthy, the test result is classified false positive (FP). In the same way, if the result of the diagnosis test suggests the disease is absent when the patient is unhealthy, then the test result is labelled false negative (FN). Sensitivity, specificity and accuracy are described in terms of true positive (TP), true negative (TN), false negative (FN) and false positive (FP) cases as

$$\text{Sensitivity} = \frac{\text{TP}}{\text{TP+FN}}, \quad \text{Specificity} = \frac{\text{TN}}{\text{TN+FP}}, \quad \text{Accuracy} = \frac{\text{TN+TP}}{\text{TN+TP+FN+FP}}.$$

Consequently, sensitivity is the proportion of true positives that are correctly identified by a diagnostic test, thus it shows how good the test is at detecting the disease. Specificity is instead the proportion of true negatives correctly identified, hence it estimates how likely patients without disease can be correctly ruled out. Accuracy is the proportion of true results, either positive or negative, in a population and can be see as a measurement of the degree of veracity of a diagnostic test on a particular condition.

Sensitivity and specificity are independent. A test can be very specific without being sensitive, or it can be very sensitive without being specific. However, both factors are equally important. Accuracy is affected by sensitivity and specificity, but also by how common the disease in the selected population. To have a global idea of both sensitivity and specificity, we can compute the Receiver Operating Characteristic (ROC) curve by plotting the sensitivity against the difference 1-specificity starting from coordinate $(0, 0)$ and ending at coordinate $(1, 1)$, see Figure 3.11. Each point of the ROC curve represents the trade-off between sensitivity and specificity for a specific cut-points of a diagnostic

test. In an ideal situation, a perfect classification would be represented by the coordinate $(0, 1)$ which means that the diagnostic test has a sensitivity of 1 and a specificity of 1. Otherwise, a dignostic test with 0.5 sensitivity and 0.5 specificity is visualized on the diagonal going from $(0, 0)$ to $(1, 1)$. Hence, the closer the points on the ROC curve are to the ideal coordinate $(0, 1)$, the more accurate the test is. On the other hand, the closer the points on the ROC curve to the diagonal, the less accurate the test is. The area under the ROC curve (AUC) provides a way to measure the accuracy of a diagnostic test. The higher is AUC, the more accurate the diagnostic test is.

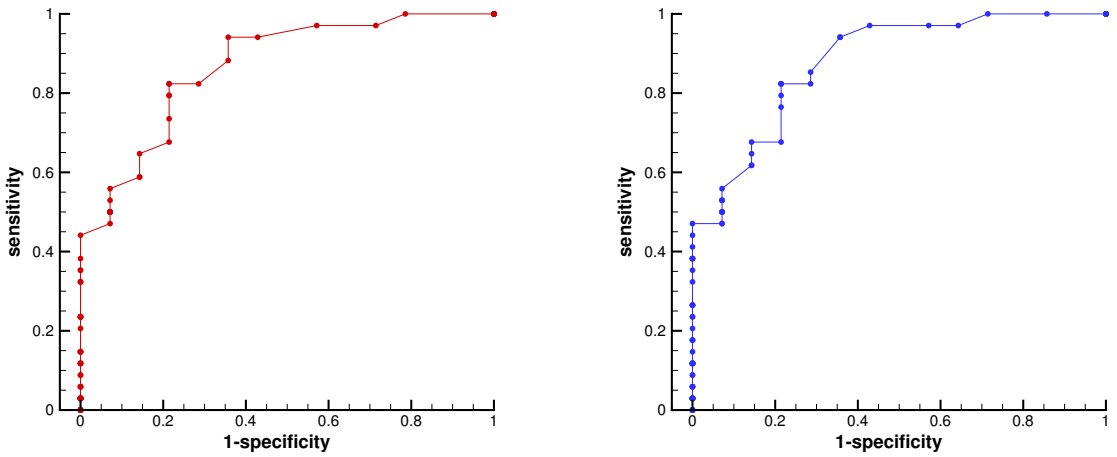

Figure 3.11: ROC curve for the wire-absent (left) and wire-included (right) configuration.

Table 3.4 reports the statistics that describe the efficiency of our model as diagnostic test, while in Figure 3.12 we have their qualitative representation highlighting with different colors true and false results predicted by the model for both configurations considered in the study. In addition, Figure 3.11 shows the obtained ROC curves for both configurations analyzed. We observe that the inclusion of the guidewire in the model leads to an overall improvement of the diagnostic capability of the model balancing accuracy, specificity and sensitivity. In addition, the bias from the clinical measured FFR drops from 0.13 to 0.08 in the Murray's law setup and from 0.03 to -0.01 in the vessel length-based flow setup when the physical presence of the pressure guidewire is taken into account.

	Murray's flow setup	
	wire-absent model	wire-included model
Sensitivity	0.35	0.53
Specificity	1.00	0.86
Accuracy	0.54	0.62
Standard deviation	0.14	0.16
Bias	0.13	0.08
AUC	0.84	0.86
	vessel length-based flow setup	
	wire-absent model	wire-included model
Sensitivity	0.76	0.82
Specificity	0.86	0.86
Accuracy	0.79	0.83
Standard deviation	0.17	0.18
Bias	0.03	-0.01
AUC	0.88	0.90

Table 3.4: Diagnostic index of wire-absent and wire-included model for both flow distribution setups. Sensitivity, specificity and accuracy are described in terms of true positive, true negative, false positive and false negative. The AUC presents the area under the Receiver Operating Characteristics curve (ROC) plotted by using sensitivity against 1-specificity for different cut-points of the diagnostic test.

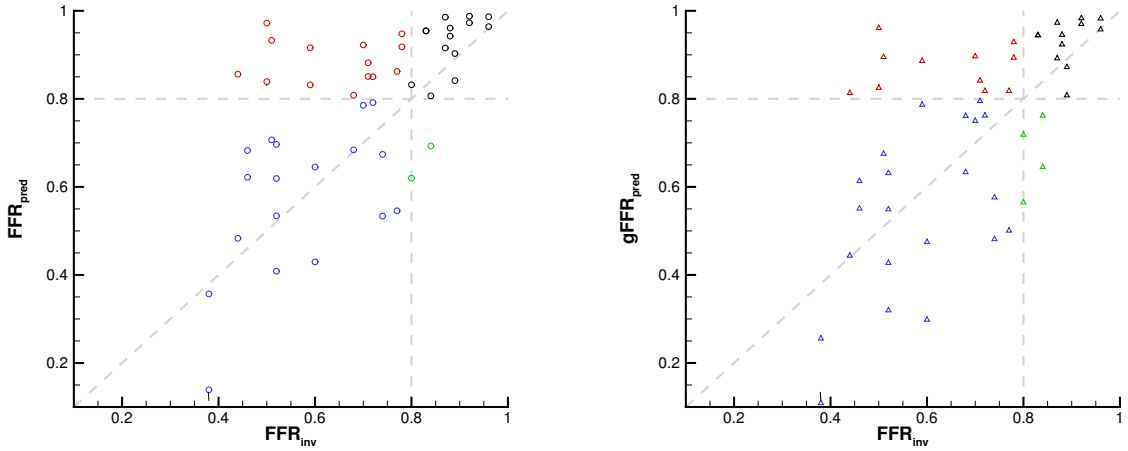

Figure 3.12: Comparison of FFR_{pred} (left) and $gFFR_{pred}$ (right) against FFR_{inv} for both flow distribution setups. The horizontal and vertical dashed lines represent the FFR cut-off value for classifying ischemia causing stenoses. False negative results are highlighted in red, false positive results are colored in green, while results correctly identified are reported in blue in case of true positive or in black in case of true negative.

Concluding remarks and limitations

In this study, we have presented a framework to perform blood flow simulations for the estimation of FFR based on clinical imaging and patient-specific characteristics with the absence and the presence of a pressure guidewire.

Analyzing and comparing the results, we can say that the introduction of the pressure guidewire in CFD simulations could play a significant role. Its presence is associated with an additional pressure loss and a decrease of flow rate, as reported in Table 3.3. These haemodynamic changes affect the prediction of FFR leading to a tendency of predicting a lower FFR value. We have observed that the FFR reduction depends on the severity of the stenosis, as it is shown in Figure 3.9. Indeed, the difference between the FFR_{pred} and the gFFR_{pred} is less prominent in cases of moderate stenosis, while it is major in more severe cases, where an averaged drop of 11.5% is recorded compared to an average reduction of 2.4% in a less severe disease status.

We can conclude that for stenoses with associated FFR included in class 4, class 2 or class 1 the impact of the pressure guidewire on stenosis evaluation and clinical decision is of less significance in clinical practice. Indeed, in the first case, the guidewire has negligible effects on predicted FFR, while, on the other hand, the presence of the wire worsens a clinical situation already severe in which the therapy to follow is already evident. The situation is different for intermediate stenoses associated with a FFR included in class 3. In this case, the presence of the pressure guidewire could change the diagnosis and a predicted FFR indicating a non-significant ischemia could drop to the "gray zone" of clinical uncertainty or even suggest the need of surgical intervention when the wire is included in the model, as it is shown in the left plot of Figure 3.10.

In conclusion, the obtained results show that the impact of accounting for the presence of the pressure guidewire in model-based FFR prediction pipelines potentially play a relevant role, especially for intermediate and severe stenoses. Including this feature in a modeling pipeline would allow to reduce modeling errors, representing more reliably the clinical setting in which FFR measurements are performed.

We highlight that some simplifications have been made and the model could be improved. First of all, the pressure guidewire is assumed to be rigid and statically placed axially along the stenotic branch. This represents an ideal situation that may not always correspond to the actual guidewire location. Indeed, in practice, the wire is an elastic structure being pushed into arteries, susceptible to unsteady blood flow and coronary deformation. Effects of different positions of the guidewire inside the vessel and a its interaction with the fluid should be then investigated.

Another limitation is due to the rigid wall assumption. Although for the application under study such assumption could be considered acceptable since the main focus of the research carried out in this chapter is to compare two scenarios (with and without guide)

both affected by the same limitation, it might be interesting to explore how the use of a fluid-structure interaction model affects the numerical results especially when the presence of the guidewire is considered.

In addition, some other modeling hypotheses should be further investigated in future works. As emerged in the study conducted in [149], the most important parameters in terms of sensitivity and uncertainty of FFR prediction coincide with the hyperemic factor and the definition of baseline flow through the coronary tree. Hence, different TCRI modelling choices as well as quantification methods of total baseline coronary flow should be analyzed. For example, a variable TCRI that accounts for lesion-induced reduced vasodilatory capacity during adenosine administration could be addressed.

Finally, we have confined the analyses to six FFR measurements for each of the four classes. A larger patient population should be considered in order to include a wider range of disease states.

Future research

The work developed in this thesis aimed at proving new numerical strategies to efficiently study the blood dynamics in the cardiovascular system, specially focused on their application to the study of the coronary artery disease. In particular, we have proposed two novel approaches: a fully implicit scheme to solve the 3D incompressible Navier-Stokes equations and a semi-implicit method for the discretization of a 1D blood flow model for networks of elastic and viscoelastic vessels. Moreover, the FEniCS library CBCFLOW based on an implicit finite element approach to solve the 3D model has also been considered and used for performing a model-based non-invasive FFR prediction for stable coronary artery disease management with real patient data. In the future, we would like to continue improving and extending the proposed methodologies to accurate and efficiently address new problems in blood flow dynamics. Therefore, to conclude, we briefly introduce some of the research lines that may be developed as part of future research:

- Extension of the implicit hybrid FV/FE scheme to an Arbitrary-Lagrangian-Eulerian framework.

  In this thesis, we have introduced and numerically solved the incompressible Navier-Stokes equations in a fixed domain and adopting an Eulerian approach, i.e., the independent spatial variables are coordinates of a fixed Eulerian system. An important step forward would be to consider a computational domain allowed to move and deform over time. This is needed in many practical situations, such as in the study of the flow inside a compliant artery, where the wall position may vary with time. Thus, the vessel wall should be let to move freely or according to a prescribed mesh motion and the inlet and outlet boundaries should instead be kept at the same spatial location along the vessel axis. With that purpose, an Arbitrary-Lagrangian-Eulerian (ALE) framework can be introduced extending the proposed implicit hybrid finite volume/finite element scheme. In fact, ALE methods are well-known for being able to solve time-dependent partial differential equations on moving meshes, thus capturing moving material interfaces and discontinuities, [37, 93, 44].

- Coupling of the implicit hybrid FV/FE scheme with a solid mechanics model.

  The wall deformations mentioned in the previous point may be related to the flow behaviour and to the properties of the walls. To capture the interplay between the fluid and a moving rigid or elastic solid body, it is of fundamental importance to address a fluid-structure interaction (FSI) problem. As a consequence, a FSI method is needed to couple the fluid and structural domains. Indeed, FSI allows the study of physical phenomena that are not easily measured and are relevant factors

in disease initiation, progression, diagnosis, or treatment, [113]. For example, a FSI model would constitute an essential tool for investigating pathological alterations of vessels wall's properties and the consequent development of a cardiovascular disease. A better quantification of coronary blood flow-induced shear stress and coronary artery motion-induced tensile strain could provide more detailed information on how coronary artery biomechanics affects arteriosclerosis development and viceversa, [144]. Another example of application would be the clinical situation addressed in Chapter 3, if one aims to study the interaction between blood flow and the pressure guidewire. In this case, a FSI model would allow to investigate the complex phenomena which occur when an elastic structure is pushed into coronaries which are themselves subjected to myocardial contraction.

In this framework, fluid and structure interact through the fluid-solid interface which coincides with both the physical fluid boundary and the internal vessel wall boundary. This results in an unknown displacement of the structure and of the fluid domain at the interface. Hence, coupled FSI models lead to nontrivial problems at both the mathematical and the numerical level. In particular, they require to manage three sources of non-linearities, i.e., geometric non-linearity, fluid constitutive non-linearity and structure constitutive non-linearity, together with two kinds of coupling, i.e., geometric adherence and physical coupling. For further details on FSI methodologies in the context of blood flow simulation, we refer to [175, 176] and references therein.

- Formulation of a geometric multiscale modelling framework.

  There are essentially three classes of models for the vascular system which have been discussed or used in this thesis: fully three-dimensional models, one-dimensional models and lumped parameter models.

  As we have already seen, the first class, i.e., 3D models, can account for many different features of blood flow problems, such as vascular wall dynamics, iteration between blood flow and wall deformation. These models are perfectly adequate for investigating qualitatively and quantitatively the effects of the geometry on the blood flow and the possible relations between local haemodynamics and the development of some pathologies, [175]. On the other hand, the high computational costs restrict their use to cover only few contiguous vascular districts.

  As we have illustrated in Chapert 2, one-dimensional models provide an optimal tool for the analysis of wave propagation phenomena in the vascular tree. In particular, they are convenient when the local flow details are less relevant than the accounting for propagative phenomena on large parts of the vascular tree and when the numerical results are needed in a relatively short time, [35, 152, 53, 234, 159, 117, 153].

  Finally, 0D models can provide a general representation of a large part or even the whole circulatory system, since they get rid of the explicit space dependence [166]. In a simple but still quantitative way, these models can include the presence of the heart, the venous system, the pulmonary circulation and the micro-circulation, [99, 100, 153].

  Trying to conserve the different advantages of each of these classes of models and to circumvent their main shortcomings, a possible approach would consist on combining

them in a geometrical multiscale approach, i.e., developing a strategy for modelling the complete circulatory system by exploiting the complementary features of the three types of models. The idea we would like to pursue as future work consists in coupling the methods proposed in Chapter 1 and Chapter 2, to form an integrated tool to simulate blood flow in the complete cardiovascular system. In this way, the higher dimensional model would be exploited in those regions where a very detailed description of the flow is required, while the 1D model, which is already coupled with 0D boundary conditions, would be applied to the remaining part of the network under study. This formulation would allow the simulation of a complete circulatory system with minimal loss of accuracy in the regions of interest while keeping a reduced total computational effort [85, 176, 32, 30].

- Extension of the semi-implicit FV scheme to an implicit formulation.

  In Chapter 1, we have seen the advantages in terms of computational costs of using an implicit scheme rather than a semi-implicit one when addressing haemodynamics within patient-specific 3D geometries. Therefore, it could be interesting to extend also the proposed one-dimensional semi-implicit finite volume scheme for blood flow in elastic and viscoelastic vessels to a fully implicit framework analyzing the potential gain in efficiency. Moreover, if we consider the coupling of this methodology with the implicit 3D solver, a fully implicit scheme for the 1D network may also be needed to avoid that any CFL-type restriction affects the global time step.

- Design of a low order model for FFR estimation.

  The FFR-based model that we have proposed in Chapter 3 is quite time consuming since it involves the use of a 3D solver. This aspect collides with the clinical applicability which requires the problem to be solved in real time. To this end, we propose the use of 1D-0D models to predict FFR. Several works, [89, 88, 31], have already assessed the predictive capabilities of one-dimensional blood flow models with respect to three-dimensional models and experimental data in the context of patient-specific coronary haemodynamics in hyperemic conditions. However, up to our knowledge, no one has yet included the presence of the pressure guidewire in the modelling pipeline. Hence, the objective will be on the development of a new one-dimensional model able to account for its presence. Then, the resulting system will be solved by extending the semi-implicit scheme proposed in Chapter 2. Finally, we would investigate the impact of the guidewire on the flow, trying to provide the medical community with an efficient, accurate and non-invasive diagnostic tool.

Appendices

Appendix A

The explicit FORCE-MH scheme for a 1D blood flow model

This appendix describes the explicit scheme employed in Section 2.4 to have a comparison with the numerical results obtained using the novel semi-implicit scheme. Having implemented both methods in a consistent manner, thus same programming language (Fortran), and run in the same computer, has allowed us to make a fair time comparison of the proposed semi-implicit scheme and a fully explicit method for the numerical tests presented in Section 2.4. In particular, we employ a FORCE MUSCL-Hancock explicit scheme to solve the blood flow equations (2.1.41) described in Section 2.1.

A.1 Mathematical model

As we have already explained, after some manipulations, the original system, (2.1.41), can be rewritten in an equivalent version given by (2.1.50) in which the pressure gradient has been split in a sum of two terms. One of them accounts for the purely elastic deformation of the vessel wall with pressure variations, while the other represents the viscoelastic behavior of the vessel wall. As we have done for the proposed semi-implicit methodology, we apply an operator splitting technique which allows us to decouple the diffusive term, represented by the second spatial derivative of the flow, from the convective terms in the momentum balance equation. In this way, system (2.2.4a) is solved in two stages:

- **Diffusive stage.** The diffusive scalar equation is given by

$$\frac{\partial q}{\partial t} - \frac{A}{\rho}\frac{\partial}{\partial x}\left(\varphi \frac{\partial q}{\partial x}\right) = 0. \tag{A.1.1}$$

  This stage is considered only if a viscoelastic vessel is analyzed, that is if $\Gamma \neq 0$ in (2.1.47). It is discretized explicitly in time according to the forward-in-time centered-in-space scheme (FTCS).

- **Convective-pressure stage.** The convective and pressure terms are solved in a

unique step and form the following subsystem:

$$\frac{\partial A}{\partial t} + \frac{\partial q}{\partial x} = 0, \tag{A.1.2a}$$

$$\frac{\partial q}{\partial t} + \frac{\partial F(q)}{\partial x} + \frac{A}{\rho}\frac{\partial \hat{p}}{\partial x} = -K_R \frac{q}{A}. \tag{A.1.2b}$$

A FORCE method combined with the Muscl-Hancock scheme (FORCE-MH), [215], is employed to discretize the aforementioned subsystem. Note that system (A.1.2) represents a blood flow model largely adopted in literature [197, 81, 103, 152, 148] when a purely elastic tube law is considered. In practice, the tube law is reduced to

$$p = p_e + \psi(A, A_0, K) = \hat{p}(A, Z) \tag{A.1.3}$$

where Z is the set of parameters specific of a given tube law and which includes the reference cross-sectional area A_0 and the stiffness parameter K. As a result of assuming constant tube law parameters, (A.1.3) satisfies the following property

$$\frac{\partial \hat{p}}{\partial x} = \frac{\partial \hat{p}}{\partial A}\frac{\partial A}{\partial x}. \tag{A.1.4}$$

Under the condition specified in (A.1.4), the convective-pressure subsystem can be rewritten in the classical form of balance laws, i.e.,

$$\frac{\partial \mathbf{Q}}{\partial t} + \frac{\partial \mathbf{F}(\mathbf{Q})}{\partial x} = \mathbf{S}(\mathbf{Q}) \tag{A.1.5}$$

with $\mathbf{Q} = (A, q)^T$ the vector of conserved variables,

$$\mathbf{F}(\mathbf{Q}) = \begin{bmatrix} q \\ \dfrac{q}{A} + \displaystyle\int_{\hat{A}}^{A} c^2(a)\,\mathrm{da} \end{bmatrix} \tag{A.1.6}$$

the physical flux function and

$$\mathbf{S}(\mathbf{Q}) = \begin{bmatrix} 0 \\ -K_R \dfrac{q}{A} \end{bmatrix} \tag{A.1.7}$$

the source term vector. Moreover, $\hat{A}$ in (A.1.6) is a reference value in order to have a definite integral in the flux expression and $c^2(A)$ is the square of the speed wave given by

$$c^2(A) = \frac{A}{\rho}\frac{\partial \hat{p}}{\partial A}. \tag{A.1.8}$$

We then introduce the Jacobian matrix of the flux vector $\mathbf{F}$,

$$\mathbf{J}(\mathbf{Q}) = \frac{\partial \mathbf{F}}{\partial \mathbf{Q}} = \begin{bmatrix} 0 & 1 \\ c^2 - u^2 & 2u \end{bmatrix}, \tag{A.1.9}$$

whose eigenvalues read

$$\lambda_1 = u - c, \quad \lambda_2 = u + c, \tag{A.1.10}$$

with corresponding right eigenvectors

$$\mathbf{R}_1 = \gamma_1 \begin{bmatrix} 1 \\ u - c \end{bmatrix}, \quad \mathbf{R}_2 = \gamma_2 \begin{bmatrix} 1 \\ u + c \end{bmatrix}, \tag{A.1.11}$$

for arbitrary scaling factors $\gamma_1, \gamma_2 \in \mathbb{R}$. From this analysis, under suitable assumptions for coefficients m and n in $\hat{p}(A, Z)$, we know system (A.1.2) to be strictly hyperbolic. Furthermore, both λ_1- and λ_2-characteristic fields are genuinely nonlinear and, therefore, they are associated with shocks and rarefaction waves. The generalized Riemann invariants associated with the genuinely nonlinear fields are the following:

$$\Lambda_1 = u + \int_{\hat{A}}^{A} \frac{c(a)}{a}\,\mathrm{da}, \quad \Lambda_2 = u - \int_{\hat{A}}^{A} \frac{c(a)}{a}\,\mathrm{da}, \tag{A.1.12}$$

where Λ_1 is associated with the left wave, while Λ_2 with the right one. This eigenstructure analysis will be necessary to define suitable boundary conditions to be prescribed at the inlets and outlets of vessels. For a detailed analysis we refer to [215].

A.2 Numerical discretization

In order to approximate the solutions of (2.1.50), we first need to introduce a discretization of the spacial computational domain. In contrast to what we have done to derive the semi-implicit methodology, here we employ an unstaggered computational grid. Hence, only the primal mesh introduced in Section 2.2.1 is built. Consequently, the one-dimensional domain $[0, L]$ is divided into a total of N_p non-overlapping control volumes with uniform length $\Delta x = x_{i+\frac{1}{2}} - x_{i-\frac{1}{2}}$ and all the discretized unknowns of (2.1.50) are computed at the barycenter x_i of each cell $C_i \equiv [x_{i-\frac{1}{2}}, x_{i+\frac{1}{2}}]$. The time domain $[0, t_{\text{end}}]$ is also discretized into a discrete set of temporal levels with time step $\Delta t = t^{n+1} - t^n$ constrained by a proper CFL stability condition that will be later specified.

The explicit methodology involves first the solution of the diffusive subsystem, (A.1.1), providing an intermediate approximation of q, q^*, which accounts only for the diffusive terms. Then, the result is used within the convective-pressure system, (A.1.2), obtaining the final approximation of q and A at time t^{n+1}. Finally, the pressure at the new time is recovered thanks to (2.1.45) using A^{n+1}.

A.2.1 Diffusive stage

An explicit finite volume approach is employed in order to treat the diffusion term and solve the corresponding scalar equation (A.1.1). To this end, we propose again the forward in time centered in space scheme (FTCS) which has already been introduced in Section 2.2.3 as an alternative to the use of an implicit scheme for the solution of the

diffusive subsystem. Accordingly, the discretization of the diffusive equation yields

$$q_i^* = q_i^n + \frac{\Delta t}{\Delta x}\frac{A_i^n}{\rho}\left(\varphi_{i+\frac{1}{2}}^n \frac{q_{i+1}^n - q_i^n}{\Delta x} - \varphi_{i-\frac{1}{2}}^n \frac{q_i^n - q_{i-1}^n}{\Delta x}\right), \tag{A.2.1}$$

where

$$\varphi_{i-\frac{1}{2}}^n = \frac{\varphi(A_{i-1}^n) + \varphi(A_i^n)}{2}, \quad \varphi_{i+\frac{1}{2}}^n = \frac{\varphi(A_i^n) + \varphi(A_{i+1}^n)}{2}, \tag{A.2.2}$$

and q^* represents the intermediate approximation of q^{n+1} accounting only for the diffusive terms. Since we are exploiting an explicit methodology, the scheme (A.2.1) must satisfy a stability condition characterized by the classical CFL restriction which in this case reads

$$2 \max_{i\in\{1,\dots,N_p\}} \left(\frac{A_i}{\rho \Delta x^2}\varphi_{i+\frac{1}{2}}\right)\Delta t < \text{CFL}, \tag{A.2.3}$$

with $\text{CFL} \leq 1$.

A.2.2 Convective-pressure stage

Once the intermediate solution q^* is obtained within the diffusive stage, we can address system (A.1.2) following an explicit finite volume scheme. We integrate (A.1.2) on a control volume $V_i = C_i \times [t^n, t^{n+1}]$ and introduce suitable approximations of the integral averages. Accordingly, to evolve the numerical solution to time $t^{n+1} = t^n + \Delta t$ we employ the following discrete relation

$$\mathbf{Q}_i^{n+1} = \mathbf{Q}_i^* - \frac{\Delta t}{\Delta x}\left(\mathbf{F}_{i+\frac{1}{2}} - \mathbf{F}_{i-\frac{1}{2}}\right) + \Delta t\, \mathbf{S}_i \tag{A.2.4}$$

where $\mathbf{F}_{i+\frac{1}{2}}$ denotes an approximation of the time integral average over $[t^n, t^{n+1}]$ of the physical flux given by (A.1.6) at the primal cell interface $x_{i+\frac{1}{2}}$, while $\mathbf{S}_i$ is the approximated volume integral average over the control volume V_i of the source term $\mathbf{S}$ given by (A.1.7). It is important to highlight that the first component of $\mathbf{Q}_i^*$ is the area obtained at the previous time step, A_i^n, while its second component corresponds to the intermediate solution q_i^*, which updates q_i^n by considering only the diffusive terms, hence $\mathbf{Q}_i^* = (A_i^n, q_i^*)^T$.

The integrals in (A.2.4) are approximated according to the FORCE-MUSCL-Hancock approach, where the FORCE method is combined with the MUSCL-Hancock (Monotonic Upstream-Centred Scheme for Conservation Laws) scheme to achieve second order of accuracy. The MUSCL-Hancock method, originally proposed in [127] and formulated to deal only with conservation laws without source terms, has been then extended to account also for the source terms employing the ADER approach (Arbitrary high-order DERivatives Riemann solver), [51].

In the FORCE-MUSCL-Hancock framework, the computation of the intercell flux $\mathbf{F}_{i+\frac{1}{2}}$ involves the following four steps:

Step 1. Data reconstruction. We consider a reconstruction of the data in terms of first-degree polynomials. The reconstruction polynomial vector $\Phi_i(x)$ is defined for each cell C_i by finding a linear polynomial for each component of the vector of conserved variables, that is,

$$\phi_{i,k}(x) = Q_{i,k}^* + (x - x_i)\Delta_{i,k}^*, \quad \text{for } k = 1, 2, \tag{A.2.5}$$

where $Q^*_{i,k}$ is the $k-$th component of $\mathbf{Q}^*_i$ and $\Delta^*_{i,k}$ denotes the associated slope. To circumvent Godunov's theorem, we consider a non-linear reconstruction of the slopes. More precisely, the ENO (Essentially Non-Oscillatory) interpolation method, [109], is applied within the polynomial reconstruction step. Consequently, the slopes are adaptively chosen as follows:

$$\Delta^*_{i,k} = \begin{cases} \Delta^*_{i,k\,C} = \dfrac{Q^*_{i+1,k} - Q^*_{i-1,k}}{2\Delta x}, & \text{if } |\Delta^*_{i,k\,C}| = \min\{|\Delta^*_{i,k\,C}|, |\Delta^*_{i,k\,U}|, |\Delta^*_{i,k\,D}|\}, \\ \Delta^*_{i,k\,U} = \dfrac{Q^*_{i+1,k} - Q^*_{i,k}}{\Delta x}, & \text{if } |\Delta^*_{i,k\,U}| = \min\{|\Delta^*_{i,k\,C}|, |\Delta^*_{i,k\,U}|, |\Delta^*_{i,k\,D}|\}, \\ \Delta^*_{i,k\,D} = \dfrac{Q^*_{i,k} - Q^*_{i-1,k}}{\Delta x}, & \text{if } |\Delta^*_{i,k\,D}| = \min\{|\Delta^*_{i,k\,C}|, |\Delta^*_{i,k\,U}|, |\Delta^*_{i,k\,D}|\}. \end{cases} \tag{A.2.6}$$

Step 2. Computation of boundary extrapolated values. The boundary extrapolated values are computed by simply evaluating the polynomials appropriately:

$$\mathbf{Q}^L_i = \Phi_i\left(x_{i-\frac{1}{2}}\right), \quad \mathbf{Q}^R_i = \Phi_i\left(x_{i+\frac{1}{2}}\right). \tag{A.2.7}$$

Step 3. Evolution of boundary extrapolated values. Boundary-extrapolated values are evolved by half a time step accounting for the source term:

$$\begin{aligned} \overline{\mathbf{Q}}^L_i &= \mathbf{Q}^L_i - \frac{\Delta t}{2\Delta x}\left(\mathbf{F}(\mathbf{Q}^R_i) - \mathbf{F}(\mathbf{Q}^L_i)\right) + \frac{\Delta t}{2}\mathbf{S}(\mathbf{Q}^L_i), \\ \overline{\mathbf{Q}}^R_i &= \mathbf{Q}^R_i - \frac{\Delta t}{2\Delta x}\left(\mathbf{F}(\mathbf{Q}^R_i) - \mathbf{F}(\mathbf{Q}^L_i)\right) + \frac{\Delta t}{2}\mathbf{S}(\mathbf{Q}^R_i). \end{aligned} \tag{A.2.8}$$

Step 4. Computation of the numerical flux. The intercell numerical flux is based on the evolved boundary extrapolated values (A.2.8) and it is computed according to the FORCE flux function introduced by Toro and Billett in [216]. It is defined as the mean of Lax-Friedrichs flux and Lax-Wendroff flux, i.e.,

$$\mathbf{F}^{FO}_{i+\frac{1}{2}} = \frac{1}{2}\left(\mathbf{F}^{LF}_{i+\frac{1}{2}} + \mathbf{F}^{LW}_{i+\frac{1}{2}}\right) \tag{A.2.9}$$

where

$$\mathbf{F}^{LF}_{i+\frac{1}{2}} = \frac{1}{2}\left(\mathbf{F}\left(\overline{\mathbf{Q}}^R_i\right) + \mathbf{F}\left(\overline{\mathbf{Q}}^L_{i+1}\right)\right) - \frac{1}{2}\frac{\Delta x}{\Delta t}\left(\overline{\mathbf{Q}}^L_{i+1} - \overline{\mathbf{Q}}^R_i\right) \tag{A.2.10}$$

and

$$\mathbf{F}^{LW}_{i+\frac{1}{2}} = \frac{1}{2}\left(\overline{\mathbf{Q}}^R_i + \overline{\mathbf{Q}}^L_{i+1}\right) - \frac{1}{2}\frac{\Delta x}{\Delta t}\left(\mathbf{F}\left(\overline{\mathbf{Q}}^L_{i+1}\right) - \mathbf{F}\left(\overline{\mathbf{Q}}^R_i\right)\right). \tag{A.2.11}$$

Finally, we compute the numerical source $\mathbf{S}_i$ following the ADER approach. Accordingly, it is obtained by approximating the volume-integral average of the source term exploiting the midpoint rule in space and time, where the midpoint value $\mathbf{Q}\left(x_i, \frac{1}{2}\Delta t\right)$ is computed by performing a Taylor series expansion in time and applying the Cauchy-Kovalevskaya procedure at point x_i. Hence, we get

$$\mathbf{S}_i = \mathbf{S}\left(\mathbf{Q}^*_i + \frac{\Delta t}{2}(-\mathbf{J}(\mathbf{Q}^*_i)\Delta^*_i + \mathbf{S}(\mathbf{Q}^*_i))\right), \tag{A.2.12}$$

with $\mathbf{J}(\mathbf{Q}_i^*)$ the Jacobian matrix of the flux given by (A.1.9) and Δ_i^* the ENO slope defined in (A.2.6).

The resulting scheme can be proven to be second order accurate in space and time. Since an explicit methodology has been adopted, the method will be stable under the CFL condition

$$\max_{i\in\{1,\dots,N_p\}} \left(\frac{2|u_i^n|}{\Delta x}\right) \Delta t \leq \text{CFL}. \tag{A.2.13}$$

where CFL indicates the standard Courant-Friedrichs-Lax number satisfying $0 < \text{CFL} \leq \frac{1}{2}$.

Once $\mathbf{Q}_i^*$ is evolved in time according to (A.2.4) where the numerical flux is given by (A.2.9) and the numerical source is computed under (A.2.12), we finally get the conserved variables at the new time, namely A_i^{n+1} and q_i^{n+1}. Besides, the averaged pressure at each primal cell, p_i^{n+1}, can be recovered from the cross-sectional area A_i^{n+1} exploiting relation (2.1.45).

Note that if $\Gamma = 0$, i.e. a pure elastic vessel is considered, the diffusive stage is no longer needed. Consequently, only the convective-pressure stage needs to be solved and the second component of $\mathbf{Q}_i^*$ in (A.2.4) will coincide with q_i^n, that is, $q_i^* = q_i^n$.

A.2.3 Boundary conditions and networks of vessels

In this section, we present the major key points to treat the different boundary conditions to be employed in the test cases analyzed in Section 1.7 and the strategy adopted to define suitable coupling conditions at the vessel junctions.

Boundary conditions

In contrast to the semi-implicit scheme described in Chapter 2, the conserved variables, A_{BC}^n and q_{BC}^n, need to be prescribed at the boundary of a vessel. To impose Dirichlet boundary conditions, the computational domain is augmented with two additional ghost cells placed before and after the first and last cell, respectively. Then, proper values of the conserved variables at the boundary state are defined according to the generalized Riemann invariants framework. In particular, one of the conserved variables is supposed to be known at the boundary, enforced or provided by an additional algebraic relation to be satisfied at the boundary. Then, the other variable is determined by imposing the continuity of the generalized Riemann invariant Λ_2, if we are at the left boundary interface, or Λ_1, if located at the right one, between the boundary state $(A_{BC}^n, q_{BC}^n)^T$ and the corresponding initial condition state.

In practice, if we identify with index i a terminal cell and we want to impose the mass flux q_{BC}^n at the boundary interface at time t^n, then the unknown cross-sectional area A_{BC}^n is the solution of the nonlinear equation

$$\frac{q_{BC}^n}{A_{BC}^n} - \frac{q_i^n}{A_i^n} + \varsigma \int_{A_i^n}^{A_{BC}^n} \frac{c(a)}{a}\,\mathrm{da} = 0 \tag{A.2.14}$$

where ς is a sign function, set to $\varsigma = -1$ if we are at the left boundary interface or $\varsigma = 1$ if we are instead at the right one, according to (A.1.12). On the other hand, if we want to

impose the pressure at the boundary, then A^n_{BC} is recovered from the known p^n_{BC} exploiting (2.1.45), while the unknown flux q^n_{BC} is computed according to (A.2.14).

As explained in Section 2.2.7, in blood flow simulations terminal vessels are usually connected to single-resistance elements or RCR Windkessel models in order to take into account the effect of microcirculation distal to the computational domain. At the boundary interface between the vessel and the attached terminal element, the relation (2.2.49) holds, which in this context can be rewritten as

$$q^n_{BC} = \frac{p(A^n_{BC}) - p_w}{R_1} \tag{A.2.15}$$

where p_w and R_1 are the pressure in the Windkessel model and its proximal resistance, respectively. Then, once again, by replacing (A.2.15) for q^n_{BC} in (A.2.14), we obtain a non-linear equation to be solved in the only unknown A^n_{BC}.

Junction model

Single 1D vessel domains can be coupled through junction models to construct networks of vessels. The adopted junction model for the FORCE-MH approach is the 0D junction approach described in Section 2.3.2. Consequently, the network is seen as a set of parallel vessels which do not communicate to each other except through algebraic coupling conditions. These coupling relations are derived from physical hypothesis, as the continuity of mass and total pressure, equations (2.3.17) and (2.3.18), respectively, and from modeling assumptions, in particular the constancy of generalized Riemann invariants which are assumed through (2.3.20). The solution of the resulting algebraic system provides the values of q_{BC} and A_{BC} to be imposed at the boundary state.

Appendix B

Scientific publications

The main original research developed in this thesis has been presented in the following scientific publications:

- Alessia Lucca, Saray Busto, and Michael Dumbser. "An implicit staggered hybrid finite volume/finite element solver for the incompressible Navier-Stokes equations". In: *East Asian Journal on Applied Mathematics 13* (2023), pp. 671–716.
- Alessia Lucca, Saray Busto, Lucas O. Müller, Eleuterio F. Toro and Michael Dumbser. "A semi-implicit finite volume scheme for blood flow in elastic and viscoelastic vessels". In: *Journal of Computational Physics*, (2023).
- Alessia Lucca, Luigi Fraccarollo, Fredrik E. Fossan, Anders T. Bråten, Silvia Pozzi, Christian Vergara, and Lucas O. Müller. "Impact of pressure guidewire on model-based FFR prediction". Submitted to: *Cardiovascular Engineering and Technology* (2023).

Appendix C

Summary

The simulation of blood flow dynamics in the human cardiovascular system has become a major field of research during the last decades, [87, 176]. This effort is motivated mainly by the fact that cardiovascular diseases are responsible for a large percentage of early mortality in industrialized societies, [165]. The advancements in the power of modern computers, the progress in imaging and geometry extraction techniques as well as the development of better numerical algorithms make cardiovascular modeling an invaluable tool for the interpretation and analysis of the circulatory system functionality, in both physiological and pathological situations.

The mathematical modelling of the cardiovascular system is, however, still an incredibly challenging problem. The vascular networks are closed, tortuous multi-generation systems of branching and merging junctions of deformable vessels with widely different diameters and lengths, making its treatment as a whole unfeasible. It is then useful to identify a hierarchy of models, each one suited for a different type of investigation or to different parts of the system. Following this idea, in the first part of this thesis, we propose two different space scale numerical strategies for blood flow simulations in complex vascular geometries.

On the one hand, for a detailed study of the flow, we propose a novel fully implicit hybrid finite volume/finite element (FV/FE) method for the solution of incompressible flows in 2D and 3D unstructured staggered grids. Following the semi-implicit hybrid method in [24, 46, 185], the proposed approach performs an adequate flux-vector splitting of the governing PDE system, which results in the decoupling of the bulk flow velocity from the fast sound waves. Then, the pressure field is computed by deriving a Poisson-type equation from the mass and momentum conservation equations. Meanwhile, the velocity field is approximated solving a proper transport-diffusion subsystem complemented with a pressure correction stage where the velocity is updated using the new pressure in order to ensure a divergence-free velocity field. The method relies on the use of a primal triangular/tetrahedral mesh for the implicit discretization of the pressure subsystem according to a classical finite element method, while the convective-viscous subsystem is solved on a edge-based/face-based staggered dual mesh exploiting an implicit finite volume scheme for the convective terms combined with a Galerkin approach, employing Crouzeix-Raviart basis functions, to handle diffusion terms. The main concern of the former semi-implicit methodology, when addressing haemodynamics in complex 3D geometries, is that it results too computational demanding, even if the time step restriction, imposed by

the CFL condition, is less restrictive than for fully explicit schemes since it only depends on the bulk velocity. The new fully implicit approach overcomes this issue. Since it is unconditionally stable, it allows larger time steps leading to a considerable computational gain.

The most significant innovations in the implicit hybrid methodology concern the convective-viscous subsystem. Its implicit discretization leads to a nonlinear and nonsymmetric system which is solved with the aid of a Newton-Krylov approach. Specifically, we employ an inexact Newton algorithm combined with one of the following Krylov subspace methods: either a generalized minimal residual approach (GMRES) [188] or a stabilized biconjugate gradient algorithm (BiCGStab) [223]. Moreover, the use of the LU factorization symmetric Gauss-Seidel preconditioner, together with a proper reordering of the nodes, is also proposed in order to improve the convergence behavior of these iterative algorithms, [73, 63].

Even if 3D solvers provide an accurate tool to solve the Navier-Stokes equations, their use is not always feasible in the study of blood flow. The large number of vessels involved and the multitude of different length scales required to accurately reproduce haemodynamics in the various regions of the cardiovascular system make blood flow simulations based on full physics-based models very challenging in terms of computational effort.

A natural step towards the development of a numerical strategy able to simulate a complete cardiovascular network is the use of lower order models which are designed to retain the essential features of blood flow while reducing the dimension and, therefore, the final cost of a whole network simulation. Accordingly, we develop a novel staggered semi-implicit finite volume method for the simulation of one-dimensional blood flow in networks of elastic and viscoelastic vessels. The one-dimensional blood flow model is derived from the incompressible Navier-Stokes equations, specifying a viscoelastic behaviour of the vessel wall deformation. Then, following the idea behind the fully implicit hybrid finite volume/finite element method, a splitting strategy is applied dividing the original system into two subsystems and allowing thus the decoupling of the mean flow velocity and pressure waves computation, [167, 219]. Then, the equation dominated by convection effects is efficiently solved using an explicit algorithm, while the second subsystem, related to the pressure, is approximated using an implicit scheme. As such the CFL condition of the overall algorithm is independent of the pressure waves and thus the time step is larger than in a fully explicit approach. Besides, a viscoelastic model embodied by the Kelvin-Voigt unit is considered to define pressure-cross sectional area relation. One of the most significant numerical difficulties we encounter when addressing viscoelastic wall models is the time step restriction that may result from an explicit discretization of the parabolic terms. To circumvent this issue, we again apply an operator splitting strategy to decouple the pure convective terms and the diffusive terms. Consequently, we end up with a simple and computationally efficient algorithm, where the hyperbolic convective terms of the governing equations are discretized explicitly, while the viscous parabolic terms and the elliptic pressure terms are treated implicitly.

To extend the one-dimensional methodology to networks of vessels, we incorporate a proper description of flow motion at the bifurcation. In contrast with the widespread choice of decomposing the domain and treating the junction as a single point, ignoring the bifurcation angle [197, 83, 141, 158], we introduce a novel highly simplified three-

dimensional approach. Within the proposed methodology, the junction is represented as a single three-dimensional cell to be modeled using the Euler equations and its discretization is fully coupled to the proposed semi-implicit method used for 1D vessels. In this way, the proposed junction model accounts for the minimum set of essential geometrical features that describe the junction, namely the normal vectors of all incident vessels and their corresponding cross-sectional areas.

Therefore, the main improvements of the new approach compared to existing semi-implicit schemes for flows in compliant vessels are: the extension of the type of tube law from arteries to veins, the addition of viscoelastic effects and the development of a new simplified 3D approach to describe junctions.

In the second part of the thesis, we focus on the modeling and simulation of coronary blood flow, with emphasis on stable Coronary Artery Disease (CAD), the pathological condition which occurs when an abnormal narrowing is built within the vessel wall. In case of stable CAD, the current gold standard for diagnosis of functional significance of coronary stenoses is the Fractional Flow Reserve (FFR). FFR measures invasively the trans-stenotic pressure drop under drug-induced hyperemia, i.e. maximal blood flow is induced by administration of vasodilatory drugs, such as adenosine or papaverine. In particular, a guiding wire equipped with a pressure sensor is inserted into the coronary artery to record the pressure at ostium and the pressure distal to the lesion. FFR is then determined as a ratio of the mean values of pressure tracings and takes values between 0, standing for a complete occlusion of the vessel, and 1, corresponding to a healthy patient. The obtained measurements are then compared against FFR thresholds defined in order to guide the therapy and to decide whether a surgical procedure is needed or if patients can just be treated with optimal medical therapy.

To avoid this invasive procedure and its associated cost, primary due to the need of trained internationalists, medical facilities availability and expensive medical device/equipment, we propose a methodology that, departing from clinical images and non-invasive data, allows to predict FFR by means of three-dimensional patient-specific simulations. Several CCTA-derived FFR models have been proposed in literature and most of them neglect the potential influence of the guidewire on the computed flow and pressure. Although its small size, studies conducted both in vitro [10] and computationally with idealized geometries and in a patient-specific domain [235] have shown that the haemodynamic alteration caused by the presence of the guidewire, can lead to an underestimation of the predicted FFR. To overcome this issue, we extend the CCTA-based FFR model proposed by Fossan et al. [89] and Müller et al. [149] to incorporate the presence of catheter in the FFR modeling pipeline analyzing its impact on local fluid dynamics and FFR prediction. In order to reproduce the fluid dynamics in the presence of the wire, a specific mesh is created. The guidewire is modeled as a curvilinear tube of given diameter created starting from the centerline of the branches in which the pressure guidewire has been inserted. Then, its presence inside the computational domain is reproduced by performing a Boolean difference between the mere anatomical model and the resulting tube representing the catheter. In this way, for each patient involved in the study, two computational domains are available. The first of them represents the coronary tree that, in whichever part it is transversely cut, has a full section. Meanwhile, the second stands for the configuration which accounts of the presence of the pressure wire, hence the cross-sections along the vessels in which the catheter has been inserted result to be perforated sections.

In order to investigate this modeling feature, we exploit the open-source library CBCFLOW based on the FEniCS solver which allows us to efficiently solve the incompressible Navier-Stokes equations in complex three dimensional coronary trees. Accordingly, three-dimensional simulations in the configuration with and without the presence of the pressure guidewire on a sample of 18 patients with suspected stable CAD are performed. Flow rates, pressure distributions and predicted FFR in both configurations are then analyzed and compared.

Bibliography

[1] R. Abgrall. "A general framework to construct schemes satisfying additional conservation relations. Application to entropy conservative and entropy dissipative schemes". In: *Journal of Computational Physics* 372 (2018), pp. 640–666.

[2] F.B. Ahmad and R.N. Anderson. "The Leading Causes of Death in the US for 2020". In: *JAMA* 325.18 (2021), pp. 1829–1830.

[3] J. Alastruey, A.W. Khir, K.S. Matthys, P. Segers, S.J Sherwin, P.R Verdonck, K.H. Parker, and J. Peiró. "Pulse wave propagation in a model human arterial network: assessment of 1-D visco-elastic simulations against in vitro measurements". In: *Journal of biomechanics* 44.12 (2011), pp. 2250–2258.

[4] J. Alastruey, K.H. Parker, J. Peiró, and S.J. Sherwin. "Lumped Parameter Outflow Models for 1-D Blood Flow Simulations: Effect on Pulse Waves and Parameter Estimation". In: *Communications in Computational Physics* 4 (2008), pp. 317–336.

[5] S. Albensoeder and H.C. Kuhlmann. "Accurate three-dimensional lid-driven cavity flow". In: *Journal of Computational Physics* 206.2 (2005), pp. 536–558.

[6] L. Antiga, M. Piccinelli, L. Botti, B. Ene-Iordache, A. Remuzzi, and D.A. Steinman. "An image-based modeling framework for patient-specific computational hemodynamics". In: *Medical & biological engineering & computing* 46.11 (2008), pp. 1097–1112.

[7] B.F. Armaly, F. Durst, J.C.F. Pereira, and B. Schönung. "Experimental and theoretical investigation of backward-facing step flow". In: *Journal of fluid Mechanics* 127 (1983), pp. 473–496.

[8] R.L. Armentano, J.G. Barra, J. Levenson, A. Simon, and R.H. Pichel. "Arterial wall mechanics in conscious dogs: assessment of viscous, inertial, and elastic moduli to characterize aortic wall behavior". In: *Circulation research* 76.3 (1995), pp. 468–478.

[9] V.I. Arnold. "Sur la topologie des écoulements stationnaires des fluides parfaits". In: *Vladimir I. Arnold-Collected Works*. Springer, 1965, pp. 15–18.

[10] K.D. Ashtekar, L.H. Back, S.F. Khoury, and R.K. Banerjee. "In Vitro Quantification of Guidewire Flow-Obstruction Effect in Model Coronary Stenoses for Interventional Diagnostic Procedure". In: *Journal of Medical Devices* 1.3 (2007), pp. 185–196.

[11] A.C.L. Barnard, W.A. Hunt, W.P. Timlake, and E. Varley. "A Theory of Fluid Flow in Compliant Tubes". In: *Biophysical Journal* 6.6 (1966), pp. 717–724.

[12] T. Barth and D. Jespersen. *The design and application of upwind schemes on unstructured meshes*. Tech. rep. 1989.

[13] F. Bassi, A. Crivellini, D.A. Di Pietro, and S. Rebay. "An artificial compressibility flux for the discontinuous Galerkin solution of the incompressible Navier-Stokes equations". In: *Journal of Computational Physics* 218.2 (2006), pp. 794–815.

[14] F. Bassi, A. Crivellini, D.A. Di Pietro, and S. Rebay. "An implicit high-order discontinuous Galerkin method for steady and unsteady incompressible flows". In: *Computers & Fluids* 36 (2007), pp. 1529–1546.

[15] S. Baumann, L. Chandra, E. Skarga, M. Renker, M. Borggrefe, I. Akin, and D. Lossnitzer. "Instantaneous wave-free ratio (iFR®) to determine hemodynamically significant coronary stenosis: a comprehensive review". In: *World Journal of Cardiology* 10.12 (2018), pp. 267–277.

[16] J.B. Bell, P. Colella, and H.M. Glaz. "A second-order projection method for the incompressible Navier-Stokes equations". In: *Journal of Computational Physics* 85.2 (1989), pp. 257–283.

[17] F. Bellamoli, L.O. Müller, and E.F. Toro. "A numerical method for junctions in networks of shallow-water channels". In: *Applied Mathematics and Computation* 337 (2018), pp. 190–213.

[18] S. Bellavia. "Inexact interior-point method". In: *Journal of Optimization Theory and Applications* 96.1 (1998), pp. 109–121.

[19] S. Bellavia and S. Berrone. "Globalization strategies for Newton-Krylov methods for stabilized FEM discretization of Navier-Stokes equations". In: *Journal of Computational Physics* 226.2 (2007), pp. 2317–2340.

[20] S. Bellavia and B. Morini. "A globally convergent Newton-GMRES subspace method for systems of nonlinear equations". In: *SIAM Journal of Scientific Computing* 23.3 (2002), pp. 940–960.

[21] A. Bermúdez. *Continuum thermomechanics*. Vol. 43. Progress in Mathematical Physics. Birkhäuser Verlag, 2005.

[22] A. Bermúdez, S. Busto, M. Dumbser, J.L. Ferrín, L. Saavedra, and M.E. Vázquez-Cendón. "A staggered semi-implicit hybrid FV/FE projection method for weakly compressible flows". In: *Journal of Computational Physics* 421 (2020), p. 109743.

[23] A. Bermúdez, A. Dervieux, J.A. Desideri, and M.E. Vázquez-Cendón. "Upwind schemes for the two-dimensional shallow water equations with variable depth using unstructured meshes". In: *Computer Methods in Applied Mechanics and Engineering* 155.1 (1998), pp. 49–72.

[24] A. Bermúdez, J.L. Ferrín, L. Saavedra, and M.E. Vázquez-Cendón. "A projection hybrid finite volume/element method for low-Mach number flows". In: *Journal of Computational Physics* 271 (2014), pp. 360–378.

[25] A. Bermúdez, X. López, and M.E. Vázquez-Cendón. "Treating network junctions in finite volume solution of transient gas flow models". In: *Journal of Computational Physics* 344. Supplement C (2017), pp. 187–209.

[26] A. Bermúdez and M.E. Vázquez-Cendón. "Upwind methods for hyperbolic conservation laws with source terms". In: *Computational Fluids* 23.8 (1994), pp. 1049–1071.

[27] G. Bertaglia, V. Caleffi, and A. Valiani. “Modeling blood flow in viscoelastic vessels: the 1D augmented fluid–structure interaction system”. In: *Computer Methods in Applied Mechanics and Engineering* 360 (2020), p. 112772.

[28] G. Bertaglia, A. Navas-Montilla, A. Valiani, M.I. Monge-Garcıéa, J. Murillo, and V. Caleffi. “Computational hemodynamics in arteries with the one-dimensional augmented fluid-structure interaction system: viscoelastic parameters estimation and comparison with in-vivo data”. In: *Journal of Biomechanics* 100 (2020), p. 109595.

[29] D. Bessems, C.G. Giannopapa, M.C.M. Rutten, and F.N. Van De Vosse. “Experimental validation of a time-domain-based wave propagation model of blood flow in viscoelastic vessels”. In: *Journal of Biomechanics* 41 (2008), pp. 284–291.

[30] P.J. Blanco, G.D. Ares, S.A. Urquiza, and R.A. Feijóo. “On the effect of preload and pre-stretch on hemodynamic simulations: an integrative approach”. In: *Biomechanics and Modeling in Mechanobiology* 15.3 (June 2016), pp. 593–627.

[31] P.J. Blanco, C.A. Bulant, L.O. Müller, G.D. Talou, C.G. Bezerra, P.A. Lemos, and R.A. Feijóo. “Comparison of 1D and 3D models for the estimation of fractional flow reserve”. In: *Scientific reports* 8.1 (2018), pp. 1–12.

[32] P.J. Blanco and R.A. Feijóo. “A dimensionally-heterogeneous closed-loop model for the cardiovascular system and its applications”. In: *Medical Engineering & Physics* 35.5 (May 2013), pp. 652–667.

[33] *Blender Foundation*. URL: `www.blender.org`.

[34] A.N. Bocharov, N.M. Evstigneev, V.P. Petrovskiy, O.I. Ryabkov, and I.O. Teplyakov. “Implicit method for the solution of supersonic and hypersonic 3D flow problems with Lower-Upper Symmetric-Gauss-Seidel preconditioner on multiple graphics processing units”. In: *Journal of Computational Physics* 406 (2020), p. 109189.

[35] E. Boileau, P. Nithiarasu, P.J. Blanco, L.O. Müller, F.E. Fossan, L.R. Hellevik, W.P. Donders, W. Huberts, M. Willemet, and J. Alastruey. “A benchmark study of numerical schemes for one-dimensional arterial blood flow modelling”. In: *International Journal for Numerical Methods in Biomedical Engineering* 31.10 (2015), e02732.

[36] R. Borsche. “Numerical schemes for networks of hyperbolic conservation laws”. In: *Applied Numerical Mathematics* 108 (Oct. 2016), pp. 157–170.

[37] W. Boscheri and M. Dumbser. “A direct Arbitrary-Lagrangian-Eulerian ADER-WENO finite volume scheme on unstructured tetrahedral meshes for conservative and non-conservative hyperbolic systems in 3D”. In: *Journal of Computational Physics* 275 (2014), pp. 484–523.

[38] A.T. Bråten and R. Wiseth. *Diagnostic Accuracy of CT-FFR Compared to Invasive Coronary Angiography With Fractional Flow Reserve*. 2017. URL: `ClinicalTrials.gov`.

[39] M. Briani, G. Puppo, and M. Ribot. “Angle dependence in coupling conditions for shallow water equations at channel junctions”. In: *Computers & Mathematics with Applications* 108 (2022), pp. 49–65.

[40] B.S. Brook, S. Falle, and T.J. Pedley. “Numerical solutions for unsteady gravity-driven flows in collapsible tubes: evolution and roll-wave instability of a steady state”. In: *Journal of Fluid Mechanics* 396 (1999), pp. 223–256.

[41] B.S. Brook, S.A.E.G. Falle, and T.J. Pedley. “Numerical solutions for unsteady gravity-driven flows in collapsible tubes: evolution and roll-wave instability of a steady state”. In: *Journal of Fluid Mechanics* 396 (1999), pp. 223–256.

[42] L. Brugnano and V. Casulli. “Iterative solution of piecewise linear systems”. In: *SIAM Journal on Scientific Computing* 30 (2007), pp. 463–472.

[43] S. Busto and M. Dumbser. “A staggered semi-implicit hybrid finite volume/finite element scheme for the shallow water equations at all Froude numbers”. In: *Applied Numerical Mathematics* 175 (2022), pp. 108–132.

[44] S. Busto, M. Dumbser, and L. Río-Martín. “An Arbitrary-Lagrangian-Eulerian hybrid finite volume/finite element method on moving unstructured meshes for the Navier-Stokes equations”. In: *Applied Mathematics and Computation* 437 (2023), p. 127539.

[45] S. Busto, M. Dumbser, and L. Río-Martín. “Staggered Semi-Implicit Hybrid Finite Volume/Finite Element Schemes for Turbulent and non-Newtonian Flows”. In: *Mathematics* 9 (2021), p. 2972.

[46] S. Busto, J.L. Ferrín, E.F. Toro, and M.E. Vázquez-Cendón. “A projection hybrid high order finite volume/finite element method for incompressible turbulent flows”. In: *Journal of Computational Physics* 353 (2018), pp. 169–192.

[47] S. Busto, L. Río-Martín, M.E. Vázquez-Cendón, and M. Dumbser. “A semi-implicit hybrid finite volume/finite element scheme for all Mach number flows on staggered unstructured meshes”. In: *Applied Mathematics and Computation* 402 (2021), p. 126117.

[48] S. Busto, M. Tavelli, W. Boscheri, and M. Dumbser. “Efficient high order accurate staggered semi-implicit discontinuous Galerkin methods for natural convection problems”. In: *Computational Fluids* 198 (2020), p. 104399.

[49] A. Canestrelli, A. Siviglia, M. Dumbser, and E.F. Toro. “Well-balanced high-order centred schemes for non-conservative hyperbolic systems. Applications to shallow water equations with fixed and mobile bed”. In: *Advances in Water Resources* 32.6 (2009), pp. 834–844.

[50] J. Carson and R. Van Loon. “An implicit solver for 1D arterial network models”. In: *International Journal for Numerical Methods in Biomedical Engineering* 33.7 (2017), e2837.

[51] C.E. Castro and E.F. Toro. “Solvers for the high-order Riemann problem for hyperbolic balance laws”. In: *Journal of Computational Physics* 227.4 (2008), pp. 2481–2513.

[52] V. Casulli. “A semi-implicit numerical method for the free-surface Navier-Stokes equations”. In: *International Journal for Numerical Methods in Fluids* 74 (2014), pp. 605–622.

[53] V. Casulli, M. Dumbser, and E.F. Toro. "Semi-implicit numerical modeling of axially symmetric flows in compliant arterial systems". In: *International Journal for Numerical Methods in Biomedical Engineering* 28.2 (2012), pp. 257–272.

[54] V. Casulli and P. Zanolli. "A nested Newton–type algorithm for finite volume methods solving Richards' equation in mixed form". In: *SIAM Journal on Scientific Computing* 32 (2009), pp. 2255–2273.

[55] V. Casulli and P. Zanolli. "Iterative solutions of mildly nonlinear systems". In: *Journal of Computational and Applied Mathematics* 236 (2012), pp. 3937–3947.

[56] M. Cheng, G. Wang, and H.H. Mian. "Reordering of hybrid unstructured grids for an implicit Navier-Stokes solver based on OpenMP parallelization". In: *Computers & Fluids* 110 (2015), pp. 245–253.

[57] A. Chikitkin, M. Petrov, V. Titarev, and S. Utyuzhnikov. "Parallel versions of implicit LU-SGS method". In: *Lobachevskii Journal of Mathematics* 39.4 (2018), pp. 503–512.

[58] S. Childress. "New solutions of the kinematic dynamo problem". In: *Journal of Mathematical Physics* 11.10 (1970), pp. 3063–3076.

[59] E. Chiti. "Coronary blood flow distribution methods for model-based fractional flow reserve prediction". Master's thesis. Università di Trento, 2021.

[60] A.J. Chorin. "A numerical method for solving incompressible viscous flow problems". In: *Journal of Computational Physics* 2 (1967), pp. 12–26.

[61] R.M. Colombo and M. Garavello. "On the 1D modeling of fluid flowing through a Junction". In: *Discrete & Continuous Dynamical Systems-Series B* 25.10 (2020).

[62] R.M. Colombo, M. Herty, and V. Sachers. "On 2×2 conservation laws at a junction". In: *SIAM Journal on Mathematical Analysis* 40.2 (2008), pp. 605–622.

[63] P. Concus, G.H. Golub, and Y. Sun. "Object-oriented parallel algorithms for computing three-dimensional isopycnal flow". In: *International Journal for Numerical Methods in Fluids* 39.7 (2002), pp. 585–605.

[64] C. Contarino, E.F. Toro, G.I. Montecinos, R. Borsche, and J. Kall. "Junction-generalized Riemann problem for stiff hyperbolic balance laws in networks: an implicit solver and ADER schemes". In: *Journal of Computational Physics* 315 (2016), pp. 409–433.

[65] C.M Cook, R. Petraco, M.J. Shun-Shin, Y. Ahmad, S. Nijjer, R. Al-Lamee, Y. Kikuta, Y. Shiono, J. Mayet, D.P. Francis, S. Sen, and J.E. Davies. "Diagnostic accuracy of computed tomography–derived fractional flow reserve: a systematic review". In: *JAMA cardiology* 2.7 (2017), pp. 803–810.

[66] P. Crosetto, P. Reymond, S. Deparis, D. Kontaxakis, N. Stergiopulos, and A. Quarteroni. "Fluid-structure interaction simulation of aortic blood flow". In: *Computers and Fluids* 43.1 (2011), pp. 46–57.

[67] R.S. Dembo, S.C. Eisenstat, and T. Steihaug. "Inexact Newton methods". In: *SIAM Journal on Numerical Analysis* 19.2 (1982), pp. 400–408.

[68] F. Ducros, V. Ferrand, F. Nicoud, C. Weber, D. Darracq, C. Gacherieu, and T. Poinsot. “Large-eddy simulation of the shock/turbulence interaction”. In: *Journal of Computational Physics* 152 (1999), pp. 517–549.

[69] F. Ducros, F. Laporte, T. Soulères, V. Guinot, P. Moinat, and B. Caruelle. “A numerical method for large-eddy simulation in complex geometries”. In: *Journal of Computational Physics* 197 (2004), pp. 215–240.

[70] F. Ducros, F. Laporte, T. Soulères, V. Guinot, P. Moinat, and B. Caruelle. “High-Order Fluxes for Conservative Skew-Symmetric-like Schemes in Structured Meshes: Application to Compressible Flows”. In: *Journal of Computational Physics* 161 (2000), pp. 114–139.

[71] M. Dumbser, A. Hidalgo, M. Castro, C. Parés, and E.F. Toro. “FORCE Schemes on Unstructured Meshes II: Non–Conservative Hyperbolic Systems”. In: *Computer Methods in Applied Mechanics and Engineering* 199 (2010), pp. 625–647.

[72] M. Dumbser, U. Iben, and M. Ioriatti. “An efficient semi-implicit finite volume method for axially symmetric compressible flows in compliant tubes”. In: *Applied Numerical Mathematics* 89 (2015), pp. 24–44.

[73] H.C. Elman, D.J. Silvester, and A.J. Wathen. *Finite elements and fast iterative solvers: with applications in incompressible fluid dynamics*. Oxford university press, 2014.

[74] E. Erturk. “Numerical solutions of 2-D steady incompressible flow over a backward-facing step, Part I: High Reynolds number solutions”. In: *Computers & Fluids* 37.6 (2008), pp. 633–655.

[75] L. Euler. “Principia pro Motu Sanguinis per Arterias Determinando”. In: *Opera postuma* (1862), pp. 814–823.

[76] Ø. Evju and M.S. Alnæs. “CBCFLOW”. In: *Bitbucket Repository* (2017).

[77] F. Fambri, M. Dumbser, and V. Casulli. “An efficient semi-implicit method for three-dimensional non-hydrostatic flows in compliant arterial vessels”. In: *International Journal for Numerical Methods in Biomedical Engineering* 30.11 (2014), pp. 1170–1198.

[78] C.A. Figueroa, C.A. Taylor, and A.L. Marsden. “Blood flow”. In: *Encyclopedia of Computational Mechanics Second Edition* (2017), pp. 1–31.

[79] J.E. Flaherty, J.B. Keller, and S.I. Rubinow. “Post buckling behavior of elastic tubes and rings with opposite sides in contact”. In: *SIAM Journal on Applied Mathematics* 23.4 (1972), pp. 446–455.

[80] L. Formaggia, J.F. Gerbeau, F. Nobile, and A. Quarteroni. “On the coupling of 3D and 1D Navier-Stokes equations for flow problems in compliant vessels”. In: *Computer Methods in Applied Mechanics and Engineering* 191.6-7 (2001), pp. 561–582.

[81] L. Formaggia, D. Lamponi, and A. Quarteroni. “One-dimensional models for blood flow in arteries”. In: *Journal of Engineering Mathematics* 47 (2003), pp. 251–276.

[82] L. Formaggia, F. Nobile, A. Quarteroni, and A. Veneziani. "Multiscale modelling of the circulatory system: A preliminary analysis". In: *Computing and Visualization in Science* 2.2-3 (1999), pp. 75–83.

[83] L. Formaggia, K. Perktold, and A. Quarteroni. "Basic mathematical models and motivations". In: *Cardiovascular Mathematics: Modeling and Simulation of the Circulatory System* (2009), pp. 47–75.

[84] L. Formaggia, A. Quarteroni, and A. Veneziani. "Multiscale models of the vascular system". In: *Modeling, Simulation and Applications* 1 (2009), pp. 395–446.

[85] L. Formaggia, A. Quarteroni, and C. Vergara. "On the physical consistency between three-dimensional and one-dimensional models in haemodynamics". In: *Journal of Computational Physics* 244 (2013), pp. 97–112.

[86] L. Formaggia and A. Veneziani. "Reduced and multiscale models for the human cardiovascular system". In: *Lecture notes VKI lecture series* 7 (2003).

[87] L.a Formaggia, A. Quarteroni, and A. Veneziani. *Cardiovascular Mathematics: Modeling and simulation of the circulatory system*. Vol. 1. Springer Science & Business Media, 2010.

[88] F.E. Fossan, L.O. Müller, J. Sturdy, A.T. Bråten, A. Jørgensen, R. Wiseth, and L.R. Hellevik. "Machine learning augmented reduced-order models for FFR-prediction". In: *Computer Methods in Applied Mechanics and Engineering* 384 (2021), p. 113892.

[89] F.E. Fossan, J. Sturdy, L.O. Müller, A. Strand, A.T. Bråten, A. Jørgensen, R. Wiseth, and L.R. Hellevik. "Uncertainty quantification and sensitivity analysis for computational FFR estimation in stable coronary artery disease". In: *Cardiovascular Engineering and Technology* 9.4 (2018), pp. 597–622.

[90] O. Frank. *Die grundform des arteriellen pulses: mathematische analyse. erste abhandlung*. 1899.

[91] J.M. Fullana and S. Zaleski. "A branched one-dimensional model of vessel networks". In: *Journal of Fluid Mechanics* 621 (2009), pp. 183–204.

[92] Y.C. Fung. *Biomechanics: circulation*. 2nd. Springer-Verlag, 1997.

[93] E. Gaburro, W. Boscheri, S. Chiocchetti, C. Klingenberg, V. Springel, and M. Dumbser. "High order direct Arbitrary-Lagrangian-Eulerian schemes on moving Voronoi meshes with topology changes". In: *Journal of Computational Physics* 407 (2020), p. 109167.

[94] E. Gaburro, M.J. Castro, and M. Dumbser. "Well-balanced Arbitrary-Lagrangian-Eulerian finite volume schemes on moving nonconforming meshes for the Euler equations of gas dynamics with gravity". In: *Monthly Notices of the Royal Astronomical Society* 477.2 (2018), pp. 2251–2275.

[95] J.M. Gallardo, C. Parés, and M.J. Castro. "On a well-balanced high-order finite volume scheme for shallow water equations with topography and dry areas". In: *Journal of Computational Physics* 227 (2007), pp. 574–601.

[96] C. Geuzaine and J.F. Remacle. "Gmsh: A 3-D finite element mesh generator with built-in pre-and post-processing facilities". In: *International journal for numerical methods in engineering* 79.11 (2009), pp. 1309–1331.

[97] O. Ghekiere, R. Salgado, N. Buls, T. Leiner, I.E. Mancini, P. Vanhoenacker, P. Dendale, and A. Nchimi. "Image quality in coronary CT angiography: challenges and technical solutions". In: *The British journal of radiology* 90.1072 (2017), p. 20160567.

[98] U. Ghia, K.N. Ghia, and C.T. Shin. "High-Re solutions for incompressible flow using the Navier-Stokes equations and a multigrid method". In: *Journal of Computational Physics* 48.3 (1982), pp. 387–411.

[99] B. Ghitti, P.J. Blanco, E.F. Toro, and L.O. Müller. "Construction of hybrid 1D-0D networks for efficient and accurate blood flow simulations". In: *International Journal for Numerical Methods in Fluids* 95.2 (2023), pp. 262–312.

[100] B. Ghitti, E.F. Toro, and L.O. Müller. "Nonlinear lumped-parameter models for blood flow simulations in networks of vessels". In: *ESAIM: Mathematical Modelling and Numerical Analysis* 56.5 (2022), pp. 1579–1627.

[101] AMBOSS GmbH. *Heart*. URL: `https://www.amboss.com/`. Accessed August 2023.

[102] A.G. Goodwill, G.M. Dick, A.M. Kiel, and J.D. Tune. "Regulation of coronary blood flow". In: *Comprehensive Physiology* 7.2 (2017), p. 321.

[103] L. Grinberg, E. Cheever, T. Anor, J.R. Madsen, and G.E. Karniadakis. "Modeling blood flow circulation in intracranial arterial networks: a comparative 3D/1D simulation study". In: *Annals of biomedical engineering* 39 (2011), pp. 297–309.

[104] B. Guerciotti, C. Vergara, S. Ippolito, A. Quarteroni, C. Antona, and R. Scrofani. "A computational fluid–structure interaction analysis of coronary Y-grafts". In: *Medical engineering & physics* 47 (2017), pp. 117–127.

[105] J.L. Guermond, P. Minev, and J. Shen. "An overview of projection methods for incompressible flows". In: *Computer Methods in Applied Mechanics and Engineering* 195 (2006), pp. 6011–6045.

[106] E. Guilmineau and P. Queutey. "A numerical simulation of vortex shedding from an oscillating circular cylinder". In: *Journal of Fluids and Structures* 16.6 (2002), pp. 773–794.

[107] M.E. Gurtin. *An introduction to continuum mechanics*. Vol. 158. Mathematics in Science and Engineering. Academic Press Inc., 1981.

[108] F.H. Harlow and J.E. Welch. "Numerical calculation of time-dependent viscous incompressible flow of fluid with a free surface". In: *Physicss of Fluids* 8 (1965), pp. 2182–2189.

[109] A. Harten, B. Engquist, S. Osher, and S.R. Chakravarthy. "Uniformly high order accurate essentially non-oscillatory schemes, III". In: *Upwind and High-Resolution Schemes*. Springer, 1987, pp. 218–290.

[110] L.R. Hellevik, J. Vierendeels, T. Kiserud, N. Stergiopulos, F. Irgens, E. Dick, K. Riemslagh, and P. Verdonck. "An assessment of ductus venosus tapering and wave transmission from the fetal heart". In: *Biomechanics and Modeling in Mechanobiology* 8.6 (), pp. 509–517.

[111] R.J. Hemalatha, T.R. Thamizhvani, A.J.A. Dhivya, J.E. Joseph, B. Babu, and R. Chandrasekaran. "Active Contour Based Segmentation Techniques for Medical Image Analysis". In: *Medical and Biological Image Analysis*. Ed. by Robert Koprowski. Rijeka: IntechOpen, 2018. Chap. 2.

[112] N. Herring and D.J. Paterson. *Levick's introduction to cardiovascular physiology*. CRC Press, 2018.

[113] M. Hirschhorn, V. Tchantchaleishvili, R. Stevens, J. Rossano, and A. Throckmorton. "Fluid–structure interaction modeling in cardiovascular medicine–A systematic review 2017–2019". In: *Medical engineering & physics* 78 (2020), pp. 1–13.

[114] T.J.R. Hughes and J. Lubliner. "On the one-dimensional theory of blood flow in the larger vessels". In: *Mathematical Biosciences* 18.1-2 (1973), pp. 161–170.

[115] Y. Huo and G.S. Kassab. "Intraspecific scaling laws of vascular trees". In: *Journal of The Royal Society Interface* 9.66 (2012), pp. 190–200.

[116] SCOT-Heart Investigators. "Coronary CT angiography and 5-year risk of myocardial infarction". In: *New England Journal of Medicine* 379.10 (2018), pp. 924–933.

[117] M. Ioriatti, M. Dumbser, and U. Iben. "A comparison of explicit and semi-implicit finite volume schemes for viscous compressible flows in elastic pipes in fast transient regime". In: *ZAMM-Journal of Applied Mathematics and Mechanics* 97.11 (2017), pp. 1358–1380.

[118] *ITK-SNAP*. URL: `www.itksnap.org`.

[119] N.P. Johnson, R.L. Kirkeeide, and K.L. Gould. "Is discordance of coronary flow reserve and fractional flow reserve due to methodology or clinically relevant coronary pathophysiology?" In: *JACC: Cardiovascular Imaging* 5.2 (2012), pp. 193–202.

[120] R. Käppeli and S. Mishra. "Well-balanced schemes for the Euler equations with gravitation". In: *Journal of Computational Physics* 259 (2014), pp. 199–219.

[121] H.J. Kim, I.E. Vignon-Clementel, J.S. Coogan, C.A. Figueroa, K.E. Jansen, and C.A. Taylor. "Patient-specific modeling of blood flow and pressure in human coronary arteries". In: *Annals of biomedical engineering* 38.10 (2010), pp. 3195–3209.

[122] H.Y. Kim, H.S. Lim, J.H. Doh, C.W. Nam, E.S. Shin, B.K. Koo, M.H. Yoon, S.J. Tahk, D.K. Kang, Y.B. Song, et al. "Physiological severity of coronary artery stenosis depends on the amount of myocardial mass subtended by the coronary artery". In: *JACC: Cardiovascular Interventions* 9.15 (2016), pp. 1548–1560.

[123] J. Knuuti, W. Wijns, A. Saraste, D. Capodanno, E. Barbato, C. Funck-Brentano, E. Prescott, R.F. Storey, C. Deaton, T. Cuisset, S. Agewall, K. Dickstein, T. Edvardsen, J. Escaned, B.J. Gersh, P. Svitil, M. Gilard, D. Hasdai, R. Hatala, F. Mahfoud, J. Masip, C. Muneretto, M. Valgimigli, S. Achenbach, J.J. Bax, and ESC Scientific Document Group. "2019 ESC Guidelines for the diagnosis and management of chronic coronary syndromes: The Task Force for the diagnosis and management of chronic coronary syndromes of the European Society of Cardiology (ESC)". In: *European Heart Journal* 41.3 (2019), pp. 407–477.

[124] V.P. Kolgan. "Application of the principle of minimizing the derivative to the construction of finite-difference schemes for computing discontinuous solutions of gas dynamics". In: *Journal of Computational Physics* 230.7 (2011), pp. 2384–2390.

[125] J. W. Lambert. “On the nonlinearities of fluid flow in nonrigid tubes”. In: *Journal of the Franklin Institute* 266.2 (1958), pp. 83–102.

[126] B. van Leer. “A historical oversight: Vladimir P. Kolgan and his high-resolution scheme”. In: *Journal of Computational Physics* 230.7 (2011), pp. 2378–2383.

[127] B. van Leer. “On the relation between the upwind-differencing schemes of Godunov, Engquist-Osher and Roe”. In: *SIAM Journal on Scientific Computing* 5.1 (1984), pp. 1–20.

[128] J. Leipsic, S. Abbara, S. Achenbach, R. Cury, J.P. Earls, G.B. J. Mancini, K. Nieman, G. Pontone, and G.L. Raff. “SCCT guidelines for the interpretation and reporting of coronary CT angiography: a report of the Society of Cardiovascular Computed Tomography Guidelines Committee”. In: *Journal of cardiovascular computed tomography* 8.5 (2014), pp. 342–358.

[129] R.J. LeVeque. *Finite Volume Methods for Hyperbolic Problems*. Cambridge University Press, 2002.

[130] F.Y. Liang, S. Takagi, R. Himeno, and H. Liu. “Biomechanical characterization of ventricular–arterial coupling during aging: A multi-scale model study”. In: *Journal of Biomechanics* 42.6 (2009), pp. 692–704.

[131] M. Liu, G. Gao, H. Zhu, and C. Jiang. “A cell-based smoothed finite element method stabilized by implicit SUPG/SPGP/Fractional step method for incompressible flow”. In: *Engineering Analysis with Boundary Elements* 124 (2021), pp. 194–210.

[132] X. Liu, A. Chertock, A. Kurganov, and K. Wolfkill. “One-dimensional/two-dimensional coupling approach with quadrilateral confluence region for modeling river systems”. In: *Journal of Scientific Computing* 81 (2019), pp. 1297–1328.

[133] A. Logg, K. Mardal, and G. Wells. *Automated solution of differential equations by the finite element method: The FEniCS book*. Vol. 84. Springer Science & Business Media, 2012.

[134] C. Loudon and A. Tordesillas. “The use of the dimensionless Womersley number to characterize the unsteady nature of internal flow”. In: *Journal of Theoretical Biology* 191.1 (1998), pp. 63–78.

[135] A. Lucca, S. Busto, and M. Dumbser. “An implicit staggered hybrid finite volume/finite element solver for the incompressible Navier-Stokes equations”. In: *East Asian Journal on Applied Mathematics* 13 (2023), pp. 671–716.

[136] A. Lucca, S. Busto, L.O. Müller, E.F. Toro, and M. Dumbser. “A semi-implicit finite volume scheme for blood flow in elastic and viscoelastic vessels”. In: *Journal of computational Physics* (2023).

[137] A. Lucca, L. Fraccarollo, F.E. Fossan, A.T. Bråten, S. Pozzi, C. Vergara, and L.O. Müller. “Impact of pressure guidewire on model-based FFR prediction”. In: *Cardiovascular Engineering and Technology (submitted)* (2023).

[138] H. Luo, J.D. Baum, and R. Löhner. “A fast, matrix-free implicit method for compressible flows on unstructured grids”. In: *Journal of Computational Physics* 146.2 (1998), pp. 664–690.

[139] A.C.I. Malossi, P.J. Blanco, P. Crosetto, S. Deparis, and A. Quarteroni. "Implicit coupling of one-dimensional and three-dimensional blood flow models with compliant vessels". In: *Multiscale Modeling & Simulation* 11.2 (2013), pp. 474–506.

[140] S. Mantero, R. Pietrabissa, and R. Fumero. "The coronary bed and its role in the cardiovascular system: a review and an introductory single-branch model". In: *Journal of biomedical engineering* 14.2 (1992), pp. 109–116.

[141] K.S. Matthys, J. Alastruey, J. Peiró, A.W. Khir, P. Segers, P.R. Verdonck, K.H. Parker, and S.J. Sherwin. "Pulse wave propagation in a model human arterial network: assessment of 1-D numerical simulations against in vitro measurements". In: *Journal of Biomechanics* 40.15 (2007), pp. 3476–3486.

[142] I. Menshov and P. Pavlukhin. "Highly scalable implementation of an implicit matrix-free solver for gas dynamics on GPU-accelerated clusters". In: *The Journal of Supercomputing* 73.2 (2017), pp. 631–638.

[143] I.S. Menśhov and Y. Nakamura. "On implicit Godunov's method with exactly linearized numerical flux". In: *Computers & fluids* 29.6 (2000), pp. 595–616.

[144] D. Meza, D.A. Rubenstein, and W. Yin. "A fluid–structure interaction model of the left coronary artery". In: *Journal of biomechanical engineering* 140.12 (2018), p. 121006.

[145] G.I Montecinos, L.O. Müller, and E.F. Toro. "Hyperbolic reformulation of a 1D viscoelastic blood flow model and ADER finite volume schemes". In: *Journal of Computational Physics* 266 (2014), pp. 101–123.

[146] G.I. Montecinos and E.F. Toro. "Reformulations for general advection–diffusion–reaction equations and locally implicit ADER schemes". In: *Journal of Computational Physics* 275 (2014), pp. 415–442.

[147] M. Mortensen and K. Valen-Sendstad. "Oasis: a high-level/high-performance open source Navier–Stokes solver". In: *Computer physics communications* 188 (2015), pp. 177–188.

[148] L.O. Müller and P.J. Blanco. "A high order approximation of hyperbolic conservation laws in networks: Application to one-dimensional blood flow". In: *Journal of Computational Physics* 300 (2015), pp. 423–437.

[149] L.O. Müller, F.E. Fossan, A.T. Bråten, A. Jørgensen, R. Wiseth, and L.R. Hellevik. "Impact of baseline coronary flow and its distribution on fractional flow reserve prediction". In: *International Journal for Numerical Methods in Biomedical Engineering* 37.11 (2021), e3246.

[150] L.O. Müller, G. Leugering, and P.J. Blanco. "Consistent treatment of viscoelastic effects at junctions in one-dimensional blood flow models". In: *Journal of Computational Physics* 314 (2016), pp. 167–193.

[151] L.O. Müller, G.I. Montecinos, and E.F. Toro. "Some issues in modelling venous haemodynamics". In: *Numerical Methods for Hyperbolic Equations: Theory and Applications. An international conference to honour Professor E.F. Toro.* Ed. by P. García-Navarro M.E. Vázquez-Cendón A. Hidalgo and L. Cea. Taylor & Francis Group, Boca Raton London New York Leiden, 2013, pp. 347–354.

[152] L.O. Müller, C. Parés, and E.F. Toro. “Well-balanced high-order numerical schemes for one-dimensional blood flow in vessels with varying mechanical properties”. In: *Journal of Computational Physics* 242 (2013), pp. 53–85.

[153] L.O. Müller and E.F. Toro. “A global multiscale mathematical model for the human circulation with emphasis on the venous system”. In: *International Journal for Numerical Methods in Biomedical Engineering* 30.7 (2014), pp. 681–725.

[154] L.O. Müller and E.F. Toro. “Well-balanced high-order solver for blood flow in networks of vessels with variable properties”. In: *International Journal for Numerical Methods in Biomedical Engineering* 29.12 (2013), pp. 1388–1411.

[155] L.O. Müller, S.M. Watanabe, E.F. Toro, R.A. Feijóo, and P.J. Blanco. “An anatomically detailed arterial-venous network model. Cerebral and coronary circulation”. In: *Frontiers in Physiology* 14 (2023), p. 1162391.

[156] J. Murillo and P. Garcıéa-Navarro. “A Solution of the Junction Riemann Problem for 1D Hyperbolic Balance Laws in Networks including Supersonic Flow Conditions on Elastic Collapsible Tubes”. In: *Symmetry* 13.9 (2021), p. 1658.

[157] C.D. Murray. “The physiological principle of minimum work: I. The vascular system and the cost of blood volume”. In: *Proceedings of the national academy of sciences of the united states of america* 12.3 (1926), p. 207.

[158] J.P. Mynard and P. Nithiarasu. “A 1D arterial blood flow model incorporating ventricular pressure, aortic valve and regional coronary flow using the locally conservative Galerkin (LCG) method”. In: *Communications in Numerical Methods in Engineering* 24.5 (2008), pp. 367–417.

[159] J.P. Mynard and J.J. Smolich. “One-dimensional haemodynamic modeling and wave dynamics in the entire adult circulation”. In: *Annals of Biomedical Engineering* 43.6 (2015), pp. 1443–1460.

[160] J.P. Mynard and K. Valen-Sendstad. “A unified method for estimating pressure losses at vascular junctions”. In: *International Journal for Numerical Methods in Biomedical Engineering* 31.7 (2015).

[161] F.J. Neumann, M. Sousa-Uva, A. Ahlsson, F. Alfonso, A.P. Banning, U. Benedetto, R.A. Byrne, J.P. Collet, V. Falk, and S.J. Head. “ESC/EACTS guidelines on myocardial revascularization”. In: *European heart journal* 40 (2018), pp. 87–165.

[162] N.C. Nguyen, J. Peraire, and B. Cockburn. “An implicit high-order hybridizable discontinuous Galerkin method for the incompressible Navier-Stokes equations”. In: *Journal of Computational Physics* 230 (2011), pp. 1147–1170.

[163] S. Noelle, G. Bispen, K.R. Arun, M. Lukáčová-Medvid’ová, and C.D. Munz. “An Asymptotic Preserving all Mach Number Scheme for the Euler Equations of Gas Dynamics”. In: *Report 348, Institut für Geometrie und Praktische Mathematik, RWTH Aachen, Germany.* 2014.

[164] M.S. Olufsen, C.S. Peskin, W.Y. Kim, E.M. Pedersen, A. Nadim, and J. Larsen. “Numerical simulation and experimental validation of blood flow in arteries with structured-tree outflow conditions”. In: *Annals of Biomedical Engineering* 28 (2000), pp. 1281–1299.

[165] World Health Organization. *Top 10 Causes of Death*. URL: https://www.who.int/news-room/fact-sheets/detail/the-top-10-causes-of-death. 2020.

[166] J.T. Ottesen, M.S. Olufsen, and J.K. Larsen, eds. *Applied Mathematical Models in Human Physiology*. SIAM Monographs on Mathematical Modeling and Computation 9. Society for Industrial and Applied Mathematics, 2004.

[167] J.H. Park and C.D. Munz. "Multiple pressure variables methods for fluid flow at all Mach numbers". In: *International journal for numerical methods in fluids* 49.8 (2005), pp. 905–931.

[168] S.V. Patankar and D.B. Spalding. "A calculation procedure for heat, mass and momentum transfer in three-dimensional parabolic flows". In: *International Journal of Heat and Mass Transfer* 15.10 (1972), pp. 1787–1806.

[169] V.S. Patankar. *Numerical Heat Transfer and Fluid Flow*. Hemisphere Publishing Corporation, 1980.

[170] F. Piccioli, G. Bertaglia, A. Valiani, and V. Caleffi. "Modeling blood flow in networks of viscoelastic vessels with the 1-D augmented fluid–structure interaction system". In: *Journal of Computational Physics* 464 (2022), p. 111364.

[171] N.H.J. Pijls and J.W.E.M. Sels. "Functional Measurement of Coronary Stenosis". In: *Journal of the American College of Cardiology* 59.12 (2012), pp. 1045–1057.

[172] N.H.J. Pijls, B. Van Gelder, P. Van der Voort, K. Peels, F. Bracke, H. Bonnier, and M. I.H. El Gamal. "Fractional flow reserve: a useful index to evaluate the influence of an epicardial coronary stenosis on myocardial blood flow". In: *Circulation* 92.11 (1995), pp. 3183–3193.

[173] E. Pimentel-García, L.O. Müller, E.F. Toro, and C. Parés. "High-order fully well-balanced numerical methods for one-dimensional blood flow with discontinuous properties". In: *Journal of Computational Physics* 475 (2023), p. 111869.

[174] A. Quarteroni and L. Formaggia. "Mathematical Modelling and Numerical Simulation of the Cardiovascular System". In: *Handbook of Numerical Analysis* 12 (2004), pp. 3–127.

[175] A. Quarteroni, L. Formaggia, and A. Veneziani. "Cardiovascular Mathematics: Modeling and simulation of the circulatory system". In: *Modeling, Simulation and Applications* 1 (2009), pp. 1–512.

[176] A. Quarteroni, A. Manzoni, and C. Vergara. "The Cardiovascular System: Mathematical Modelling, Numerical Algorithms and Clinical Applications". In: *Acta Numerica* 26 (May 2017), pp. 365–590.

[177] A. Quarteroni, S. Ragni, and A. Veneziani. "Coupling between lumped and distributed models for blood flow problems". In: *Computing and Visualization in Science* 4.2 (2001), pp. 111–124.

[178] S.H. Ralston, I.D. Penman, M.W.J. Strachan, and R. Hobson. *Davidson's Principles and Practice of Medicine E-Book*. Elsevier Health Sciences, 2018.

[179] A.B. Ramachandra, A.M. Kahn, and A.L. Marsden. "Patient-specific simulations reveal significant differences in mechanical stimuli in venous and arterial coronary grafts". In: *Journal of cardiovascular translational research* 9.4 (2016), pp. 279–290.

[180] T. Ramanathan and H. Skinner. "Coronary blood flow". In: *Continuing Education in Anaesthesia, Critical Care & Pain* 5.2 (2005), pp. 61–64.

[181] N.A. Ramjattan, V. Lala, O. Kousa, and A.N. Makaryus. *Coronary CT Angiography.* StatPearls Publishing, Treasure Island (FL), 2022.

[182] P. Reymond, F. Merenda, F. Perren, D. Rufenacht, and N. Stergiopulos. "Validation of a one-dimensional model of the systemic arterial tree". In: *American Journal of Physiology-Heart and Circulatory Physiology* 297.1 (2009), H208–H222.

[183] S. Rhebergen and B. Cockburn. "A space-time hybridizable discontinuous Galerkin method for incompressible flows on deforming domains". In: *Journal of Computational Physics* 231 (2012), pp. 4185–4204.

[184] S. Rhebergen, B. Cockburn, and J.J.W. Van Der Vegt. "A space-time discontinuous Galerkin method for the incompressible Navier-Stokes equations". In: *Journal of Computational Physics* 233 (2013), pp. 339–358.

[185] L. Río-Martín, S. Busto, and M. Dumbser. "A massively parallel hybrid finite volume/finite element scheme for computational fluid dynamics". In: *Mathematics* 9 (2021), p. 2316.

[186] G. Rogers and T. Oosthuyse. "A comparison of the indirect estimate of mean arterial pressure calculated by the conventional equation and calculated to compensate for a change in heart rate". In: *International journal of sports medicine* 21.02 (2000), pp. 90–95.

[187] A. Rossi, S.L. Papadopoulou, F. Pugliese, B. Russo, A.S. Dharampal, A. Dedic, P.H. Kitslaar, A. Broersen, W.B Meijboom, and R. van Geuns. "Quantitative computed tomographic coronary angiography: does it predict functionally significant coronary stenoses?" In: *Circulation: Cardiovascular Imaging* 7.1 (2014), pp. 43–51.

[188] Y. Saad and M.H. Schultz. "GMRES: A generalized minimal residual algorithm for solving nonsymmetric linear systems". In: *SIAM Journal on Scientific and Statistical Computing* 7.3 (1986), pp. 856–869.

[189] S. Sakamoto, S. Takahashi, A.U. Coskun, M.I. Papafaklis, A. Takahashi, S. Saito, P.H. Stone, and C.L. Feldman. "Relation of distribution of coronary blood flow volume to coronary artery dominance". In: *The American journal of cardiology* 111.10 (2013), pp. 1420–1424.

[190] F.M. Sant'Anna and L.B. Sant'Anna. "Analysis of FFR Measurement Clinical Impact and Cost-Effectiveness Compared to Angiography In Multi-Arterial Patients Undergoing PCI." In: *Arq Bras Cardiol.* 112.1 (2019), pp. 48–49.

[191] H. Schlichting and K. Gersten. *Boundary-layer theory.* Springer, 2016.

[192] H. Schlichting and J. Kestin. *Boundary layer theory.* Vol. 121. Springer, 1961.

[193] W. Schroeder, K. Ken Martin, and B. Lorensen. *The Visualization Toolkit (4th ed.)* Kitware, 2006. ISBN: 978-1-930934-19-1.

[194] F. Setzwein, P. Ess, and P. Gerlinger. "An implicit high-order k-exact finite-volume approach on vertex-centered unstructured grids for incompressible flows". In: *Journal of Computational Physics* 446 (2021), p. 110629.

[195] J.S. Shahoud, M. Ambalavanan, and V.S. Tivakaran. “Cardiac dominance”. In: (2019).

[196] D. Sharov and K. Nakahashi. “Reordering of 3-D hybrid unstructured grids for vectorized lu-sgs navier-stokes computations”. In: *AIAA 13th Computational Fluid Dynamics Conference* (1997), pp. 131–138.

[197] S.J. Sherwin, L. Formaggia, J. Peirò, and V. Franke. “Computational modelling of 1D blood flow with variable mechanical properties and its application to the simulation of wave propagation in the human arterial system”. In: *International Journal for Numerical Methods in Fluids* 43 (2003), pp. 673–700.

[198] S.J. Sherwin, V. Franke, J. Peirò, and K. Parker. “One-dimensional modelling of a vascular network in space-time variables”. In: *Journal of Engineering Mathematics* 47 (2003b), pp. 217–250.

[199] J.C. Simo and F. Armero. “Unconditional stability and long-term behavior of transient algorithms for the incompressible Navier-Stokes and Euler equations”. In: *Computer Methods in Applied Mechanics and Engineering* 111.1-2 (1994), pp. 111–154.

[200] K. Sommer, R. Schmidt, D. Graafen, H. Breit, and L. M. Schreiber. “Contrast agent bolus dispersion in a realistic coronary artery geometry: influence of outlet boundary conditions”. In: *Annals of biomedical engineering* 42.4 (2014), pp. 787–796.

[201] A. Spilimbergo, E.F. Toro, and L.O. Müller. “One-dimensional blood flow with discontinuous properties and transport: Mathematical analysis and numerical schemes”. In: *Communications in Computational Physics* 29.3 (2021), pp. 649–697.

[202] C. Spiller, E.F. Toro, M.E. Vázquez-Cendón, and C. Contarino. “On the exact solution of the Riemann problem for blood flow in human veins, including collapse”. In: *Applied Mathematics and Computation* 303 (2017), pp. 178–189.

[203] S. Standring. *Gray’s anatomy e-book: the anatomical basis of clinical practice*. Elsevier Health Sciences, 2021.

[204] D.A. Steinman. “Image-based computational fluid dynamics modeling in realistic arterial geometries”. In: *Annals of biomedical engineering* 30.4 (2002), pp. 483–497.

[205] J.C. Stettler, P. Niederer, M. Anliker, and M. Casty. “Theoretical analysis of arterial hemodynamics including the influence of bifurcations. Part II: Critical evaluation of theoretical model and comparison with noninvasive measurements of flow patterns in normal and pathological cases”. In: *Annals of Biomedical Engineering* 9 (1981), pp. 165–175.

[206] M. Tavakol, S. Ashraf, and S.J. Brener. “Risks and complications of coronary angiography: a comprehensive review”. In: *Global journal of health science* 4.1 (2012), p. 65.

[207] M. Tavelli and M. Dumbser. “A pressure-based semi-implicit space-time discontinuous Galerkin method on staggered unstructured meshes for the solution of the compressible Navier-Stokes equations at all Mach numbers”. In: *Journal of Computational Physics* 341 (2017), pp. 341–376.

[208] M. Tavelli and M. Dumbser. "A staggered semi-implicit discontinuous Galerkin method for the two dimensional incompressible Navier-Stokes equations". In: *Applied Mathematics and Computation* 248 (2014), pp. 70–92.

[209] M. Tavelli and M. Dumbser. "A staggered space-time discontinuous Galerkin method for the three-dimensional incompressible Navier-Stokes equations on unstructured tetrahedral meshes". In: *Journal of Computational Physics* 319 (2016), pp. 294–323.

[210] M. Tavelli, M. Dumbser, and V. Casulli. "High resolution methods for scalar transport problems in compliant systems of arteries". In: *Applied Numerical Mathematics* 74 (2013), pp. 62–82.

[211] C.A. Taylor, M.T. Draney, J.P. Ku, D. Parker, B.N. Steele, K. Wang, and C.K. Zarins. "Predictive medicine: computational techniques in therapeutic decision-making". In: *Computer Aided Surgery: Official Journal of the International Society for Computer Aided Surgery (ISCAS)* 4.5 (1999), pp. 231–247.

[212] *The Vascular Modeling Toolkit*. URL: `www.vmtk.org`.

[213] A. Thomann, G. Puppo, and C. Klingenber. "An all speed second order IMEX relaxation schemefor the Euler equations". In: (2020).

[214] E.F. Toro. "Brain venous haemodynamics, neurological diseases and mathematical modelling. A review". In: *Applied Mathematics and Computation* 272 (2016), pp. 542–579.

[215] E.F. Toro. *Riemann solvers and numerical methods for fluid dynamics: A practical introduction*. Springer, 2009.

[216] E.F. Toro and S.J. Billett. "Centred TVD schemes for hyperbolic conservation laws". In: *IMA Journal of Numerical Analysis* 20.1 (2000), pp. 47–79.

[217] E.F. Toro and G.I. Montecinos. "Advection-diffusion-reaction equations: hyperbolization and high-order ADER discretizations". In: *SIAM J. Sci. Comp.* 36.5 (2014), A2423–A2457.

[218] E.F. Toro and A. Siviglia. "Flow in collapsible tubes with discontinuous mechanical properties: mathematical model and exact solutions". In: *Communications in Computational Physics* 13.2 (2013), pp. 361–385.

[219] E.F. Toro and M.E. Vázquez-Cendón. "Flux splitting schemes for the Euler equations". In: *Computers & Fluids* 70 (2012), pp. 1–12.

[220] P.R. Trenhago, L.G. Fernandes, L.O. Müller, P.J. Blanco, and R.A. Feijóo. "An integrated mathematical model of the cardiovascular and respiratory systems". In: *International Journal for Numerical Methods in Biomedical Engineering* 32.1 (2016), e02736.

[221] S. Turek. "A comparative study of time-stepping techniques for the incompressible Navier-Stokes equations: from fully implicit non-linear schemes to semi-implicit projection methods". In: *International Journal for Numerical Methods in Fluids* 22.10 (1996), pp. 987–1011.

[222] D. Valdez-Jasso, M.A. Haider, H.T. Banks, D.B. Santana, Y.Z. Germán, R.L. Armentano, and M.S. Olufsen. "Analysis of viscoelastic wall properties in ovine arteries". In: *IEEE transactions on biomedical engineering* 56.2 (2008), pp. 210–219.

[223] H.A. Van der Vorst. "Bi-CGSTAB: A fast and smoothly converging variant of Bi-CG for the solution of nonsymmetric linear systems". In: *SIAM Journal on Scientific and Statistical Computing* 13.2 (1992), pp. 631–644.

[224] K.J. Van Stralen, V.S. Stel, J.B. Reitsma, F.W. Dekker, C. Zoccali, and K.J. Jager. "Diagnostic methods I: sensitivity, specificity, and other measures of accuracy". In: *Kidney international* 75.12 (2009), pp. 1257–1263.

[225] M.E. Vázquez-Cendón. "Improved treatment of source terms in upwind schemes for the shallow water equations in channels with irregular geometry". In: *Journal of Computational Physics* 148.2 (1999), pp. 497–526.

[226] M.E. Vázquez-Cendón and L. Cea. "Analysis of a new Kolgan-type scheme motivated by the shallow water equations". In: *Applied Numerical Mathematics* 62.4 (2012), pp. 489–506.

[227] I.E. Vignon-Clementel, C.A. Figueroa, K.E. Jansen, and C.A. Taylor. "Outflow boundary conditions for 3D simulations of non-periodic blood flow and pressure fields in deformable arteries". In: *Computer methods in biomechanics and biomedical engineering* 13.5 (2010), pp. 625–640.

[228] I.E. Vignon-Clementel, C.A. Figueroa, K.E. Jansen, and C.A. Taylor. "Outflow boundary conditions for three-dimensional finite element modeling of blood flow and pressure in arteries". In: *Computer methods in applied mechanics and engineering* 195.29-32 (2006), pp. 3776–3796.

[229] I. Wayand. *A staggered semi-implicit discontinuous Galerkin scheme for the simulation of incompressible flows through junctions in pipe networks*. May 2017.

[230] N. Westerhof, J. Lankhaar, and B.E. Westerhof. "The arterial windkessel". In: *Medical & biological engineering & computing* 47.2 (2009), pp. 131–141.

[231] N. Westerhof, N. Stergiopulos, M.I.M. Noble, and B.E. Westerhof. *Snapshots of hemodynamics: an aid for clinical research and graduate education*. Vol. 7. Springer, 2010.

[232] C.H.K. Williamson and G.L. Brown. "A series in $1/\sqrt{Re}$ to represent the Strouhal-Reynolds number relatioship of the cylinder wake". In: *Journal of Fluids and Structures* 12.8 (1998), pp. 1073–1085.

[233] J.R. Womersley. "Method for the calculation of velocity, rate of flow and viscous drag in arteries when the pressure gradient is known". In: *The Journal of Physiology* 127 (1955), pp. 553–563.

[234] N. Xiao, J. Alastruey, and C.A. Figueroa. "A systematic comparison between 1-D and 3-D hemodynamics in compliant arterial models". In: *International Journal for Numerical Methods in Biomedical Engineering* 30.2 (2014), p. 204.

[235] J. Yi, F. Tian, A. Simmons A., and T. Barber. "A Computational Analysis of the Influence of a Pressure Wire in Evaluating Coronary Stenosis". In: *Fluids* 6.4 (2021), p. 165.

[236] S. Yoon and A. Jameson. "Lower-upper symmetric-Gauss-Seidel method for the Euler and Navier-Stokes equations". In: *AIAA journal* 26.9 (1988), pp. 1025–1026.

[237] T. Young. “I. The croonian lecture. On the functions of the heart and arteries”. In: *Philosophical Transactions of the Royal Society of London* 99 (1809), pp. 1–31.

[238] P.A. Yushkevich, J. Piven, H.C. Hazlett, R.G. Smith, S. Ho, J.C. Gee, and G. Gerig. “User-guided 3D active contour segmentation of anatomical structures: significantly improved efficiency and reliability”. In: *Neuroimage* 31.3 (2006), pp. 1116–1128.

[239] W. Zhu, N. Zeng, and N. Wang. “Sensitivity, specificity, accuracy, associated confidence interval and ROC analysis with practical SAS implementations”. In: *NESUG proceedings: health care and life sciences, Baltimore, Maryland* 19 (2010), p. 67.

Nomenclature

We include a list of the main notations used in this thesis.

The implicit staggered hybrid finite volume/finite element solver for the incompressible Navier-Stokes equations

Physical variables

Notation	Description	Units
ρ	density	$\mathrm{kg/m^3}$
p	pressure	Pa
$\mathbf{u}$	velocity	m/s
τ	viscous part of the Cauchy stress tensor	Pa
μ	dynamic viscosity	kg/(m s)
g	gravity	kg/s
$\mathcal{F}$	flux tensor	$(\mathrm{ms})^{-1}$

Notation related to the discrete equations

Notation	Description
$\mathbf{w}^n$	approximation of momentum
$\mathbf{w}^*$	intermediate approximation of momentum
δp	pressure correction
$\delta \mathbf{w}^{**}$	convective-pressure contribution to residual
$\mathbf{M}$	global mass matrix
$\mathbf{K}$	global stiffness matrix
$\mathcal{P}^{-1}$	preconditioning matrix

Numerical functions

Notation	Description
ϕ^R	Rusanov numerical flux function
α^r	Rusanov numerical dissipation coefficient
ϕ^D	Ducros numerical flux function
α^d	Ducros numerical dissipation coefficient
$\mathbf{f}$	residual in Newton's transport-diffusion system

Mesh related notations

Notation	Description
T_k	tetrahedron of the FE mesh
B_k	barycenter of T_k
V_j	vertex of T_k
C_i	cell of the FV mesh
$\|C_i\|$	volume of cell C_i
N_i	node of C_i
$\mathcal{K}_i$	set of the neighbouring nodes of N_i
Γ_i	boundary of C_i
Γ_{ij}	interface between cells C_i and C_j
N_{ij}	barycenter of Γ_{ij}
$\boldsymbol{n}_{ij}$	outward unit normal vector to Γ_{ij}
$\|\|\boldsymbol{\eta}_{ij}\|\|$	area of Γ_{ij}
$\boldsymbol{\eta}_{ij}$	weighted outward normal vector, $\boldsymbol{n}_{ij}\|\|\boldsymbol{\eta}_{ij}\|\|$
T_{ij}	auxiliary tetrahedra related to face Γ_{ij}
T_{ijL}, T_{ijR}	upwind auxiliary tetrahedra related to face Γ_{ij}

The semi-implicit finite volume scheme for blood flow in elastic and viscoelastic vessels

Physical variables

Notation	Description	Units
A	cross-sectional area	m^2
K_R	viscous resistance coefficient	m^2/s
$\hat{p}$	elastic pressure	Pa
q	mass flux	m/s
F	convective physical flux	$(\mathrm{ms})^{-1}$
M	fluid mass	m^3

Notation related to the tube law

Notation	Description	Units
σ	vessel's wall stress	
ϵ	vessel's wall strain	
A_0	reference cross-sectional area	m^2
p_e	external pressure	Pa
K	stiffness coefficient	
Γ	viscoelastic parameter	
φ	function accounting for the viscoelastic behavior of the vessel wall	
ψ	function accounting for the elastic behavior of the vessel wall	

Notation related to the spatial discretization

Notation	Description
C_j	primal cell
D_j	dual cell
x_j	node of the primal cell C_j
$x_{j+\frac{1}{2}}$	node of the dual cell D_j
N_p	number of primal control volumes
N_d	number of dual control volumes

Notation	Description
Δx	primal cell length
Δx^D	dual cell length
Δt	time step
t_{end}	final time of a simulation
$q^n_{j+\frac{1}{2}}$	discrete mass-flux
$q^*_{j+\frac{1}{2}}$	intermediate discrete mass-flux
$q^{**}_{j+\frac{1}{2}}$	second intermediate discrete mass-flux
A^n_j	discrete cross-sectional area
p^n_j	discrete pressure
f^n_i	discrete numerical flux function
$\gamma^n_{j+\frac{1}{2}}$	discrete source term coefficient
α_i	numerical dissipation coefficient
CFL	Courant-Friedrichs-Lewy number
c	wave speed
$\mathbf{M}$	diagonal matrix of mass fluid
$\mathbf{T}$	symmetric-positive-definite matrix in pressure system
$\mathbf{p}^{n+1}$	vector of the pressure at the primal vertices
R	resistance
C	compliance
$\mathbf{f}^n_i$	three-dimensional physical flux at the i-th junction
$\mathbf{q}^n_i$	multidimensional flux at the i-th junction
σ_{ij}	sign function

Impact of pressure guidewire on model-based FFR prediction in 3D

Clinical notation

Notation	Description
LCA	left coronary artery
RCA	right coronary artery
LCX	circumflex artery
LAD	left anterior descending
PDA	posterior descending artery
CAD	coronary artery disease
FFR	Fractional Flow Reserve
CCTA	coronary computed tomography angiography
ECG	electrocardiogram
MAP	mean aortic pressure
CO	cardiac output

Notation related to the micro-circulatory model

Notation	Description
R_a	coronary arterial resistance
$R_{a-micro}$	coronary arterial micro-circulation resistance
R_v	coronary venous resistance
C_a	coronary arterial compliance
C_{myo}	myocardial compliance
p_{LV}	left ventricle pressure
p_v	venous pressure
C_{tot}	total peripheral compliance
TCRI	total coronary resistance index

Notation related to results

Notation	Description
FFR_{pred}	FFR predicted in the wire-absent configuration
gFFR_{pred}	FFR predicted in the wire-included configuration
ΔP	trans-stenotic pressure drop

Notation related to clinical statistic indexes

Notation	Description
TP	true positive
TN	true negative
FP	false positive
FN	false negative
ROC	receiver operating characteristic curve
AUC	area under curve